# Growth of axial and core-shell (In,Ga)N/GaN heterostructures on GaN nanowires on TiN

D I S S E R T A T I O N

zur Erlangung des akademischen Grades

d o c t o r  r e r u m  n a t u r a l i u m
(Dr. rer. nat.)
im Fach Physik
Spezialisierung: Experimentalphysik
eingereicht an der
Mathematisch-Naturwissenschaftlichen Fakultät
Humboldt-Universität zu Berlin

von
**M. Sc. David van Treeck**

Präsident der Humboldt-Universität zu Berlin:
Prof. Dr. Peter Frensch (kommissarisch)

Dekan der Mathematisch-Naturwissenschaftlichen Fakultät:
Prof. Dr. Elmar Kulke

Gutachter:
(i) Prof. Dr. Henning Riechert
(ii) Prof. Dr. Bruno Daudin
(iii) Prof. Dr. Ted W. Masselink

*Tag der mündlichen Prüfung:* 04.02.2022

*"I may not have gone where I intended to go, but I think I have ended up where I needed to be."*

Douglas Adams

**Abstract**

In this thesis, the growth and the optical characteristics of self-assembled GaN nanowires on TiN and nanowire-based (In,Ga)N/GaN heterostructures for LED applications is investigated. To this end, the self-assembled growth of long, thin and uncoalesced GaN nanowires on TiN by molecular beam epitaxy is demonstrated. So far, the self-assembled formation of nanowires combining all these beneficial properties has been very difficult. The study shows that due to interfacial reactions of the initial Ti film, morphologically well-developed nanowire ensembles with good luminescence properties can only be obtained for certain film thicknesses and very specific nitridation and growth conditions. Moreover, the study reveals that the absence of coalescence in these nanowire ensembles results from the low nanowire number density, which can be explained by diffusion-induced repulsion of neighboring nanowires during the nucleation phase.

Subsequently, these well-separated and uncoalesced GaN nanowires on TiN are used as a basis for the fabrication of axial and radial heterostructures. In contrast to the growth of axial heterostructures on typical irregular aggregates on other substrates, the growth of GaN nanowires on TiN results in well-defined axial (In,Ga)N quantum wells, which show a rectangular cross-section and extend along the c-plane. Despite the well-defined morphology of the active regions, the luminous efficiency of these heterostructures is found to be rather low.

As an alternative to axial heterostructures, the growth of nitride-based core-shell structures on the non-polar nanowire side facets, which promise a large active region area, is investigated. To better understand the potential of molecular beam epitaxy for the growth of core-shell structures in general, the aspect of the side facets of the nanowires being only sequentially exposed to the different material beams is studied by modeling the shell growth of GaN shells on GaN nanowires. It is shown that Ga adatom diffusion processes between different facets strongly affect the growth on the side facets. Based on these fundamental investigations, the growth of radially symmetric (In,Ga)N shells is studied and it is demonstrated that the growth of shells emitting in the green spectral range is feasible by molecular beam epitaxy. However, due to an increased material diffusion towards the nanowire top, large top segments form during the growth of the (In,Ga)N/GaN core-shell structures which may affect a homogeneous processing of the final LED device.

To tackle these challenges, a new growth approach which allows the controlled deposition of III-nitride shells on different sides of the nanowire and which may reduce the formation of enlarged top segments is presented. Using the directionality of the material beams in an molecular beam epitaxy system, the novel approach facilitates the sequential deposition of different compound materials on a specific side of the nanowires to grow a one-sided shell. To investigate this growth approach, the deposition of one-sided and two-sided (In,Ga)N shells on GaN nanowires is investigated in detail. It is shown that in particular the deposition sequence of In and Ga as well as the amount of deposited metal have a strong influence on the In incorporation. Moreover, it is discussed that this sequential directional deposition method may in principle allow the combination of multiple active regions with different properties

on different lateral sides of one and the same nano- or microstructure. Such architectures might be interesting for the realization of multi-color pixels for micro-LED displays.

**Keywords:** GaN, Nanowire, core-shell, axial heterostructures, (In,Ga)N quantum well, modeling, adatom kinetics

## Zusammenfassung

In dieser Arbeit werden das Wachstum und die optischen Eigenschaften von selbstorganisierten GaN Nanodrähten auf TiN und nanodrahtbasierten (In,Ga)N/GaN Heterostrukturen für LED Anwendungen untersucht. Zu diesem Zweck wird das selbstorganisierte Wachstum von langen, dünnen und nicht koaleszierten GaN Nanodrähten auf TiN mittels Molekularstrahlepitaxie demonstriert. Bislang war das selbstorganisierte Wachstum von Nanodrähten, die all diese vorteilhaften Eigenschaften vereinen, sehr schwierig. Die Studie zeigt, dass aufgrund von Grenzflächenreaktionen des ursprünglichen Ti Films morphologisch gut entwickelte Nanodrahtensembles mit guten Lumineszenzeigenschaften nur für bestimmte Filmdicken und sehr spezifische Nitridierungs- und Wachstumsbedingungen realisiert werden können. Darüber hinaus zeigt die Studie, dass die Abwesenheit von Koaleszenz in diesen Nanodrahtensembles aus der geringen Anzahldichte der Nanodrähte resultiert, die durch eine diffusionsbedingte Abstoßung benachbarter Nanodrähte während der Nukleationsphase erklärt werden kann.

In weiteren Untersuchungen werden diese gut separierten und nicht koaleszierten GaN Nanodrähte auf TiN als Basis für die Herstellung von axialen und radialen Heterostrukturen verwendet. Im Gegensatz zum Wachstum von axialen Heterostrukturen auf typischerweise koaleszieten Nanodrähten auf den meisten anderen Substraten, führt das Wachstum von GaN Nanodrähten auf TiN zu wohldefinierten axialen (In,Ga)N Quantentöpfen, die einen rechteckigen Querschnitt aufweisen und sich entlang der c-Ebene erstrecken. Trotz der definierten Morphologie der aktiven Zonen ist die Lichtausbeute dieser Heterostrukturen eher gering.

Als Alternative zu axialen Heterostrukturen wird das Wachstum von nitridbasierten Kern-Hüllen-Strukturen auf den unpolaren Nanodrahtseitenfacetten untersucht, die die den Vorteil einer großen aktiven Zone mit sich bringen. Um das Potenzial der Molekularstrahlepitaxie für das Wachstum von Kern-Hüllen-Strukturen im Allgemeinen besser zu verstehen, wird der Aspekt, dass die Seitenfacetten der Nanodrähte nur sequentiell den verschiedenen Materialstrahlen ausgesetzt werden, durch Modellierung des Wachstums von GaN Hüllen auf GaN Nanodrähten untersucht. Es wird gezeigt, dass Ga Adatomdiffusionsprozesse zwischen verschiedenen Facetten das Wachstum auf den Seitenfacetten stark beeinflussen. Basierend auf diesen grundlegenden Untersuchungen wird das Wachstum von radialsymmetrischen (In,Ga)N Hüllen untersucht und es wird gezeigt, dass das Wachstum von Hüllen, die im grünen Spektralbereich emittieren, mittels Molekularstrahlepitaxie realisierbar ist. Aufgrund einer erhöhten Materialdiffusion in Richtung der Nanodrahtspitze bilden sich jedoch während des Wachstums der (In,Ga)N/GaN Kern-Hüllen-Strukturen große Segmente an den Nanodrahtspitzen, die eine homogene Prozessierung des letztendlichen LED-Bauelements beeinträchtigen können.

Um diesen Herausforderungen zu begegnen, wird ein neuer Wachstumsansatz vorgestellt, der die kontrollierte Abscheidung von III-Nitridhüllen auf verschiedenen Seiten des Nanodrahtes ermöglicht und die Bildung von vergrößerten Segmenten an den Nanodrahtspitzen reduzieren kann. Unter Ausnutzung der Richtungsabhängigkeit der Materialstrahlen in einer Molekularstrahlepitaxieanlage ermöglicht

der neuartige Ansatz die sequentielle Abscheidung verschiedener Verbundstoffmaterialien auf einer bestimmten Seite der Nanodrähte, um eine einseitige Schale zu wachsen. Um diesen Wachstumsansatz zu untersuchen, wird die Abscheidung von einseitigen und zweiseitigen (In,Ga)N Hüllen auf GaN Nanodrähten im Detail untersucht. Es wird gezeigt, dass insbesondere die Abscheidungsreihenfolge von In und Ga sowie die Menge des abgeschiedenen Metalls einen starken Einfluss auf den Einbau von In haben. Darüber hinaus wird diskutiert, dass diese sequentielle gerichtete Abscheidungsmethode prinzipiell die Kombination mehrerer aktiver Zonen mit unterschiedlichen Eigenschaften auf verschiedenen lateralen Seiten ein und derselben Nano- oder Mikrostruktur ermöglichen kann. Solche Architekturen könnten für die Realisierung von mehrfarbigen Pixeln für Mikro-LED-Displays interessant sein.

**Stichwörter:** GaN, Nanodraht, Hüllenwachstum, axiale Heterostrukturen, (In,Ga)N Quantentöpfe, Modellierung, Adatomkinetik

# List of publications

## Publications of parts of this work

J. Bartolomé, M. Hanke, D. van Treeck, and A. Trampert, *Strain Driven Shape Evolution of Stacked (In,Ga)N Quantum Disks Embedded in GaN Nanowires*, Nano Lett. **17**, 4654 (2017)

D. van Treeck, G. Calabrese, J. Goertz, V. M. Kaganer, O. Brandt, S. Fernández-Garrido, and L. Geelhaar, *Self-assembled formation of long, thin, and uncoalesced GaN Nanowires on crystalline TiN Films*, Nano Res. **11**, 565 (2018)

G. Calabrese, G. Gao , D. van Treeck, P. Corfdir, C. Sinito, T. Auzelle, A. Trampert, L. Geelhaar, O. Brandt, and S. Fernández-Garrido, *Interfacial reactions during the molecular beam epitaxy of GaN nanowires on Ti/$Al_2O_3$*, Nanotechnol. **30**, 114001 (2019)

D. van Treeck, S. Fernández-Garrido, and R. Lewis, *Semiconductor device with at least one functional element containing multiple active regions, and method of manufacturing thereof*, European Patent Office, patent application EP3531459 (2019)

D. van Treeck, S. Fernández-Garrido, and L. Geelhaar, *Influence of the source arrangement on shell growth around GaN nanowires in molecular beam epitaxy*, Phys. Rev. Mater. **4**, 013404 (2020)

D. van Treeck, J. Lähnemann, O. Brandt, and L. Geelhaar, *Growth of (In,Ga)N/GaN core-shell structures by molecular beam epitaxy*, in preparation

D. van Treeck, J. Lähnemann, G. Gao, O. Brandt, and L. Geelhaar, *Sequential directional deposition of III-nitride shells on lateral side facets of GaN nanowires by molecular beam epitaxy*, in preparation

## Further publications

D. Klein, M. Letilly, D. van Treeck, *Verfahren zur Herstellung von strukturierten a-SiNx-Schichten und deren Verwendung*, Deutsches Patent- und Markenamt, Patent DE102013110421 (2015)

*List of publications*

M. Musolino†, D. van Treeck†, A. Tahraoui, L. Scarparo, C. De Santi, M. Meneghini, E. Zanoni, L. Geelhaar, and H. Riechert, *A physical model for the reverse leakage current in (In,Ga)N/GaN light-emitting diodes based on nanowires*, J. Appl. Phys. **119**, 044502 (2016)

† both authors contributed equally to this work

M. Musolino, A. Tahraoui, D. van Treeck, L. Geelhaar, and H. Riechert, *A modified Shockley equation taking into account the multi-element nature of light-emitting diodes based on nanowire ensembles*, Nanotechnol. **27**, 275203 (2016)

P. Corfdir, H. Li, O. Marquardt, G. Gao, M. R. Molas, J. K. Zettler, D. van Treeck, T. Flissikowski, M. Potemski, C. Draxl, A. Trampert, S. Fernández-Garrido, H. T. Grahn, and O. Brandt, *Crystal-phase quantum wires: One-dimensional heterostructures with atomically flat interfaces*, Nano Lett. **18**, 247 (2018)

D. van Treeck, J. Ledig, G. Scholz, J. Lähnemann, M. Musolino, A. Tahraoui, O. Brandt, A. Waag, H. Riechert, and L. Geelhaar, *Electroluminescence and current-voltage measurements of single (In,Ga)N/GaN nanowire light-emitting diodes in the nanowire ensemble*, Beilstein J. Nanotechnol. **10** , 1177 (2019)

G. Calabrese , D. van Treeck , V. M. Kaganer , O. Konovalov , P. Corfdir , C. Sinito , L. Geelhaar , O. Brandt , and S. Fernández-Garrido *Radius-Dependent Homogeneous Strain in Uncoalesced GaN Nanowires*, Acta Mat. **195**, 87 (2020)

## Conference presentations

D. van Treeck, J. Ledig , G. Scholz , J. Lähnemann , M. Musolino , A. Tahraoui , O. Brandt , A. Waag , H. Riechert , and L. Geelhaar, *Electroluminescence and current-voltage measurements of single (In,Ga)N/GaN nanowire light-emitting diodes in the nanowire ensemble*, **(Poster)**, PULSE Summer School: Epitaxy updates and promises, Île de Porquerolles, France, September 2015

D. van Treeck, G. Calabrese, C. Pfüller, O. Brandt, L. Geelhaar, and S. Fernández-Garrido, *Growth of GaN nanowires on crystalline TiN films by molecular beam epitaxy*, **(contributed talk)**, Spring Meeting of the German Physical Society (DPG), Regensburg, March 2016

M. Musolino , A. Tahraoui, D. van Treeck, L. Geelhaar , and H. Riechert, *A modified Shockley equation taking into account the multi-element nature of light-emitting diodes based on nanowire ensembles*, **(Poster)**, Nanoscale Energy Converters, Falsterbo, Schweden, August 2016

D. van Treeck, G. Calabrese, J. Goertz, V. M. Kaganer, O. Brandt, S. Fernández-Garrido, and L. Geelhaar, *Self-assembled formation of long, thin, and uncoalesced GaN Naowires on crystalline TiN Films*, **(contributed talk)**, $19^{th}$ International Conference on Molecular Beam Epitaxy, Montpellier, France, September 2016

D. van Treeck, O. Brandt, L. Geelhaar, and S. Fernández-Garrido, *Analysis of radial growth of GaN nanowires for the fabrication of homogeneous multi-shell nanowire heterostructures*, **(Poster)**, $12^{th}$ International Conference on Nitride Semiconductors, Strasbourg, France, July 2017

D. van Treeck, J. Lähnemann, G. Gao O. Brandt, S. Fernández-Garrido, and L. Geelhaar, *Sequential directional deposition of III-nitride shells on lateral side facets of GaN nanowires by molecular beam epitaxy*, **(contributed talk)**, International Workshop on Nitride Semiconductors, Kanazawa, Japan, September 2018

D. van Treeck, *Breaking the wall of device size*, **(contributed talk)**, Falling Walls Lab Adlershof, Berlin, September 2019

# Abbreviations

| | |
|---|---|
| 1D | one-dimensional |
| 3D | three-dimensional |
| AFM | atomic force microscopy |
| CL | cathodoluminescence |
| EBL | electron-beam lithograhy |
| EDX | energy-dispersive X-ray spectroscopy |
| FDM | finite difference method |
| FWHM | full width at half maximum |
| HVPE | hydride vapor phase epitaxy |
| IR | infrared |
| LED | light-emitting diode |
| LCD | liquid-crystal display |
| LS-QMS | line-of-sight quadrupole mass spectrometry |
| LT-CL | low-temperature cathodoluminescence |
| LT-PL | low-temperature photoluminescence |
| MBE | molecular beam epitaxy |
| MEE | migration enhanced epitaxy |
| ML | monolayer |
| MOCVD | metalorganic chemical vapour deposition |
| NN | nearest neighbor |
| NW | nanowire |
| OLED | organic LED |
| PA-MBE | plasma-assisted MBE |
| PL | photoluminescence |
| QB | quantum barrier |
| QMS | quadrupole mass spectrometry |
| QW | quantum well |
| RGB-LED | Red-Green-Blue light-emitting diode |
| rmp | rounds per minute |
| RHEED | reflection high energy election diffraction |
| SAG | selective-area growth |
| SAS | selective-area sublimation |
| SDD | sequential directional deposition |
| SEM | scanning electron microscopy |

| | |
|---|---|
| SF | stacking fault |
| TEM | transmission electron microscopy |
| UHV | ultra high vacuum |
| UV | ultra violet |
| WZ | wurtzite |
| XRD | x-ray diffractometry |
| ZB | zincblende |

# List of basic symbols

| Symbol | Name | Unit |
|---|---|---|
| $a$ and $c$ | lattice spacing parameters | Å |
| $d$ | NW diameter | nm |
| $D_{\text{sub, side, top}}$ | diffusion coefficients of adatoms on substrate, side or top facet of NW | $\text{cm}^2/\text{s}$ |
| $E_{diff}$ | potential barrier on substrate surface | eV |
| $E_g$ | band gap energy | eV |
| $\mathbf{G}$ | reciprocal lattice vector | $\text{m}^{-1}$ |
| $GM_{\text{j}}$ | grown material in the respective region $j$ | nm |
| $GR_{\text{j}}$ | growth rate in the respective region $j$ | nm/min |
| $\text{h}_c$ | height at which NWs merge due to coalescence above substrate | nm |
| $h_{\text{para}}(t)$ | height of the parasitic layer | nm |
| $k_B$ | Boltzmann constant ($1.381 \times 10^{-23}$) | $\text{J K}^{-1}$ |
| $\mathbf{k}$ | wavevector or reciprocal space vector | $\text{m}^{-1}$ |
| $\text{L}_c$ | certain critical length at which NWs tend to coalesce | nm |
| $l$ | total NW length starting from the substrate | nm |
| $l_{\text{eff}}$ | NW length between parasitic layer and NW top facet | nm |
| $m$ | parameter related to number of Ga atoms in critical nucleus | |
| $n$ | adatom concentration | $\text{at}/\text{cm}^2$ |
| $\text{P}_{pz}$ | piezoelectric polarization | $\text{C}/\text{m}^2$ |
| $\text{P}_{sp}$ | spontaneous polarization | $\text{C}/\text{m}^2$ |
| $p(\mathbf{r})$ | probability for a new NW to nucleate at a site $\mathbf{r}$ | |
| $\alpha$ | polar angle of the material sources in the MBE system | ° |
| $\beta$ | azimuthal angle of the material sources in the MBE system | ° |
| $\lambda$ | adatom diffusion length | nm |
| $\omega$ | photon frequency | $\text{s}^{-1}$ |
| $\Phi_{\text{In, Ga, N}}$ | molecular fluxes of In, Ga, N | nm/min |
| $\tau_{\text{sub, side, top}}$ | lifetimes of adatoms on substrate, side or top facet of NW | s |
| $T_{\text{sub}}$ | substrate temperature during growth | K |

# Contents

# 1. Introduction

Over the last decades, information and communication technologies have advanced more rapidly than any other innovation in our history. The impact of these technologies on modern economies and our personal lives is tremendous. The steadily increasing compactness and variety of functionalities of electronic devices lead to deep technological penetration of the world's societies, where today, it is natural to access huge amounts of information and knowledge anywhere and at any time on our mobile devices. One downside of the ongoing technologization is the ever-growing demand for resources and energy. Hence, besides multifunctionality and compactness of devices, life time and energy efficiency are key factors for future applications.

Most of today's electronic devices are based on highly developed Si technologies. However, with regard to optoelectronic applications, the indirect bandgap of Si is a fundamental disadvantage. In this field, III-V compound semiconductors have evolved as the most important materials over the last decades. Most of the III-V materials exhibit a direct band gap and therefore provide a much higher electron-photon coupling than it is the case for Si.[1] Moreover, the bandgap of the different III-V material systems can be tuned over wide energy range by adjusting their compound.[1,2] This allowed, for instance, the realization of III-nitrides-based light-emitting diodes (LEDs) in the visible and ultraviolet (UV) spectrum for applications like solid state lighting or for medical purposes. In comparison to established technologies like common light bulbs or mercury-vapor lamps, LEDs were a huge breakthrough in terms of energy efficiency and life time.[3] But also for display technologies, solid-state LEDs offer some striking advantages. For instance, in the latest generation of liquid-crystal displays (LCDs), LEDs are used as backlight which significantly improved the energy efficiency and the dynamic rage of LCDs.[4,5] With the rising demand for portable and wearable device technologies, e. g. for virtual and augmented reality (VR/AR) applications, there is also a need for high-brightness and high-resolution multi-color compact projectors and small-size displays. Here, solid state-based micro-LEDs promise longer lifetimes, a higher efficiency and considerably greater brightness with decreasing pixel size and pitch compared to LCDs or displays based on organic LEDs (OLEDs).[5–8] Hence, it is not surprising that big companies like Samsung, Google, and Apple recently made significant investments to push the development of III-N microstructure-based self-emissive multicolor displays.[9]

In general, however, there are still some major challenges in the field of III-nitride LEDs. For example, the efficiency of the LEDs drops significantly for high current densities, a phenomenon which is called "droop". Moreover, regarding green and red (In,Ga)N-

based LEDs, the efficiency decreases strongly with increasing In content in the active region.[3,5] Some efficiency problems are related to the fact that due to the lack of cost-efficient non-polar substrates, the p-n junction of III-nitride based LEDs are usually grown along the polar *c*-direction which may cause a spatial separation of electrons and holes.[1] Another demanding challenge is the integration of III-V materials with other material platforms, especially with mature Si-based technologies. Common problems of epitaxial growth of dissimilar materials are the mismatch of lattice constants and thermal expansion coefficients.[10] This, for instance, may result in structural defects or a poor dissipation of heat which may strongly impact the performance of the final device. Regarding the fabrication of efficient micro-LEDs, size effects resulting from surface recombination and side-wall damage have strong influences on their electrical and optical performances.[5] Moreover, to realize multi-color micro-LEDs with very high resolutions, mass transfer processes for the integration of structures with different luminescence properties on a common platform have to be optimized or even reinvented for very small structures.[5,11] Here, innovative concepts are needed.

In general, a promising solution to these impediments of nitride-based LEDs and display technologies came with the progress in the field of three-dimensional (3D) nano- and microstructures like nanowires (NWs), which can be either grown by top-down or bottom-up approaches. A big advantage of top-down approaches is that they allow the fabrication of highly ordered NW arrays which is beneficial for the processing of many devices. In contrast to top-down NWs, where the material quality depends on the quality of the original planar layer, for instance, self-assembled bottom-up GaN NWs grown by molecular beam epitaxy (MBE) allow the realization of high crystal quality material on a wide variety of foreign substrates, independent of the lattice mismatch.[12] For the self-assembly process, dislocations originating from the lattice mismatch of the material at the interface, do not propagate through the whole NW but bend towards the NW sidewalls in the bottom part of the NWs.[13] In general, the 3D geometry of NWs also allows the fabrication of core-shell structures. The major advantage of such a core-shell design over planar structures is that the active region area can be drastically increased by simply increasing the aspect ratio. This makes core-shell structures particularly interesting for (In,Ga)N/GaN LEDs, where large active regions can be grown on the non-polar side facets of GaN NWs which may increase the overall efficiency per substrate area.[14,15] Moreover, core-shell approaches might solve some of the problems of micro size LEDs related to surface recombination and may allow new device designs.

However, the growth of self-assembled GaN NWs on foreign substrates as well as the fabrication of core-shell structures for NW-based LEDs by MBE are far from being fully explored or optimized. For example, not all substrates allow the growth of well-separated self-assembled GaN NWs with a beneficial ensemble morphology. Indeed, on most substrates, the NW ensembles show high NW densities (i.e. on Si).[16] As a result, the large portions of the NWs coalescence and form aggregates with irregular shapes which in turn affects axial and radial heterostructures based on these NWs.[17] Moreover,

the high NW densities do not allow the growth of core-shell structures due to the mutual shadowing from the impinging beams. Up to now, there are only a few approaches which allow the growth of uncoalesced self-assembled NWs with a sufficiently low NW density. A further prerequisite for using these NWs as the basis for LEDs are conductive substrates. In particular the growth of high quality material on metals would be of high technological interest for LED applications. Besides a high electrical conductivity, metals usually have a high optical reflectivity in the visible range as well as a good thermoconductivity.[18,19] However, the usage of metal substrates has barely been investigated for the growth of GaN NWs so far. Moreover, the growth of (In,Ga)N/GaN core-shell structures with high In contents emitting in the green to red spectral range remains very challenging, regardless of the growth technique.[20–22] Although MBE is often said to have high potential to achieve shells of high In content on NWs, so far there are no reports in literature that support these assumptions.

The goal of this thesis is to establish the growth of well-developed and low-density self-assembled GaN NW ensembles on a metal, namely TiN, by molecular beam epitaxy, which serve as basis to study new aspects of the formation of NW-based axial and core-shell (In,Ga)N/GaN heterosturctures emitting up to the green spectral range. To this end, in chapter 2 the fundamentals of MBE are introduced, the *in situ* and *ex situ* analysis methods used in the scope of this thesis are presented, and the current research on the growth of GaN NWs in general is reviewed.

Following this introductory part, in chapter 3, the self-assembled growth of long, thin and uncoalesced GaN NWs on TiN is demonstrated after reviewing the previous work on this topic. The role of interfacial reactions for the morphology and the optical quality of these NWs is discussed and the relation between the low NW density, the low coalescence degree, and the nucleation mechanism of NWs on TiN is investigated.

Subsequently, in chapter 4, the growth of axial (In,Ga)N QWs grown on top of the well-developed and regular GaN NWs on TiN is examined with the intention to grow high quality active regions. To this end, a high-temperature growth approach is applied for the fabrication of the (In,Ga)N/GaN heterostructures. Here, the morphology of the NW ensemble as well as the microstructure of single NWs is analyzed. Finally, the optical properties of the (In,Ga)N/GaN heterostructures are studied.

In chapter 5, a fundamental study of shell growth of nitride-based materials by MBE is presented, where the well-separated GaN NWs on TiN are used as template NWs. As a first step, GaN shells around the GaN NWs on TiN are investigated to understand the principles of adatom kinetics on the NW during shell growth. In this context, the decisive role of the geometry of the MBE system for the formation of homogeneous shells is discussed. Using these fundamental insights as a basis, the growth of radially symmetric (In,Ga)N shells emitting in the blue/green spectral range is demonstrated and the influence of the growth conditions on the NW morphology and the emission properties is discussed.

In chapter 6, the directed nature of the material beams in an MBE system is explored to enable a sequential directional deposition of GaN and (In,Ga)N on only one side of GaN template NWs. This growth process, for instance, allows to combine different active regions with different properties on different lateral sides of one and the same nano- or microstructure and hence enables the fabrication of new typs of multifunctional nanodevices. To better understand the growth of one-sided (In,Ga)N shells, the influence of different growth parameters and growth modes is studied. To evaluate the feasibility of the growth of multiple one-sided shells on one and the same template NW, the deposition of two one-sided (In,Ga)N shells with different In content on opposite sites of the same template NWs on TiN is investigated. Furthermore, the developed growth approach for one-sided (In,Ga)N shells is transferred to ordered GaN NWs fabricated by selective area sublimation (SAS), which are in general more suitable for device processing. Finally, a novel device design which combines multiple active regions with different functionalities is proposed. This design may be applied to realize a multicolor RGB-LED based on single nano- or microstructures.

# 2. Growth and analysis of III-nitride-based nanowires

Group-III nitride structures have been fabricated using various growth techniques such as metalorganic chemical vapor phase deposition (MOCVD), hydride vapor phase epitaxy (HVPE), and molecular beam epitaxy. Allowing high growth rates and a superior material quality due to high growth temperatures, MOCVD is the most commonly used technique for the industrial fabrication of nitride-based optoelectronic devices. MBE, however, is wide-spread in the research community, not least due to the availability of in situ analysis tools like RHEED and QMS, which are not available for MOCVD. Also for the investigation of nitride-based NWs, MBE appears to be the most commonly used technique.

In this thesis, we investigate the MBE-growth of GaN NWs on a metal substrate, TiN, and the fabrication of (In,Ga)N/GaN heterostructures, in particular radial core-shell structures. Especially in the case of NW-based heterostructures, achieving a controlled growth on certain facets, like on the C-planes or *m*-planes, is not straight forward and may strongly depend on the growth method. To better understand the peculiarities of MBE, in this chapter we will introduce the fundamentals of this growth technique, introduce different *in situ* and *ex situ* analysis methods, and review the current research on the growth of GaN NWs.

## 2.1. The group III-N material system

Although, today Si is the most commonly used material for fundamental applications like transistors, solar cells, and semiconductor detectors, it has a huge drawback when it comes to active light emission: its indirect bandgap, which prevents an efficient electron-hole recombination. Nowadays, most semiconductor light-emitting devices are based on III-V materials.

Figure 2.1 shows the bandgap energy and associated emission wavelength of the most relevant III-V materials as a function of their lattice parameters. Due to their direct bandgaps, compound materials like (In,Ga,Al)As and (In,Ga,Al)Sb, as well as (In,Ga)P have facilitated the fabrication of efficient red and infrared LEDs. Although AlAs, GaP, and AlP have bandgaps in the green spectral range, due to their indirect bandgap, they are not suitable for efficient green light-emitting devices. In contrast, III-N compounds have a direct bandgap independent of their composition. Moreover, by adjusting the

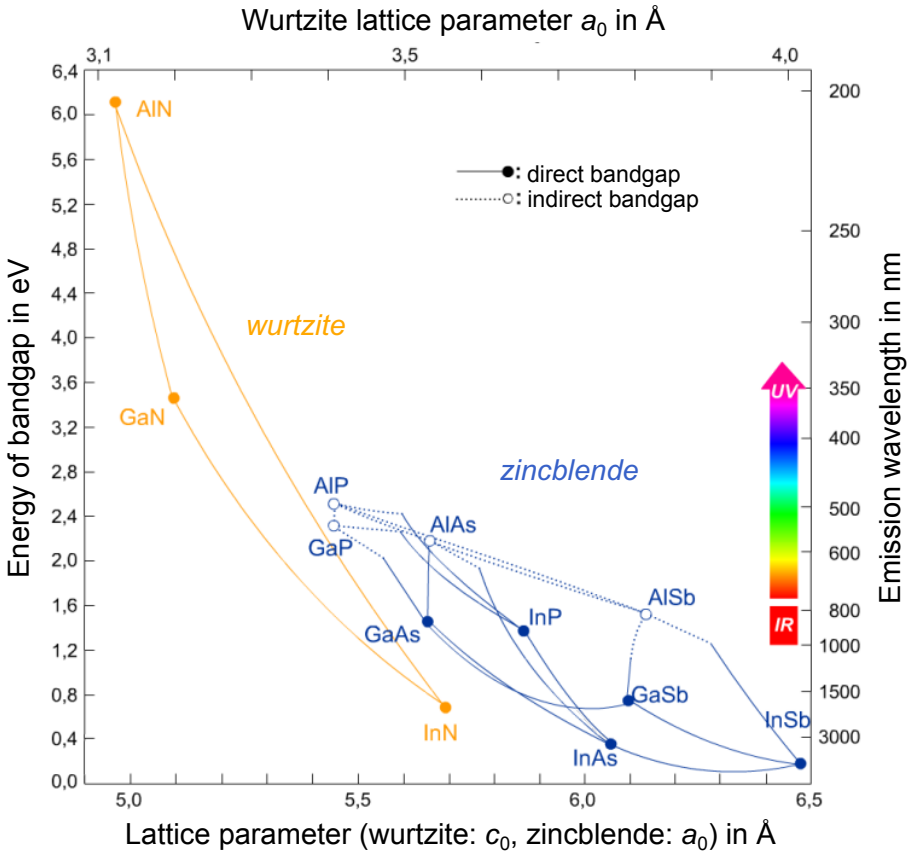


**Figure 2.1**: Bandgap energy of the most relevant III-V material systems. Graph by Degreen, original modified with English annotations (CC BY-SA 2.0 DE).

(In,Ga,Al)N composition, the bandgap can be tuned from the infrared (IR, 0.7 eV for InN) to the ultraviolet (UV, 6.2 eV for AlN) spectral range.

At ambient conditions, the thermodynamically stable crystal structure of III-nitride materials is the hexagonal wurtzite (WZ) structure. For particular growth conditions or growth on cubic substrates, however, III-nitride compounds may also crystallize in the otherwise less stable cubic zincblende (ZB) structure. Figure 2.2 (a) shows the unit cells of both the WZ and the ZB crystal structure characterized by the lattice parameters $a$ and $c$. As the sketch reveals, the WZ structure expresses an ABAB... (2H) stacking sequence, whereas ZB structure reveals a ABCABC... (3C) sequence.

Since the wurtzite structure has no inversion plane perpendicular to the c-axis, the GaN surfaces along the $c$-direction are either terminated by a Ga or a N layer. Due to the big difference in electronegativity of the metals Al, Ga, and In with respect to N, this break of the crystal symmetry introduces an electric field which leads to a spontaneous polarization $P_{sp}$ along the c-axis of the crystal. Hence, in [0001] direction the crystal is called metal-polar (i. e. Al-polar, Ga-polar, In-polar) and N-polar in the [000$\bar{1}$] direction. Lähnemann *et al.* determined an experimental value of $P_{sp}^{GaN} = 0.022\,\mathrm{C/m^2}$ in

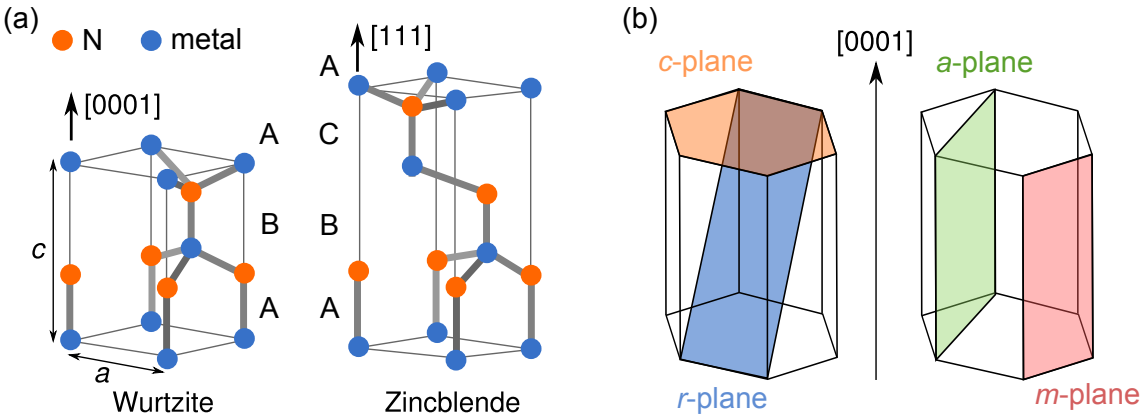


**Figure 2.2**: (a) Unit cell of for the wurtzite and zincblende crystal structure of III-nitides. (b) Main crystal planes of the hexagonal lattice.

relaxed GaN.[23] Spontaneous polarization is also expressed in III-nitride compounds like (In,Ga)N, (Al,Ga)N and (Al,In)N. Another source of polarization, the so called piezoelectric polarization $P_{pz}$, is induced by strain that results, for example, from heterointerfaces between different III-nitride material compounds.[2,24] In the case of a *c*-plane (In,Ga)N quantum well (QW) on a planar GaN layer, $P_{pz}$ and $P_{sp}$ have an opposite sign, since the QW experiences a compressive in-plane strain. The resultant polarization is generally dominated by $P_{pz}$ due to the large lattice mismatch between GaN and InN of about 11%. This leads to an internal polarization field that points in $[000\bar{1}]$ direction and modifies the electronic band structure.[25] Figure 2.2 (b) shows the main crystal planes for the hexagonal lattice, the polar *c*-plane, the semi-polar *r*-plane, as well as the non-polar *m*- and *a*-plane.

## 2.2. Plasma-assisted molecular beam epitaxy

MBE enables the synthesis of high quality material by molecular beams impinging on a heated substrate. The main difference between MBE and other growth approaches are the ultra-high vacuum (UHV) conditions where the mean free path is long enough for the atoms to reach the substrate without interacting with other materials. Moreover, the low pressure conditions preserve a low concentration of impurities in the reactor chamber and allow the application of in situ surface analysis by RHEED and a desorption monitoring by line-of-sight QMS. The molecular beams are generated by thermally evaporating the respective materials from effusion cells. This technique can be used for most source materials. However, since nitrogen molecules are rather inert regarding chemical reactions, for plasma-assisted MBE (PA-MBE) a plasma sources is used to generate excited $N_2$ molecules and N atoms. The different molecular fluxes can be controlled by mechanical shutters in front of the cell apertures. The ability to precisely control the different material

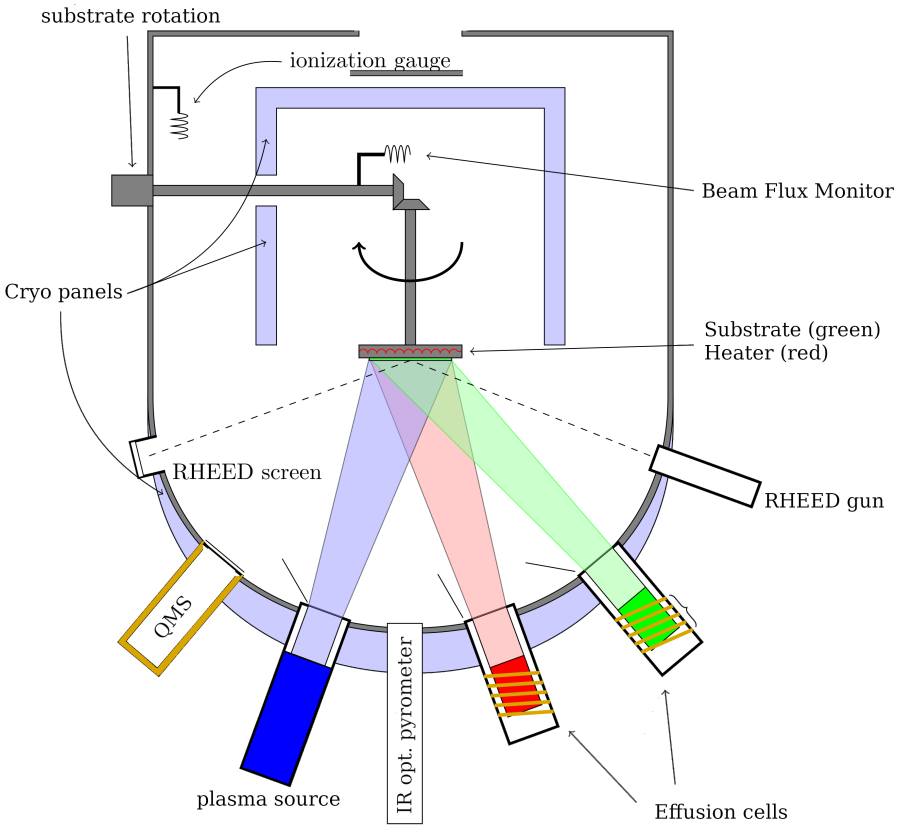


**Figure 2.3**: Cross-sectional sketch of a representative MBE system showing the main components. Modified illustration of Vegar Ottesen (CC BY 3.0).

beams as well as the possibility to apply very small fluxes in MBE allow the fabrication of very smooth and sharp interfaces with monolayer precision and well-defined stacking sequences.[26]

In general, the crystal growth on the substrate is defined by the interplay of different mechanisms. Once the impinging atoms are adsorbed at the surface of the heated substrate, the adatoms may either diffuse along the surface, incorporate at a certain site and contribute to the material growth, or desorb again eventually.[27] These processes as well as the decomposition of already crystalized material will be discussed in more detail below in section2.4.

The growth experiments presented in the scope of this thesis were performed in two different MBE systems, M2 and M9, at the Paul-Drude-Institut. Figure 2.3 shows a cross-sectional sketch of a representative MBE system. The reactor chambers of M2 and M9 were fabricated by CreaTec Fischer & Co and equipped with Knudsen effusion cells for the group-III materials Al, Ga, and In as well as for the dopants Mg and Si/Ge. Active nitrogen was provided by radio-frequency plasma sources from SVT in M9 and

Riber/Veeco* in M2. The impinging fluxes $\Phi_{Ga}$ and $\Phi_N$ were calibrated in equivalent growth rate units of planar GaN layers as described elsewhere.[28] The substrate was heated by a filament, where the respective temperature was controlled by a thermocouple. To calibrate the growth temperature, an emissivity-corrected infrared optical pyrometer was installed in both systems. If not indicated otherwise, for all experiments on a TiN substrate in this thesis, the optical pyrometer itself was calibrated by estimating the *real* temperature of the TiN substrate with a disappearing-filament pyrometer. Furthermore, *in situ* analysis tools like RHEED and line-of-sight QMS were mounted at the respective apertures of the chamber. To maintain the UHV ambiance of about $1 \times 10^{-10}$ mbar in the growth chamber under stand-by conditions, M2 was pumped by a turbo molecular pump, a cryo pump, and an ion getter pump, M9 by two turbo molecular pumps and an ion getter pump. Moreover, the cryo shroud of the growth chamber, filled with liquid nitrogen, reduces the amount of residual vapors in the system due to condensation at the chamber walls. During the growth experiments the pressure typically rose to about $2 \times 10^{-5}$ mbar resulting from the flow of the nitrogen gas from the plasma source.

## 2.3. *In situ* and *ex situ* analysis of nanowires

This section will give an overview of the most important *in situ* and *ex situ* analysis tools applied in this thesis. Besides the *in situ* growth analysis tools RHEED and line-of-sight QMS (LS-QMS), a short introduction to the *ex situ* spectroscopical analysis of the photoluminescence (PL) and the cathodoluminescence (CL) of grown structures, as well as the study of the sample morphology by scanning electron microscopy (SEM) will be given. Moreover, further microscopical and spectroscopical methods, namely transmission electron microscopy (TEM), atomic force microscopy (AFM), X-ray diffraction (XRD) and energy-dispersive X-ray spectroscopy (EDX), that were not performed by myself or only contribute to some side aspects of certain studies, are introduced shortly.

### 2.3.1. Analysis and monitoring of the growth process

To monitor and analyze the different growth processes presented in this thesis we used RHEED and LS-QMS. Although there are no dedicated studies which focus on a growth analysis by either RHEED or LS-QMS, both tools were very important to control the growth and to conduct successful growth runs. RHEED was specifically used to monitor the formation of the TiN layer and the onset of NW nucleation. QMS was an important tool to monitor the surface reactions of Ga on the sputtered Ti film, to measure the amount of impinging and desorbing In at certain substrate temperatures, and to roughly monitor the sublimation process of prepatterned GaN layers.

*M2 has been equipped with two different plasma sources, one from Riber and one Veeco.

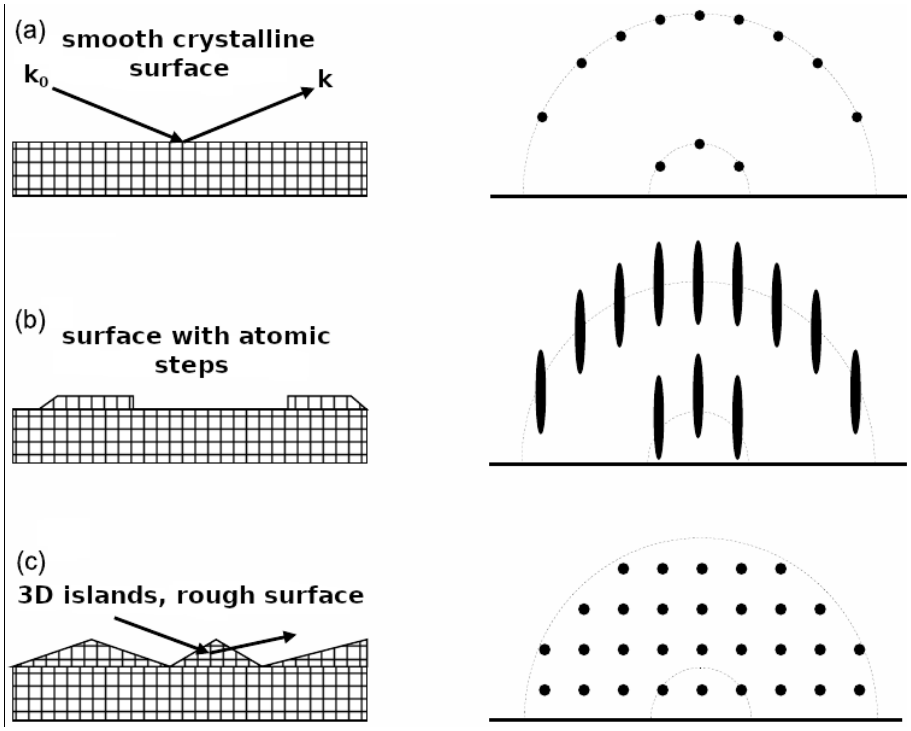


**Figure 2.4**: RHEED patterns resulting from different surface morphologies. Illustration from Ref. 29, slightly modified.

### Reflection high-energy electron diffraction

RHEED is an established *in situ* tool to probe the surface structure, i. e. the uppermost atomic layers, of a sample during the growth and is used to investigate properties like the surface morphology, growth rates, crystal structure, surface reconstructions and epitaxial relations in heterostructures. In RHEED, a high-energy electron beam (20 keV in our case) is generated by an electron gun and incides at a grazing angle onto the sample substrate. To control the beam, a deflection unit is used. The electrons are reflected and diffracted at the sample surface and hit a fluorescent screen on the opposite side of the electron gun. Here the interference pattern of the diffraction, which corresponds to the coincidence of the Ewald sphere with the reciprocal lattice of the sample surface, can be monitored. The Ewald sphere shows the allowed diffraction conditions of elastically scattered electrons. It is centered at the sample surface and the *de Broglie wavelength* $\lambda_0$ of the incident electrons determine its radius $\mathbf{k}_0 = 2\pi/\lambda_0$ in the reciprocal space. Diffraction conditions are satisfied where the rods of reciprocal lattice intersect the Ewald sphere. Here the condition $\mathbf{k} - \mathbf{k}_0 = \mathbf{G}$ is fulfilled with $\mathbf{k}$ being the wave vector of the elastically diffracted electrons and $\mathbf{G}$ corresponding to a reciprocal lattice vector. Diffraction from a perfect crystalline surface, as shown in Figure 2.4 (a), results in a pattern of laterally equidistant spots located on circles centered on the incident beam. However, in reality, atomic steps as well as crystal imperfections on the surface lead to an elongation of the

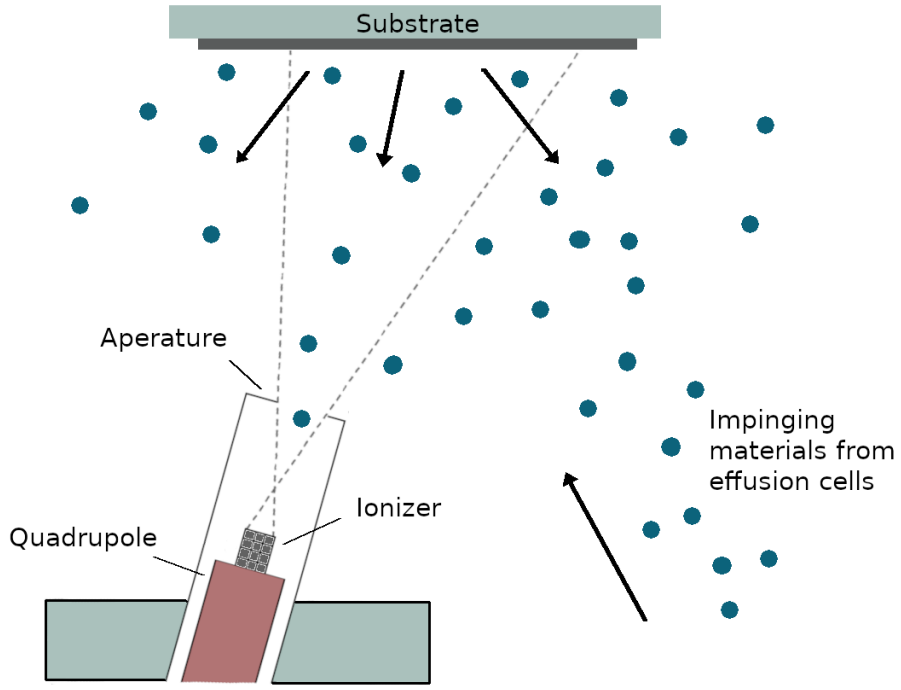


**Figure 2.5**: Sketch of a line-of-sight QMS detecting elements from the substrate.

diffraction spots and hence to a streaky pattern as shown in Figure 2.4 (b). Once three-dimensional features form on the sample surface, like in the case of NWs or for high surface roughness, diffraction conditions are also met in out-of-plane direction. As a result, a spotty RHEED pattern as shown in Figure 2.4 (c) can be observed. A more detailed description of RHEED can be found in Ref. 18.

### Line-of-sight quadrupole mass spectrometry

QMS allows to study the growth and surface kinetic processes *in situ* by analyzing the desorbing elements from the substrate. In the case of a line-of-sight QMS, as mounted for M2 and M9, the spectrometer is arranged in line-of-sight configuration to the substrate with a specifically designed aperture in order to only detect the atoms desorbing directly from the sample surface. The capturing of desorbed materials is sketched in Figure 2.5.

Once the desorbed atoms (or molecules) reach the QMS, they are ionized at the entry of the mass spectrometer. The charged atoms then travel through an oscillating electric field created by four electrodes. The electric field is adjusted in a way that only particles with a certain (preset) mass-to-charge ratio have a stable trajectory and reach the detector. For more information on the functional principle of a QMS, the reader is referred to the literature.[18]

### 2.3.2. Morphological, structural and chemical analysis

In order to image the morphology of the NW ensembles presented in this thesis, scanning electron microscopy (SEM) has been performed in a Hitachi S-4800 field-emission microscope using an acceleration voltage of 5 kV. In contrast to optical microscopes, in an scanning electron microscope the much shorter wavelength of an electron beam is used to obtain resolutions on the nanometer scale. The final image is constructed from the signal of secondary electrons emitted from the sample as well as of backscattered electrons after the sample has been excited by the electron beam. In this thesis, the length and diameter distributions, as well as the number density of the NW ensembles were determined by analyzing cross-sectional and plan view SE micrographs with the help of the open-source software ImageJ.[30] To this end, the diameters and lengths of several hundred NWs were measured manually in numerous cross-sectional SE micrographs. The density was determined by automatically counting the NWs in plan view images. Furthermore, the nearest neighbor distances of the NWs in the ensemble were extracted from top-view SE micrographs by identifying the NW positions within a micrograph by ImageJ and subsequently using a Python script to calculate the distance to the nearest NW for each NW in the micrograph. A similar process has been used by Kaganer *et al.* described in Ref. 31. For each statistic, a sufficient number of data points was acquired. For the analysis of the NW length and diameter more than 300 NWs have been investigated for each sample. To evaluate the NW density and the nearest neighbor distances usually about 600 to 1000 NWs have been taken into account. The majority of the SE micrographs in this thesis have been acquired by A.-K. Bluhm.

To obtain a better understanding of the NW or the substrate structure, TEM has been performed for several samples in this thesis using a JEOL JEM-3010 microscope. For TEM, the sample has to be prepared sufficiently thin (only several tens of nm) for the electron beam to pass through. Due to the small de Broglie wavelength of the high-energy electrons (typically 40 to 400 keV), TEM allows to resolve the crystal structure on an atomic level. The TEM measurements shown in this thesis have been carried out by either one of my two colleagues G. Gao or J. Bartolomé.

In order to assess the chemical composition of the substrate or (In,Ga)N shells grown around GaN NWs in this thesis, EDX has been performed on several samples either in an scanning electron microscope or a transmission electron microscope. EDX uses characteristic X-rays, which are created by the interaction of the electron beam with the sample (bremsstrahlung), to identify the different elements in the investigated sample area. The measurements carried out for the presented studies were performed by J. Lähnemann and C. Pfüller (SEM) as well as by G. Gao (TEM).

### 2.3.3. Spectroscopical analysis of the luminescence properties

Luminescence spectroscopy is an important analysis technique to investigate the opto-electronic properties of semiconductors. Once a valence band electron is excited into the

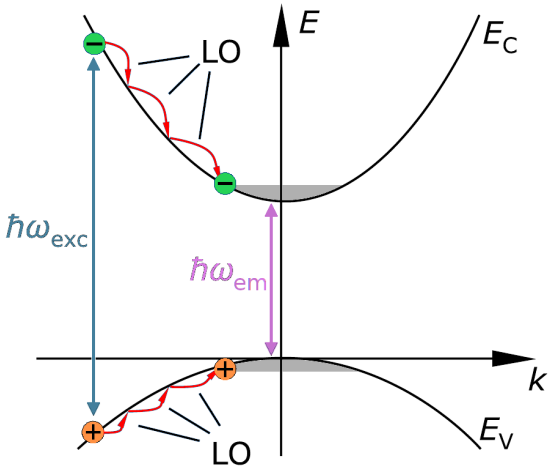


**Figure 2.6**: Sketch of the different steps of a luminescence process: the excitation of an electron into the conduction band by absorbing a photon of the energy $\hbar\omega_{exc}$, the thermalization of the electron and the hole towards the conduction and valence band minimum and maximum, respectively, and the emission of a photon with energy $\hbar\omega_{em}$ due to the recombination of an electron-hole pair. Reproduced from Ref. 32.

conduction band, it can recombine with a hole either non-radiatively by electron-phonon interaction or raditively by emitting a photon. Luminescence spectroscopy investigates the latter process where the observed transition energies are strongly influenced by the bandstructure of the semiconductor as well as by the presence of defect or impurity states therein.

In general, luminescence can be characterized by three different steps, as shown in Figure 2.6. First, electron-hole pairs are created by exciting valence band electrons into the conduction band. In the case of photoluminescence spectroscopy, the excitation of the electrons is provided by the photons of a laser beam with a certain excitation energy $\hbar\omega_{exc} \geq E_g$. In the case of cathodoluminescence spectroscopy, the electron beam of a scanning electron microscope provides the localized excitation. Subsequently, the electrons and holes thermally relax towards the conduction band minimum and the valence band maximum, respectively, through the emission of longitudinal optical (LO) phonons. Since the thermalization processes are much faster than the radiative electron-hole recombination, it can be assumed that the electrons and the holes form quasi-equilibrium distributions around the minima of the energy bands, where electron-hole pairs recombine spontaneously by emitting photons of the energy $\hbar\omega_{em}$.

In general, there are numerous recombination processes which lead to radiative recombination: band-to-band recombination, acceptor or donor bound recombination, as well as donor-acceptor pair recombination. Moreover, as a result of the Coulomb attraction, the electron-hole pairs may form excitons, electrically neutral quasiparticles. The formation of excitons is favored at low temperatures, where the binding energy is higher than the kinetic/thermal energy. Thus, luminescence at low temperatures is usually governed

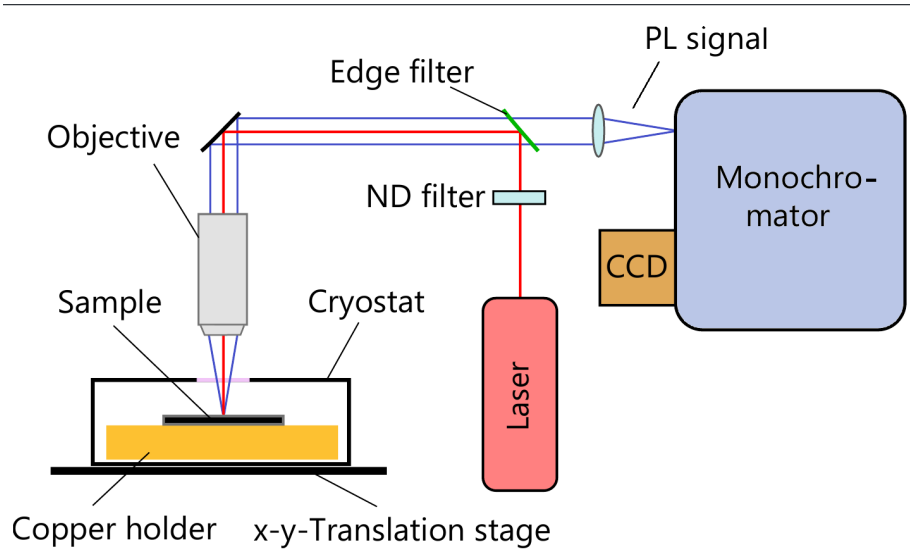


**Figure 2.7**: Sketch of the PL setup. Reproduced from 37.

by excitonic transitions. The binding energy of an exciton in the ground state can be calculated similar to the procedure for the hydrogen atom. The binding energy of the free exciton $E_{FX}$ in WZ GaN is roughly 25–27 meV with a Bohr radius of about 3 nm.[33,34] The energy of the photon that has been generated by an exciton decay is reduced by the exciton binding energy in comparison to the energy of photons originating from band-to-band recombination of free carriers. Besides the free exciton, there are also bound exciton states. For instance, excitons can be bound to donor (acceptor) states with a binding energy $E_{DX}$ ($E_{AX}$) that is higher than the one of free excitons. This makes luminescence spectroscopy very sensitive to impurities, even at very low concentrations.

Apart from radiative recombination, electron-hole pairs can also recombine non-radiatively. For instance, mid-gap states are known to increase the non-radiative Shockley-Read-Hall recombination, where most of the energy is dissipated in the form of phonon emission.

For more information on recombination mechanisms, the reader is referred to Refs. 32, 35, and 36.

### Photoluminescence spectroscopy

The PL spectroscopy carried out for this thesis was performed with a HORIBA JOBIN YVON LABRAM HR 800 UV µ-PL setup which is sketched in Figure 2.7. The GaN NW ensembles were excited with a continuous-wave HeCd laser from Kimmon emitting at 325 nm. To attenuate the maximum laser power of 30 mW, different neutral density (ND) filters and a filter wheel with a gradual change in optical density were used. For measurements at 300 K, the laser beam was focused to a spot with a diameter of about 3 µm using an 15× objective, which resulted in an excitation of about 70 NWs. For the LT-PL measurements at about 10 K a 50× objective was used. Here, the samples were placed

in a cryostat and cooled by liquid He. The diameter of the laser spot on the sample was approximately 1 µm exciting about 10 NWs. In both cases, the PL signal was collected by the same objectives and was guided into a 0.8 m focal length monochromator equipped with a 600 lines/mm grating for spectral dispersion, and detected with a liquid-nitrogen-cooled charge-coupled device camera.

In order to investigate single NWs, for some samples LT-PL measurements on dispersed NWs on an Au covered Si wafer were performed in addition to ensemble measurements. Due to the small dimensions of the NWs and the restricted resolution of the objective, it was not possible to unequivocally determine from the microscope image, whether one or a few NWs were excited.

For more information on this PL setup, the reader is referred to the Ph. D. thesis of C. Hauswald.[38]

**Cathodoluminescence spectroscopy**

In order to investigate the luminescence characteristics along the whole length of single NWs, in particular of (In,Ga)N/GaN core-shell NWs, spectral CL line scans as well as monochromatic CL images of dispersed NWs on a Au covered Si wafer were acquired at 10 K. The setup used for the CL measurements presented in this thesis is a Gatan MonoCL 4 system attached to the Zeiss Ultra 55 field-emission SEM. In contrast to the µ-PL with laser excitation, the main advantage of CL in comparison to other spectroscopy methods is that the electron beam allows a local excitation of the specimen with a spatial resolution on the order of a few ten nm. Hence, in the case of a NW, the luminescence along its whole axis can be both spatially and spectrally resolved and CL emission of different parts of the NW can be analyzed independently. In general, it should be noted that the spatial resolution of the CL measurement is also limited by charge carrier diffusion. Depending on the material system and the investigated structure, the charge carries may diffuse away from the directly excited area and cause luminescence in the adjacent regions. Although this luminescence originates from different areas, it is attributed to the current position of the exciting electron beam and thus affects the spatial resolution of the CL measurement. In the setup, the CL signal is collected by a parabolic mirror mounted above the sample and guided into the spectrometer. To obtain CL maps of the NWs, the diffracted light was reflected onto a liquid-nitrogen-cooled charge-coupled device array and the spectrum is directly imaged on the pixels of the detector unit. For the CL measurements in this thesis, an acceleration voltage of 5 kV was chosen in order to obtain a high spatial resolution at a probe current of 1–1.5 nA. Moreover, a grating with 300 lines/mm and a slit of 1 mm was used for the spectrometer. For the CL line scans a step size of 20 nm with an integration time of 1 s was applied.

The CL measurements in this thesis were performed by my colleague J. Lähnemeann. Futher details on this CL setup and CL measurements in general can be found in his Ph. D. thesis.[35]

## 2.4. Fundamentals of nanowire growth

In general, there are two approaches for the fabrication of 3D micro- and nanostructures, the *bottom-up* and the the *top-down* approach. Top-down approaches allow to predefine the NW diameter, NW length, and the pitch between the different structures. Here a widely used method is to lithographically pattern a planar GaN layer and form NW arrays by dry etching the uncovered material.[39–42] However, the dry etching process introduces a lot of point defects at the NW sidewalls which act as non-radiative recombination centers.[43] To overcome this drawback, Wang *et al.* introduced an additional anisotropic chemical wet etching step after the dry etching, which led to defect-free and smooth side facets.[42] One further approach for the fabrication of ordered NWs with clean side facets is thermal sublimation instead of dry and wet etching processes.[44,45] Thermal sublimation is performed under vacuum conditions, eg. in MBE or MOCVD systems, at elevated temperatures. After Damilano *et al.*[44] have introduced the concept of selective area sublimation by creating randomly arranged top-down NW ensembles, Fernández-Garrido *et al.*[45] demonstrated the fabrication of ordered NW arrays by SAS using a prepatterned SiN mask. With this approach, the NW diameter, the NW length, and the pitch between NWs cloud be controlled. In chapter 6, another SAS approch using AlN as a mask material will be presented. One general drawback of the top-down approach regarding the material quality is that the final structure is limited by the properties of the initial planar layer. The planar layer may, for example, contain a high density of extended defects which is a common shortcoming of III-nitrides due to the lack of suitable low-cost substrates.[2] These defects will also be present in the final 3D structures and hence determine their material quality.

But also bottom-up approaches like the selective area growth (SAG), where highly ordered GaN NW arrays can be achieved on various substrates using a prepatterned mask,[46,47] may result in highly defective micro- or nanostructures. SAG makes use of the fact that the nucleation on the mask material is suppressed and preferentially takes place in the processed mask holes on the underlying substrate. However, due to the high probability of multiple nucleation within one hole for most substrates, SAG NWs often end up as coalesced aggregates.[48,49] Similar to the bottom-down approaches, also SAG has the disadvantage of the very cost- and time-intensive preprocessing of the mask. Moreover, the growth window to preserve the selectivity of the mask during the nucleation process is usually quiet small and does not allow a broad variation of the growth parameters. Besides using SAG with a prepatterned mask, bottom-up GaN NWs can also be grown by means of a vapor-liquid-solid approach using metallic seeds like Ni.[50,51] The usage of metal seeds, however, led to a high concentration of stacking faults and metal contamination in the obtained NWs.[52]

In contrast to the above-mentioned top-down and bottom-up approaches, *self-assembled* bottom-up NWs can be grown in high crystalline quality on a wide variety of substrates without a complex substrate preparation.[19,52–62] Their main advantage is that disloca-

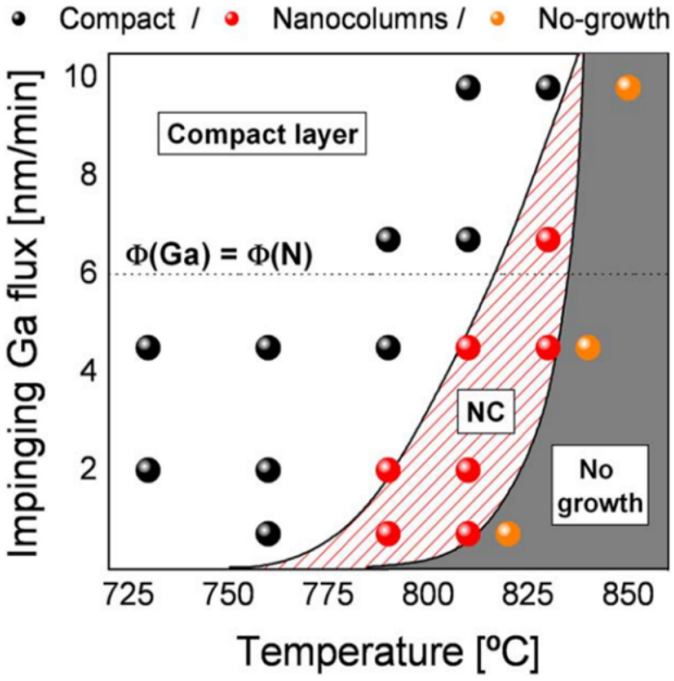


**Figure 2.8**: Growth diagram for self-assembled GaN NWs indicating three growth regimes: layer growth (Compact layer), NW growth (NC) and the absence of GaN nucleation (No growth). Figure reprinted from Ref. 67.

tions introduced at the substrate interface (due to the lattice mismatch) do not propagate along the NW but are confined at the interface[63] or bend toward the free NW sidewalls.[10,64] Moreover, the high NW aspect ratio allows the elastic relaxation of strain at the NW sidewalls during the growth[65,66] which, for instance, enables a higher In incorporation in axial (In,Ga)N/GaN NW heterostructures in comparison to the planar case. The first reports of self-assembled GaN NWs grown by MBE were published by Yoshizawa *et al.*[53] and Sánchez-García *et al.*[54] in the late 1990s. In contrast to planer GaN layers, these samples were grown under N-rich conditions at elevated temperatures.

In general, the formation of self-assembled NWs strongly depends on the III/V flux ratio and the substrate temperature, as shown in the growth diagram in Figure 2.8. The diagram, which was established by Fernández-Garrido *et al.*,[67] depicts that at low temperatures, it is rather difficult to obtain NWs, independent of the III/V ratio. Only at elevated temperatures and effectively N-rich growth conditions, NWs start to form. The existence of a *threshold temperature* for the NW growth suggests that an enhanced Ga adatom diffusion plays a major role for NW nucleation.[27] At very high temperatures, no growth takes place since NW nucleation cannot be preserved due to the high Ga desorption.

On the microscopic level, NW growth can be divided in two growth stages, *NW nucleation* and *NW elongation*, which are characterized by several main processes: Adsorption,

desorption, diffusion, incorporation, and decomposition. The nucleation process of self-assemble GaN NWs has been studied most intensively for NW ensembles on Si[12] and was described in terms of thermodynamic models.[12,27,68,69] During the early growth stage the impinging Ga and N atoms are adsorbed at the substrate surface and may diffuse along the surface or eventually desorb again. After a certain incubation time which strongly depends on the growth conditions, adatoms cluster and eventually form stable, spherical cap-shaped nuclei on a $Si_xN_y$ amorphous interlayer.[68] The $Si_xN_y$ interlayer is the result of chemical reactions between the Si surface and the impinging N. The transition from nucleus to NW was analyzed in detail by Consonni *et al.*.[68] They found that once the nuclei reach a critical diameter of a few nanometers, they undergo a shape transition towards nanowires with a hexagonal cross-sections edged by *m*-plane side facets and a C-plane top facet. This transformation is likely driven by strain relief and the anisotropy of surface energies.[68,70]

The shape transition marks the beginning of the second growth stage, the NW elongation, which is dominated by surface kinetic effects.[71,72] Here Ga adatom diffusion from the substrate towards the NW as well as along the NW side walls has a significant influence on the axial and radial growth rates. N adatom diffusion, however, was found to be negligible for the elongation process. On the one hand the diffusion length of N adatoms on polar facets was found to be much smaller than the one of Ga adatoms.[73,74] On the other hand, on non-polar facets, N adatoms are rather unstable against the formation and desorption of $N_2$ molecules.[75] Both the axial and the radial growth rate strongly depend on the effective III/V ratio at the NW top facet. For low effective III/V ratios, hence, very N-rich growth conditions, the axial growth rate along the C-direction is limited by the amount of Ga present at the top facet of the NWs. The amount of Ga is determined by the impinging Ga flux and the Ga adatoms which diffuse from the sidewalls of the NWs onto their top facet.[27,56,57,71,72,76–78] The driving force for this diffusion is a gradient in chemical potential towards the NW tip. A mechanism that will be discuss in detail in chapter 5. With increasing III/V ratio (but still N-rich conditions), also the contribution of the Ga adatom diffusion towards the tip of the NWs increases. This process continues until the axial growth rate is limited by the active nitrogen available at the NW top facet, which is about the amount of the impinging N.[72]

Regarding the radial growth, Fernández-Garrido *et al.* found that the final NW diameter is self-regulated.[72] The understanding here is that during the early phase of the elongation stage, when the NWs are still small, they are able to collect a significant amount of Ga from the surface due to diffusion. Once the Ga adatom concentration at their top facets exceeds the one of N, radial growth sets in and the effective III/V ratio decreases with increasing diameter until stoichiometry at the top facet is reached. From this point on, further radial growth takes place at a much smaller growth rate. In the case of higher Ga desorption at elevated substrate temperatures, the initial effective III/V flux ratio at the top facet of the NWs is lower and hence stoichiometry is reached earlier. This results in a smaller self-equilibrated diameter. If stoichiometry at the top facet cannot be

reached since the effective III/V ratio at the NW tip does not drop below one, as it would be the case for nominally metal-rich growth conditions, a compact layer forms due to NW coalescence. Hence, the kinetic growth model introduced by Fernández-Garrido *et al.* explains well why N-rich growth conditions are needed to grow well-defined NWs and how the NW radius is defined by the III/V ratio. There are numerous further studies, which investigated the axial and radial growth of NWs by MBE.[71,72,78–91] However, there are still open questions regarding the detailed diffusion process on the different NW facets. For instance, the influence of the circular arrangement of the material sources in the chamber on the diffusion processes and the resulting sequential deposition of the materials on different side facets of the NWs have not yet been investigated in detail. A careful analysis of this topic will be presented in chapter 5.

Regarding the polarity, most experimental results suggest that self-assembled GaN NWs on most substrates, including metals, are N-polar and hence grow along the $[000\bar{1}]$ direction.[61,92–98] Only recently Concordel et al. demonstrated that the NW polarity can be flipped from N-polar to Ga-polar by introducing a Ga-O-N intermediate layer in the NWs.[99] In general, the polarity of the NWs not only affects the direction of both spontaneous and piezoelectric polarization[25,100] but also the incorporation of In in axial (In,Ga)N/GaN structures,[101,102] the incorporation of dopants[103] or impurities,[104] as well as the formation of native point defects.[105]

# 3. Self-assembled formation of long, thin, and uncoalesced GaN nanowires on crystalline TiN

In the last two decades, GaN nanowire growth has been demonstrated on various substrates[19,52–62] including exotic materials like graphene or $Ti_3C_2$ MXenes.[106–108] But only in the recent years, metal substrates have been exploited for GaN NW growth.[19,61,62,109–114] Their high electrical and thermal conductivity as well as their optical reflectivity make metal substrates interesting for optoelectronic applications.[19]Moreover, most metals can be sputtered on various substrates and the ability to grow high quality semiconductor materials on these metals would not only allow the fabrication of new devices but also facilitate a low-cost integration of III-nitride materials with other material systems.

So far, GaN NWs have been realized on Ti and Mo films sputtered on different substrates like $Al_2O_3$, Si, silica glass, $SiO_x$ and Mo foils[18,19,109–112] as well as on bare Ti and Ta foils.[61,62] Also first NW-based LEDs grown on Ti films as well as on bare Ti and Ta foils have been demonstrated.[62,109–113] However, most of the NW ensembles in these approaches showed rather high NW densities and/or the majority of NWs was inclined due to an irregular surface morphology. Likewise, on most of the commonly used substrates, such as Si, well developed self-assembled NW ensembles usually exhibit high NW number densities of around $10^{10}\,cm^{-2}$, leading in turn to a massive coalescence of the NWs.[16,17,31,59,115–118] The coalescence process can result in the formation of boundary dislocations.[117,119–123] Thus, NW coalescence imposes restrictions on the nanowires' structural perfection, which also affects the structural quality of heterostructures based on these NWs. Moreover, high number densities of NWs prevent homogeneous growth on the NW side facets due to their strong mutual shadowing. This is also true for inclined NWs caused by an irregular substrate surface. Such a roughening of the metal substrate is usually the result of strong interfacial reactions at the interface between semiconductor and metal, which still pose serious obstacles for the direct integration of semiconductor materials on metals.[124] Besides causing an irregular morphology of the NW ensemble, these reactions may diminish the purity and crystalline quality of the NWs.[62,114] In general, it is hence desirable to find growth approaches that result in a lower number density and coalescence degree while avoiding negative influences of interfacial reactions.

Very promising seems to be the growth of the self-assembled NWs directly on crystalline TiN, which has resulted in very low NW number densities and vertical NWs.[19]

These are two aspects which are very important for the growth of high-quality and well-defined axial and core-shell heterostructures. At the same time, these NWs were still rather short and varied in length. It was not yet clear whether the observed low number density of the GaN NW ensemble on TiN could be maintained to avoid NW coalescence once the GaN NWs further elongate. Furthermore, the influence of the strong chemical reactions in the substrate on the morphology of the NW ensemble as well as on the optical properties of the single NWs has not been studied so far. Regarding the obvious difference in NW density and in the degree of coalescence between NW ensembles on TiN and Si, another open question was, how the nucleation process on TiN differs from the one on Si and how coalescence depends on the nature of the nucleation mechanism.

In this chapter and in order to investigate these points in more detail, we first review the previous work by Wölz *et al.*[19] on which parts of our study builds in section 3.1. In section 3.2, we demonstrate the self-assembled growth of uncoalesced GaN NWs on TiN with diameters smaller than 50 nm and a homogeneous length of more than 1 µm and compare their optical properties to the ones of a common NW ensemble on Si. Furthermore, we discuss the role of interfacial reactions for the morphology and the optical quality of NWs on TiN and evaluate the influence of the substrate preparation and the growth conditions in section 3.3. In section 3.4, we investigate the coalescence behavior in such NW ensembles with different average lengths and discuss how coalesence is related to the nucleation mechanism of the NWs. Besides the suppression of coalescence, the NW ensembles presented here exhibit a combination of number density, length, and diameter that makes them very suitable as the basis for the growth of core-shell heterostructures. This is of particular interest, since one goal of this thesis is to investigate core-shell structures where long, thin and uncoalesced GaN NWs on TiN should serve as the core/template NWs (see chapters 5 and 6).

Parts of this chapter have been published in D. van Treeck *et al.*, Nano Research, 11(1), 565–576 (2018)[125] and in G. Calabrese *et al.*, Nanotechnology, 30, 114001 (2019),[126] which I co-authored. Regarding the latter study, I will focus on the insights I acquired in the scope of this thesis and contributed to this publication. Work that has been carried out by my colleagues will be denoted and cited appropriately.

## 3.1. Review of relevant previous work

In the previous chapter, some fundamental properties of the NW formation on Si(111) was discussed. Si has been studied intensively as substrate for NW growth for more than two decades. The pioneer work for GaN NWs on metals was carried out by Martin Wölz at Paul-Drude-Institut. At the start of our investigation on GaN NWs on TiN in early 2015, there were only two published studies[18,19] by Wölz *et al.* on this topic. The

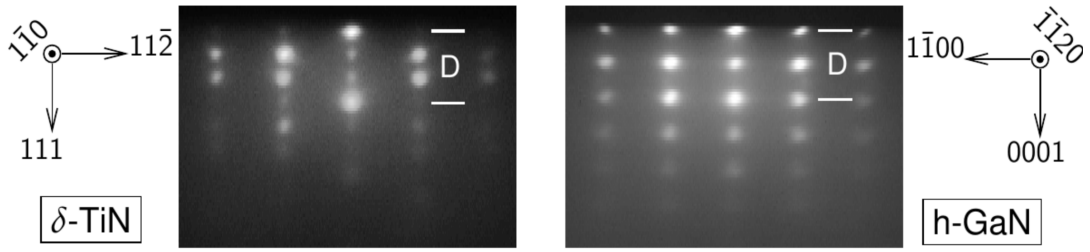


**Figure 3.1**: RHEED patterns of a sputtered Ti film on $Al_2O_3$ in the narrow-spaced azimuth, recorded immediately after the opening of the shutters (left-hand column) and after 90 min GaN growth (right-hand column). The figure was reprinted and modified from Ref. 19.

research presented in this thesis directly builds on the insights of their work. Hence, in this section, we introduce parts of their work that are relevant for a better understanding of our studies.

As a substrate Wölz *et al.* used a sputtered Ti film of about 1 µm on a C-plane $Al_2O_3$ carrier substrate. The in-plane orientation of the Ti film with regard to the $Al_2O_3$ was determined by XRD and was found to be $\alpha$-Ti$\langle 11\bar{2}0\rangle \| \alpha$-$Al_2O_3\langle 1\bar{1}00\rangle$. In their growth approach, they first heated the substrate to about 850 °C (according to the reading of an optical pyrometer calibrated on Si), a temperature which was too high for GaN nucleation. Once the Ga and N shutters were opened, the upper layer of the Ti film was nitridized and TiN formed. A analysis of the resulting RHEED pattern as shown in Figure 3.1 (a) as well as ellipsometry measurements performed after the growth (see Ref. 19) confirmed the presence of $\delta$-TiN at the substrate surface. In the subsequent step, the substrate temperature was lowered for about 90 min by 1 K/min until NW nucleation was visible in the RHEED (see Figure 3.1 (b)). The substrate temperature was then kept constant at 750 °C for 6 hours, until the NW growth was ended by closing the Ga and N shutters and the substrate temperature was ramped down. From RHEED analysis the orientation-relationship between the GaN NWs and the TiN was found to be $\alpha$-GaN$(0001)\langle 11\bar{2}0\rangle \| \delta$-TiN$(111)\langle 1\bar{1}0\rangle$, resulting in a lattice mismatch of 6.4%.

The morphology of the resulting GaN NW ensemble is shown in the SE micrographs of Figure 3.2. As the micrographs depict, the GaN NWs were vertically oriented with a mean length of about 200 nm and diameters between 20 – 40 nm. As already mentioned, very promising was the rather low number density of the NWs of about $8 \times 10^8\,\mathrm{cm}^{-2}$. On Si and most other substrates, the number density would have been an order of magnitude higher, even for such a small mean length of the NWs.[16,31]

Besides the promising results of Wölz *et al.*, the growth on metals also bears some challenges. For the direct growth of GaN NWs on sputtered Ti films, the high reactivity of Ti leads to strong interfacial reactions. Comparing the XRD profiles of a sputtered Ti

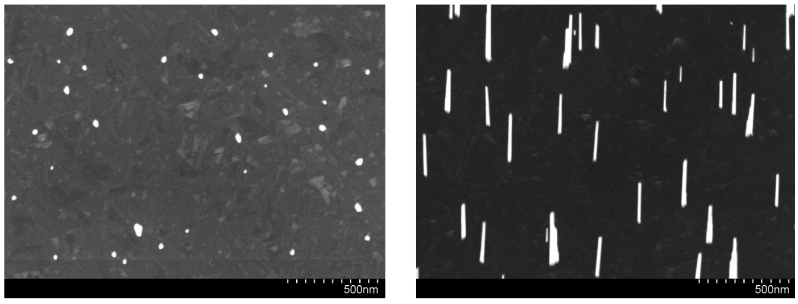


**Figure 3.2**: Plan view (left) and bird's eye (right) SE micrographs of the GaN ensemble grown on a sputtered Ti film on $Al_2O_3$ by Wölz *et al.*. The figure was reprinted and modified from Ref. 19.

film before and after the growth of NWs, Wölz *et al.* found that the $\alpha$-Ti film sputtered on a $Al_2O_3$ carrier substrate is consumed due to reactions with the underlying $Al_2O_3$ and the impinging materials once the shutters were opened. Analyzing the specific diffraction peaks of the XRD profiles, they identified two major reactions in the sputtered Ti film: oxidation and nitridation. Due to the diffusion of O from the $Al_2O_3$ carrier substrate into the Ti film, Ti oxidizes and $Ti_2O$, TiO, and $TiO_2$ are formed, where the latter mainly appears in the *anatase* mineral form. Once the N shutter is opened, nitridation takes place and the impinging active N and the Ti of the sputtered film form (predominantly) $\delta$-TiN. According to the ellipsometry measurements presented in Ref. 19 this leads to the formation of a TiN layer on top of the sputtered Ti film on which the GaN NWs nucleate. Also a small visible amount of the Al-containing compound $Ti_2AlN$ was observed in the XRD profile, suggesting that not only O but also Al diffuses into the about 1 µm thick Ti film.

In order to evaluate the crystal quality of GaN NWs on TiN, Wölz *et al.* acquired low-temperature continuous-wave µm-PL and time-resolved PL and found that the results to state-of-the-art GaN NWs grown on a crystalline Si substrate.[19] They found that with the same FWHM of the dominant donor-bound exciton transitions in the continuous-wave µm-PL spectra of about 1 meV, both samples show a value which is among the lowest reported for such GaN NW ensembles and suggests a high structural quality.[52] Furthermore, they identify luminescence that they attributed to radiative recombination of excitons bound to stacking faults in GaN. Also the time-resolved PL revealed that there was no indication for an additional nonradiative decay channel due to the growth on the metallic TiN. In the end, they concluded that the GaN NWs on TiN are of comparable crystal quality as GaN NWs grown on Si(111).

## 3.2. Towards long, thin an uncoalesced GaN nanowires

As already pointed out, one major advantage of GaN NWs on TiN is the low NW density which, for instance, allows the growth of core-shell heterostructures on the non-polar side facets of the self-assemble NWs. However, for most core-shell applications, the NWs have to be sufficiently long to use the full potential of the core-shell architecture. Hence, as a first step towards a better understanding of the growth of GaN NWs on TiN, we explored whether the low NW density observed for the small NWs presented by Wölz *et al.*[19] can be preserved once the NWs elongate.

Similar to the work of Wölz *et al.*, the substrate used for all self-assembled GaN NW ensembles presented in this thesis was a Ti film sputtered by a DC magnetron on a C-plane $Al_2O_3$ wafer.[19] However, for our studies, we had to use a different growth approach. With more than 8 hours of total growth time for rather small NWs, the approach of Wölz *et al.* was not very practical.[18,19] Especially with regard to the growth of more complex axial or radial structures based on these NWs, which would imply an even longer growth duration. In order to realize a more efficient growth process and reduce the growth time, in our first approach, the growth was directly started, i. e. the Ga and N shutters were opened simultaneously, at certain substrate temperatures where NW nucleation is likely.

As a first attempt, three different NW ensembles 3.A, 3.B, and 3.C were grown at different substrate temperatures $T_{sub}$ of 750 °C, 725 °C, and 700 °C, respectively, for 4 h* on a 2 µm thick Ti film with $\Phi_{Ga} = 4.5$ nm/min and $\Phi_N = 7.8$ nm/min. The substrate temperatures given above correspond to the reading of the thermocouple of the substrate heater. As a reference temperature the surface temperature of sample 3.B was measured by a calibrated disappearing-filament pyrometer to be about 800 °C. For the Ti film a thickness of 2 µm Ti was chosen with the attempt to minimize the diffusion of Al and O from the $Al_2O_3$ towards the growth interface. The bird's eye and plan view SE micrographs of Figures 3.3 (a)–(f) depict the NW morphology of the three samples. It should be noted that all three samples occasionally show hillock structures on which the NWs grow in a tilted way, as shown exemplarily for sample 3.C in the inset of Figure 3.3 (f). The origin of these structures will be discussed in detail in the next section. Figures 3.3 (g) and (h) show, as a reference, SE micrographs of a typical GaN NW ensemble on Si. The micrographs depict the typically high NW density and coalescence degree of NWs on Si, which is in particular visible at the bottom part of the NWs.

For all three samples 3.A – 3.C, prior to the nucleation of the first NWs, a thin TiN layer formed at the surface of the sputtered Ti. In accordance with the findings of Wölz *et al.*, the formation of a cubic TiN layer with a [111] out-of-plane orientation was confirmed

*Unfortunately, at that point of the study, the plasma source only allowed very small N fluxes which resulted in a still rather long growth time of 4 hours. In later studies we transferred the growth experiments from M9 to M2, where the plasma source delivered much higher N flux and the growth time for comparable NW ensembles could be reduced to 2 hours.

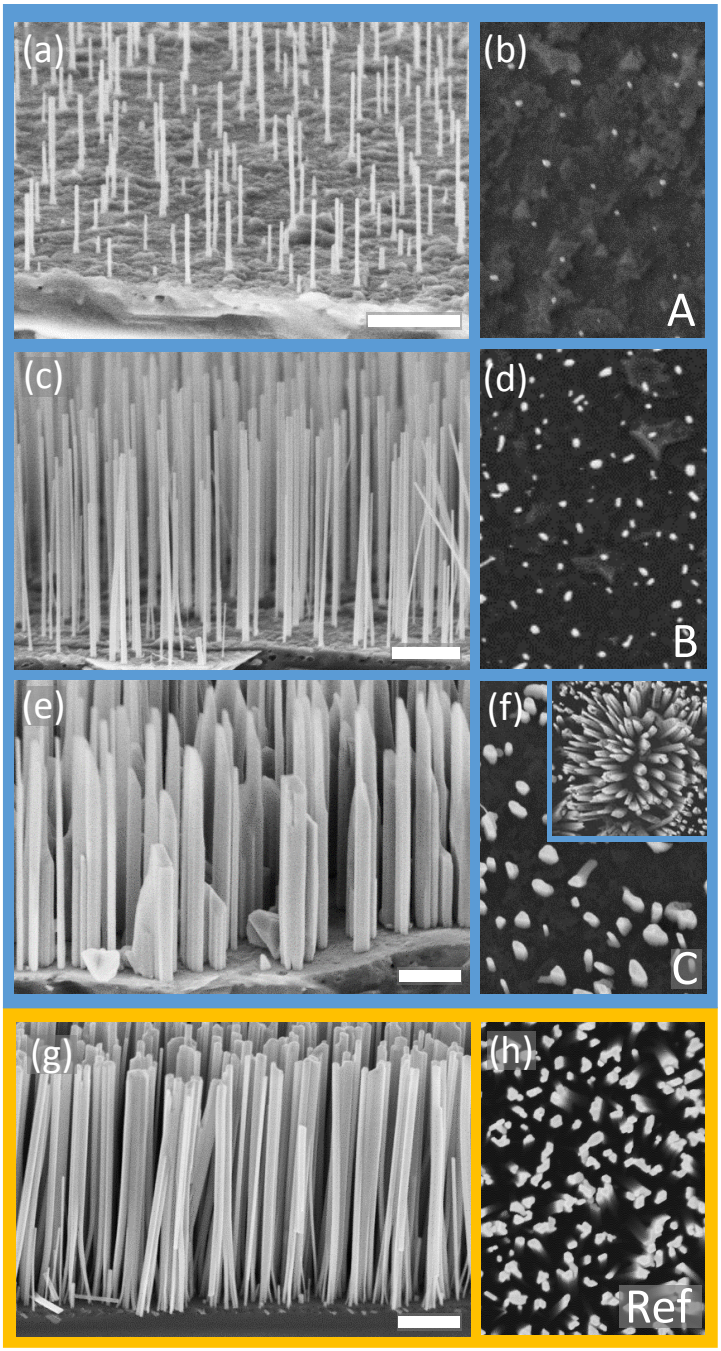


**Figure 3.3**: Bird's eye (a/c/e) and plan view (b/d/f) SE micrographs of the NW ensembles 3.A, 3.B, and 3.C grown at three different substrate temperatures 750, 725, and 700 °C on TiN at otherwise similar conditions. Bird's eye and plan view SE micrographs (g) and (h) show the reference NW ensemble on Si, which has been grown by J. Zettler. The scale bars correspond to 500 nm. SE micrographs acquired by A.–K. Bluhm.

*in situ* by RHEED and *ex situ* by ellipsometry and EDX (data not shown here). The images of sample 3.A, 3.B and 3.C reveal that changes in $T_{sub}$ of about 25 °C have a strong

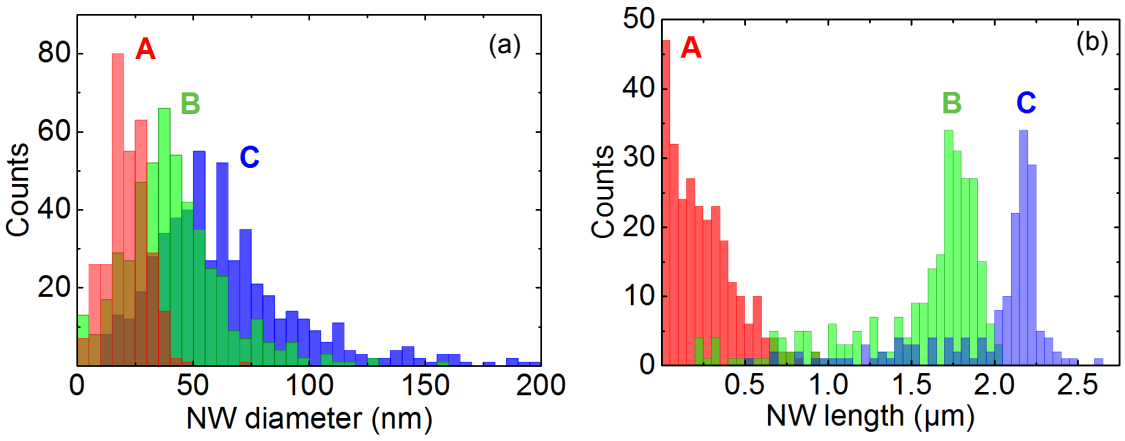


**Figure 3.4**: The histograms in (a) and (b) show the length and diameter distributions of samples 3.A, 3.B, and 3.C with mean diameters of 22, 42 and 67 nm and mean lengths of 220 nm, 1.5 µm and 2.0 µm, respectively.

influence on the final morphology of the NW ensembles on TiN. In the following, we discuss the differences in morphology on the basis of the quantitative analysis of the NW density, diameter and length. A more detailed description of the analysis is given in chapter 2.3.2. We find that with decreasing $T_{sub}$, the number density initially increases from about $1.3 \times 10^9$ cm$^{-2}$ to $2.2 \times 10^9$ cm$^{-2}$ and is then reduced to about $1.1 \times 10^9$ cm$^{-2}$. The lowering of the number density for sample 3.C is attributed to the coalescence of NWs, which leads to the formation of aggregates with larger diameters.[16,17,31,59,115,116] Consequently, in Fig. 3.4 (a) we observe in the diameter distribution of sample 3.C with a mean diameter of 67 nm a clear skew with an extended tail towards larger diameters. In contrast, the diameter distributions of sample 3.A and 3.B with mean diameters of 22 nm and 42 nm, respectively, exhibit narrower and more symmetric distributions, signifying the absence of coalescence in these two ensembles.[17] A detailed analysis of the coalescence degree of a NW ensemble on TiN grown under optimized growth conditions will be presented in section 3.4.1.

The smaller NW diameters of sample 3.A can be explained by a smaller self-equilibrated NW diameter due to an increased Ga adatom desorption at higher substrate temperatures.[72] Indications for increasing Ga desorption are also seen in the length histograms in Fig. 3.4 (b). The mean length of the NWs decreases with increasing $T_{sub}$, while the width of the length distribution broadens. These trends can be explained as follows. The longer the NWs become during the growth, the smaller is the amount of Ga which is collected from the surface and reaches the NW tips by diffusion along the NW side facets. Hence, once the self-equilibrated diameter and with that stoichiometry at the top facet is reached, due to the elevated substrate temperatures, the effective III/V ratio may become smaller than one. As a result, the axial growth rate may become Ga-limited and decreases with increasing substrate temperature. Furthermore, at high substrate temper-

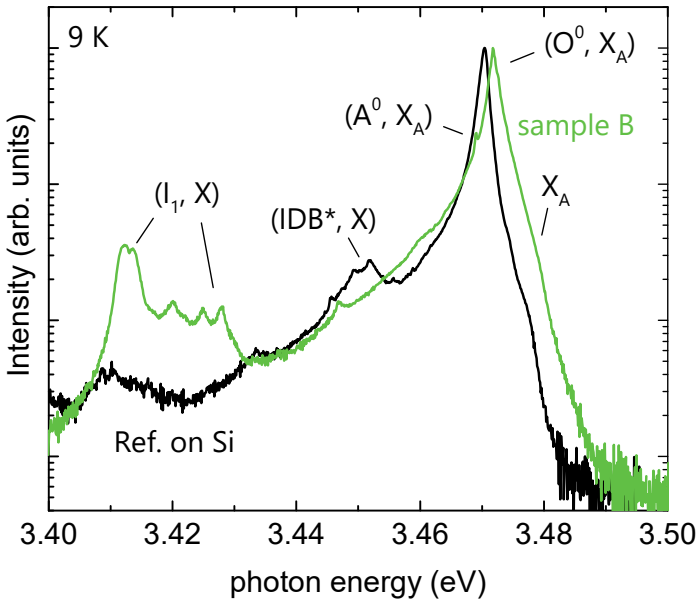


**Figure 3.5**: PL spectra of sample 3.B and the reference GaN NW ensemble on Si measured at 9 K, as indicated by the legend. Reference sample grown by J. Zettler, measurements performed by P. Corfdir.

atures the increased Ga desorption and GaN decomposition lower the probability of NW nucleation. Hence, the individual NWs nucleate at very different times, resulting in a broader length distribution as it is visible for sample 3.A. The nucleation process of GaN NWs on TiN is discussed in more detail in section 3.4.2.

From the temperature series shown in Fig. 3.3, it follows that for low substrate temperatures around 700 °C (sample 3.C), one obtains NW ensembles which are rather uniform in length. However, these NWs are fairly thick and coalesced, similar to those on the reference sample on Si. For high $T_{sub}$ of around 750 °C (sample 3.A), we found NW ensembles with very thin NWs that do not exhibit any obvious sign of coalescence. At the same time, they are rather short and very inhomogeneous in length, similar to what we previously observed for growth on TiN.[19] In contrast, for the growth at an optimum intermediate $T_{sub}$ (725 °C for sample 3.B corresponding to about 800 °C real surface temperature), NW ensembles with long and thin NWs which are homogeneous in length can be obtained. Most importantly, these NWs appear to be uncoalesced. Moreover, very little parasitic GaN growth is seen between these NWs grown on a conductive substrate. So far, the self-assembled formation of GaN NWs combining all these beneficial properties has been very difficult.

To evaluate the optical quality of these NWs on TiN, we performed PL measurements at 9 K. Figure 3.5 shows the normalized PL characteristics of sample 3.B grown at the

optimum substrate temperature as well as of the reference NW ensemble on Si. The reference has been grown at a calibrated substrate temperature of 825 °C, hence, at about 25 °C higher *real temperature* than sample 3.B, with a similar approach as presented in Ref. 127. The PL spectra of both samples, reference and sample 3.B, are dominated by the emission band originating from the recombination of A excitons bound to neutral O donors ($O^0$,$X_A$) at 3.4703 eV[128] and 3.4717 eV,[19,126] which depict a similar FWHM of about 1.7 and 1.9 meV, respectively. The shoulder at the high-energy side around 3.478 eV visible in both spectra is related to the recombination of free A excitons ($X_A$), whereas the small peak in the spectrum of sample 3.B at 3.469 eV at the low-energy side of the ($O^0$,$X_A$) line arises from excitons bound to neutral acceptors ($A^0$,$X_A$).[19,126,128] There are two further distinct emission bands visible around 3.45 and 3.41 eV which stem from the recombination of excitons at inversion domain boundaries ($IDB*$,$X_A$)[129,130] and basal-plane stacking faults ($I_1$,$X_A$).[131]

In general, the optical quality of long, thin and well-separated GaN NWs on TiN obtained for the growth conditions of sample 3.B is quite similar to the one of optimized GaN NWs on Si. The fact that the peak luminescence of sample 3.B is shifted by 14 meV to higher energies with respect to the reference sample can be attributed to homogeneous strain in the NW ensemble. This strain results from surface stress acting on the NW sidewalls and is only noticeable in ensembles of NWs with sufficiently small diameters.[132] The about ten times higher PL intensity of the ($I_1$,$X_A$) transition of sample 3.B suggests the presence of a higher concentration of stacking faults, which might be related to the lower growth temperature of sample 3.B and/or the presence of surface irritations due to interfacial reactions (discussed in detail in the next section). However, the lower stacking fault-related PL intensity of the NW ensemble on Si might also be related to the fact that it has a much higher NW density. As a result and in contrast to the low density NW ensembles on TiN, in the reference sample mainly the upper parts of the NWs, which contain less extended defects than the bottom parts, are excited during the PL measurements.

Despite the fact that for sample 3.B the majority of the sample area depicts long, thin and well separated NWs, the frequently appearing hillock structures, as shown in the inset of Figure 3.3 (f), are a major issue. For instance, using these ensembles for NW-based devices, the hillocks would cause serious problems for a homogeneous processing of the device, not to speak of potential defects that would be introduced and strongly affect the final device performance. Moreover, my colleagues G. Calabrese and T. Auzelle found that the optical properties of the GaN NWs in TiN strongly depend on the substrate preparation and the growth temperature.[126] This is an aspect we pick up on in the next section.

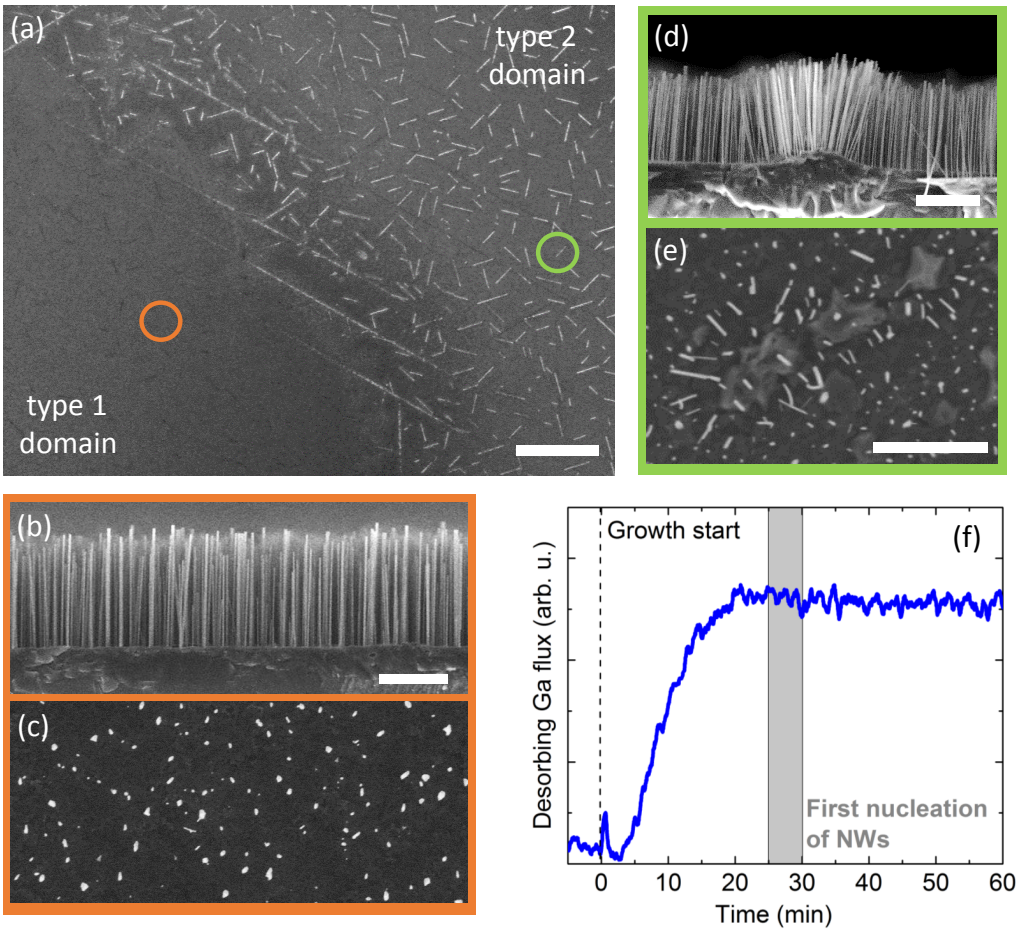


**Figure 3.6**: (a) Plan view SE micrograph of sample 3.D showing the two different morphology domains, type 1 and type 2. Cross-sectional (b) and (d) as well as plan view (c) and (e) SE micrographs of the NW morphology representative for the type 1 and type 2 domain, respectively. Moreover, the images (d) and (e) show the morphology of a hillock structure which appears frequently in the type 2 domain. (f) Desorbing Ga flux during the first 60 min of the growth of sample 3.D determined by QMS. The start of the growth is indicated by the dashed line. The grey time window marks the appearance of the first GaN nuclei detected *in situ* by RHEED. SE micrographs partially acquired by A.–K. Bluhm.

## 3.3. The role of interfacial reactions

Analyzing the morphology of the samples 3.A – 3.C, we found that hillocks (e. g. see inset of Figure 3.3 (f)) form all over the sample and diminish the morphological quality of the NW ensembles on TiN. In order to prevent the formation of the hillocks, several different approaches have been tested. Neither an intentional nitridation of the substrate at growth temperature before the Ga was opened, nor a further increase of the Ti film thickness resulted in an improved morphology of the NW ensemble. Also using Ti films

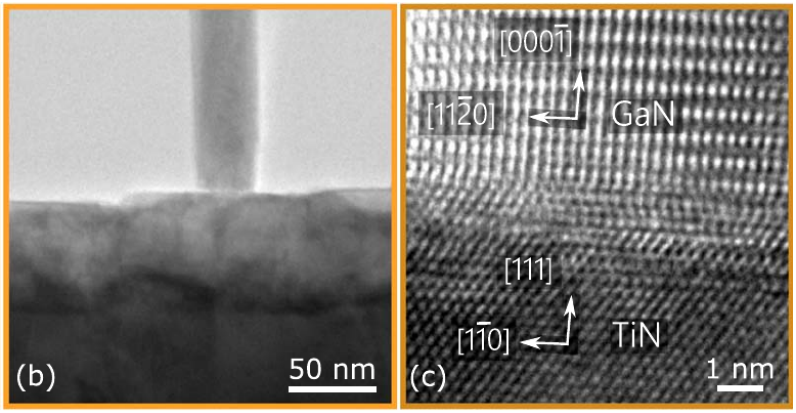


**Figure 3.7**: (a) Bright-field cross-sectional TE micrographs of the bottom part of a NW on TiN. (b) High-resolution cross-sectional TE micrograph of the GaN/TiN heterointerface for a single NW. Both micrographs were acquired for a sample grown at similar conditions as sample 3.D. The micrographs were acquired by G. Gao. The analysis was carried out by G. Gao and A. Trampert in cooperation with G. Calabrese.

thinner than 1 µm lead to very coalesced ensemble morphology.

Interestingly, NW ensembles on a 1.3 µm thick Ti grown at the optimum substrate temperature of sample 3.B, depict two different macroscopic domains with areas in the $mm^2$-range, as shown in the representative plan view micrograph of sample 3.D in Figure 3.6 (a). The sample 3.D was grown with a Ga flux $\Phi_{Ga} = 4.5$ nm/min and a N flux $\Phi_N = 5.6$ nm/min for 6 h, reaching a mean NW length of about 1.5 µm and a mean diameter of 43 nm. The type 1 domain exclusively consists of long, thin, well-separated, and vertically oriented GaN NWs as shown in the cross-sectional and plan view SE micrographs of Figure 3.6 (b) and (c), respectively. There are no hillock structures. The type 2 domain, however, is dominated by elongated hillocks which appear in between vertically aligned NWs. Similar to the samples 3.A – 3.C, the NWs grown on the hillocks are highly tilted, as depicted in the high magnification bird's eye and plan view SE micrographs of Figure 3.6 (d) and (e), respectively. The formation of such hillocks can be mainly attributed to strong chemical reactions between the oxidized Ti substrate and the impinging elements. The low and only steadily rising QMS signal of the desorbing Ga flux of sample 3.D, shown in Figure 3.6 (f), indicates that a lot of Ga is incorporated into the substrate during the incubation time, i. e. in the phase between the opening of the Ga and N shutters (growth start) and the time, when the first GaN nucleation could be detected by RHEED.

To better understand the chemical reactions in the sputtered Ti film, a NW ensemble similar to sample 3.D has been analyzed structurally and chemically by cross-sectional TEM and EDX, respectively. The bright-field TE micrograph of Figure 3.7 (a) shows the base of a NW on a about 40–80 nm thick layer. The layer material was identified to be

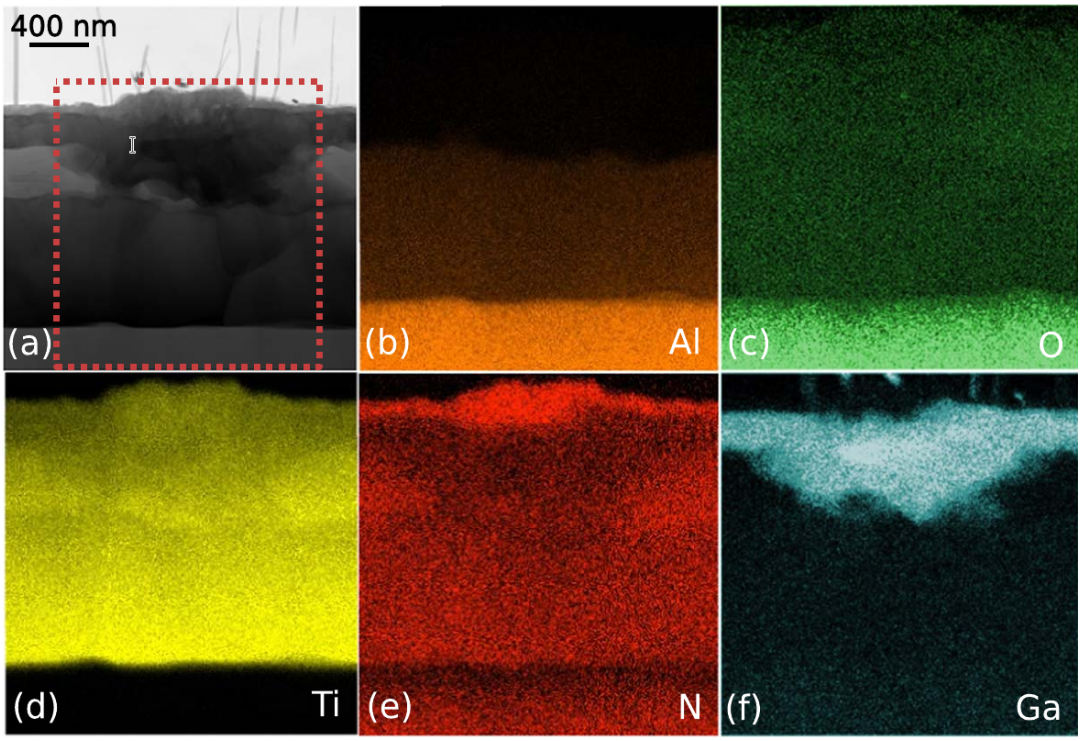


**Figure 3.8**: Bright-field cross-sectional TE micrograph of a sample grown at similar conditions as sample 3.D. (b)–(f) EDX maps measured in the highlighted region of (a) for the elements Al, O, Ti, N and Ga, as indicated by the corresponding labels. Measurements carried out by G. Gao.

TiN by EDX measurements in a TEM (see analysis below), by EDX line scans along the substrate surface in an SEM, and by ellipsometry measurements (the latter two measurements are not shown here). Similar to the representative example here, the investigated NWs on TiN did not show any threading dislocations or basal-plane stacking faults. Figure 3.7 (b) shows a high-resolution TE micrograph of the interface between an individual GaN NW and the TiN layer. The epitaxial orientation-relationship between the N-polar GaN NWs and the TiN layer was determined to be $\alpha$-GaN$(0001)\langle 11\bar{2}0\rangle \| \delta$-TiN$(111)\langle 1\bar{1}0\rangle$, resulting in a lattice-mismatch of about 6.4%, which is in agreement with the reports of Wölz *et al.*. The interface between GaN and $\delta$-TiN consists of a disordered transition layer containing nano-twins and edge dislocations. Moreover, as a consequence of the large lattice mismatch between GaN and TiN, misfit dislocations have formed which extend within the interface plane but do not propagate along the NW axis.

The bright-field TE micrograph of Figure 3.8 (a) shows the cross-section of the $Al_2O_3$ carrier substrate (bright region in the bottom part of the image) below the sputtered about 1.3 µm thick Ti film, which now depicts several different material compounds. Between the topmost TiN layer and the $Al_2O_3$, three more layers with a different contrast can be identified in the micrograph. The layers appear rather homogeneous except in the image

center, where the cross-section of a hillock is captured. In order to assess the chemical composition of the whole substrate, the marked area of Figure 3.8 (a) has been analyzed by EDX as presented in the maps of Figures 3.8 (b)–(f) for the elements Al, O, Ti, N and Ga. The EDX maps of N and Ti clearly indicate that the topmost layer consists of TiN, as already confirmed by the analysis of the high-resolution image in Figure 3.7 (a). It should be noted that the high N background signal visible for the entire thickness of the sputtered film in Figure 3.8 (e) originates mostly from the epoxy glue used for the TEM sample preparation. Only showing a strong signal for Al and O, the bottom layer of Figure 3.8 (a) was confirmed to be the $Al_2O_3$ carrier substrate. The EDX maps further reveal that Al and O also diffuse into the sputtered film. At the end of the growth, Al has diffused up to about 800 nm into the sputtered layer, whereas O even diffused throughout the whole 1.3 µm thick film. The appearance of these interdiffusion processes can be attributed to the elevated substrate temperature needed for the growth of the NWs. The presence of Al, O and Ti in the bottommost 800 nm of the sputtered film suggests the formation of $Al_xTi_yO_{1-x-y}$ compounds in this area, whereas the rest of the Ti film is oxidized and various Ti suboxides are expected to form during the heating of the substrate and/or during the growth. The presence of $Ti_2O$, TiO, and $TiO_2$ in a similar substrate has already been reported by Wölz *et al.* and has been confirmed for our approach by an additional XRD analysis (data not shown here). Finally, as indicated by the EDX map for Ga, the second layer from the top (below the TiN layer), which extends deeper into the sputtered film underneath the hillock in the center part, is not only composed of Ti and O but also contains a high concentration of Ga. The incorporation of Ga into the sputtered film and the formation of $Ga_xTi_yO_{1-x-y}$ compounds explains the Ga consumption detected by QMS during the incubation phase (see Figure 3.6 (f)).

To better understand the formation of the hillocks, the surface structure of a sputtered Ti film right before the growth start is analyzed. Figure 3.9 shows plan view micrographs of the surface of a sputtered film that has been heated at growth temperature for 40 min without exposing it to Ga and N. Additional EDX measurements of the surface carried out in a SEM system revealed that the surface of the substrate right before the opening of the Ga and N shutter consists of $Ti_xO_y$. The micrographs clearly reveal that there are elongated depressions within the $Ti_xO_y$ surface, supposedly in the areas where later the hillocks occur. The presence of depressions prior to the growth might explain the deeper penetration of the $Ga_xTi_yO_{1-x-y}$ layer in the hillock area observed in the Figures 3.8 (a)–(f). About the reason why hillocks would form inside the surface depressions can only be speculated. One explanation might be the accumulation of Ga inside the depressions during the incubation phase resulting in an increased formation of $Ga_xTi_yO_{1-x-y}$.

In further investigations, my colleague G. Calabrese found that with an intentional nitridation step during the initial heating phase towards the growth temperature of the GaN NWs, in combination with a thicker Ti film (3.4 µm), the formation of hillock structures can be prevented on the whole sample. The PL of such a further optimized sample

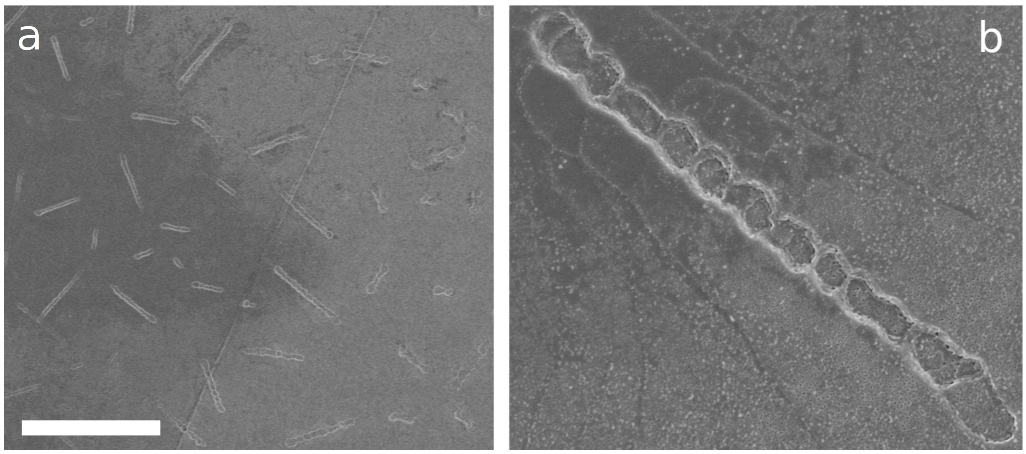


**Figure 3.9**: Plan view SE micrographs of the surface of a sputtered Ti film that has been heated at the growth temperature of sample 3.D for 40 min without exposing it to Ga and N. The micrographs depict elongated depressions within the $Ti_xO_y$ surface. The scale bar coreponds to 30 µm and 3 µm for migrograph (a) and (b) respectively.

depicts an even smaller FWHM of the ($O^0$,$X_A$) band than sample 3.B and also a reduced intensity of the ($IDB*$,$X_A$) line. This suggests the presence of a much smaller number of stacking faults for NWs on TiN and a higher overall crystal quality in comparison to the reference sample on Si. Besides the thickness of the Ti film and the nitridation procedure, also the substrate temperature plays a significant role for the optical properties of the NWs. The more the substrate temperature is raised above the optimum temperature, the higher is the O incorporation into the GaN NWs. About 10 – 20 °C deviation is sufficient to see a doping effect due to O incorporation in the PL spectrum. A more detailed analysis (not part of this thesis) on how the interfacial reactions and the substrate temperature affect the optical characteristics of the NWs on TiN can be found in Ref. 126.

It should be noted that the optimized GaN NW ensembles grown on 3.4 µm Ti films with an intentional nitridation step prior to the NW growth, were only developed after the analysis carried out in the following sections of this chapter. For the analysis of the coalescence and the nucleation behavior of GaN NWs on TiN shown in the following section 3.4 we focus on the type 1 domain of the respective samples.

## 3.4. About the correlation of coalescence and nucleation

In the previous sections, we established the growth of long thin and uncoalesced NWs on TiN under the consideration of the suitable substrate and growth parameters. The obvious difference in NW density and in the degree of coalescence between NW ensembles on TiN and Si raises the question of the origin of these fundamental differences. For Si and diamond as substrates, it was shown that the NW density can be reduced by

high temperature growth, however, as a consequence the NWs are rather short and very inhomogeneous in length.[133,134] Moreover, further experiments on Si showed that the growth of *long* NWs with *uniform length* at such elevated substrate temperatures again results in high NW densities, similar to growth under conventional conditions.[135] This result is supported by recent findings that the final NW number density on Si is only limited by the shadowing of the impinging fluxes by already existing NWs.[31] An alternative substrate which allows the growth of GaN NW ensembles with lower NW densities is an AlN buffer layer on Si.[57,94,136,137] In particular, Brubaker *et al.*[93] demonstrated the growth of long and thin NWs with densities in the $10^8\,\mathrm{cm}^{-2}$ range on a 40-nm-thick AlN buffer layer. However, on AlN in addition to the NWs a rather thick parasitic GaN layer forms on the substrate.[138] Furthermore, the AlN buffer layer enabling such low NW densities is usually several tens of nm thick and insulating, which is a drawback regarding the use of the NW ensembles in optoelectronic applications.

So indeed, the self-assembled NW growth on TiN resulting in such low NW number densities seems to be very different compared to most other substrates. To better understand the origin of low NW density and the absence of coalescence, this section focuses on the investigation of the coalescence behavior as well as the underlying nucleation mechanism of GaN NWs on TiN.

### 3.4.1. Coalescence

In order to elucidate why the NW ensembles on TiN have such beneficial properties, we first investigate the nature of coalescence of these NW ensembles. In the following, we study the evolution of the morphology at the optimum substrate temperature for different growth times. Figure 3.10 shows bird's eye [(a) and (b)] and top view [(c) and (d)] micrographs of the NW ensembles of sample 3.D [(a) and (c)] and 3.E [(b) and (d)]. Sample 3.E was grown for 45 min at otherwise similar growth conditions as sample 3.D, reaching a mean NW length of about 120 nm. Hence, the NWs of sample 3.E are much shorter than the about 1.5 µm long NWs of sample 3.D with a growth time of 6 h. From the analysis of top-view SE micrographs, we extract a NW number density for the samples 3.D and 3.E of $1.1 \times 10^9\,\mathrm{cm}^{-2}$ and $5.9 \times 10^8\,\mathrm{cm}^{-2}$, respectively. Consistent with the results for sample 3.B, both samples 3.D and 3.E exhibit mainly well separated NWs, which already suggests a low coalescence degree. Nevertheless, a closer inspection reveals that NWs may nucleate quite close to each other [see orange circle in Fig. 3.10 (d)], and such NWs might eventually coalesce during growth and form an elongated aggregate [see orange circle in Fig. 3.10 (c)]. In order to quantify the degree of coalescence of NW ensembles, analyzing the circularity of the NW top facets as well as the dependence of the top facet area on its perimeter proved to be a good measure for NWs on Si.[17,117] However, on TiN the slight tilt of the NWs makes such an analysis of the circularity of the NWs impractical. Instead, we manually counted visibly coalesced NWs in top-view micrographs and divided this number by the total number of objects. Thus, we were able to estimate the coalescence

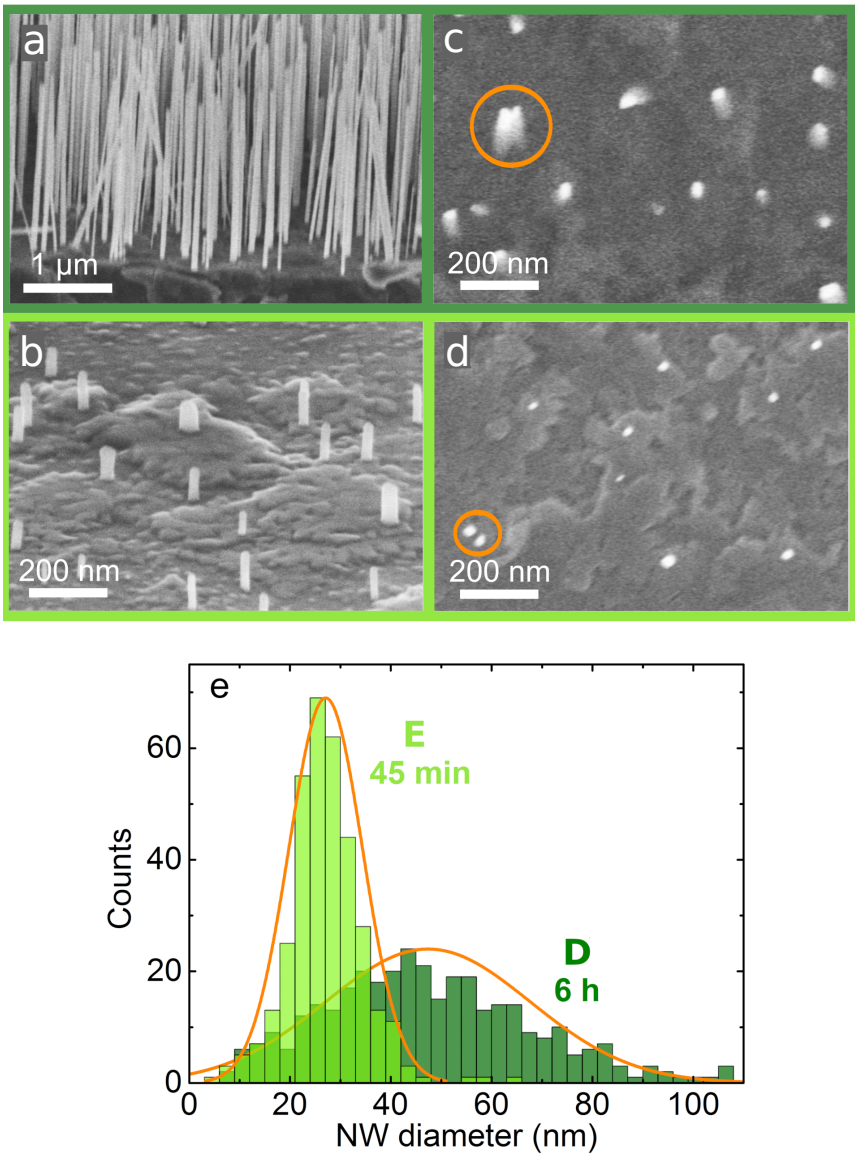


**Figure 3.10**: Bird's eye [(a) and (b)] and top view [(c) and (d)] SE micrographs of NW ensembles 3.D [(a) and (c)] and 3.E [(b) and (d)] grown at the optimum substrate temperature for 45 min and 6 h, respectively. The corresponding number densities are $5.9 \times 10^8$ cm$^{-2}$ and $1.1 \times 10^9$ cm$^{-2}$, respectively. The histogram in (e) shows the diameter distributions of the two NW ensembles. The diameters of the NWs in both samples follow a Gaussian distribution (orange graphs), indicating a low coalescence degree of these NW ensembles. SE micrographs partially acquired by A.–K. Bluhm.

degree of sample 3.D to be around 7%, which is about a factor ten lower than what has been reported for NW ensembles of the same length grown on Si.[17,117] For the short growth time of sample 3.E, hardly any indication of coalesced NWs were found, leading to a coalescence degree of less than 1%.

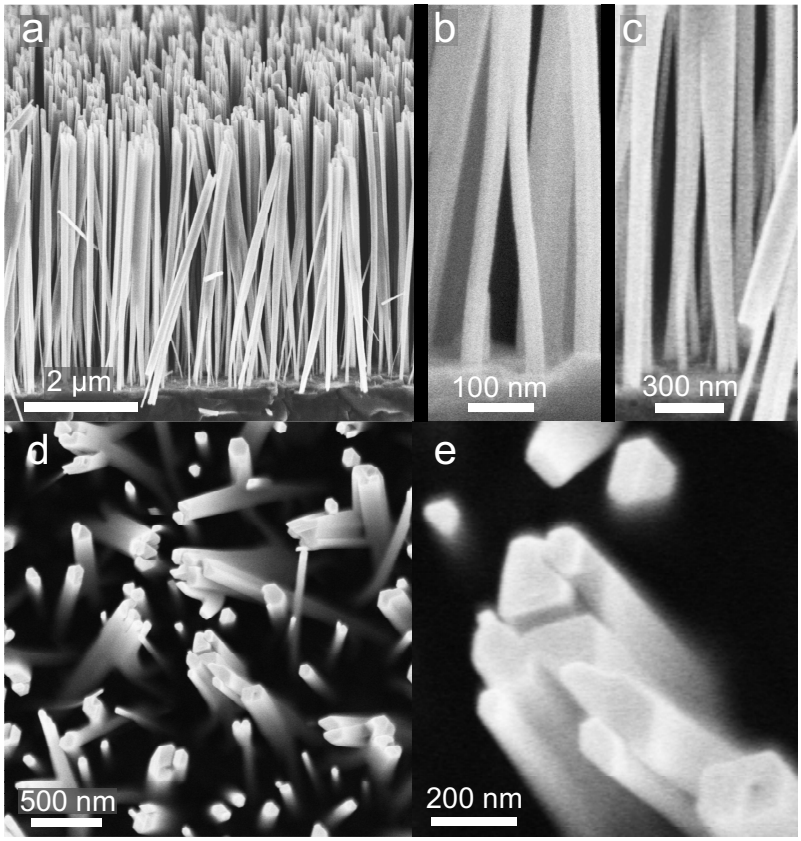


**Figure 3.11**: Bird's eye [(a), (b) and (c)] and top view [(d) and (e)] micrographs of sample 3.F. The mean length of the NWs is with about 4.7 µm three times longer than for sample 3.D. Most of the NWs are coalesced, as the high magnification images (b), (c) and (e) reveal. The sample has been grown for 7 h under the same conditions as the sample 3.D presented in Figs. 3.10 (a) and (c), however, the flux of active N species was twice as high. SE micrographs partially acquired by A.–K. Bluhm.

Another way to analyze the coalescence of NW ensembles is to consider the distribution of the NW diameters. In particular, the diameter distribution of a NW ensemble with mainly uncoalesced NWs can be well described by a Gaussian distribution.[17] Once the NWs coalesce, they form aggregates of larger diameters. As a result, the diameter distribution of a highly coalesced NW ensemble is clearly skewed with an extended tail towards larger diameter values and is then rather described by a gamma distribution.[17,139] Figure 3.10 (e) shows the diameter histograms of samples 3.D and 3.E, with a mean diameter of 43 nm and 24 nm, respectively. The comparatively small diameters of sample 3.E can be explained by the fact that in this early growth stage, most of the NWs have not yet reached their self-equilibriated diameter.[72] As the orange curves indicate, both diameter histograms are fit well by Gaussian distributions. Therefore, the different ways of analysis all show that GaN NW ensembles can be grown on TiN with very low coalescence degree up to a mean NW length of at least 1.5 µm.

Next, we investigate whether coalescence becomes relevant in much longer GaN NWs grown on TiN. To this end, we consider sample 3.F as shown in Figure 3.11 with a mean NW length of about 4.7 µm. It was grown for 7 h with a N flux twice as high ($\Phi_N = 11.9$) in comparison to sample 3.D and 3.E to increase the growth rate at otherwise similar growth conditions. The micrographs already reveal that for NW ensembles of such a length most NWs are coalesced also on TiN. The number density of objects, where one object can be a single NW or an aggregate of several NWs [see Fig. 3.11 (d)] is about $6.9 \times 10^8\,\mathrm{cm}^{-2}$. Counting the individual wires visible in the thick, merged aggregates, as well as the free-standing NWs in between, the actual number density of nucleated NWs could be estimated to be at least $1.7 \times 10^9\,\mathrm{cm}^{-2}$. Following the same procedure as for samples 3.D and 3.E, a coalescence degree of around 77% was determined. In other words, in NW ensembles grown on TiN with a length of about 5 µm uncoalesced NWs are an exception, similar to the situation on Si for a length of about 1 µm.[17,116,117]

We now analyze the coalescence mechanism in more detail. Kaganer *et al.*[31] showed that on Si the coalescence process is mainly caused by the bundling of NWs and not by the merging of wires due to radial growth and/or their mutual misorientation. Once the NWs reach a certain critical length $L_c$, it is energetically favorable for them to bundle and thus reduce their total surface energy at the expense of the elastic energy of bending. This critical length for coalescence by bundling strongly depends on the NW radii and the distance between the single NWs. The height (above substrate) at which the NWs merge together is then given by $h_c = 3\,L_c/4$.

Figure 3.11 reveals that the base of many NW aggregates on TiN consists of at least two initially uncoalesced NWs which bend towards each other and bundle at a certain height, similar to the behavior on Si. By a close inspection of various aggregates, we found that usually the smaller the NW diameter and the distance between the NWs, the smaller is the height at which the NWs coalesce. Figure 3.11 (b) shows an example where two NWs, which initially nucleated around 100 nm apart from each other, merge at a height of about 425 nm. Applying the quantitative model of Ref. 31 using diameters of 50 and 60 nm extracted from the SE micrographs for the two NWs, we obtain a height $h_c$ of about 415 nm, i. e., a value very similar to the measured one. As the second example, Figure 3.11 (c) depicts an event of multiple bundling, demonstrating that bundling also occurs among already coalesced aggregates. Inspecting the base of the two aggregates, we find that they themselves were originally formed by the coalescence of several thin and uncoalesced NWs, which had nucleated very close to each other. Both aggregates with diameters of around 100 nm bundle at a height of about 1.2 µm. Taking into account the distance between the two thick aggregates of 270 nm, the model predicts a value for $h_c$ of around 1.25 µm, which is once again close to the measured value. The two examples in Figure 3.11 (b) and (c) show that the coalescence of GaN NWs on TiN can be well described by the model of Ref. 31. We conclude that, in general, the coalescence of GaN NWs on TiN seems to be governed by the same mechanism as on Si.

The analysis of samples 3.D, 3.E, and 3.F has shown that for a certain NW number

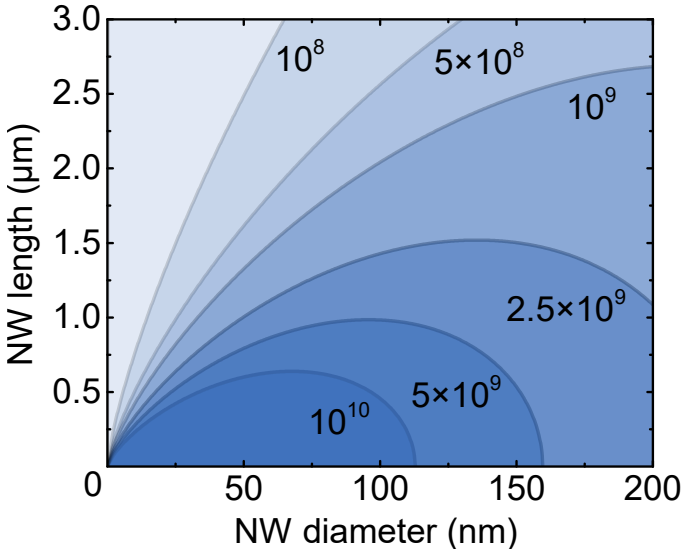


**Figure 3.12**: The different graphs describe the critical length $L_c$ [31] above which it is energetically more favorable for the NWs to bundle/coalesce. The behavior of $L_c$ is shown for NW ensembles with number densities from $10^8$ to $10^{10}\,cm^{-2}$. Note that here all NWs in the ensemble are assumed to have the same diameter, the same length and to be arranged in a hexagonal lattice at equal distances.

density, the coalescence degree depends mainly on how long the NWs are grown. The graphs in Figure 3.12 illustrate the critical length $L_c$ in dependence of the NW diameter, above which coalescence sets in for a certain NW number density of the ensemble. For an optimized NW ensemble on TiN with a number density of about $1 \times 10^9\,cm^{-2}$ and a mean diameter between 40 and 50 nm, coalescence only occurs for NWs longer than around 1.3 µm. In comparison, for typical NW ensembles on Si, during the early growth stage the NW density rises to more than $1 \times 10^{10}\,cm^{-2}$, resulting in coalescence already for very short NWs of only a few hundred nm length.[16,31] Hence, the key factor for the growth of long and well-developed NW ensembles with low coalescence degree is the low NW number density that can be achieved for the self-assembled formation of GaN NWs on TiN. This consideration raises the question about the origin of the low NW number density on TiN.

### 3.4.2. Nucleation

In the previous section, we learned that the coalescence behavior of GaN NWs on TiN is similar to the one for NWs on Si. Hence, the low degree of coalescence found for GaN NWs on TiN in comparison to most other substrates, must be directly related to the low NW number density. In order to better understand this aspect, we now focus on the nucleation of GaN NWs on TiN since it is this process that determines the NW number density.

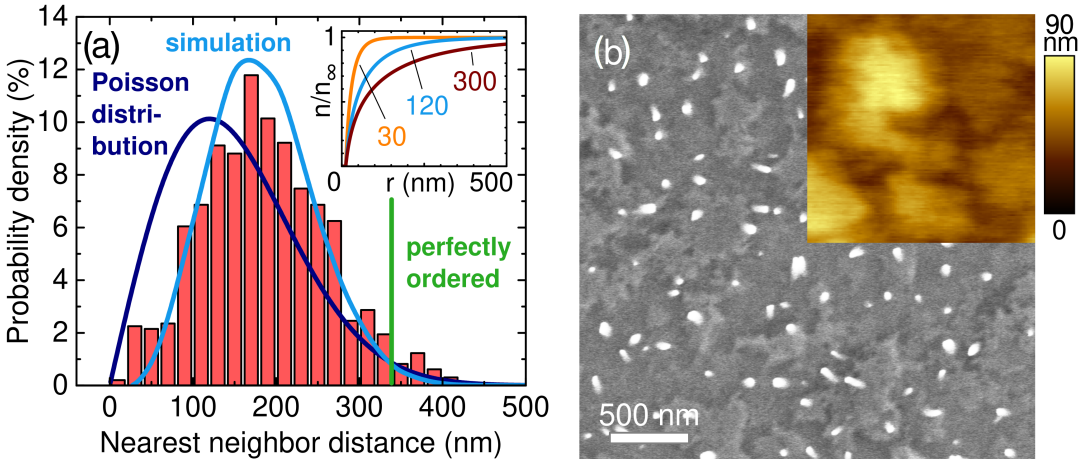


**Figure 3.13**: (a) Analysis of nearest neighbor distances (red histogram, 976 NWs investigated) of sample 3.D [see Figs. 3.10 (a) and (c)]. The vertical green line indicates the NW spacing that would occur in a perfectly ordered NW array with the same number density for a hexagonally closed-packed arrangement. The dark blue curve corresponds to the Poisson distribution that would be found in a NW ensemble with the same number density for completely random and independent nucleation sites. The light blue curve shows the nearest neighbor distance distribution of a simulated NW ensemble for a Ga adatom diffusion length on the surface of $\lambda = 120$ nm and $m = 4$. A detailed explanation of the simulation is given in the text. The inset depicts the behavior of the adatom concentration $n(r)$ around a single NW in dependence on the distance $r$ for different values of $\lambda$: 30, 120, and 300 nm. (b) Top-view SE micrograph of this NW ensemble. The inset depicts an atomic force micrograph of the TiN surface of a reference sample, where the growth has been stopped right before NW nucleation takes place (same magnification as SE micrograph (b)).

We carried out a statistical analysis of the nearest neighbor (NN) distances between single NWs, and the result for sample 3.D is shown in Figure 3.13 (a). We observe a broad distribution with values ranging from about 20 to 420 nm with a maximum around 185 nm and a slight tail towards longer NN distances. It is instructive to compare this experimental distribution with the distributions expected for perfect spatial order and complete disorder *for the same NW number density*. If the NWs nucleated in a perfectly ordered array at an equal distance from each other, the NN distance for each NW would be 340 nm (vertical green line). In contrast, if the NWs nucleated independently from each other, the NN distance distribution would follow the Poisson probability density distribution $p(x) = 2\pi\rho x \exp(-\pi\rho x^2)$ (dark blue curve), where $x$ is the NN distance and $\rho$ the number density of the ensemble. Obviously, neither of these two opposite extremes describes the case of NW ensembles grown on TiN. Nevertheless, the shift of the NN distance distribution towards higher values with respect to the Poisson distribution is a clear indication that NWs do not form completely independently on the surface. Such a non-random nucleation behavior is a natural consequence of a diffusion-induced re-

pulsion of neighboring NWs. In this scenario, once a NW nucleates, the adatoms diffuse towards the nucleus and the adatom concentration in the surrounding area decreases. As a result, the probability for further nucleation close to this NW is reduced.

In the following, we discuss this nucleation process and the role of the Ga adatom diffusion on the surface in more detail. As a starting point, we consider the adatom concentration $n(r)$ at a distance $r$ around an already existing NW. It can be described by the stationary diffusion equation $\lambda^2 \triangle n(r) - n(r) + n_\infty = 0$, where $\lambda$ is the diffusion length of the Ga adatoms on the surface and $n_\infty$ is the adatom concentration far away from the nucleus. Considering the NW to be a perfect sink for Ga adatoms, the boundary condition is $n|_{r=R} = 0$. The solution of this two-dimensional diffusion problem is given by $n(r)/n_\infty = 1 - K_0(r/\lambda)/K_0(R/\lambda)$, where $K_0$ is the modified Bessel function of zeroth order. The inset of Figure 3.13 (a) shows the behavior of $n(r)/n_\infty$ for three different Ga diffusion lengths of 30, 120, and 300 nm. In the immediate surrounding of the NW, the adatom concentration is small and equal to zero at the interface, but rises continuously with increasing distance $r$ towards $n_\infty$. Moreover, a clear trend can be seen for the influence of the Ga diffusion length $\lambda$; with increasing $\lambda$, the surface area for which the NW affects the nucleation of further NWs is enlarged.

In order to simulate the nucleation behavior of GaN NWs on TiN, we assume that the nucleation probability of a NW directly depends on the Ga adatom concentration on the surface. Using the explicit expression for the adatom concentration derived above, the probability $p(\mathbf{r})$ for a new NW to nucleate at a site $\mathbf{r}$ in between a number of $j$ already existing NWs is assumed to be $p(\mathbf{r}) = \prod_j [n(|\mathbf{r} - \mathbf{r}_j|)/n_\infty]^m$, where $\mathbf{r}_j$ is the position of the $j$th already existing NW and $m$ is a parameter related to the number of Ga atoms contained in the critical nucleus.[140–142]

For the simulation of a whole NW ensemble by a Monte Carlo approach, we randomly choose nucleation sites on a predefined area, where NWs nucleate with a respective probability $p(\mathbf{r})$ until a specific NW density is reached. Figure 3.13 (a) shows that the NN distance distribution of sample 3.D can be very well modeled by the NN distance distribution of a simulated NW ensemble (light blue curve) using a diffusion length of $\lambda = 120$ nm and $m = 4$. The value for $\lambda$ is actually comparable to that reported by Kishino *et al.*,[143] who assessed the diffusion length of Ga adatoms on a nitridized Ti mask for selective-area growth by measuring the distance between single nucleation sites on the mask. The NN distance distribution of a simulated NW ensemble with a smaller adatom diffusion length (not shown here) would be close to the Possion distribution, similar to what has been found for GaN NW ensembles of similar density on Si.[31] For larger adatom diffusion lengths, however, the respective NN distance distribution would be narrower and shifted towards a perfectly ordered arrangement in comparison to sample 3.D.

This analysis shows that the Ga adatom diffusion length on the surface has an important influence on the ordering of the NWs and seems to be mainly responsible for the nucleation behavior on TiN. However, not only the ordering of the NWs is influenced,

but also the NW number density. The larger the Ga adatom diffusion length, the more unlikely it becomes for a new NW to nucleate close to already existing NWs, which in the end results in a lower NW number density for long and well developed NW ensembles.

Another origin of non-random nucleation, besides diffusion-induced repulsion of neighboring NWs, could be heterogeneous nucleation at preferred sites on the surface. Figure 3.13 (b) shows a top-view SE micrograph that indeed evidences significant roughness of the TiN layer on which NW nucleation takes place. The atomic force micrograph displayed in the inset of Figure 3.13 (b) shows that the surface consists of variously shaped islands of several hundred nm width and length with a peak-to-valley roughness of 90 nm over an area of $1 \times 1\,\mu m$. However, a close inspection of several such SE micrographs did not reveal any correlation between the surface morphology and the spatial location of the NWs. The NWs were found to nucleate neither preferentially at the edges, nor ontop nor in between the islands. Hence, diffusion-induced repulsion seems to be the best explanation for the observed NN distance distribution. Interestingly, for the Stranski-Krastanov growth of InAs quantum dots on GaAs, Moison *et al.*[144] found that higher surface roughness shifts the NN distribution towards shorter NN distances and hence closer to the Poisson distribution describing random nucleation. Due to the rather rough surface morphology of the TiN, it is likely that also in our case the diffusion of the Ga adatoms on the substrate and with that the NW density are affected by the surface roughness.

Finally, we test whether the idea of diffusion-induced repulsion of neighboring NWs can explain how the NW density evolves on TiN from the early nucleation stage to the final, fully developed NW ensemble. To this end, we consider again samples 3.D and 3.E grown under the same conditions for different durations (see Fig. 3.10). For sample 3.E with a growth time of 45 min, most NWs are found to have a similar length of around 120 nm, and there are hardly any short NWs which have just nucleated. This observation suggests that the nucleation density on TiN increases rapidly to a value (here mid $10^8\,cm^{-2}$) for which most Ga adatoms diffuse to a nearby NW and are incorporated there. As a consequence, the nucleation rate drops significantly. This interpretation is also consistent with the fact that for sample 3.D, which was grown for an additional 5 h, the NW density is only twice as high as for sample 3.E. At the same time, this increase implies that the nucleation of further NWs is not suppressed entirely. Indeed, the histogram of sample 3.B in Fig. 3.4 (b) reveals the presence of NWs of varying lengths all significantly shorter than the average. One explanation for this ongoing nucleation is that the influence of the already existing NWs on the Ga adatom concentration on the surface decreases once they reach a certain length. Hence, diffusion-induced repulsion and a consequential low (but non-zero) probability of continuous nucleation explain satisfactorily the way in which the NW number density evolves with time on TiN.

We note that this finding is in contrast to the self-assembly of GaN NWs on Si, for which Kaganer *et al.*[31] recently showed that the number density is limited not by adatom diffusion but by shadowing of the substrate from the impinging molecular beams by elon-

gating NWs. On TiN, we estimate that 70 and 2% of the surface are shadowed for sample 3.D and 3.E, respectively. The similar number densities for these samples despite a vast difference in the shadowing efficiency clearly shows that shadowing alone cannot be the main process limiting the number density on TiN. Obviously, shadowing will inevitably contribute to the reduction in nucleation rate with time and completely suppress it for a certain NW length. Still, the key factor that enables number densities as low as $10^9\,\mathrm{cm}^{-2}$ for well developed NW ensembles on TiN is diffusion-induced repulsion.

The comparison of the processes limiting the NW number density on TiN and Si implies that the adatom surface diffusion length is noticeably larger on the former substrate. This result is rather surprising in view of the significant surface roughness of TiN films compared to the atomically smooth Si substrates. Note, however, that the diffusion length of about 120 nm estimated from the modeling of the NN distance distribution in Figure 3.13 (a) is actually smaller than the typical size of the islands seen in Figure 3.13 (b). Thus, the main question is rather why the surface diffusion length of Ga adatoms is so short on Si. Further research is needed to develop an atomistic understanding of these diffusion processes.

## 3.5. Summary and Conclusions

In this study, we have demonstrated the growth of self-assembled, long, thin and well-separated GaN NWs on metallic TiN. We found that due to the influence of interfacial reactions, such morphologically well-developed NW ensembles with optical properties comparable to state-of-the-art NW ensembles on Si can only be obtained for certain thicknesses of the Ti film and very specific nitridation and growth conditions. Moreover, we have shown that during the self-assembled growth process on TiN substrates, the mutual coalescence of NWs is largely absent for NW lengths up to about 1.5 µm. For lengths clearly exceeding this value, coalescence takes place mainly by bundling, similar to what occurs on Si already for much shorter NWs. The key factor leading to coalescence degrees as low as 7% in fully developed NW ensembles on TiN is the low NW number density of about $10^9\,\mathrm{cm}^{-2}$. On TiN, the number density is limited not by shadowing that prevents the nucleation of further NWs on Si, but by the diffusion-induced repulsion of neighboring NWs. In other words, the adatom diffusion length on the substrate is the crucial factor which determines the NW number density and hence the coalescence degree of GaN NWs on TiN.

As a perspective, the properties of the NW ensembles shown in the present work are an excellent basis for the fabrication of more complex structures. Due to the low coalescence degree, the GaN NWs on TiN exhibit a much more regular plan-view cross-section than the typical irregular aggregates on other substrates. This feature may significantly improve the structural quality of axial heterostructures. Finally, let us consider the suitability of self-assembled GaN NW ensembles on TiN for the growth of core-shell het-

erostructures on the non-polar side facets. High number densities result in strong mutual shadowing of the NWs and thus prevent homogeneous growth on their side facets. In contrast, on TiN the NWs in a fully-developed ensemble with the dimensions of sample 3.D are only shadowed for less than 20% of the time from either Ga or N. Hence, these NW ensembles are promising templates for the realization of well-defined and homogeneous multi-shell heterostructures whose properties may prove useful for applications.

# 4. Axial (In,Ga)N/GaN heterostructures on GaN nanowires on TiN

NW-based axial (In,Ga)N/GaN heterostructures grown by MBE have been employed for a diversity of applications, in particular for optoelectronic devices.[118] One advantage of the 3D nature of NWs is that the strain introduced by the lattice mismatch between (In,Ga)N and GaN can be accommodated elastically due to relaxation at the nanowire sidewalls. This way, the effects of strain-induced piezoelectric fields within the QWs are reduced and insertions with high In contents can be achieved while avoiding the formation of extended defects.[66,145]

However, as already discussed in the previous chapter, on most of the commonly used substrates, such as Si, well developed self-assembled NW ensembles usually exhibit high NW number densities.[16,31,59,115–118] As a result the NWs coalesce and form aggregates with very irregular radial cross-sections and an altered faceting,[17,123,125] a process which likely introduces inhomogenous strain and results in the formation of boundary dislocations.[17,117,119–123] The irregular morphology of the NWs might also affect the structural and optical quality of axial heterostructures grown on top of these NWs. In fact, many of the NW-based axial heterostructures grown so far show irregular shapes.[18,146–151] For example, (In,Ga)N/GaN heterostructures often depict cone-shaped or parachute-like (In,Ga)N insertions with an inhomogenoeus In distribution which are surrounded by a GaN shell. In the light of these facts, the well-defined and uncoalesced GaN NWs on TiN presented in the previous chapter offer an interesting alternative as a basis for axial heterostructures. The question is, whether the regular shape of these NWs allows to improve the morphology and possibly the luminescence properties of common NW-based (In,Ga)N/GaN heterostructures. Beyond that, the fact that the NWs on TiN are well separated due to the low NW number density and exhibit rather homogeneous diameters and lengths, is very beneficial for systematic growth studies.

In this chapter, we demonstrate that the low coalescence degree and the resulting regular plan-view cross-section of GaN NWs on TiN, as presented in chapter 3, allows the growth of (In,Ga)N QWs extending along the c-plane with a well-defined shape. With the intention to minimize the incorporation of point defects as well as the formation of stacking faults, we introduce a high-temperature growth approach for the fabrication of the (In,Ga)N/GaN heterostructures. In order to evaluate the structural quality of (In,Ga)N/GaN heterostructures, we first analyze the morphology of the NW ensem-

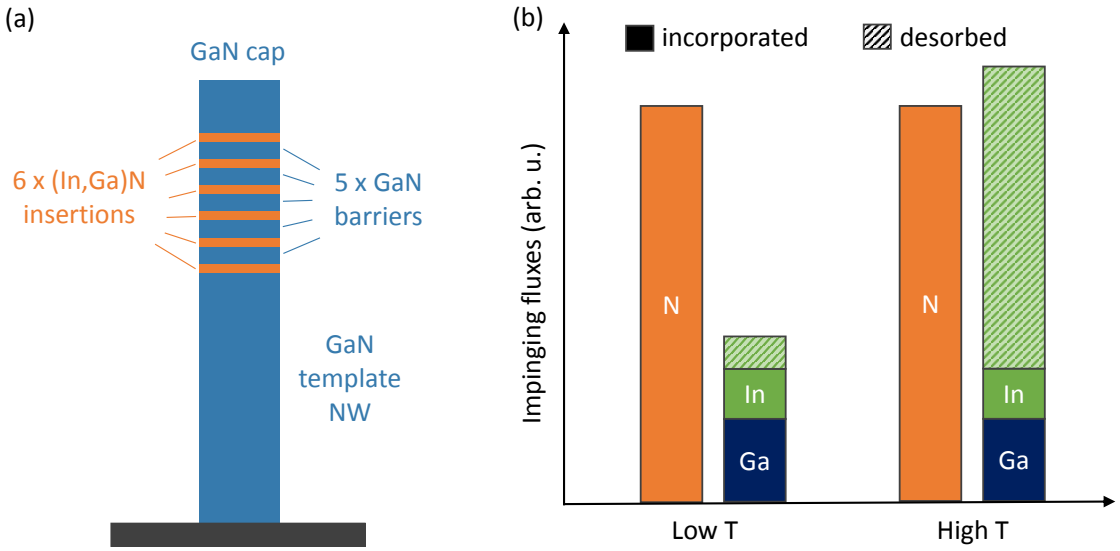


**Figure 4.1**: (a) Sketch of the intended axial (In,Ga)N/GaN heterostructure on top of GaN NWs on TiN. (b) Bar diagram which sketches two different approaches for the growth of the axial heterostructures – one at low temperature with nominally N-rich growth conditions and one at higher growth temperature with nominally metal-rich growth conditions.

ble by SEM as well as the microstructure of single NWs by TEM. Finally, we study the optical properties of the (In,Ga)N/GaN heterostructures.

## 4.1. The growth approach

In this chapter we will investigate four different axial (In,Ga)N/GaN heterostructures (4.A, 4.B1, 4.B2, and 4.B3) grown at three different temperatures on top of GaN NWs on TiN as presented in the previous chapter 3. Note that in this chapter, the substrate temperatures correspond to the reading of the thermocouple of the substrate heater, since the infrared optical pyrometer used for other studies in this thesis was not well calibrated at that time. Figure 4.1 (a) shows a sketch of the intended axial heterostructure. As a first step, GaN template NWs with a length of about 1 µm were grown at otherwise comparable conditions* as for sample 3.D (SE micrographs, see Figure 3.6). Subsequently, the substrate temperature was lowered for the growth of the active region consisting of six QWs separated by five GaN barriers and a GaN cap on top of the last QW. The nominal thicknesses of the QWs, the GaN barriers and the GaN cap were with 3.1 nm, 10 nm and 35 nm, respectively. These parameters were kept constant for all samples investigated in

*The template NWs in this chapter have been grown at a higher N flux in comparison to sample 3.D. After the maintenance of the plasma source, the N flux increased from $\Phi_N = 7.8$ nm/min to 13.2 nm/min.

this chapter except for sample 4.A, where the nominal QW thicknesses was with 3.4 nm slightly larger.

Usually, axial (In,Ga)N/GaN heterostructures on NWs have been grown under nominally very N-rich growth conditions at rather low temperatures, as indicated in the bar diagram for *Low T* of Figure 4.1 (b). At low temperatures the In desorption is reduced, hence, the usual In/Ga ratio around one is sufficient to achieve QWs with high In contents. In this study, in order to avoid the formation of stacking faults and the incorporation of point defects, the active region has been grown at much higher temperatures. For planar N-polar (In,Ga)N/GaN heterostructures Chèze *et al.* [152] showed that growing the active region at higher substrate temperatures increases the luminous efficiency. This effect was attributed to reduced incorporation of point defects at the heterointerfaces. To compensate the tremendous In desorption at elevated temperatures, the (In,Ga)N QWs of all our samples were grown under nominally metal-rich growth conditions with a V/III ratio of 0.91 and an In/Ga ratio as high as 15, as indicated in the bar diagram for *High T* of Figure 4.1 (b). For all three samples, this results in a desorption of more than 95% of the impinging In measured by QMS.

## 4.2. Morphology and structural analysis

Figure 4.2 (a) and (b) show a cross-sectional and a plan view SE micrograph of sample 4.A, respectively, which has been grown at a substrate temperature of 540 °C. The images reveal that the NWs are still well separated and that the low temperature growth of (In,Ga)N and GaN did not lead to a coalescence of the NWs. This is clearly visible in the plan view micrograph, where the long NWs are colored in yellow. The active regions which constitute the upper 100 – 150 nm of the NWs depict a rather straight shape with a slight tapering towards the NW top. In between the long template NWs, small parasitic NWs have formed that cover the entire substrate (see plan view image).

To analyze the microstructure of the active region, TEM measurements were performed on sample 4.A. Figure 4.2 (c) shows a TE micrograph of the active region of a representative NW. In comparison to the parachute-like (In,Ga)N insertions commonly observed in NWs grown on Si (see example in inset), the QWs in our NWs on TiN do not show a semi-polar faceting, but extend along the c-plane and appear well-defined with a rectangular cross-section. These findings suggest that, indeed, a regular shape of the base NWs, as it is the case for the GaN on TiN, has a major influence on the structural perfection of the subsequent QW structures. Moreover, it is striking that the aspect ratio of the QWs decreases along the growth direction, i. e. the width of the QWs increases, while their thickness decreases. Interestingly, as revealed in the TE micrograph of Figure 4.2 (d), also the small parasitic NWs which grow directly on the substrate show defined QWs. Moreover, for a large portion of the long NWs, parasitic heterostructures grow directly attached to the NW bottom parts, as shown in the TEM image of Figure 4.2 (e).

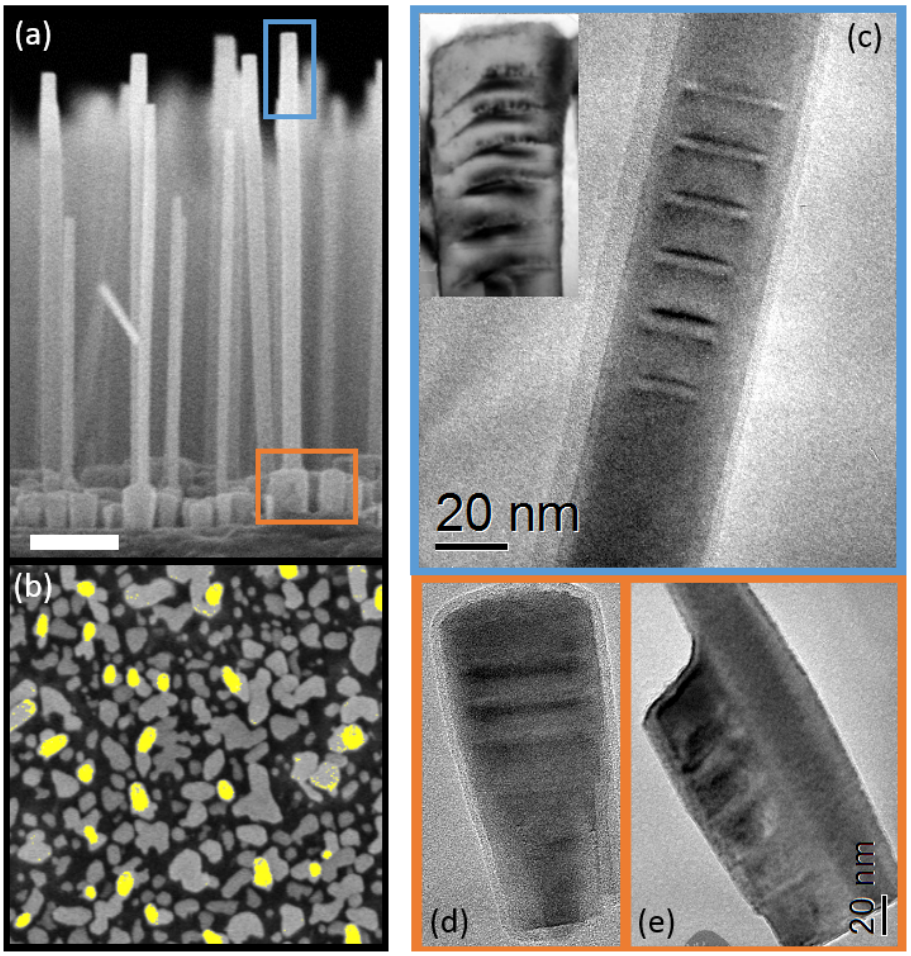


**Figure 4.2**: Cross-sectional (a) and plan view (b) SE micrographs of sample 4.A. In the plan view image, the long NWs are colored in yellow. The scale bar corresponds to 250 nm. In addition, the Figure shows TE micrographs of (c) a heterostructure grown on top of a long NW, (d) a parasitic NW grown on the substrate in between the long NWs, and (e) a parasitic heterostructure that grew on the side of the bottom part of a long NW. All three TEM images were obtained from sample 4.A and have been acquired by J. Bartolomé. The inset of Figure (c) shows a bright field TE micrograph of a common 6-fold QW heterostructure on a GaN NW grown on Si (measured by C. N. Huang).

In general, the majority of the investigated (In,Ga)N/GaN heterostructures on top of the long GaN NWs is free of extended defects. However, some NWs showed single stacking faults that extended through the middle of the lowest, first-grown QWs in the stack. In contrast to the heterostructures on top of the long GaN NWs, the parasitic NWs/heterostructures usually show an irregular faceting as well as a high number of extended defects (evaluated from further HR-TEM images which are not shown here) and rather resemble the heterostructures commonly seen for NWs on Si [see inset to Figure 4.2 (c)].

The well-defined shape of the active region allowed a detailed study of the strain dis-

tribution within the heterostructure carried out by my colleagues J. Bartolomé, M. Hanke, and A. Trampert.[153] They found that this phenomenon of the decreasing aspect ratio of the (In,Ga)N QWs towards the NW top can be explained by vertical strain interaction between the QBs and the QWs.[153] Once the first QW is grown on the GaN NW, the strain introduced by the lattice mismatch of (In,Ga)N and GaN is relaxed towards the free surfaces by an elastical lattice deformation of both the QW and the NW. The larger the aspect ratio of the QW, the more efficient is this reduction of the strain energy. However, with increasing aspect ratio, also the surface energy increases, which results in an equilibrium size of the QW where the total energy of the system is minimized. Once the first QB is grown on top, the strain field introduced by the QW below alters the lattice parameters along the whole width of the QB. This is true as long as the thickness of the QB is smaller than its width (Saint-Venant's principle), which is the case here. Due to the tensely strained top surface, the lattice mismatch of the QB and subsequent second QW is reduced. This way, the average strain of the QBs in the stack increases with increasing number of QWs, which in the end is responsible for the increase of the QWs' aspect ratio.

The regular and well-defined nature of the (In,Ga)N/GaN heterostructures presented in this section seems to be the result of the unique morphology of the base NWs on TiN. In order to evaluate whether this superior morphology translates into a high structural quality, in the following section, we investigate the optical properties of the active region.

## 4.3. Optical properties

Figure 4.3 (a) shows the ensemble PL of sample 4.A at 300 K. Apart from the GaN luminescence around 357 nm, there are two further distinct luminescence bands at about 400 nm and in the range 500 – 550 nm. Since it is an ensemble measurement, the origin of these luminescence bands is not clear. In order to allocate the emission bands, CL line scans along single dispersed NWs were performed at 10 K. The inset of Figure 4.3 (a) depicts the spectral CL map of a representative long NW that also reveals two emission centers - one around 410 nm and a second one at about 425 nm. Figures 4.3 (b) and (c) show SE micrographs of this very same NW as well as of a cluster of coalesced parasitic NWs, respectively. The micrographs are superimposed by monochromoatic CL images which were recorded for different wavelengths at 10 K.

The spectral CL line scan as well as the monochromatic CL/SEM images of the long NW reveal that the luminescence at about 410 nm can be attributed to a parasitically grown heterostructure at the foot of the NW (see Figure 4.2 (e)). Surprisingly, the luminescence of this parasitic structure is much brighter than the luminescence around 425 nm which originates from the structurally well-defined (In,Ga)N QWs at the NW top. The analysis of the monochromatic CL/SEM images of Figures 4.3 (b) and (c) for the different wavelengths (i) – (v) shows that the major emission bands of the ensemble PL can mainly be attributed to the luminescence of parasitic heterostructures grown at the NW bottom

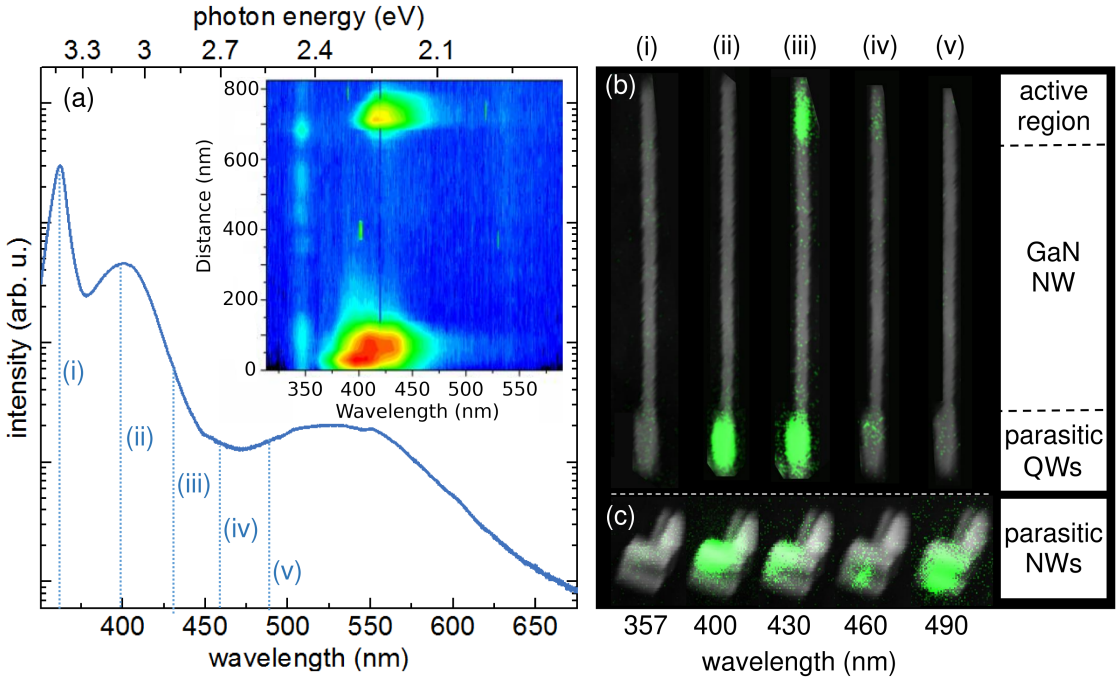


**Figure 4.3**: (a) PL spectrum of the NW ensemble of sample 4.A measured at 300 K. The inset depicts the spectral CL map of a representative long NW, acquired at 10 K. Figures (b) and (c) show SE micrographs of this very same NW as well as of a cluster of coalesced parasitic NWs, respectively. The micrographs are superimposed by monochromoatic CL images which were recorded for different wavelengths (i) – (v) at 10 K. The different wavelengths (i) – (v) are also indicated in the PL spectrum (a). CL data acquired by C. Pfüller.

parts as well as to the small parasitic NWs. Both types of parasitic structures seem to contribute to the luminescence band at 400 nm, whereas the broad, low-intensity band in the range 500 – 550 nm originates mainly from the small parasitic NWs (confirmed by further spectral CL measurements, which are not shown here).

The rather poor luminescence of the heterostructures on top of the long NWs, which is usually found in the range 420 – 440 nm (evaluated by numerous CL line scans), barely contributes to the PL.

At this point, it is still unclear whether the luminescence of the parasitic structures really stems from (In,Ga)N QWs or rather originates from structural defects. An investigation of axial (In,Ga)N/GaN heterostructures on NWs grown on Si by Lähnemann *et al.* [154] suggests that the luminescence in the spectral range around 410 nm may be related to zinc-blende segments acting as quantum wells in the wurzite GaN of the QBs. Also the rather low intensity of the PL around 500 – 550 nm might be attributed to luminescence of point defects. [154] The question is now whether the poor luminescence at the top of the long NWs as well may be related to defect luminescence somewhere in the heterostructure and/or whether it originates from the structurally well-defined (In,Ga)N QWs.

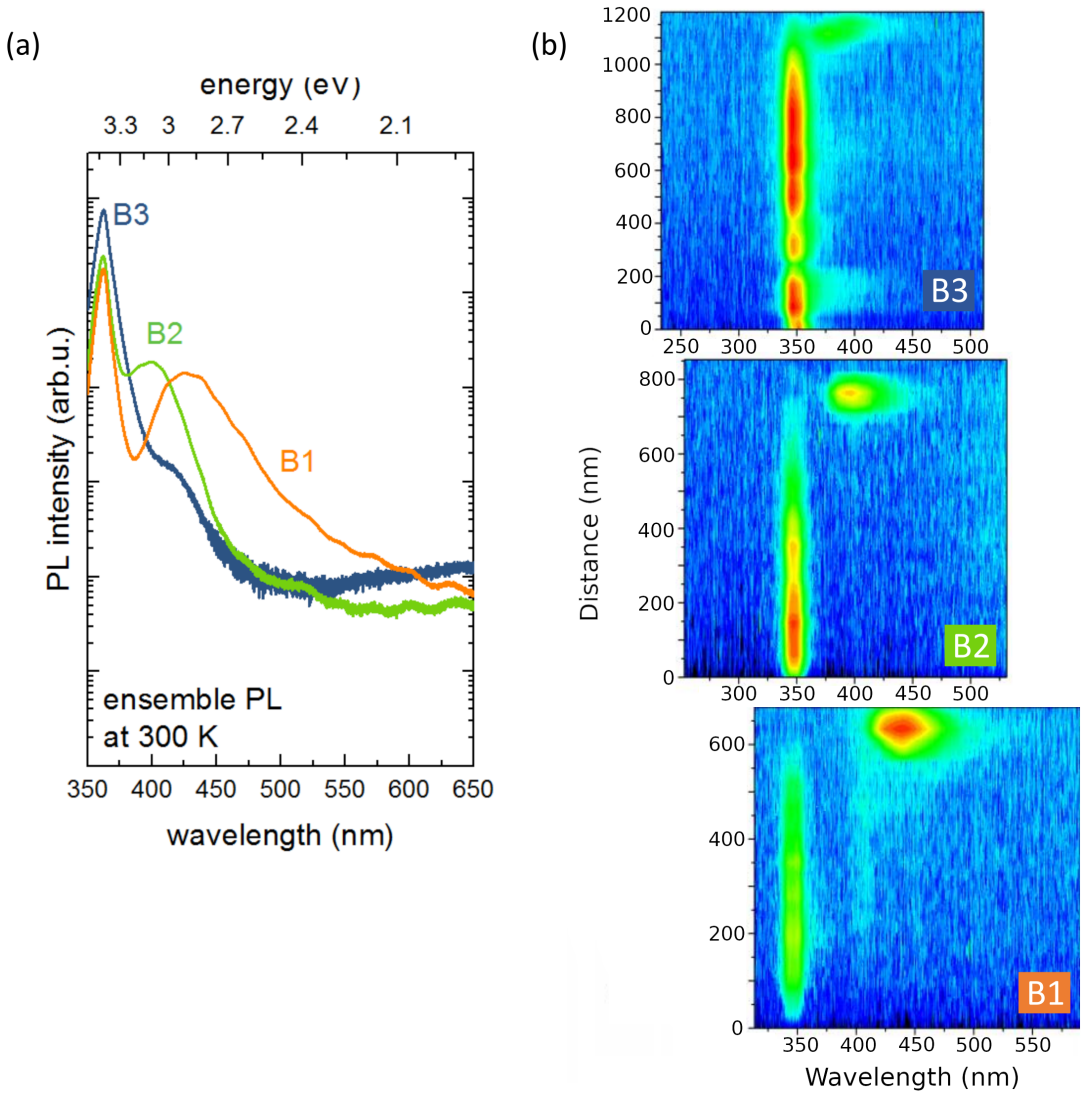


**Figure 4.4**: (a) PL spectra of the NW ensembles of samples 4.B1, 4.B2, and 4.B3 measured at 300 K. (b) Spectral CL maps (measured at 10 K,) of a representative long NW of samples 4.B1, 4.B2, and 4.B3 as indicated by the legend. CL data acquired by C. Pfüller.

To clarify this point, we analyze the PL and CL of the samples 4.B1, 4.B2[†], and 4.B3 which were grown at a substrate temperature of 505 °C, 540 °C, and 570 °C, respectively, at otherwise similar growth conditions. Figure 4.4 (a) shows the room temperature ensemble PL of the three samples. Besides the GaN luminescence around 357 nm, the samples 4.B1, 4.B2, and 4.B3 show only one further emission band at 410, 400, and 425 nm, respectively. The broad, low-intensity band in the range 500 – 550 nm, which was attributed to defect luminescence is not visible for in the PL spectra of the three samples. Only the

[†]Sample 4.B2 has been grown with the same conditions as sample 4.A, except for the QW thickness, which was adjusted from 3.4 to 3.1 nm. This allowed to compare 4.B2 to the samples 4.B1 and 4.B3.

spectrum of sample 4.B3 shows a slight onset of an emission band at higher wavelength. Analyzing monochromatic CL/SEM images of the NW ensemble (not shown here), we found that also for these samples, the luminescence of the active regions on top of the long NWs is rather poor in comparison to the one related to the parasitic structures, which renders the contribution of the former to the overall PL negligible. If the long-wavelength PL band of the different samples originated from the luminescence of well-defined (In,Ga)N QWs, one would have expected a systematic blue-shift of the luminescence with increasing substrate temperature from about 505 °C for sample 4.B1 to around 570 °C for sample 4.B3. However, this is obviously not the case and it is likely that the defective nature of the parasitic structures dominates the PL characteristic.

In order to assess the luminescence properties of the active region on top of the long NWs, we analyzed spectral CL maps of representative NWs of the three different samples as shown in Figure 4.3 (b). In contrast to the luminescence characteristic of the parasitic structures, the emission band originating from the top part of the long NWs red-shifts consistently with decreasing substrate temperature. This behavior suggests a systematic increase of the In content in the QWs[47] and hence is a strong indication that the luminescence at the top of the NWs actually stems from the (In,Ga)N QWs. However, as already mentioned, despite the regular and well-defined morphology of the (In,Ga)N/GaN heterostructures, the intensity of the QW luminescence in the upper part of the NWs is quite poor and was found to be much smaller than the one observed for a comparable structure grown on Si (evaluated in a side-by-side PL analysis which is not shown here).

About the reason for the poor luminescence can only be speculated at this point of the study, since a deeper investigation of this phenomenon is outside the scope of this thesis. In a study on (In,Ga)N/GaN heterostructures on GaN NWs on Si with a similar structure as shown in the inset of Figure 4.2 (c), Feix *et al.*[155] found that the recombination dynamics of these NW heterostructures are characterized by both strong carrier localization and a highly efficient nonradiative decay channel leading to an internal quantum efficiency far below 1%. Also in the case of N-polar c-plane QWs of planar (In,Ga)N/GaN heterostructures grown by MBE, Fernández-Garrido *et al.*[156] found that the luminescence quenches. They attributed this to the incorporation of a high density of point defects at the interfaces between QWs and QBs which act as efficient nonradiative recombination channels. This phenomenon is known to appear also for heterostructures based on other III-V materials, where point defects segregate on the growth front and are incorporated at the heterointerfaces due to the sudden change in the electrochemical potential.[156–158] The fact that the structures on TiN are not completely dark but show some luminescence might be due to the strong carrier localization which eventually prevents charge carriers from recombining at nonradiative centers.[155,156] It should be mentioned that also the presence of stacking faults in the center of the lower QWs in the stack observed for a few NWs, might have an effect on the luminescence intensity of the respective QWs.

## 4.4. Summary and Conclusions

In this chapter, we demonstrated that the uncoalesced, long, and thin GaN template NWs grown on TiN, as presented in chapter 3, facilitate the growth of well-defined axial (In,Ga)N/GaN heterostructures which extend along the c-plane and show a rectangular cross-section. However, the luminescence properties of these heterostructures are very poor. In the face of the very promising well-defined morphology of the active region, this result was rather unexpected. We found that even the parasitic NWs which grew in between the long GaN NWs as well as the parasitic heterostructures at their bottom parts are brighter than the QWs of the actual active region on top of the long NWs. A similar quenching of the luminescence has been observed for planar N-polar (In,Ga)N/GaN heterostructures and was attributed to nonradiative recombination channels resulting from a MBE-related high incorporation of point defects at the interfaces between QWs and QBs.[156] Since we were aware of these limitations, we deliberately chose to grow the heterostructures at higher temperatures than usual. .

The low luminous efficiency of the presented active regions despite their well-defined morphology, as well as the insight from the studies by Fernández-Garrido *et al.*[156] and Feix *et al.*[155] raises the question, whether axial N-polar (In,Ga)N/GaN heterostructures grown by MBE are generally suitable for optical applications. Investigating the nature of the point defects behind the efficient nonradiative decay channels, for planar Ga-polar structures, Young *et al.*[158] identified Ca impurities as a likely candidate. The Ca impurities originate from the substrate and are very difficult to remove during substrate cleaning. By burying the Ca in a superlattice, they were able to increase the output power of a planar (In,Ga)N/GaN LED structure by an order of magnitude. Despite the promising approach, suppressing the incorporation of point defects in NW heterostructures using superlattices is not a practical solution. The sacrificial (In,Ga)N/GaN layer has to be either grown on the substrate, which would make a nucleation of GaN template NWs on top impossible, or has to be included in the NW structure itself, which strongly affects the properties of the final NW structure and prevents an accurate control of the subsequent active region.

Another aspect that lowers the appeal of axial (In,Ga)N/GaN NW heterostructures for optical applications, besides the fundamental problem of the low luminous efficiency, is the fact that the active region area of NW ensembles with axial heterostructures is much smaller than for planar structures. Hence, it seems to be more attractive to grow heterostructures on the non-polar NW side facets. This way, the problem of the high point defect densities at the N-polar interfaces would be avoided and the active region area would be tremendously increased by using the full area of the NW side walls. To explore these potential advantages, in the following chapters, we will focus on the growth of (In,Ga)N/GaN core-shell structures.

# 5. Shell growth of III-nitride materials on GaN nanowires

Devices based on 3D nano- and microstructures with radial (lateral) core-shell designs for the active region have been demonstrated with different functionalities for numerous applications.[159–161] One major advantage of core-shell NWs over planar structures is that the active region area can be drastically increased by simply increasing their aspect ratio. This makes core-shell structures particularly interesting for applications like solar cells or LEDs, where large active regions are beneficial.[14,15] Especially regarding the rising demand for compact high-resolution multi-color displays, LEDs based on nano- and microstructures will certainly play a significant role for the next generation of display technologies.[5,8]

Regarding µ-rod-based (In,Ga)N/GaN core-shell LEDs, the fabrication processes have successively been optimized over the last years.[22,162,163] Although the growth of blue core-shell µ-rod LEDs by MOCVD is well established[162,163] and emission up to the red spectral range has already been demonstrated for axial (In,Ga)N/GaN MQWs grown by MBE[146,164–170] , the growth of (In,Ga)N-based core-shell structures with high In contents emitting in the green to red color spectrum remains very challenging. In general, fundamental aspects like the different nature of In and Ga regarding atom size and bond strength to N, as well as the high vapor pressure of N over InN, inhibit high In contents in (In,Ga)N/GaN heterostructures.[171–174] In particular for MOCVD growth, the incorporation of high In contents in (In,Ga)N/GaN core-shell structures seems far from being straightforward due to the usually lower In incorporation efficiency on the *m*-plane sidewalls in comparison to the *c*-plane.[20–22]

Only recently Kapoor *et al.*[22] demonstrated the growth of an (In,Ga)N/GaN µ-rod core-shell LED grown by MOCVD emitting in the deep green at 550 nm. Although MBE is often said to have high potential to achieve shells of high In content on µ-rods or NWs, so far there are no reports that demonstrate MBE-grown shells emitting in the green, not to mention the red spectral range. There is only one group, Albert *et al.*, that investigated (In,Ga)N shell growth by MBE and demonstrated shell emission in the violet spectral range.[87,175]

In this chapter, we aim for a fundamental understanding of shell growth of nitride-based materials by MBE. To this end, we made use of the self-assembled long, thin and well separated GaN NWs on TiN we developed in chapter 3 as template/core NWs. As

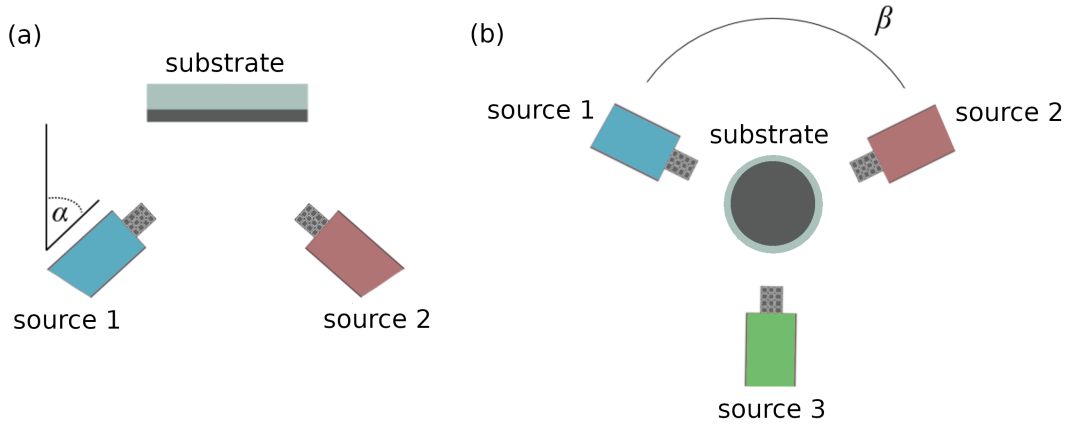


**Figure 5.1**: (a) Cross sectional and (b) plan view sketch of the source arrangement in an MBE system indicating the polar angle $\alpha$ the azimuthal angle $\beta$.

a first step, by investigating GaN shells around GaN core NWs in section 5.1, we use a rather simple structure and material system to understand the principles of adatom kinetics on the NW during shell growth. In this context, the decisive role of the geometry of the MBE system for the formation of homogeneous shells is discussed. Using these fundamental insights as a basis, in section 5.2, we study in more detail the growth of (In,Ga)N shells. Here, we demonstrate the growth of radially symmetric shells emitting in the blue/green spectral range and analyze the influence of the growth conditions on the NW morphology and the emission properties.

Parts of this chapter, in particular of section 5.1, have been published in D. van Treeck *et al.*, Phys. Rev. Mater., 4, 013404 (2020).[176]

## 5.1. Principals of shell growth by MBE

The molecular beams characteristic for MBE deposit material in direct line of sight from the source. Due to this directional nature, for 3D structures like NWs, the chamber geometry plays, in contrast to conventional planar growth, a major role in the deposition process. Firstly, the position of the material sources in the chamber determines the polar angle $\alpha$ between the respective directions of the material beams and the substrate normal as shown in the sketch of Figure 5.1 (a). As a consequence, the effective material fluxes on the NW top facet and the side facets may differ considerably. Secondly, due to the circular arrangement of the material sources in the chamber, where each material source has a certain azimuthal angle $\beta$ as depicted in Figure 5.1 (b), the side facets are only exposed sequentially to the different material fluxes during substrate rotation. Both geometrical aspects have a significant influence on the shell growth by MBE.[79]

Among the enormous literature devoted to axial and radial growth of NWs by MBE,

numerous studies mentioned the role of the source positions explicitly.[71,72,78–91] It has been found that for the usual angles of $\alpha = 30$–$40^\circ$, gradients in the chemical potential lead to an increased adatom diffusion along the NW sidewalls towards the NW top facet or droplet. For arsenide and nitride material systems, it has been shown that in addition to the NW dimensions and the V/III ratio, the polar angle $\alpha$ of the material sources has a significant influence on the final NW morphology.[80,82,84]

The aspect that the side facets are only sequentially exposed to the different material beams has been widely ignored so far. Usually, only the fact that the flux impinging on the side facets can be lowered by self-shadowing has been considered by introducing a geometrical factor. As notable exceptions, H. Küpers[37] investigated the role of flux directionality for the optical quality of As-based core-shell structrures and Foxon et al. [79] pointed out that the growth on the sidewalls of for GaN NWs may rather resemble migration enhanced epitaxy (MEE) than a classical MBE growth process. Hence, phenomena like Ga diffusion on the sidewall towards the NW top or substrate even before the side facet is exposed to the N beam might significantly affect the local growth rate and influence the thickness homogeneity of the shell. Therefore, a more detailed understanding of the diffusion and growth processes on the NW side facets under changing conditions during rotation is needed for the controlled growth of homogeneous and complex core-shell structures.

Here in section 5.1, we investigate for GaN NWs, both experimentally and theoretically, the influence of the different azimuthal angles of the Ga and the N source on the Ga adatom kinetics on the NW and the resulting shell morphology. We experimentally study the shell growth of GaN as a function of the V/III ratio and the temperature, where we analyze in detail the shell morphology with and without substrate rotation. On the basis of these experimental results, we develop a diffusion model which takes into account the different side and top facets of the NW as well as the substrate. The model allows to describe well the shell profile and conveys a deeper understanding of the adatom kinetics on the NW. Investigating the adatom concentration and diffusion on the NW side facet during substrate rotation, we analyze in particular the influence of the circular arrangement of the material sources on the thickness homogeneity of the NW shell. Moreover, we discuss how the shell morphology can be controlled by optimizing the rotation speed and V/III ratio.

### 5.1.1. GaN shells around GaN nanowires on TiN

In the following, we investigate nine different core-shell NW ensembles named 5.A, 5.B1 – 5.B3, 5.C1 – 5.C3, 5.D and 5.E grown by plasma-assisted MBE. The GaN core NWs, also referred to as template NWs, were grown at a V/III ratio of 2.5 and a substrate temperature of about 780 °C by means of self-assembly processes on a 3.4 µm thick Ti film sputtered on a $Al_2O_3$ (0001) substrate. The Ti film was nitridized prior to the nucleation of the first NWs while ramping to the growth temperature and a thin TiN layer formed.

The template NWs have a mean diameter and length of about 35 nm and 790 nm, respectively, with a NW density of about $10^9$ cm$^{-2}$. Due to the rather low NW density almost all NWs are uncoalesced and mutual shadowing from the impinging fluxes is drastically reduced. More information on the template NW ensemble can be found in chapter 3 and in the literature.[19,125,126,132] The above mentioned growth conditions for the template NW ensembles were used for all core-shell samples 5.A – 5.E.

The shell growth was performed directly after the growth of the template NWs and investigated as a function of the V/III ratio and the substrate temperature keeping the growth time constant at 35 min. The different samples were grown at four different substrate temperatures, namely 580 °C for sample 5.A, 600 °C for samples 5.B1 – 5.B3 and 5.E, 620 °C for samples 5.C1 – 5.C3, and 640 °C for sample 5.D. The V/III ratio was changed from 0.98 to 1.4 by modifying the Ga flux $\Phi_{Ga}$ while keeping the N flux $\Phi_N$ constant at $9.2 \pm 0.5$ nm/min. The desorbing Ga flux during the experiments was monitored *in situ* by LS-QMS.[177] In our MBE system the Ga and N cell have a polar angle $\alpha$ between the impinging beams and the substrate normal of 37.5° and are separated by an azimuthal angle $\beta$ of 144°. During the growth, samples 5.A – 5.D were continuously rotated in the direction in which the side facets are first exposed to the Ga beam and then, after a rotation of 144° to the N beam. The rotation speed was 7 rounds per minute (rpm). Sample 5.E was grown without substrate rotation.

In order to image the morphology of the core-shell NWs presented in this study, micrographs were recorded in a field-emission scanning electron microscope using an acceleration voltage of 5 kV. The length and diameter distributions, as well as the number density of the NW ensembles were determined by analyzing cross-sectional and top-view SE micrographs with the help of the open-source software ImageJ.[30]

The model to describe the shell growth on the NW side facets as well as the growth on the NW top facet and the substrate is based on a system of coupled one-dimensional (1D) diffusion equations which is solved by a numerical finite difference method (FDM) using the NumPy package[178,179] for scientific computing with Python. More information on the technical details of the model can be found in appendix A.

As a first step towards a comprehensive understanding of shell growth by MBE, in Figure 5.2 we investigate the radial growth of GaN around GaN template NWs as a function of the V/III ratio and the substrate temperature. The inset in the upper left corner of the growth map shows a cross section and a plan view SE micrograph of the template NW ensemble. For purposes of direct comparison, the inset on the right-hand side of sample 5.A shows an SE micrograph of a single average template NW, and the green rectangle next to the inset illustrates the extension of a template NW underneath a GaN shell. The SE micrograph of sample 5.A depicts that a substrate temperature of 600 °C and nominally metal-rich growth conditions with a V/III ratio of 0.98 result in a homogeneous shell along the whole NW length, however, also lead to the formation of wide, trapezoid-shaped top segments. The same is true for sample 5.B1 which was grown at 600 °C at

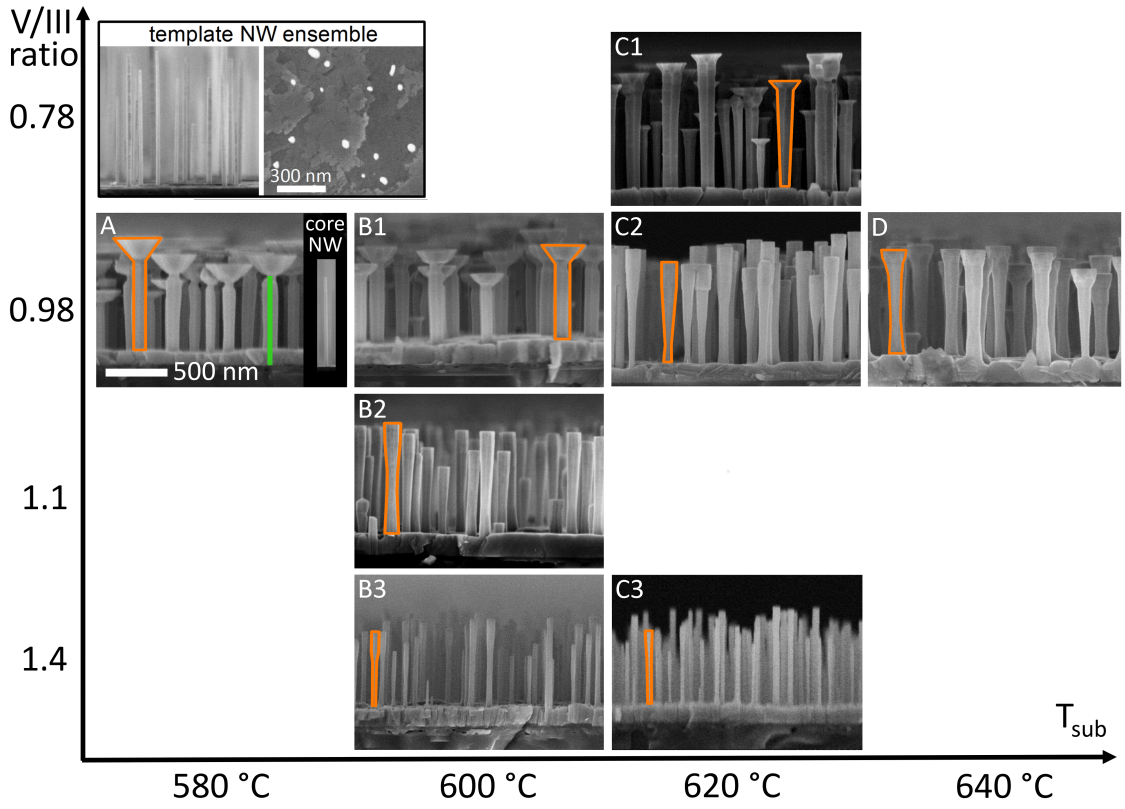


**Figure 5.2**: SE micrographs showing the radial growth of GaN around GaN template NWs as a function of the V/III ratio and the substrate temperature. The orange outlines sketch the characteristic shapes of the respective NWs. The inset in the upper left corner shows a cross section and a plan view SE micrograph of the template NW ensemble, which was grown under conditions outside the range of this diagram. The inset in the SE micrograph of sample 5.A depicts a template NW and the green rectangle next to the inset illustrates the extension of a template NW underneath a GaN shell. SE micrographs partially acquired by A.–K. Bluhm.

otherwise similar conditions and has a very similar morphology in comparison to sample 5.A. It should be noted that at 580 °C and 600 °C there was no Ga adatom desorption detected in the QMS.

Increasing the V/III ratio to 1.1, hence, to slightly N-rich growth conditions, NWs with straight top segments are obtained as shown for sample 5.B2. However, the radial growth along the NW side facets is not homogeneous anymore. Increasing radial growth towards the NW top and the NW bottom leads to a pronounced hourglass shape of the NWs. Also for much higher V/III ratios as for sample 5.B3 this characteristic shape of the shell is maintained, whereas due to the reduced Ga flux less material is grown. An increase in growth temperature from 600 °C to 620 °C leads to a distinct desorption of Ga adatoms which was detected by QMS. Comparing the samples 5.B1 and 5.C2, the reduced amount of Ga adatoms on the sample leads to a significant change in morphology. The wide top segments visible for sample 5.B1 are not present anymore for the conditions of sample

5.C2. The morphology of sample 5.C2 rather resembles the one of sample 5.B2, however, with less radial growth towards the NW bottom. An increase in V/III ratio from sample 5.C2 to 5.C3 by reducing the Ga flux causes a strong decrease in the shell thickness. Lowering the V/III ratio to 0.78, hence, to nominally very Ga-rich growth conditions as for sample 5.C1, leads to the formation of predominantly tapered NWs with an increasing shell thickness from bottom to top and with enlarged top segments. An increase in temperature up to 640 °C from sample 5.C2 to 5.D results in NWs with an hourglass shape of the shell similar to the ones of samples 5.B2 and 5.C2. The more pronounced top segments in comparison to sample 5.B2 and 5.C2 are likely the result of an increased adatom diffusion towards the NW top at higher temperatures.[72,180]

Furthermore, we note that growth does not only take place on the side and top facets of the template NWs. All samples exhibit a parasitic GaN layer that has grown on the TiN substrate at the foot of the NWs as a result of the low substrate temperature. Such a parasitic GaN layer does not form at elevated substrate temperatures as in the case of the template NW ensemble (see inset).[19,125,126,132]

In general, it was not possible to obtain a homogeneous shell along the whole length of the template NWs at low temperatures while avoiding the formation of wide top segments. A widening at the NW top is well known to occur for metal-rich growth conditions and has been attributed to preferential nucleation at the edge between side and top facet due to the high adatom concentration, with the formation of stacking faults and cubic insertions possibly being another relevant factor for lateral growth.[72,180–182] The homogeneous shell obtained for Ga-rich growth conditions is most likely the result of a continuous wetting of the side facets during the growth; i. e. the Ga on the side facets is never fully consumed when the facets are exposed to the N beam and growth takes place. However, despite the homogeneous shell, the NW morphology obtained for metal-rich growth with its wide top segments is not suitable for a further device processing of the NW ensemble. Moreover, the side facets are shadowed more and more from the impinging beams by the top segments which renders the growth of more complex shell structures impossible. Hence, the best result in terms of shell homogeneity was obtained for sample 5.B2 grown at 600 °C under nominally N-rich growth conditions, where no trapezoid-shaped top segments are formed.

In order to better understand the mechanisms leading to the formation of an hourglass shape of the GaN shell for various growth conditions, in Figures 5.3(a) – (f) we compare sample 5.B2 grown with continuous substrate rotation to sample 5.E grown without substrate rotation at otherwise similar growth conditions. The goal of analyzing core-shell structures grown without substrate rotation is to learn more about the adatom diffusion processes on the different NW facets. Since in our MBE system, the Ga and the N beam are, with an azimuthal angle $\beta$ of 144°, opposed to each other as shown in the sketch in Figure 5.3 (g), shell growth without substrate rotation can only take place if there is diffusion of adatoms.

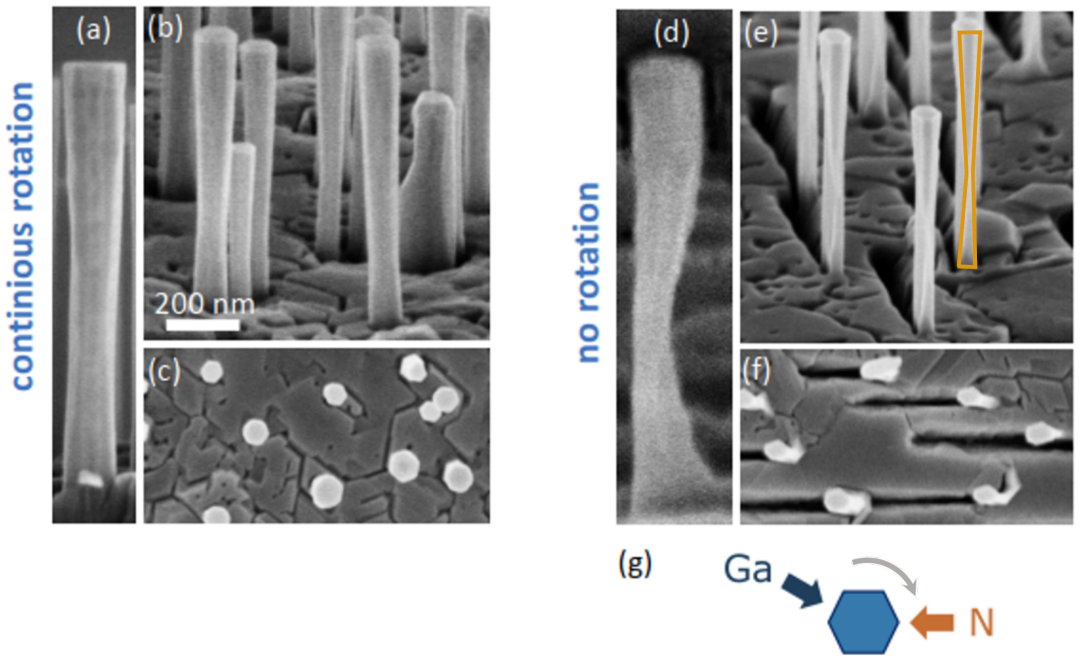


**Figure 5.3**: The SE micrographs show (a) – (c) sample 5.B2 grown *with* continuous substrate rotation and (d) – (f) sample 5.E grown *without* substrate rotation. The cross section micrographs (a) and (d) depict typical single NWs from these ensembles where the scale bars correspond to 100 nm. The bird's eye (b/e) and plan view (c/f) micrographs give a representative overview of both samples. The orange outline in (e) sketches the double half cone shape of the shell of sample 5.E. Note that the perspective of micrograph (e) is rotated with respect to (d) and (f) to give a better impression of the shell morphology in the radial direction. The direction of the impinging N is revealed by the grooves in the parasitic GaN layer seen in (e) and (f). The micrographs (b), (c), (e) and (f) are to scale and (b) and (e) were measured at a tilt angle of 20° and 25° with respect to the substrate, respectively. The plan view sketch (g) shows the source geometry of our MBE system, where the Ga and the N beam are separated by an azimuthal angle $\beta$ of 144°. The grey arrow depicts the rotation direction of sample 5.B2. SE micrographs partially acquired by A.–K. Bluhm.

The NW depicted in Figure 5.3 (a) shows the characteristic tapering found for the optimum sample 5.B2 with bottom, center, and top diameters of 121 nm, 109 nm, and 146 nm, respectively, and a length of 920 nm. Figures 5.3 (b) and (c) are representative SE micrographs of the NW ensemble. The NWs are almost completely uncoalesced and have a hexagonal faceting as it can be seen in the plan view image (c). For some NWs, mutual shadowing of adjacent NWs cannot be excluded, however, we found that also isolated NWs which where not shadowed by any other NWs in their surrounding showed a similar hourglass morphology. Hence, mutual shadowing of the NWs cannot be the decisive mechanism responsible for this characteristic shell shape.

Analyzing the NW morphology of sample 5.E in Figure 5.3 (d), one can directly see that the growth of an hourglass-shaped shell also appears for the non-rotated sample,

however, only on the N exposed side (right-hand side in the image). The NW length is about 780 nm and the diameters along the NW from bottom to center to top are 145 nm, 62 nm, and 119 nm, respectively. Hence, with the template NWs having a mean diameter of about 35 nm, there is only very little radial growth in the NW center. This phenomenon can also be seen in Figure 5.3 (e), where the shell seems to have a kind of double half cone shape with less radially grown material towards the NW center. Furthermore, the shadowing of the N beam by the NWs leads to deep grooves in the parasitic GaN layer clearly visible in the plan view micrograph shown in Figure 5.3 (f). It should be noted that most NWs which have an hourglass-shaped shell are not affected by shadowing by a neighboring NW, which otherwise would be indicated by a groove crossing the NW foot.

In general, the fact that shell growth only takes place at the N exposed side of the NW implies that N diffusion on the NW facets is negligible, in agreement with literature.[72,74,75] The absence of N adatom diffusion also explains the groove formation in the parasitic GaN layer. Moreover, that radial growth is much less pronounced in the NW center, indicates that Ga adatom diffusion around the NWs from *m*-plane to *m*-plane is strongly suppressed for these growth conditions. Hence, the Ga adatoms contributing to the growth on the N exposed side have to diffuse there either from the top facet or the substrate, which eventually results in the observed hourglass shape of the shell. The findings for sample 5.E suggest that also for the rotated sample 5.B2, where the NWs show a less pronounced but similar hourglass shape, the inhomogeneity of the shell is mainly caused by Ga adatom diffusion processes and at most to a small extent by directly impinging Ga. In other words, the fact that the anion and cation beams impinge on different NW sides plays a major role for the final shell morphology.

In order to elucidate in more depth how the arrangement of the material sources in an MBE system influences adatom diffusion and thus the final NW shape, we developed a 1D diffusion model for the Ga adatom concentration on the NW. The model takes into account five different regions as sketched in Figure 5.4 (a). In general, we assume that the diffusion of N is negligible as indicated by the analysis of sample 5.E in Figure 5.3. Hence, in the model we only consider the diffusion of Ga adatoms. Moreover, we assume that in the presence of Ga on a given facet, each N adatom impinging on the facet contributes to the growth. For metal-rich growth conditions, the growth rate is thus limited by the impinging N flux. It should be noted that in agreement with our experimental findings above, inter-diffusion of Ga adatoms between the different side facets (region II and IV in the model) is neglected. In the following we will introduce the model for the two different scenarios, *with* and *without* substrate rotation, and apply it to the shape occurring for samples 5.B and 5.E, respectively. Since experimentally we did not observe any significant Ga desorption for the samples 5.B and 5.E, Ga adatom desorption is not considered in the model.

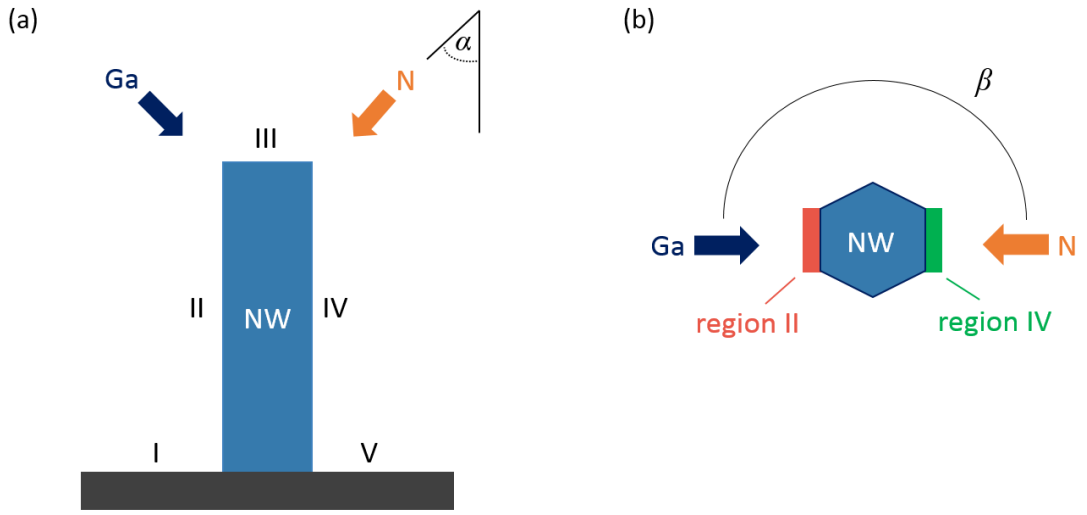


**Figure 5.4**: (a) The cross section sketch of a NW depicts the five different regions distinguished in our model: (I) the substrate, (II) the NW facet which is directly exposed to the Ga flux, (III) the NW top facet, (IV) the NW facet which is directly exposed to the N flux, and (V) again the substrate. The polar angle $\alpha$ is the angle between the flux direction of the material sources and the substrate normal. (b) The top view sketch of the NW shows the azimuthal arrangement of the side facet regions II and IV as well as of the Ga and the N source which are separated by an azimuthal angle $\beta$. Figure published in Ref. 176.

### 5.1.2. Modeling shell growth without substrate rotation

In the case *without* substrate rotation, the regions in Figure 5.4 (a) can be attributed to (I) the substrate, (II) the NW facet which is directly exposed to the Ga flux, (III) the NW top facet, (IV) the NW facet which is directly exposed to the N flux, and (V) again the substrate. The angle $\alpha$ is the angle between the impinging beams and the substrate normal and is the same for both sources. The plain-view sketch of Figure 5.4 (b) illustrates the two different side facet regions II and IV. The Ga and N source and hence region II and IV are separated by an azimuthal angle $\beta$ which depends on the chamber geometry of the MBE system. The Ga adatom concentrations $n$ of the different regions (I)–(V) are described by the following 1D diffusion equations:

$$\text{(I)}\quad \frac{\partial n_{\mathrm{I}}(x_{\mathrm{I}},t)}{\partial t} = -D_{\mathrm{sub}}\frac{\partial^2 n_{\mathrm{I}}(x_{\mathrm{I}},t)}{\partial x_{\mathrm{I}}^2} + \frac{n_{\mathrm{I}}(x_{\mathrm{I}},t)}{\tau_{\mathrm{sub}}} + \chi_{\parallel} J_{\mathrm{Ga}}$$

$$\text{(II)}\quad \frac{\partial n_{\mathrm{II}}(x_{\mathrm{II}},t)}{\partial t} = D_{\mathrm{side}}\frac{\partial^2 n_{\mathrm{II}}(x_{\mathrm{II}},t)}{\partial x_{\mathrm{II}}^2} + \chi_{\perp} J_{\mathrm{Ga}}$$

$$\text{(III)}\quad \frac{\partial n_{\mathrm{III}}(x_{\mathrm{III}},t)}{\partial t} = D_{\mathrm{top}}\frac{\partial^2 n_{\mathrm{III}}(x_{\mathrm{III}},t)}{\partial x_{\mathrm{III}}^2} + \frac{n_{\mathrm{III}}(x_{\mathrm{III}},t)}{\tau_{\mathrm{top}}} + \chi_{\parallel} J_{\mathrm{Ga}}$$

$$\text{(IV)}\quad \frac{\partial n_{\mathrm{IV}}(x_{\mathrm{IV}},t)}{\partial t} = D_{\mathrm{side}}\frac{\partial^2 n_{\mathrm{IV}}(x_{\mathrm{IV}},t)}{\partial x_{\mathrm{IV}}^2} + \frac{n_{\mathrm{IV}}(x_{\mathrm{IV}},t)}{\tau_{\mathrm{side}}}$$

$$\text{(V)}\quad \frac{\partial n_{\mathrm{V}}(x_{\mathrm{V}},t)}{\partial t} = D_{\mathrm{sub}}\frac{\partial^2 n_{\mathrm{V}}(x_{\mathrm{V}},t)}{\partial x_{\mathrm{V}}^2} + \frac{n_{\mathrm{V}}(x_{\mathrm{V}},t)}{\tau_{\mathrm{sub}}} + \chi_{\parallel} J_{\mathrm{Ga}}$$

where $D_{\mathrm{sub}}$, $D_{\mathrm{side}}$, and $D_{\mathrm{top}}$ are the diffusion coefficients and $\tau_{\mathrm{sub}}$, $\tau_{\mathrm{side}}$, and $\tau_{\mathrm{top}}$ are the lifetimes of Ga adatoms on the substrate, the side facet, and the top facet of the NW, respectively. In our model these six parameters describing the diffusion terms $D\,\partial^2 n/\partial x^2$ and the incorporation terms $n/\tau$ are considered as fitting parameters. We would like to point out that, in general, the diffusion coefficients $D$ may be affected by the Ga/N ratio. In our model, we assume that all diffusion coefficients are constant within one region and in time. Hence, the parameter values of the diffusion coefficients are mean values in time and space for the respective region.

The different contributions of the impinging Ga flux for facets oriented parallel and perpendicular to the substrate are described by the flux terms $\chi_{\parallel} J_{\mathrm{Ga}}$ and $\chi_{\perp} J_{\mathrm{Ga}}$, respectively, where $\chi_{\parallel} = \cos\alpha$ and $\chi_{\perp} = \sin\alpha$. Since in this section, we assume that the Ga and N species do not impinge on a given sidewall facet at the same time, the equations (I) – (V) are only valid for azimuthal angles in the range $120^\circ < \beta < 240^\circ$. A more general model will be introduced in section 5.1.3. Moreover, it should be noted that for region I, we did not consider the shadowing from the N beam by the NW, since the characteristics of this region are mainly governed by the non-shadowed area. We will discuss this in more detail below. The spatial ranges for the different regions are defined as

$$\begin{aligned} x_{\mathrm{I,V}} &\in [0,\infty] \\ x_{\mathrm{II,IV}} &\in [0, l_{\mathrm{eff}}(t)] \\ x_{\mathrm{III}} &\in [0, d(t)] \end{aligned} \tag{5.1}$$

with the effective NW length $l_{\mathrm{eff}}(t) = l(t) - h_{\mathrm{para}}(t)$ between parasitic layer and NW top facet, where $l(t)$ is the total length of the NW starting from the substrate and $h_{\mathrm{para}}(t)$ is the height of the parasitic layer. The parameter $d(t)$ is the top facet diameter starting at the diameter of the template NW. Regarding the boundary conditions, the adatom concentration $n$ as well as the diffusion fluxes are chosen to be continuous at the boundaries between the different regions j (with j ∈ I, ..., V ) for all times $t$:

$$\begin{aligned} & n_{\mathrm{I}}(\infty,t) = n_{\infty}, \\ & n_{\mathrm{I}}(0,t) = n_{\mathrm{II}}(0,t), && \frac{\partial n_{\mathrm{I}}}{\partial x_{\mathrm{I}}}\Big|_{x_{\mathrm{I}}=0} = -\frac{\partial n_{\mathrm{II}}}{\partial x_{\mathrm{II}}}\Big|_{x_{\mathrm{II}}=0}, \\ & n_{\mathrm{II}}(l_{\mathrm{eff}}(t),t) = n_{\mathrm{III}}(0,t), && \frac{\partial n_{\mathrm{II}}}{\partial x_{\mathrm{II}}}\Big|_{x_{\mathrm{II}}=l_{\mathrm{eff}}(t)} = \frac{\partial n_{\mathrm{III}}}{\partial x_{\mathrm{III}}}\Big|_{x_{\mathrm{III}}=0}, \\ & n_{\mathrm{III}}(d(t),t) = n_{\mathrm{IV}}(l_{\mathrm{eff}}(t),t), && \frac{\partial n_{\mathrm{III}}}{\partial x_{\mathrm{III}}}\Big|_{x_{\mathrm{III}}=d(t)} = -\frac{\partial n_{\mathrm{IV}}}{\partial x_{\mathrm{IV}}}\Big|_{x_{\mathrm{IV}}=l_{\mathrm{eff}}(t)}, \\ & n_{\mathrm{IV}}(0,t) = n_{\mathrm{V}}(0,t), && \frac{\partial n_{\mathrm{IV}}}{\partial x_{\mathrm{IV}}}\Big|_{x_{\mathrm{IV}}=0} = -\frac{\partial n_{\mathrm{V}}}{\partial x_{\mathrm{V}}}\Big|_{x_{\mathrm{V}}=0}, \\ & n_{\mathrm{V}}(\infty,t) = n_{\infty}, \end{aligned} \tag{5.2}$$

hence, we assume equality of the chemical potentials at the boundaries and the conservation of the number of adatoms in the whole system. For region I and V, $n$ goes to an equilibrium value of $n_\infty$ far away from the NW. For the initial conditions, the adatom concentration $n_\mathrm{j}$ is chosen to be zero for all $x_\mathrm{j}$ in all regions j:

$$n_j(x_\mathrm{j}, 0) = 0 \tag{5.3}$$

Since the Ga adatom concentration on the NW during the growth is experimentally not accessible, one has to model the final shell morphology, i. e. the grown material, in order to learn more about the adatom concentration and kinetics. The thickness of the grown material $GM_\mathrm{j}$ at a certain point $x_\mathrm{j}$ of the different regions $j$ is described by integrating the growth rate $GR_\mathrm{j} = n_\mathrm{j}(x_\mathrm{j}, t)/\tau_\mathrm{j}$ (incorporated material per time) over the total growth time $t_\mathrm{g}$:

$$GM_\mathrm{j}(x_\mathrm{j}) = \int_0^{t_g} \frac{n_\mathrm{j}(x_\mathrm{j}, t)}{\tau_\mathrm{j}}\, dt \quad \text{for j} \in \text{I, .., V} \tag{5.4}$$

According to our assumptions, the growth rate $GR_\mathrm{j}$ in each region can only be as high as the impinging N flux, which can be expressed as $n_\mathrm{j}(x_\mathrm{j}, t)/\tau_\mathrm{j} \leq \chi_\mathrm{j} J_N$. Hence, only one Ga adatom per impinging N atom is incorporated, excess adatoms are free to further diffuse.

The modeling of the grown material for the shell, the top segment and the parasitic layer on the substrate can be achieved according to Eq. (5.4) by adjusting the fitting parameters $D$ and $\tau$ in the different regions. It should be noted that in order to get a good description of the shell growth, we took into account that the growth of the top facet and the parasitic layer affects the section of the side facet where growth can take place; i. e. once the parasitic layer increases, the lower part of the NW side wall is covered and once the top segment grows longer the side facet is enlarged.

The shell profile which develops on the side facet is mainly described by the adatom diffusion length on the side facet $\lambda_\mathrm{side} = \sqrt{D_\mathrm{side}\tau_\mathrm{side}}$, where $D_\mathrm{side}$ mainly determines the symmetry of the shell along the NW and $\tau_\mathrm{side}$ regulates the shell thickness. The boundary areas at the very top and bottom part of the side facet, are also strongly influenced by the parameters $D_\mathrm{top}/D_\mathrm{sub}$ and $\tau_\mathrm{top}/\tau_\mathrm{sub}$, which mainly characterize the Ga adatom diffusion onto the side facet. Playing with these parameters allows to lower or increase the adatom concentration at the boundaries to region IV and thus the thickness of the shell at the bottom and the top of the side facet. However, the variation of $D$ and $\tau$ in the regions III and IV is restricted, since also the modeling of the experimentally observed thickness of the top segment and the parasitic layer is taken into account and is essential for a reasonable description of the shell growth. As a reference for the modeling of the thickness of the parasitic layer, we used 227.5 nm which corresponds to the value obtained for Ga limited growth with $\chi_\parallel \Phi_\mathrm{Ga} = 6.5$ nm/min and $t_\mathrm{g} = 35$ min far away from NWs, i. e. excluding shadowing effects of adjacent NWs. Since a decrease of the layer thickness towards

the NW was usually not observed in SE micrographs, we assumed the thickness to be close to 227.5 nm for distances larger than 100 nm from the NW. Due to the smooth shape of the NWs, it was not possible to identify the onset for the top segment growth from SE micrographs which rendered an estimation of the top segment thickness impossible. Therefore, for the modeling we assumed the mean height of the top segments to be between 227.5 (value explained above) and 255.5 nm, where the latter thickness is obtained for N-limited growth at the top facet, hence, the maximum possible thickness.

Due to the fact that all regions are interconnected and depend on each other in a particular way, the whole system, i. e. a certain configuration of shell, top segment, and parasitic layer thickness, can only be described by a unique set of the fitting parameters. Hence, a good modeling of the experimentally observed thicknesses can be achieved only within a small parameter window. Regarding the sensitivity of the fits with respect to a change of the different fitting parameters, we found that varying the parameters $\tau_{\mathrm{top}}$, $\tau_{\mathrm{side}}$, $\tau_{\mathrm{sub}}$ and $D_{\mathrm{side}}$ by about ±10% around the optimum value, results in a deviation of the modeled shell profile of about ±5%. The dependence of the fits on the parameters $D_{\mathrm{top}}$ and $D_{\mathrm{sub}}$ is comparatively less sensitive. For these parameters, a variation of about ±85% results in a deviation of ±5% of the modeled shell profile. More details on the behavior and sensitivity of the fits as well as on the general fitting procedure can be found in appendix B. We would like to emphasize that with this model, our main objective is to develop a qualitative understanding of the complex diffusion processes on the NW rather than extracting precise values for the parameters $D$ and $\tau$ in the different regions. Once a good description of the shell thickness, the top segment and the parasitic layer is achieved, the model allows to analyze the adatom concentration in the different regions for all times $t \in [0, t_{\mathrm{g}}]$.

Figure 5.5 shows the modeled grown material as well as the adatom concentrations at $t = t_{\mathrm{g}}$ of the different regions II, III, IV and V of a representative NW of sample 5.E. The respective fitting parameters are given in Table 5.1. The angle $\alpha$ was chosen according to our MBE system (see experimental section) and the angle $\beta = 144^{\circ}$ is within the range in which the equations (I) – (V) are valid. Analyzing the adatom concentration of region II, one finds that up to about one monolayer (ML) of Ga accumulates on the Ga exposed side facet of region II ($m$-plane: 1 ML = $1.21 \times 10^{15}$ at/cm$^2$) and that the adatom concentration decreases towards the substrate (region I) and towards the NW top facet (region III). Since region II is only exposed to Ga there is no growth on this side facet.

The adatom concentration on the top facet has a value of around 0.3 ML close to region II ($c$-plane: 1 ML = $1.14 \times 10^{15}$ at/cm$^2$) and decreases to about 0.1 ML at the boundary to region IV. A similar behavior is observed for the thickness of the top segment from one to the other boundary. Close to the Ga exposed side facet (region II), the segment reaches the maximum thickness of 255.5 nm. In contrast, close to the N exposed side facet (region IV), the thickness is 213 nm. It should be noted that a difference in thickness of the top segment from one to the other side was not observed experimentally by analyzing SE

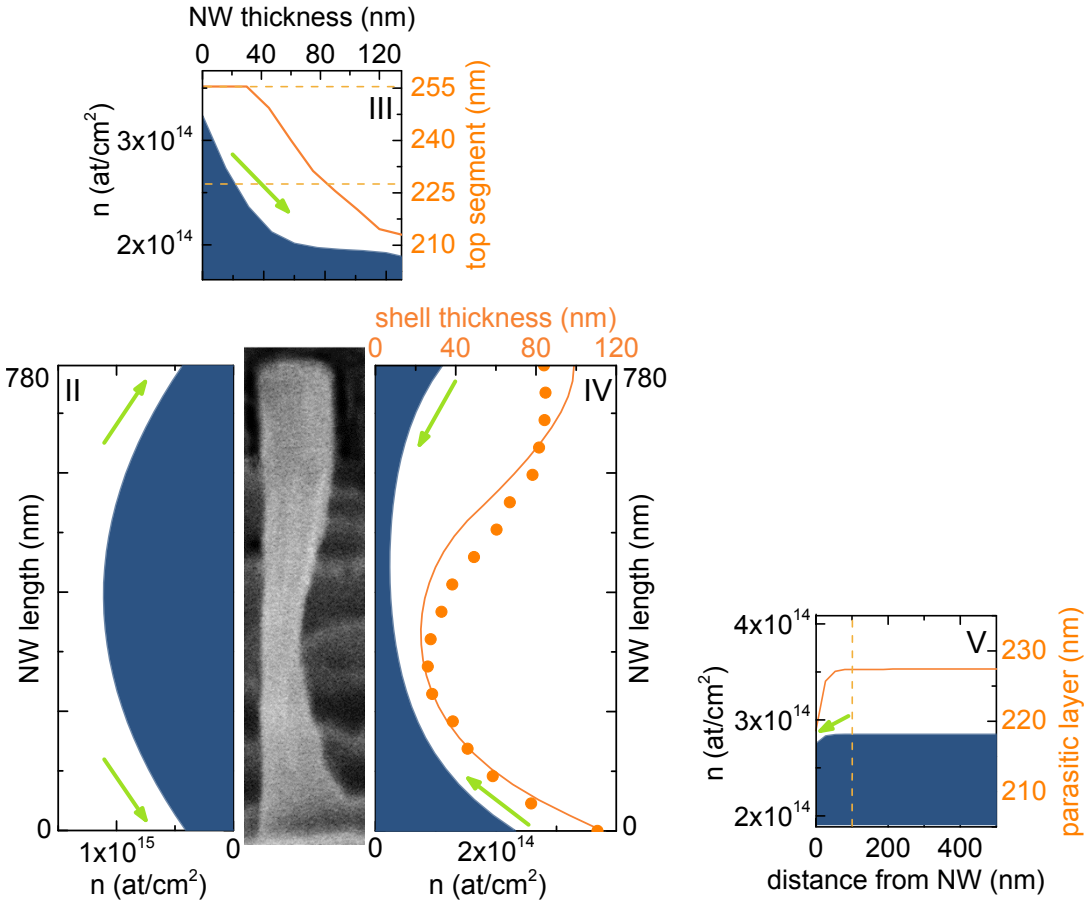


**Figure 5.5**: The different graphs show the modeled Ga adatom concentration $n$ (blue) and the thickness of the grown material $GM$ (orange) according to Eq. (5.4) on the side facet (region IV), the top facet (region III), and the substrate (region V) for a representative NW of sample 5.E for $t = t_g$. The micrograph in the center depicts the modeled NW. The dashed lines in the graph of region III at 255.5 and 227.5 nm mark the thickness obtained for N-limited and Ga-limited growth, respectively. The dotted data in the graph of region IV is the experimentally determined shell thickness of sample 5.E. The dashed line in the graph of region V at 100 nm marks the distance to the NW above which we assume a constant thickness of the parasitic layer. The green arrows indicate the mean diffusion direction of Ga adatoms. Figure published in Ref. 176.

micrographs of single NWs of sample 5.E. The average thickness of the top segment is 236 nm. Regarding the N exposed side facet (region IV), the adatom concentration has its maximum values at the boundaries to the top region III and the substrate region V with values of about 0.1 ML and around 0.2 ML, respectively. In the NW center, the adatom concentration is much lower than at the edges. The modeling of the shell thickness of region IV shows that the experimentally observed tapered shell profile (dots) along the NW of the non-rotated sample 5.E can be well described by our model (line). The Ga adatom concentration on the substrate far away from the NW is with about 0.25 ML between the two extreme values of the top facet. The grown layer thickness is around

| sample | region | $D$ (cm$^2$/s) | $\tau$ (s) | $\lambda$ (nm) |
|---|---|---|---|---|
| E | top (III) | $2.5\times10^{-12}$ | 0.25 | 8 |
| | side (II+IV) | $4.5\times10^{-10}$ | 0.45 | 142 |
| | sub (I+V) | $3.5\times10^{-12}$ | 0.6 | 14 |

**Table 5.1**: Fitting parameters for sample 5.E.

227.5 nm which coincides well with the experimentally found layer thickness in non-shadowed areas and only drops visibly for distances smaller than about 50 nm.

In general, the belly shape of the adatom concentration in region II can be explained by the diffusion of Ga adatoms towards the substrate and the top of the NW, as indicated by the green arrows. The driving force for these diffusion processes are the different chemical potentials in the regions I, II, and III resulting from different material incorporation rates (growth rates) and impinging fluxes. For instance, without any additional diffusion fluxes one would expect region III to have a similar adatom concentration as the substrate regions I and V far away from the NW, since for both regions growth takes place in *c*-plane direction and both are exposed to the same Ga and N fluxes. However, as a consequence of the continuous Ga supply in region II and the nominally N-rich growth conditions in region III resulting in a gradient in the chemical potential, Ga adatoms diffuse onto the top facet, which even leads to a Ga excess and hence N-limited growth near the boundary of the two regions. In contrast, the adatom concentration is decreased towards region IV which results from the low chemical potential on the N exposed side facet IV and leads to a segment thickness below 227.5 nm, the one expected for growth at the rate of the impinging Ga flux. Hence, on this side of the NW, the gradient in the chemical potential causes Ga adatoms to diffuse from the top facet and the substrate onto the side facet of region IV and towards the NW center. The resulting profile of the adatom concentration resembles the characteristic hourglass shape which according to Eq. (5.4) manifests itself in the final shell profile. It should be mentioned that the flattening shell profile towards the NW top results from the shift of $l_{\mathrm{eff}}(t)$ along the NW with increasing total NW length $l(t)$ and parasitic layer height $h(t)$. Moreover, the top facet diameter $d(t)$ changes from 35 nm (diameter of template NW) to about 120 nm (template NW + shell) leading to a decrease in the diffusion towards region IV with increasing growth time.

Regarding the fitting parameters shown in Table 5.1, we already mentioned that the intention of our model is not to extract precise values for $D$ and $\tau$ but to qualitatively understand the adatom kinetics for the shell growth. Nevertheless, we would like to address a few points. In a realistic scenario, it can be assumed that there are diffusion barriers at the boundaries between the different regions,[183] e. g. because the surfaces of the regions have different crystallographic orientations. Since in our model we did not explicitly consider any diffusion barriers at the boundaries of the regions, their impact on the diffusion from region to region might be included in our fitting parameters. In

general, diffusion barriers on the surface affect the diffusion coefficient which is defined by $D = D_0 \exp(-E_{\mathrm{diff}}/k_{\mathrm{B}}T)$ where $D_0$ is the temperature-independent pre-factor, $k_{\mathrm{B}}$ is the Boltzmann factor, and $E_{\mathrm{diff}}$ is the height of the potential barriers on the surface. Analyzing the fitting parameters of table 5.1, one finds that the values of $D_{\mathrm{top}}$ and $D_{\mathrm{sub}}$ of the *c*-plane regions which result in a good description of the shell profile are about two orders of magnitude lower than $D_{\mathrm{side}}$ of the *m*-plane region IV. Considering the fact that the Ga adatoms which contribute to the growth of the shell have to diffuse from the top facet and the substrate onto the side facet, processes which are determined by $D_{\mathrm{top}}$ and $D_{\mathrm{sub}}$, it is indeed likely that for these diffusion processes, the barrier effects at the boundaries are included in $D_{\mathrm{top}}$ and $D_{\mathrm{sub}}$ and not in the parameters $D_{\mathrm{side}}$ and $\tau_{\mathrm{side}}$ describing the diffusion on the side facet. Hence, the diffusion coefficients $D_{\mathrm{top}}$ and $D_{\mathrm{sub}}$ are likely dominated by the barrier heights at the boundaries and have to be seen as effective diffusion coefficients rather than realistic values for the respective regions. It should be noted that a difference of a few hundred meV in barrier height would be enough to explain the observed two orders of magnitude difference in $D$ between the side facet and the top facet/substrate. According to density-functional theory calculations of Lymperakis *et al.*,[75] it is rather unlikely that the differences between $D_{\mathrm{side}}$ and $D_{\mathrm{top/sub}}$ result from the different barrier heights directly on the *m*- or *c*-plane since the barrier heights on the *m*-plane are actually higher, which would result in a comparatively smaller diffusion coefficient $D_{\mathrm{side}}$. Moreover, if the barrier heights at the boundaries dominate the values of $D_{\mathrm{top}}$, we might underestimate the diffusion length of the Ga adatoms on the top facet in our model. A larger diffusion length would result in a less pronounced thickness difference of the top segment from one to the other side, which would explain why the SE micrographs of sample 5.E do not show recognizable change in thickness of the top segment. The only values for $D$ found in any literature are with $2\times10^{-15}\,\mathrm{cm}^2/\mathrm{s}$ at 740 °C on the *m*-planes [184] and about $1.1\times10^{-15}\,\mathrm{cm}^2/\mathrm{s}$ at 700 °C on the *c*-planes [74] several orders of magnitude lower than the values we obtained, but due to very different experimental conditions not directly comparable to our results.

Regarding the Ga adatom lifetimes $\tau$, the values for the different regions are all in the hundred ms range with variations of about a factor two. Similar values have been found analyzing planar GaN growth by metal organic vapor deposition using a kinetic growth model.[74] It should be mentioned that modeling the shell growth for much larger Ga adatom lifetimes (two orders of magnitude or more) leads to an accumulation of several tens of ML of Ga in the different regions, increasing with further growth time. Since such a scenario is not realistic, the values we obtained for $\tau$ seem to be reasonable.

Since $D$ and $\tau$ are hard to determine experimentally, it is generally more revealing to compare the corresponding diffusion length $\lambda$ obtained for the respective regions. For Ga adatom diffusion on the m-polar side facets of NWs, diffusion lengths of about 40 to 100 nm were reported to be reasonable for high temperature growth (around 800 °C).[71,75,77,82] The higher Ga adatom diffusion length of 144 nm we found for sample 5.E can be explained by the absence of Ga desorption, which is the limiting factor at high tempera-

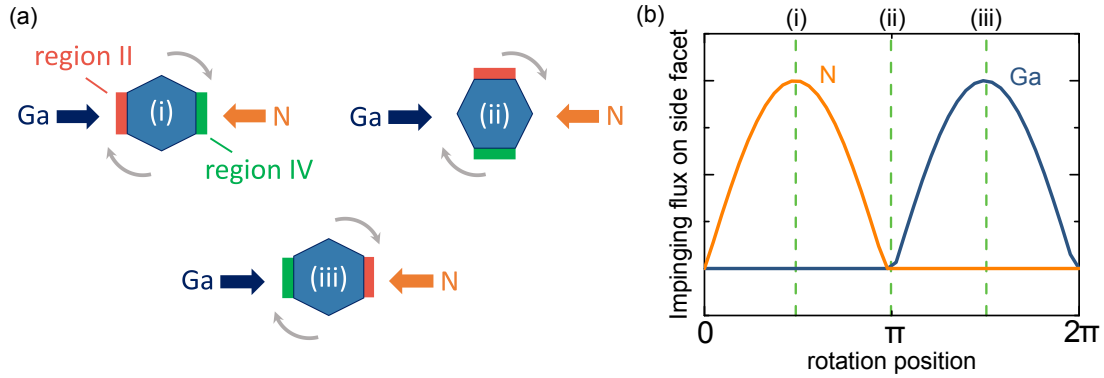


**Figure 5.6**: (a) The plan view sketches show the orientation of region II and IV with respect to the Ga and N source for three different rotation positions: (i) $\pi/2$, (ii) $\pi$, and (iii) $3\pi/2$ in the case of $\beta = 180°$. (b) The graph shows the Ga and N flux impinging on region IV depending on the rotation position. The dashed green lines indicate the different positions (i) – (iii) as sketched above. Figure published in Ref. 176.

tures.[82]

From modeling sample 5.E, we can conclude that in the extreme case without rotation, indeed, the different azimuthal angles of Ga and N causing adatom diffusion from the top and the substrate onto the N exposed region seem to be mainly responsible for the inhomogeneous shape of the shell. However, the question is now, whether these conclusions also hold for the scenario *with* substrate rotation which is necessary to obtain a radially homogeneous shell and, moreover, whether a homogeneous shell thickness along the NW can be achieved for a different arrangement of the material sources or different growth conditions.

### 5.1.3. Modeling shell growth with substrate rotation

In order to simulate substrate rotation in our model, region II and IV have to be rotated with respect to the Ga and N source. The sketches in Figure 5.6 (a) show three different rotation positions for the scenario where region II and IV are located on opposite sides ($\beta = 180°$). At position (i), region II and region IV are directly exposed to Ga and N, respectively. Once rotation is started, the regions move away from the direct beams of the sources. For instance, region IV first rotates out of the N beam until it is neither exposed to N nor to Ga (ii), then rotates into the Ga beam (iii) and subsequently back to the position where only N impinges on the facet. The flux sequence impinging on region IV during one rotation is shown Figure 5.6 (b). The dashed green lines indicate the different positions (i) – (iii) sketched in Figure 5.6 (a).

To implement the continuous rotation in our model, the diffusion equations of region II and IV as they were defined in section 5.1.2 have to be modified. Since in the rotation scenario, during one rotation both regions are exposed to Ga and N, the diffusion equations of region II and IV have to include both the incorporation term $n/\tau$ and the flux

term $\chi_\perp J_{\mathrm{Ga}}$, which are modulated according to the rotation position by time-dependent factors $p$ and $q$, respectively. The modified equations (II) and (IV) are given as

$$\begin{aligned}
\text{(II)}\quad \frac{\partial n_{\mathrm{II}}(x_{\mathrm{II}},t)}{\partial t} &= D_{\mathrm{side}}\frac{\partial^2 n_{\mathrm{II}}(x_{\mathrm{II}},t)}{\partial x_{\mathrm{II}}^2} \\
&\quad + p_{\mathrm{II}}(t)\frac{n_{\mathrm{II}}(x_{\mathrm{II}},t)}{\tau_{\mathrm{side}}} + q_{\mathrm{II}}(t)\chi_\perp J_{\mathrm{Ga}} \\
\text{(IV)}\quad \frac{\partial n_{\mathrm{IV}}(x_{\mathrm{IV}},t)}{\partial t} &= D_{\mathrm{side}}\frac{\partial^2 n_{\mathrm{IV}}(x_{\mathrm{IV}},t)}{\partial x_{\mathrm{IV}}^2} \\
&\quad + p_{\mathrm{IV}}(t)\frac{n_{\mathrm{IV}}(x_{\mathrm{IV}},t)}{\tau_{\mathrm{side}}} + q_{\mathrm{IV}}(t)\chi_\perp J_{\mathrm{Ga}}
\end{aligned}$$

with the time-dependent modulation factors for region II

$$\begin{aligned}
p_{\mathrm{II}}(t) &= \begin{cases} \sin(2\pi\nu t-\beta) & \text{for } \sin(2\pi\nu t-\beta)\geq 0 \\ 0 & \text{for } \sin(2\pi\nu t-\beta)<0 \end{cases} \\
q_{\mathrm{II}}(t) &= \begin{cases} \sin(2\pi\nu t) & \text{for } \sin(2\pi\nu t)\geq 0 \\ 0 & \text{for } \sin(2\pi\nu t)<0 \end{cases}
\end{aligned} \tag{5.5}$$

and region IV

$$\begin{aligned}
p_{\mathrm{IV}}(t) &= \begin{cases} \sin(2\pi\nu t) & \text{for } \sin(2\pi\nu t)\geq 0 \\ 0 & \text{for } \sin(2\pi\nu t)<0 \end{cases} \\
q_{\mathrm{IV}}(t) &= \begin{cases} \sin(2\pi\nu t+\beta) & \text{for } \sin(2\pi\nu t+\beta)\geq 0 \\ 0 & \text{for } \sin(2\pi\nu t+\beta)<0 \end{cases}
\end{aligned} \tag{5.6}$$

where $\nu$ is the rotation speed in rotations per minute. The diffusion equations of region I, II, and V are the same as defined in section 5.1.2. It should be noted that the modified model presented here in section 5.1.3 is valid for all azimuthal angles $\beta$ between the N and the Ga source.

Figure 5.7 shows the modeling of the grown material of a representative NW of the rotated sample 5.B2 on the side facets (region II and IV), the top facet (region III), and the substrate (region I and V) according to Eq. (5.4). The angles $\alpha$ and $\beta$ were chosen according to the geometry of our MBE system as explained in the experimental section. One can see that the shell thickness of sample 5.B2 (dots) can be very well described for fitting parameters similar to the ones obtained for the non-rotated case (see Table 5.2). In general, it should be noted that the two scenarios, with and without rotation, do not necessarily have to have the same diffusion parameters. For instance, in the static non-rotated case of sample 5.E, the Ga adatom concentration on the Ga exposed side facet is higher than for sample 5.B2, which results in a higher Ga adatom concentration on the top facet and hence affects the growth rate $n/\tau$.

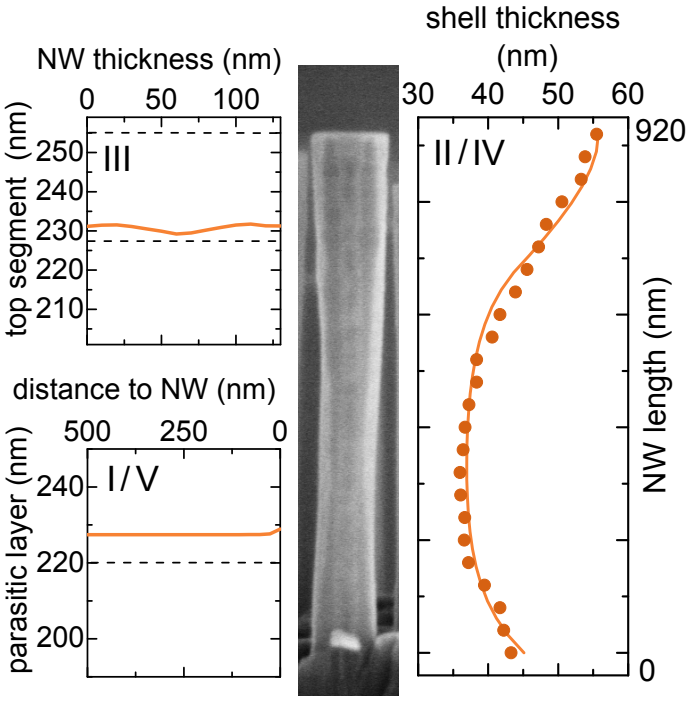


**Figure 5.7**: The different graphs show the modeled thickness (lines) of a representative NW of the rotated sample 5.B2 on the side facets (region II and IV), the top facet (region III), and the substrate (region I and V) according to Eq. (5.4). The micrograph in the center depicts the modeled NW. The dots in the diagram of region II/IV indicate the experimental data. The dashed lines in the graph of region III mark the range in which a set of modeling parameters is considered reasonable. The upper dashed line at 255.5 nm corresponds to the thickness obtained for N-limited growth, the bottom line at 227.5 nm corresponds to the value obtained for Ga-limited growth. The dashed line in the graph of region I/V with a value of 220 nm shows the average value found analyzing the thickness of the parasitic layer in areas with low NW density. Figure published in Ref. 176.

Besides the modeled shell profile for region II and IV, Figure 5.7 depicts the simulated thickness of the parasitic layer (region I/V) and the top segment (region III). Since in our model the shadowing of the surface is not taken into account, we use 227.5 nm as reference value for the layer thickness far away from the NW (see section 5.1.2). In the model we obtained a thickness of 227 nm for distances larger than about 50 nm from the NW for a set of parameters which resulted in the best description of the shell on the side facet. This value compares well with the experimentally found thickness of the parasitic layer of 220 nm (dashed line) in areas with low NW density. Analyzing the thickness of the top segment with an average value of about 231 nm, one finds that the segment becomes slightly thicker towards the edge of the NW. The higher growth rate in the lateral area of the top facet could be explained by the locally higher Ga adatom concentration induced by adatom diffusion from the Ga exposed side facet, similar to the non-rotated case shown in Figure 5.5.

In order to better understand the adatom kinetics for the rotation case, in Figure 5.8

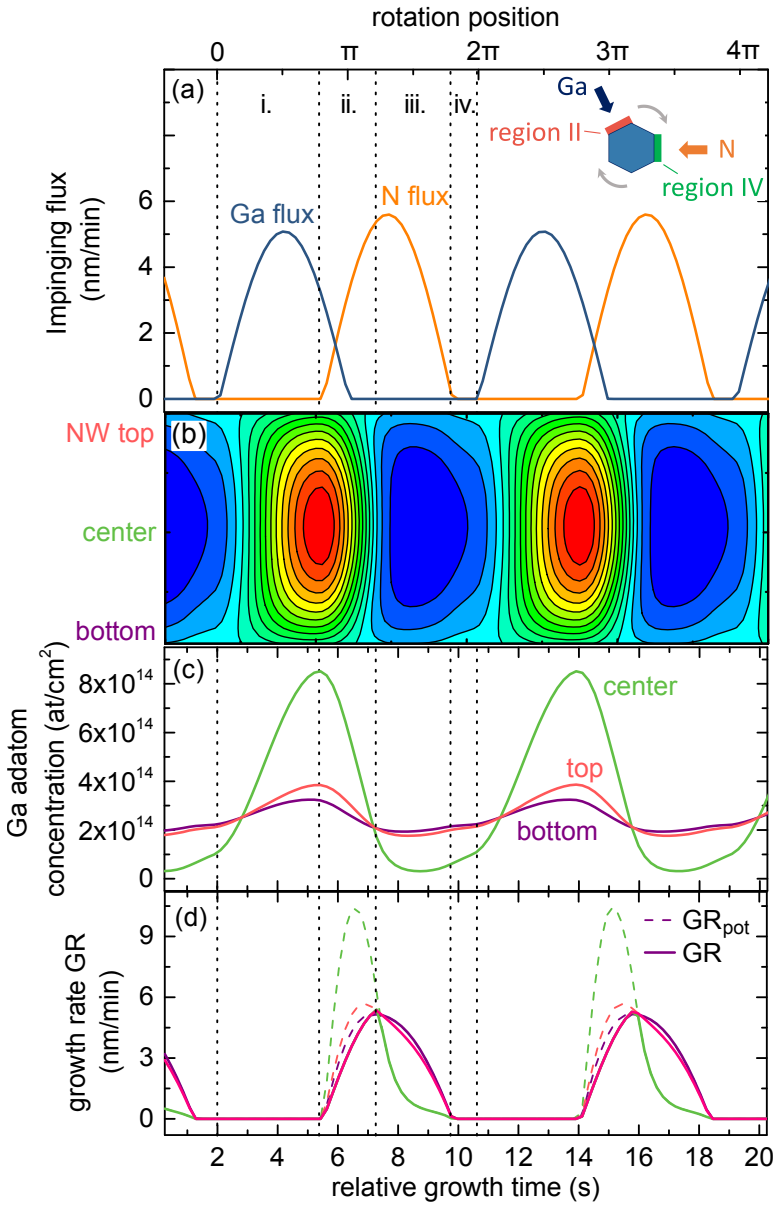


**Figure 5.8**: (a) Impinging Ga and N fluxes on the side facet region IV for different growth times/rotation positions and for the conditions of sample 5.B2. The inset depicts the arrangement of the material sources and the regions II and IV for $\beta = 144°$, corresponding to the geometry of our MBE system. (b) The contour plot depicts the modeled Ga adatom concentration of region IV of sample 5.B2 for different growth times/rotation positions along the whole NW length. The values for the maximum (red) and the minimum (blue) are $8{\times}10^{14}$ at/cm$^2$ (0.65 ML) and $3{\times}10^{13}$ at/cm$^2$ (0.025 ML), respectively, where the contour lines mark steps of $5.5{\times}10^{13}$ at/cm$^2$ (0.045 ML). (c) Detailed evolution of the Ga adatom concentration at the top (red), the center (green), and the bottom (violet) of the NW side facet. The data was extracted from the contour plot data of figure (b). (d) Actual growth rate $GR$ (line) and potential growth rate $GR_{\text{pot}}$ (dashes) at the top, the center and the bottom of the side facet region IV modeled for sample 5.B2. The five vertical dotted lines between 2 and 10.6 seconds in Figures (a)–(d) indicate the four different rotation phases i.–iv. as discussed in the main below. Figure published in Ref. 176.

| sample | region | $D$ (cm$^2$/s) | $\tau$ (s) | $\lambda$ (nm) |
|---|---|---|---|---|
| 5.B2 | top (III) | $3\times10^{-12}$ | 0.5 | 11 |
| | side (II+IV) | $4\times10^{-10}$ | 0.55 | 155 |
| | sub (I+V) | $3\times10^{-12}$ | 0.5 | 12 |

**Table 5.2**: Fitting parameters for sample 5.B2.

we analyze the adatom concentration on the side facets during rotation. It should be mentioned that in our model, the growth on region II and region IV is symmetric under rotation. For simplicity, we focus on region IV in the following discussion. Figure 5.8 (a) shows the Ga and N fluxes impinging on region IV with proceeding growth time, where the maximum values are 5 and 5.6 nm/min, respectively. The inset depicts the arrangement of the material sources and the regions II and IV for $\beta = 144^\circ$, corresponding to the geometry of our MBE system. The contour plot of Figure 5.8 (b) depicts the adatom concentration of region IV for different growth times/rotation positions along the whole NW length, where red is the maximum and blue is the minimum adatom concentration with $8\times10^{14}$ at/cm$^2$ (0.65 ML) and $3\times10^{13}$ at/cm$^2$ (0.025 ML), respectively. For a better understanding, Figure 5.8 (c) shows the precise evolution of the Ga adatom concentration plotted in Figure 5.8 (b) at three different positions on the NW: the top (red), the center (green) and the bottom (violet) of the NW. At the time when region IV is exposed to Ga only, the adatom concentration rises fast in the center and slower at the edges. Subsequently, once region IV rotates away from the Ga beam and into the N beam, the adatom concentration is reduced, fast in the center and slower at the edges, until it is almost homogeneous along the whole NW. From this point on the situation on the side facet changes. While decreasing, the adatom concentration is now higher at the top and the bottom edges of the NW and has its minimum in the center. The minimum is reached shortly after the impinging N flux reached its highest value. Subsequently, once region IV rotates into the Ga beam again, the adatom concentration rises and a new rotation cycle begins.

Figure 5.8 (d) shows the actual growth rate $GR$ (line) and the potential growth rate $GR_{\text{pot}}$ (dashes) at the top, the center and the bottom of the NW side facet region IV. The actual growth rate is defined as $GR = n(x,t)/\tau$ and reaches its maximum value once $n(x,t)/\tau = \chi J_N$, as introduced in section 5.1.2. The potential growth rate $GR_{\text{pot}}$ is not limited by the latter condition and it is assumed that all Ga adatoms can be incorporated, hence, $\chi J_N > n(x,t)/\tau$ for all times. Or in other words, $GR_{\text{pot}}$ being larger than $GR$ indicates metal-rich conditions on the facet. Figure 5.8 (d) depicts that once the Ga-wetted surface is exposed to N, both $GR$ as well as $GR_{\text{pot}}$ increase, where in the beginning $GR_{\text{pot}}$ is much larger in the center. At the top and the bottom there is not a big difference between the two growth rates. Once region IV passes the N peak flux and rotates away from the N source, $GR$ and $GR_{\text{pot}}$ are identical.

In general, during one rotation period, a side facet passes through four different phases. The first phase is the wetting phase from 2 to 5.3 s ($0-3/4\pi$), where Ga is deposited on a side facet which is still shadowed from the N beam. While the facet rotates away from the Ga source, Ga adatoms diffuse towards the NW top and the substrate due to gradients in the chemical potential. These diffusion processes cause the belly shape of the adatom concentration along the NW, similar to the situation on region II for the non-rotated case in section 5.1.2. The second phase is the metal-rich growth phase between 5.3 and 7.2 s ($3/4\pi-6/5\pi$). Once the facet rotates into the N beam, growth takes place, as shown in Figure 5.8 (d). However, in the beginning the growth rate is still low due to the large angle between the facet and the direct N beam and there are more Ga adatoms on the surface than N adatoms being provided by the impinging N flux. The consequence are Ga-rich growth conditions where the growth rate $GR$ is limited by the impinging N flux and is the same along the whole NW length. The Ga excess during that rotation phase is illustrated in Figure 5.8 (d) where $GR_{\mathrm{pot}}$ is higher than $GR$. The Ga adatoms which are not incorporated are free to diffuse away, which leads to a flattening of the belly shape.

Only with further rotation away from the Ga source and into the N beam, N-rich conditions are established on the side facet. This is the third phase, the N-rich growth phase from 7.2 to 9.8 s ($6/5\pi-9/5\pi$). The priorly deposited Ga is consumed and the chemical potential on the side facet is lowered, which leads to diffusion from the top facet and the substrate onto the side facet. In this phase where $\chi J_N > n(x,t)/\tau$, the growth rate is higher at the top and the bottom of the side facet resulting in the experimentally observed hourglass shape of the shell. The fourth and last phase is the dissociation phase between 9.8 and 10.6 s ($9/5\pi-2\pi$). With ongoing rotation, depending on the arrangement of the sources, there may be a rotation phase during which the side facet is neither exposed to Ga nor to N. In this phase, the probability for thermal dissociation of the grown material is the highest. However, in the case of GaN and for substrate temperatures far below 800 °C, the dissociation rate is negligibly small.

The analysis in Figure 5.8 shows that the Ga adatom kinetics on the different NW facets is very complex during a common growth with substrate rotation and that it has a major influence on the final NW morphology. Also for the case with substrate rotation, we conclude that the main driving force for the pronounced adatom diffusion are large differences in the chemical potential on the various facets originating from the different azimuthal angles of the material sources. The experimental results shown in Figure 5.2 and 5.3 as well as our conclusions from the modeling of sample 5.B2 and E reveal that it seems not to be straightforward to experimentally obtain homogeneous shell growth. However, since the model describes very well the experimentally observed shell profile as well as the growth on top facet and substrate, it allows to further explore different growth conditions which were experimentally not accessible due to technical restrictions. In Figure 5.9 we analyze the evolution of the shell shape for different azimuthal angles, V/III ratios and rotation speeds at otherwise similar parameters as obtained for the mod-

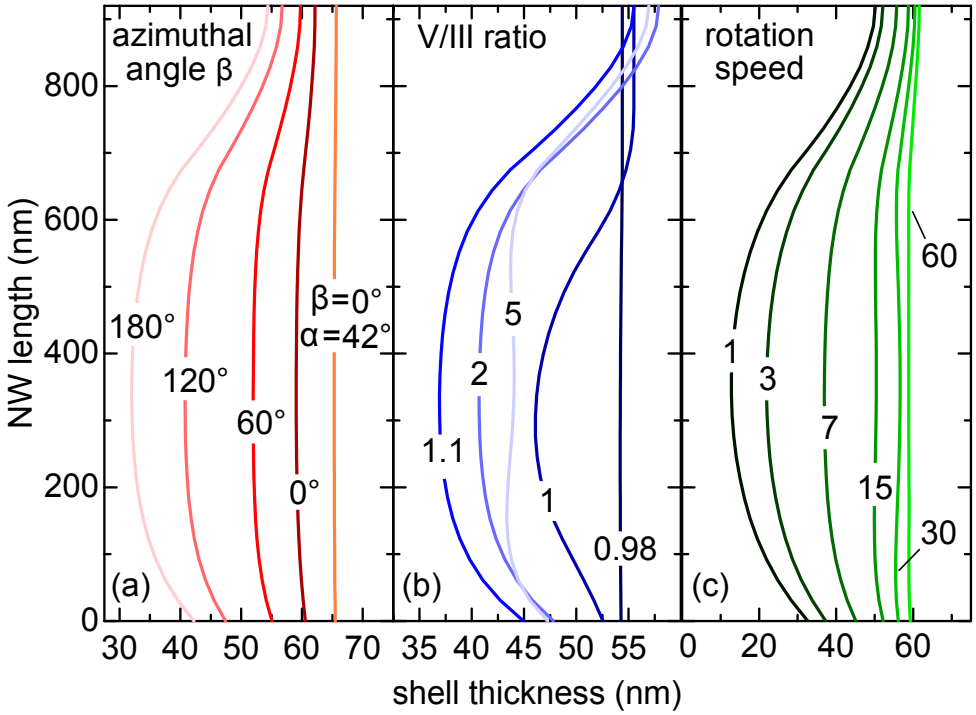


**Figure 5.9**: Modeled evolution of the shell thickness along the NW for (a) different angles $\beta$ between the Ga and N source, (b) different V/III ratios, and (c) different rotation speeds. If not indicated otherwise in the graph, the modeling is based on the growth and fitting parameters of sample 5.B2 as mentioned in the experimental section and table 5.2, respectively. The V/III ratio was varied by changing the N flux and maintaining a constant Ga flux of $\Phi_{Ga} = 8.2$ nm/min. Figure published in Ref. 176.

eling of sample 5.B2 (see table 5.2). Since the growth in region II and IV is identical, also for the analysis in Figure 5.9 we focus on region IV.

Figure 5.9 (a) shows the evolution of the shell morphology for different angles $\beta$ between the Ga and N source. For a large $\beta$ of 180 - 120° the shell depicts a distinct hourglass shape, similar to the morphology of sample 5.B2. For angles of 60° and smaller, the hourglass profile of the shell becomes less pronounced, however, the shell thickness still increases visibly towards the NW top and the bottom. The most homogeneous shell is obtained for a $\beta$ of 0°, where the Ga and N beam impinge from the same direction onto the side facet. For this source configuration, the differences in chemical potentials of the regions III, IV, and V are very small, leading to only little Ga adatom diffusion between the different facets. Hence, most of the material grows where it impinges. For the fitting parameters of sample 5.B2, a perfectly smooth shell with the same thickness along the whole NW length is only achieved for a $\beta$ of 0° and a polar angle $\alpha$ of 42° (instead of 37.5° like in our MBE system). In general, if the incorporation/growth rates $n/\tau$ were the same in all regions, an equilibrium of the chemical potentials would be achieved for an

angle $\alpha$ of 45°. For this angle, the impinging material fluxes impinging on the top facet, the substrate, and the respective side facets are identical. Since according to the fitting parameters obtained for sample 5.B2, the growth rate is slightly smaller on the side facet due to a higher adatom lifetime $\tau_{\text{side}}$, an equality of chemical potentials is achieved for $\alpha = 42°$.

Figure 5.9 (a) clarifies that, indeed, the shell morphology strongly depends on the azimuthal angles between the different sources and rather homogeneous shell morphologies can be achieved once the Ga and N sources are arranged next to each other. However, arranging the material sources close to each other is not necessarily realizable in standard MBE systems, where the different source ports are usually separated by an azimuthal angle of at least 30°. Especially, once numerous material sources are needed for the growth of more complex and/or doped shell structures, it might be challenging to optimize the source configuration. This drawback raises the question whether a more homogeneous shell morphology can also be achieved by simply optimizing e. g. the V/III ratio or the rotation speed instead of physically rearranging the material sources.

Figure 5.9 (b) depicts the shell profiles for V/III ratios from 0.98 to 5, hence, moving from nominally Ga-rich to N-rich conditions. For the modeling, the Ga flux is kept constant at $\Phi_{\text{Ga}} = 8.2$ nm/min. For V/III ratios of 1 and above, the NW exhibits a very pronounced hour glass shape. For the highest V/III ratio of 5, the shell shows in addition a belly in the NW center. For a ratio of 1, the top part of the shell is rather straight at a value of about 55 nm. For even lower V/III ratios, the hour glass shape diminishes until a homogeneous shell thickness of 54 nm along the whole NW is achieved for a V/III ratio of 0.98. The belly shape in the center of the shell for high V/III ratios can be explained by the fact that with increasing N flux, the metal-rich growth phase on the side facet becomes much shorter. Hence, the belly shape in the Ga adatom concentration that developed during the wetting phase is preserved until the early stage of the N-rich growth phase and manifests itself in the shell morphology. Only with further N-rich growth, the Ga atom concentration on the side facet is lowered and the Ga diffusion from the NW top and the substrate onto the side facet increases, resulting in an increased shell thickness towards the NW top and the bottom. For lower V/III ratios, the metal-rich growth phase is much longer and most of the initially deposited Ga has diffused away until N-rich conditions are reached and a pronounced hourglass shape develops as discussed for Figure 5.5.

The strong increase in the shell thickness between V/III ratios of 1.1 and 0.98 results from an increased diffusion of excess Ga onto the side facet once metal-rich growth conditions are reached on the top facet and/or the substrate. For a V/III ratio of 1, e. g. the top part of the shell is grown under N-limited conditions due to the diffusion of excess Ga from the Ga exposed facet towards the top facet and from the top facet onto the side facet where growth takes place. This increase in shell thickness was also experimentally observed comparing sample 5.A and B. Once the V/III ratio is lower than 1, metal-rich conditions are reached on all facets at any time of the rotation resulting in a very homoge-

neous shell. However, at V/III ratios < 1, wide, trapezoid-shaped top segments form, as seen for sample 5.A and reported before.[180] Hence, as already observed experimentally for the samples 5.A – 5.C in Figure 5.2, it does not seem possible to achieve a straight shell morphology without enlarged top segments by optimizing the V/III ratio.

The last important parameter we want to address is the rotation speed. Figure 5.9 (c) shows that with increasing rotation speed from 1 to 15 rpm the pronounced concave profile of the shell vanishes and the shell becomes more homogeneous along the NW, however, the shell thickness still increases significantly towards the NW top. For rotation speeds higher than 15 rpm the shell develops a slight belly in the NW center. Only for rotation speeds of 60 rpm and higher a shell with a rather homogeneous thickness along the whole NW length is achieved. In general, the shell thickness increases with increasing rotation speed. As discussed for Figure 5.8, the hourglass shape of the shell found for low rotation speeds can be explained by the fact that the majority of the Ga that contributes to the growth diffuses from the top and the bottom onto the side facet, while most of the directly deposited Ga has already diffused away. However, the faster the rotation, the less of the directly deposited Ga is able to diffuse away during the wetting and metal-rich phase. Hence, once N-rich conditions are reached, the adatom concentration on the side facet is still rather high and homogeneous along the NW leading to an increased and rather uniform shell thickness. Moreover, the more Ga remains on the side facet until N-rich conditions are established, the lower is the gradient in chemical potential between side facet and the other facets, which results in only little Ga diffusion from the NW top and the substrate during the N-rich phase. This explains the comparatively small increase in shell thickness towards the NW top and the NW bottom for high rotation speeds.

The analysis of Figure 5.9 (c) shows that a homogeneous shell morphology can also be achieved by high rotation speeds > 60 rpm. It should be noted that such high rotation speeds are not realizable in all MBE systems. In our case, for example, due to restrictions of the driving motor, we were only able to experimentally test rotation speeds up to 13 rpm, where we still observed a pronounced hourglass shape of the shell.

The main goal of the study presented in this section 5.1 was to understand the principles of core-shell growth by MBE. Therefore we investigated in detail the shell growth of GaN on GaN template NWs. From our experimental results we can conclude that it is not straightforward to obtain homogeneous shells along the whole NW length. We found that the hourglass shape observed for most growth conditions is the result of strong Ga adatom diffusion processes on the NW. These diffusion processes, in the end, originate from the complex chamber geometry of the MBE system, where the different material fluxes have different azimuthal angles with respect to each other. We will deepen the final discussion of this study in the conclusions of the present chapter (section 5.3).

## 5.2. (In,Ga)N/GaN core-shell structures

Since the growth of (In,Ga)N-based core-shell structures emitting in the green to red spectral range by MOCVD still poses serious difficulties, shell growth by MBE might be a possible alternative. But the literature on and hence the understanding of (In,Ga)N/GaN core-shell growth by MBE is quite sparse. Despite the promising technological perspectives of core-shell LEDs, only one group, Albert *et al.*, has investigated this topic so far.[87,175] They demonstrated the growth of (In,Ga)N shells as well as of doped core-shell LED structures around MOCVD-grown µm-rods, which show CL and EL shell emission in the violet spectral range, respectively. Hence, the In content in these structures was rather low. It seems that in order to push the In content to much higher levels and reach emission in the green or even red spectrum, a more comprehensive and fundamental knowledge about the peculiarities of (In,Ga)N shell growth by MBE is needed.

With the insights of the previous section 5.1, we have already developed a general understanding for the shell growth by MBE modeling GaN shells around GaN core NWs, hence, a rather simple system. However, the physical modeling of the shell growth of alloys like (In,Ga)N is more complex than in the case of the binary GaN. The different behavior and properties of the constituent atom species as well as their interaction have to be quantified for a reasonable modeling. But in the case of (In,Ga)N, these are mainly unknown parameters. Hence, as a first step to describe and understand the growth dynamics for (In,Ga)N shells in a more fundamental way, a more phenomenological approach has to be pursued.

In this section, we develop a qualitative model for the (In,Ga)N shell growth by MBE which enables us to find growth conditions under which homogeneous shells emitting in the blue/green spectral range can be realized. Furthermore, we analyze the influence of V/III and In/Ga ratio, as well as the impact of substrate rotation on the NW morphology and the emission properties of the (In,Ga)N shells. In the end, the experimental findings allow us to evaluate the proposed qualitative model. Moreover, it should be noted that in contrast to the MOCVD-grown µm-rod core structures with diameters of 500 nm and more presented in the previous reports[87,175] in literature, the GaN template NWs on TiN used in our approach are self-assembled, grown by MBE, and they are an order of magnitude smaller in diameter and length. Hence, with our study, we explore III-N shell growth at a much smaller scale than it has been investigated so far.

### 5.2.1. A qualitative model for (In,Ga)N shell growth

In the following, we propose a qualitative model for the growth of (In,Ga)N shells by MBE based on the insights we gained for GaN shells in section 5.1. In principle, these fundamentals should also hold for the shell growth of (In,Ga)N, i. e., with continuous substrate rotation, N as well as the two metal beams only sequentially impinge on the various side facets with a sinus-like intensity profile, whereas the top facet and the sub-

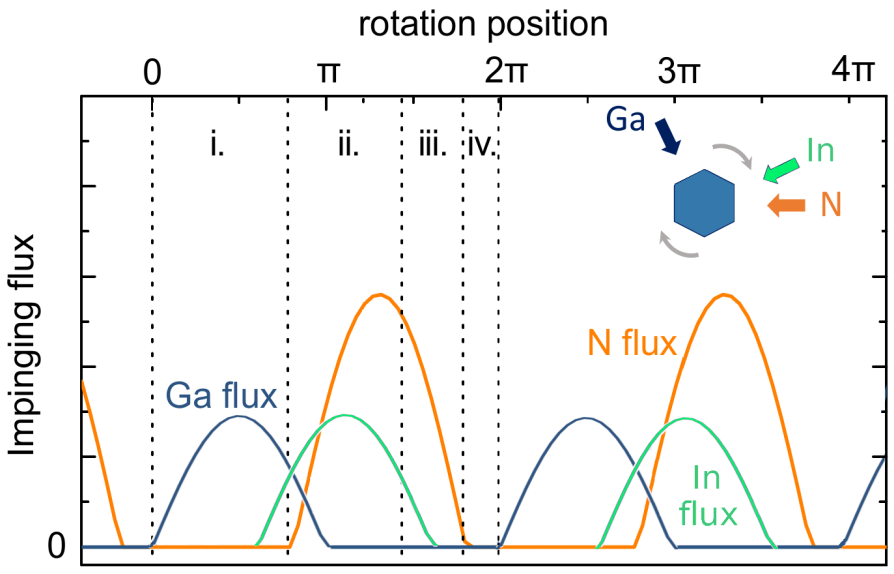


**Figure 5.10**: Sketch of impinging In, Ga and N fluxes on the side facet of a NW for different growth times/rotation positions. Note that the onset of the third phase (iii.) in this example is arbitrary. The actual onset and hence the length of this phase can only be determined by a quantitative modeling of the adatom concentration as it was carried out for the analysis of Figure 5.8 of the previous section. The inset depicts the arrangement of the material sources corresponding to the geometry of our MBE system, where the azimuthal angles between the different sources are $\beta_{\text{Ga-N}} = 144°$, $\beta_{\text{In-N}} = 36°$ and $\beta_{\text{Ga-In}} = 108°$. The rotation direction is given by the grey arrows. For the sketch a V/III and Ga/In of 1 is assumed to illustrate the general time dependence of the different fluxes with respect to each other.

strate (if not shadowed) are constantly exposed to all species. The resulting different chemical potentials on the different facets induce adatom diffusion, which may lead to locally very different adatom concentrations of the different material species.

To be more specific, Figure 5.10 shows a sketch of the Ga, In and N fluxes impinging on a certain side facet with proceeding growth time, analog to the GaN scenario of Figure 5.8 (a). For this gedankenexperiment we chose a V/III and In/Ga ratio of 1 for a clear visual illustration. The inset depicts the arrangement of the material sources corresponding to the geometry of our MBE system. The rotation direction is given by the grey arrows. Also in the case for (In,Ga)N, we assume that the diffusion of the different adatoms between *m*-planes, is negligible due to strong diffusion towards the NW top and substrate. For the case of GaN this assumption was supported by experimental evidence, as discussed for Figure 5.3. The following sections will show that this hypothesis can also be kept up for a reasonable description of (In,Ga)N shell growth.

As sketched in Figure 5.10, during one rotation round of (In,Ga)N deposition, a side facet passes trough the four different phases that we already established in section 5.1. The first phase (i) is the wetting phase, where Ga is deposited on a side facet which is

yet shadowed from both In and N. While the facet rotates away from the Ga source, Ga adatoms diffuse towards the NW top and the substrate due to gradients in the chemical potential, which result from the fact that the NW top facet and the substrate are exposed to N. Once the side facet rotates into the In beam (not yet exposed to N) and In is deposited on the side facet, we expect the diffusivity of the Ga adatoms to be drastically enhanced due to the fact that In acts as a surfactant.[185–188] As a consequence, a rather homogeneous distribution of Ga and In along the whole NW length can be assumed. The second phase (ii.) is the metal-rich growth phase. The side facet rotates into the N beam and growth takes place. At first, due to the small azimuthal angle between facet and the impinging N beam, the V/III ratio on the facet is below one, hence, there are metal-rich growth conditions. Only with further rotation into the N beam, N-rich conditions are established on the side facet. This is third phase (iii.), the N-rich growth phase. It should be noted that during the metal-rich growth phase, it can be expected that less In is incorporated in comparison to the N-rich growth phase. This assumption can be justified by the fact that due to the different bond strength of Ga and In to N, Ga is incorporated preferentially over In and thus, under metal-rich conditions, the maximum amount of In incorporation is determined by the difference in N and Ga supply.[174,189] Moreover, it was found that also under N-rich conditions, the In incorporation increases with higher V/III ratios.[173,190] The fourth and last phase is the dissociation phase (iv.). With ongoing rotation, depending on the arrangement of the sources, there may be a rotation phase during which the side facet is neither exposed to one of the metal beams nor to N. In this phase, due to the high vapor pressure of N over InN ,[2] the previously grown (In,Ga)N on this facet may thermally dissociate. In general, since the low dissociation temperature of InN may inhibit high InN mole fractions in (In,Ga)N, only sufficiently low substrate temperatures allow high In contents.[189,191] Moreover, regarding the incorporation of In in (In,Ga)N/GaN heterostructures, high and homogeneous In contents may also be prevented by strain related issues resulting from the different atom size of Ga and In.[174]

### 5.2.2. Towards the growth of high In content (In,Ga)N shells

In this and the following sections of this chapter, we use the qualitative model introduced in section5.2.1 as a basis for the analysis of (In,Ga)N shells grown under different conditions and evaluate whether the observed phenomena can be described well by this general concept. Moreover, the model allows to make some first assumptions, what growth parameters likely result in a high In incorporation. Since during the metal-rich growth phase, potentially less In is incorporated, keeping this phase as short as possible may be beneficial for the realization of high In contents. Regarding suitable growth parameters, this can be realized by a high V/III ratio and rotation speed. The latter would also have the positive effect that also the dissociation phase is shortened. Moreover, to obtain a high In content, the shell growth should be performed at a substrate temperature where

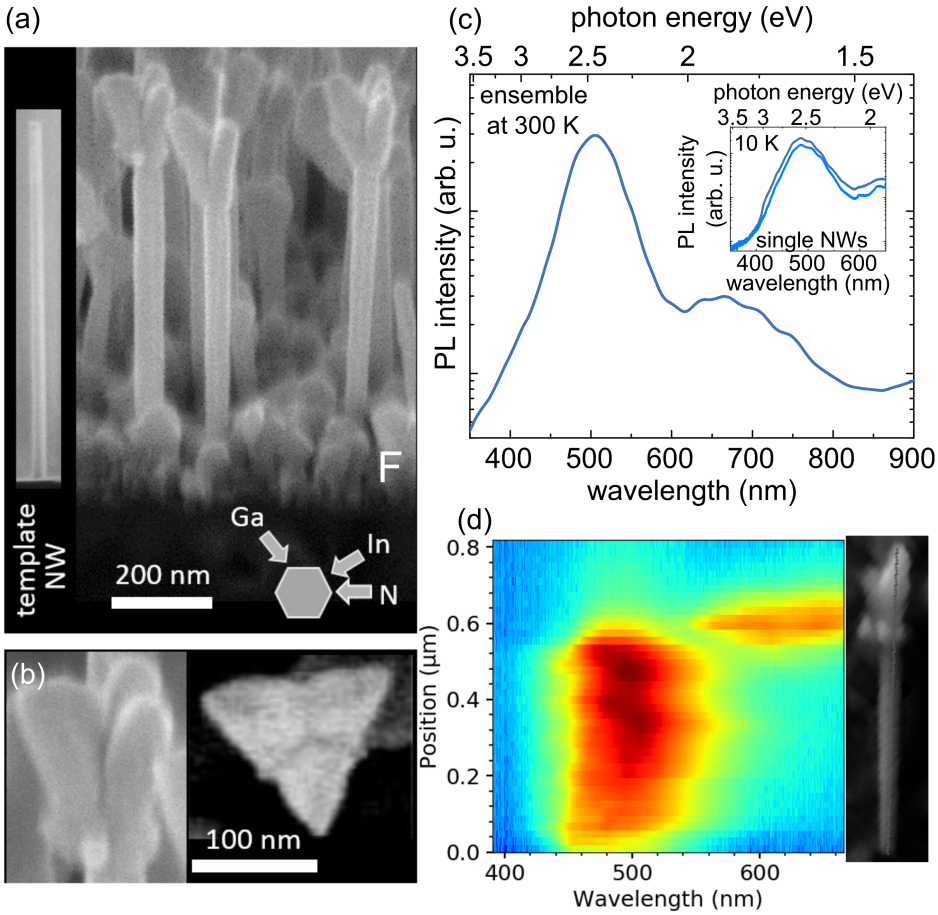


**Figure 5.11**: (a) Bird's eye SE micrograph of sample 5.F where a radially symmetric (In,Ga)N shell has been grown around template NWs (see inset on the left-hand side). The inset in at the bottom right side sketches the source arrangement of the MBE chamber. (b) Bird's eye and plan view SE micrograph of the wide top segments found for the core-shell NWs of sample 5.F. (c) Ensemble PL measured at 300 K. The inset shows the LT-PL acquired at 10 K for two representative single NWs. (d) LT-CL line scan of a single exemplary NW measured at 10 K. SE micrographs acquired by A.–K. Bluhm and CL measurement performed by Jonas Lähnemann.

In desorption and dissociation is kept to a minimum. To this end, the shells of all samples presented in this section were grown at a substrate temperature of about 490 °C. This temperature was determined in a preliminary experiment where the substrate temperature was lowered stepwise starting from 600 °C and depositing and subsequently desorbing one ML of In every 20 °C until a temperature was reached for that no In desorption was visible anymore in the QMS. Without In desorption, it could be assured that all In being deposited on the sample is incorporated. For this study, we did not further lower the temperature to avoid formation/incorporation of defects. Moreover, the lower the substrate temperature, the lower is the diffusion length of the different adatoms which might affect the homogeneity of the shell along the NW.

The practical implementation of these considerations towards the growth of high In content (In,Ga)N shells is shown for sample 5.F in Figure 5.11. The bird's eye SE micrograph in Figure 5.11 (a) shows the morphology of sample 5.F containing GaN NWs with (In,Ga)N shells of about 10 – 15 nm thickness (evaluated from SE images assuming an average diameter of the template NWs of 35 nm). The shell was grown at a substrate temperature of about 490 °C as introduced in the previous section 5.2.1. The speed of the substrate rotation was 10 rpm. Restrictions of the driving motor of the substrate rotation did not allow much higher rotation speeds. The V/III and the In/Ga ratios were 5 and 1, respectively, where $\Phi_{In} = \Phi_{Ga} = 0.1$ MLs/s. Regarding the V/III ratio, we assessed that this was about the highest possible value while preserving a reasonably high In and Ga flux for a given N supply. The arrangement of the material sources in the MBE chamber is sketched in the inset on the bottom-right where the substrate was rotated clockwise. The inset on the left-hand side depicts a cross section SE micrograph of an average template NW. Regarding the core-shell NWs, the (In,Ga)N shells are rather homogeneous in thickness along the whole length of the NWs, however, large tripod-shaped top segments have formed as visible in the magnified bird's eye and plan view SE images in Figure 5.11 (b). Moreover, small parasitic (In,Ga)N NWs grew on the substrate in between the core-shell wires.

The homogeneity of the (In,Ga)N shells, despite the low substrate temperature and the nominally very N-rich growth conditions, may be explained by In acting as a surfactant and enhancing the diffusivity of Ga adatoms on the *m*-plane side facets.[185,187,188] The effect might be similar to the one found for the (0001) facet where In forms an adlayer on the surface which significantly enhances the mobility of Ga adatoms leading to smooth layers even at very low substrate temperatures.[186,192] It should be noted that in the presence of In also the diffusion of metal adatoms around the NW, hence, from *m*-plane to *m*-plane might be increased leading to a more homogeneous adatom concentration along the NW. The formation of the pronounced top segments may be explained by the increased diffusivity and strong gradients in chemical potential due to the highly N-rich growth conditions. This leads to strong adatom diffusion towards the NW top and results in a high growth rate on the top facet. The tripod shape of these top segments could be ascribed to cubic (In,Ga)N growing along the three (111) axes of the zinc blende structure.[181] In general, low substrate temperatures (< 600 °C) promote the formation of cubic polytype as well as of stacking faults in nitride materials.[193,194] Moreover, the formation of the cubic polytype has been found to coincide with In supply.[195]

Figure 5.11 (c) depicts a RT-PL measurement of the NW ensemble of sample 5.F. The spectrum shows an intense emission band at around 505 nm (2.45 eV) with a FWHM of about 60 nm (344 meV) and a much weaker emission band at about 665 nm (1.86 eV) with a broader FWHM (precise value not determinable). The inset depicts two LT-PL spectra of single NWs acquired at two different positions. The two spectra are very similar to the ensemble PL, both showing a major emission band at around 485 nm (2.56 eV) and a second, less pronounced band at about 640 nm (1.93 eV). In order to understand better

from which part of the NW the different emission bands originate, CL line scans along single dispersed NWs were acquired at 10 K. Figure 5.11 (d) depicts a characteristic line scan which shows a rather homogeneous emission along the whole NW length at around 480 nm (2.58 eV). The second emission band, which peaks between about 600 nm (2.07 eV) and 660 nm (1.88 eV), is only visible in the area of the NW top segment. The small parasitic (In,Ga)N NWs of sample 5.F usually emit in the spectral range of the top segments (respective CL maps not shown here), however, they are comparatively dark. The CL line scan clearly shows that the more intense short-wavelength emission band, also observed in the PL, can be attributed to the (In,Ga)N shells whereas the less intense emission band at longer wavelength stems from the top segments. Hence, with sample 5.F we demonstrate for the first time MBE-grown (In,Ga)N/GaN core-shell NWs with shells emitting in the blue/green spectral range at around 505 nm. Using emission energies of planar (In,Ga)N layers as a reference,[196] a peak luminescence at about 505 nm would roughly correspond to an In content in the shell of around 25 %. It should be noted that the different strain state of the planar (In,Ga)N layer on the one hand, and the (In,Ga)N shells on the other hand is not considered for this comparison. Hence, the assumed In content is only a rough estimation.

In general, the resemblance of the ensemble and the single NW PL suggests a rather similar In incorporation from NW to NW. This is in contrast to the findings for common MBE-grown axial heterostructures on self-assembled NW ensembles on Si, where the emission wavelength varies significantly from blue to red among different NWs.[168,197–200] The absence of any luminescence of the GaN core especially at low temperatures indicates that the electron-hole pairs excited in the core efficiently diffuse to the (In,Ga)N shell and the top segment. The rather broad emission band of the (In,Ga)N shell can be attributed to local fluctuations of the In content, resulting in charge carrier localization and recombination at various wavelengths. The absence of sharp emission peaks indicating localization in the LT-PL of single NWs might be due to the high excitation power. Moreover, it should be noted that the (In,Ga)N shell shows good luminescence even without passivation by an outer GaN shell. This is another indication for carrier localization which prevents the charge carriers from diffusing towards the surface and recombining non-radiatively. A rather broad emission has also been observed for MBE-grown planar *m*-plane (In,Ga)N/GaN QW structures[201] and (In,Ga)N shells around GaN µ-rods[175] emitting in the violet spectral range. Moreover, atom probe tomography of MOCVD-grown (In,Ga)N/GaN core-shell structures emitting in the green spectral range revealed a strong variation in In content of the *m*-plane shells.[22,202]

The long-wavelength emission of the top segment can be attributed to a higher In incorporation in comparison to the shell. In general, the incorporation efficiency of In on the N-polar *c*-plane as well as on semi-polar r-planes is expected to be higher than the one on the *m*-plane.[20,21,174,203] However, from the CL analysis it is not clear from which part of the top segment the high-wavelength emission originates, i. e. whether the luminescence stems from wurtzite or cubic (In,Ga)N. At this point of the study, it is not

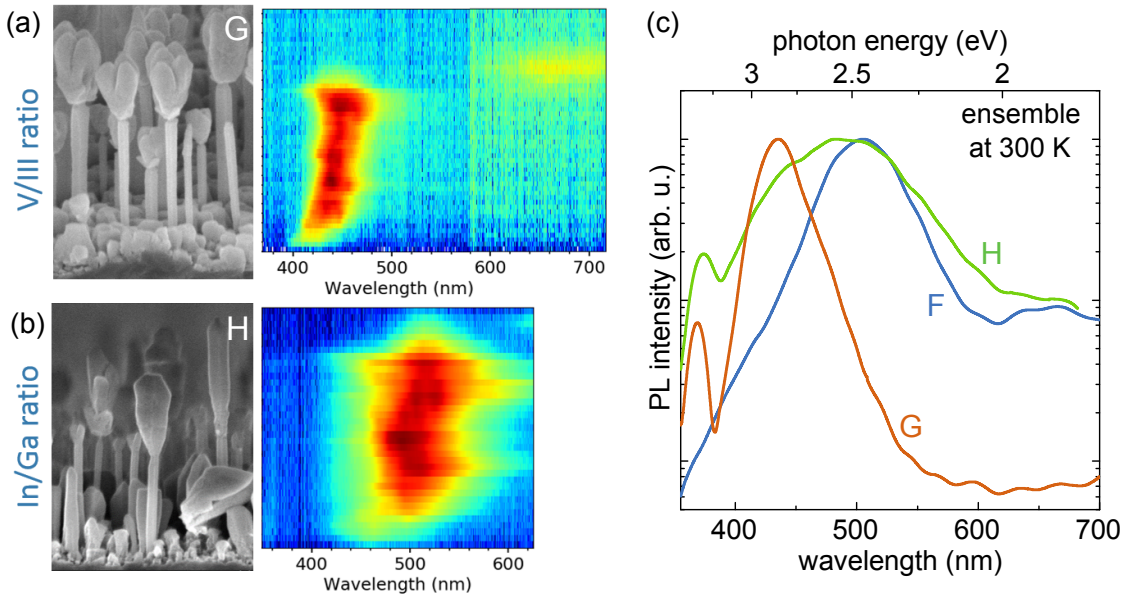


**Figure 5.12**: Bird's eye SE micrograph and LT-CL line scan measured at 10 K for (a) sample 5.G and (b) sample 5.H, which were grown with a V/III ratio of 2.5 and an In/Ga ratio of 3, respectively, at otherwise similar growth conditions as for sample 5.F. (c) RT-PL of the NW ensembles of sample 5.F, 5.G, and 5.H. SE micrographs acquired by A.–K. Bluhm and CL measurements performed by Jonas Lähnemann.

clear why the emission intensity of the top segments is comparatively much lower than the one of the shell despite their large volume. One explanation might be a rather high density of nonradiative defects.

With sample 5.F we demonstrated the feasibility of a MBE-grown (In,Ga)N/GaN core-shell structure emitting in the blue/green spectral range and analyzed the general optical properties. In the following sections, we analyze the growth of (In,Ga)N shells in more detail, discussing the influence of the substrate rotation and the ratio of the different material species on the morphology and the emission properties.

Furthermore, we show that our phenomenological model (presented in section 5.1) may explain well the influence of the various growth conditions on the NW morphology and the In incorporation in the shell.

### 5.2.3. Influence of V/III and In/Ga ratio

sample 5.G depicted in Figure 5.12 (a) was grown with a V/III ratio of 2.5, where the N flux $\Phi_N$ was reduced by a factor two, at otherwise similar growth conditions as for sample 5.F. The shells are with about 15–20 nm a bit thicker than the ones of sample 5.F and show in average a slight tapering towards the substrate. Comparing the top segments, a similar tripod shape can be found, however, they are much larger in volume. The CL line scan of a representative NW shows an inhomogeneous shell emission which

increases from about 420 nm (2.95 eV) at the NW bottom to around 445 nm (2.79 eV) at the NW top and a very weak top segment emission at about 670 nm (1.85 eV).

The lower emission wavelength of the (In,Ga)N shell in comparison to sample 5.F may be explained by a lower In incorporation on the NW *m*-planes due to a reduced V/III ratio. Or in other words, a higher V/III as in the case of sample 5.F results in a higher In incorporation. This effect has also been observed for planar MBE-grown (In,Ga)N films on *c*-plane GaN as well as for the MBE-grown (In,Ga)N shells on µ-rods of Albert *et al.* [175] and was attributed to a lower dissociation rate of InN with increasing N flux. [173,190] Besides this direct influence of the V/III ratio on the stability of InN, there is a further effect potentially lowering the In incorporation on the NW *m*-planes, which is related to the MBE geometry and the fact that we are dealing with 3D nanostructures. In Figure 5.9 (b) we saw that lowering the nominal V/III ratio from 5 to 2 in the case of GaN shells leads to a decreased metal incorporation on the side facet. A similar effect seems to take place in the case of (In, Ga)N shells. As discussed above, once the side facet rotates into the N beam, at first there are metal-rich growth conditions. During this rotation stage, with Ga being incorporated preferentially over In, the In incorporation might be rather low on the NW side wall and excess In which is not incorporated may then diffuse towards the N-rich NW top facet and/or substrate. This would lead to an inhomogeneous In adatom concentration on the side facet, which would subsequently manifest in different shell thicknesses and In contents along the NW, once N-rich conditions are reached with further rotation. And indeed, the shell is thicker at the NW top and the CL line scans show that the emission wavelength of the (In,Ga)N shell, bottom to top, is red-shifted suggesting higher In contents towards the NW tip. In general, the lower the V/III ratio, the longer it takes until N-rich conditions which favor In incorporation are established, and the lower is the overall In content. Moreover, it is likely that during the metal-rich phase most of the Ga has already been incorporated. Hence, despite the high In/Ga ratio during the N-rich phase due to the directly impinging In (in our MBE geometry), the growth of (In,Ga)N with high In content might be reduced.

Figure 5.12 (c) shows the RT-PL spectrum of sample 5.G. With a peak emission wavelength of around 435 nm (2.85 eV), the major emission band resembles well the (In,Ga)N shell emission found for CL line scans of single NWs. Hence, also the ensemble PL shows a blue shift of the shell emission with decreasing V/III ratio. There is no clear PL signal detectable from the top segments, which are also barely visible in the CL line scans. As already discussed for sample 5.F, the origin of the low emission intensity of the top segments is still unclear. A possible explanation might be a rather high density of nonradiative defects.

Besides the V/III ratio, a further important factor for the growth of (In,Ga)N is the In/Ga ratio. Sample 5.H depicted in Figure 5.12 (b) was grown with an In/Ga ratio of 3 preserving a total metal flux of 0.2 MLs/s at otherwise similar growth conditions as for sample 5.F. With about 5 – 10 nm, the shells are slightly thinner than the ones of sample

5.F but generally also show a rather homogeneous thickness along the whole NW length. The top segment shapes are very diverse. About half of the NWs show very long and broad top segments which were grown at the rate of the impinging N flux, hence, under N-limited conditions. The other half only has very small top segments revealing a similar tripod shape as it was found for the other samples. It should be noted that for the conditions of sample 5.H the parasitic NWs are larger than the ones observed for sample 5.F. Figure 5.12 (b) also shows a CL line scan of a dispersed NW of sample 5.H, where the shell can be observed at about 515 nm (2.41 eV). In contrast to sample 5.F, investigating a number of dispersed NWs, we found intense shell luminescence in the wavelength range 420 – 525 nm (2.88 – 2.36 eV), hence, there are strong variations in the luminescence properties from NW to NW. The ensemble PL of sample 5.H, shown in Figure 5.12 (c), depicts one major band (besides the GaN luminescence) which can be attributed to PL from the (In,Ga)N shells of the NWs, similar to the previous samples. The peak emission wavelength is with about 485 nm (2.56 eV) slightly lower than the one of sample 5.F. However, the shape of the spectrum is rather flat around the maximum intensity and the emission band is, with a FWHM of around 135 nm (720 meV), much broader in comparison to sample 5.F, in particular towards shorter wavelengths.

The CL and PL analysis showed that the higher In/Ga ratio did not lead to an increase in the average In content of the (In,Ga)N shells but rather resulted in stronger variations from NW to NW indicated by the broad PL spectrum and the different emission wavelengths of the single NWs measured by CL. Also Albert *et al.* did not observe a significant change in In content of the (In,Ga)N shells on GaN µ-rods with increasing In/Ga ratio.[175] Our results as well as the results of Albert *et al.* are in contrast to the observations for planar MBE-grown (In,Ga)N films on *c*-plane GaN, where an increase of the In content was found with increasing In/Ga ratio under similar N-rich conditions.[204,205] Hence, the question is whether the fact that there is no increased In incorporation on the NW *m*-planes can be attributed to the 3D nature of the NWs (µ-rods). If the additional amount of In is not incorporated in the shell, it has to be incorporated elsewhere (note that according to the QMS, there is no In desorption; see explanation in first paragraph of section 5.2.2). With regard to sample 5.H, this might explain the large amount of material that grows on the NW top facet but also the increased growth of the parasitic NWs on the substrate in comparison to sample 5.F. Hence, the additional amount of In on the side facets seems to diffuse to either the top or the substrate rather than incorporate in the shell, which may be attributed to a lower In incorporation efficiency on the *m*-plane. The formation of massive top segments and parasitic NWs might lead to distinct mutual shadowing of the long NWs which might vary locally and thus explain the the strong variations in the CL of single NWs and the broad ensemble PL.

In general, we would like to point out that with the CL line scan of Figure 5.12 (b) which shows intense shell emission up 525 nm (2.36 eV), we demonstrate that homogeneous (In,Ga)N shells emitting in the green spectral range are feasible by MBE.

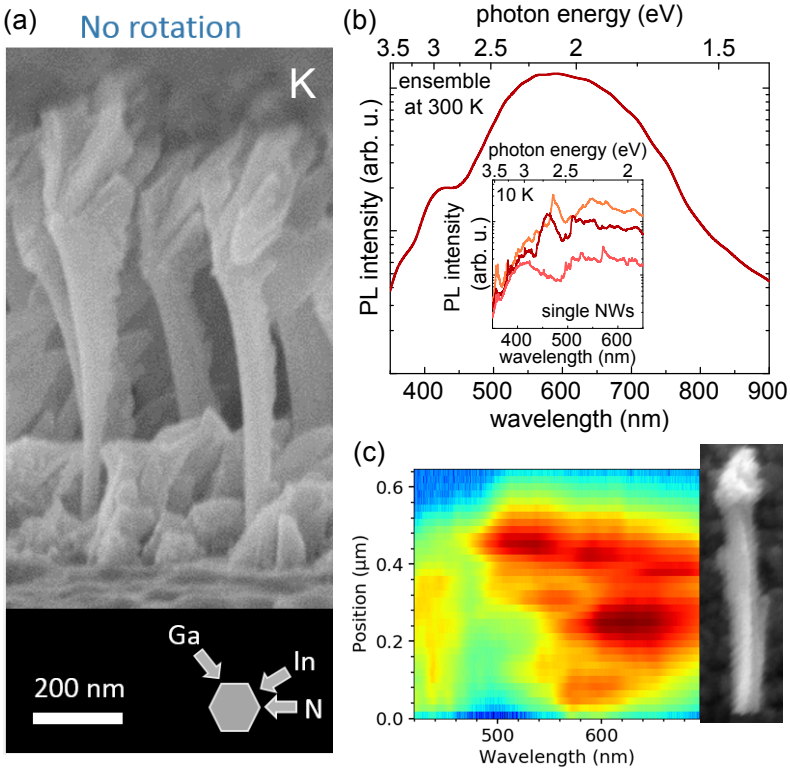


**Figure 5.13**: Cross-sectional SE micrograph of sample 5.K which has been grown without substrate rotation at otherwise similar growth conditions as sample 5.F. The sketch at the bottom depicts the source arrangement of the MBE chamber. (b) RT-PL of the NW ensemble measured at 300 K. The inset depicts LT-PL measurements (at 10 K) of single exemplary NWs. (c) LT-CL line scan of a single representative NW. SE micrograph acquired by A.–K. Bluhm and CL measurement performed by Jonas Lähnemann.

### 5.2.4. Influence of substrate rotation

In section 5.1 we found that for GaN shells, the substrate rotation, i. e. the rotation speed, has a strong influence on the shell morphology. In the case of (In,Ga)N, the effect of a change in growth parameters on the shell homogeneity seems to be less pronounced. However, analyzing the impact of the V/III and the In/Ga ratio in the previous section showed that the growth conditions in general may strongly affect the In incorporation. In this section we analyze the impact of the substrate rotation, in particular with regard to the In incorporation in the shell.

Sample K shown in Figure 5.13 (a) was grown without substrate rotation at otherwise similar growth conditions as sample 5.F. The NWs depict a distinct bending towards the left-hand side. On the right-hand side of the NW sidewalls large fan-like structures have formed with sizes from about a few nm up to around 200 nm in some cases. The fan structures are rather irregular along the NW length and also differ significantly from NW to NW. Moreover, the top segments and the "parasitic NWs" are very pronounced and

inclined towards the right-hand side. The NW morphology shows that similar to the no-rotation case for GaN shells in section 5.1, radial growth of (In,Ga)N predominantly takes place on the N-exposed side of the NWs (right-hand side). Due to the larger lattice constant of (In,Ga)N with respect to GaN, the template NWs bend towards the left-hand side once (In,Ga)N is grown on the right-hand side.[91] With the N-exposed side being shadowed from the direct Ga beam, the Ga adatoms which contribute to the *m*-plane growth must have diffused to the growth front. This most likely leads to very different adatom distributions of Ga and In causing very different nucleation and growth conditions on the NW side facet in comparison to the continuously rotated sample 5.F. The inclined character of the top segments and the "parasitic NWs" suggests that the growth mainly takes place in the direction of the impinging N species.

Figure 5.13 (b) shows a PL measurement of the NW ensemble of sample 5.K at 300 K. The spectrum is rather broad with a main emission band around 590 nm (2.1 eV) with a FWHM of 200 nm (690 meV) and a less intense shoulder at about 420 nm (2.95 eV). The inset depicts low-temperature PL measurements at 10 K, where each spectrum corresponds to the PL of one or a few NWs (number of NWs was not clearly resolvable). All spectra show a large number of narrow emission lines at various wavelengths in the whole measurement range from 350 nm (3.54 eV) to 650 nm (1.91 eV). Also in this case, we measured CL line scans of several single NWs. A representative scan is shown in Figure 5.13 (c). In contrast to sample 5.F, there is not one rather homogeneous luminescence band but a number of localized emission centers along the whole NW length emitting at very different wavelengths from 530 nm (2.34 eV) to 670 nm (1.85 eV). Moreover, there is a low-intensity emission band visible at around 430 nm (2.88 eV). In general, despite the similar growth conditions in comparison to the continuously rotated sample 5.F, the PL and CL of the no-rotation sample 5.K is strongly red-shifted indicating a higher In incorporation. The inhomogeneous and localized emission visible in low-temperature PL can be attributed to strong variations in In content leading to charge carrier localization.[22,175,202] The CL line scan shows that long-wavelength emission and localization effects also appear in the (In,Ga)N fan structures grown on the NW sidewalls.

The higher In incorporation on the NW side wall in comparison to sample 5.F may have several reasons. With the side facet where the growth takes place being constantly exposed to both In and N, there are always N-rich conditions at the growth front which in combination with a permanent In supply favors high InN mole fractions in (In,Ga)N.[173,190] Moreover, it is likely that with increasing (In,Ga)N thickness on the *m*-plane, local strain variations caused by fluctuations of the In content may induce the formation of other facets.[202] Indeed, the inclined nature as well as the rough morphology of the (In,Ga)N fan structures suggests the formation of most likely semi-polar facets along which further growth takes place. On semi-polar facets the In incorporation efficiency is supposed to be higher than on the *m*-plane,[21,202] which may explain the significantly higher emission wavelength of the (In,Ga)N grown on the NW side facet of sample 5.K in comparison to sample 5.F. For MOCVD-grown (In,Ga)N shells on GaN µ-rods Coulon *et al.*[202] found

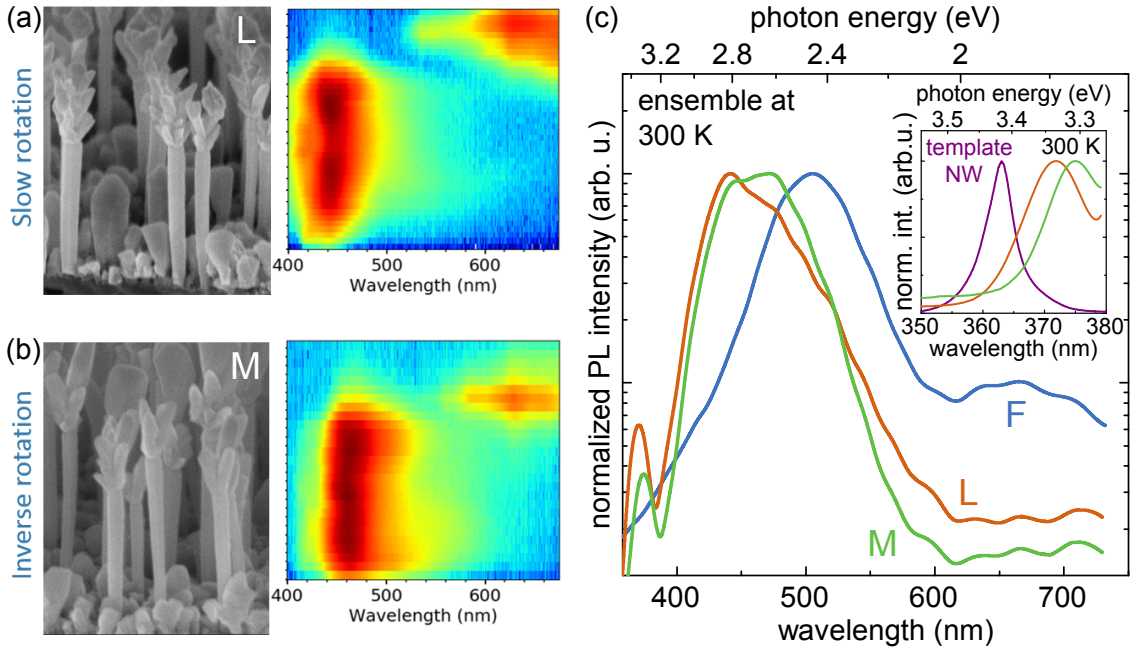


**Figure 5.14**: Bird's eye SE micrograph and LT-CL line scan measured at 10 K for (a) sample 5.L and (b) sample 5.M, which were grown with slow rotation (1 rpm) and inverse rotation (with respect to sample 5.F), respectively, at otherwise similar growth conditions as for sample 5.F. (c) RT-PL of the NW ensembles of sample 5.F, 5.L, and 5.M. The inset shows the GaN core PL of the template NW ensemble as well as of sample 5.L (orange) and M (green) at 300 K. SE micrographs acquired by A.–K. Bluhm and CL measurements performed by Jonas Lähnemann.

that on the *m*-plane first a pseudomorphically grown 2D layer with a lower In content forms before at a certain thickness the Stranski-Krastanov growth mode sets in and strain is released by 3D growth allowing higher In contents. The emission band around 430 nm (2.88 eV) which is clearly visible in the RT-PL and the LT-CL line scan seems to originate from the NW sidewall as well and might be attributed to the low In content 2D layer. However, this is rather speculative.

Although the NW morphology of sample 5.K is not suitable as a basis for heterostructures, the approach shows that the formation of quantum dot-like structures with high In contents on NW *m*-planes might be an interesting alternative to pseudomorphically grown shells for the realization of emission in the deep red spectral range.

Sample 5.L shown in Figure 5.14 (a) was grown with a ten times lower substrate rotation in comparison to sample 5.F, namely 1 rpm, at otherwise similar growth conditions. The shell morphology of the NWs is very similar to sample 5.F, whereas the top segments in most cases show a double tripod-shape and the parasitic NWs are larger. According to the CL line scan of a representative NW, the (In,Ga)N shell emits at around 440 nm (2.82 eV). The top segments show a rather broad emission at about 660 nm (1.88 eV). The lower emission wavelength of the (In,Ga)N shell in comparison to sample 5.F can be ex-

plained by a lower In incorporation with reduced speed of the substrate rotation. Lowering the rotation speed has a similar effect as lowering the V/III ratio. The lower the rotation speed, the longer it takes until the metal-rich rotation phase on the side facet (low In incorporation efficiency during this phase) is overcome and N-rich conditions which favor In incorporation are established. The rotation speed may also have an influence on a potential thermal dissociation of the (In,Ga)N shell during the rotation phase in which the facets are not exposed to any material beams. Hence, the higher the rotation speed, the smaller the thermal dissociation.

Figure 5.14 (b) depicts sample 5.M for which the rotation direction was inverted in comparison to sample 5.F, hence, the rotation was anti-clockwise. Again, the NWs look very similar to the ones of sample 5.F, however, the emission wavelength of the (In,Ga)N is slightly lower as the LT-CL line scan reveals. In this rotation scenario, the lower In content of the shell may be explained by the fact that once In is deposited first during a rotation cycle, more In has diffused away until the side facet is exposed to N and growth takes place. Moreover, with Ga being deposited after In, it is likely that the Ga adatoms replace the already bound In adatoms (due to strain and binding energy related effects, see section 5.2.1) and hence increase the probability for In to desorb from the surface or to diffuse away.

Figure 5.14 (c) shows the RT-PL of sample 5.L and M in comparison to sample 5.F. The luminescence properties found in the CL line scans are well reflected in the PL spectra. Both samples show a blue shift of the shell luminescence. The spectrum of sample 5.L has a long tail towards longer wavelength, which can be explained by contributions of NWs which show shell emission at higher wavelengths (also observed in CL line scans of further NWs). The inset shows the GaN core luminescence of the template NWs as well as of sample 5.L and M at 300 K. The peaks of the two (In,Ga)N core-shell samples are clearly red-shifted with respect to the GaN luminescence of the template NWs. Due to the lattice mismatch of GaN and (In,Ga)N, the strain in the (In,Ga)N shells is partially released in the from of tensile strain in the GaN core which lowers the bandgap energy and shifts the core emission towards the red. The strained GaN cores suggest that the shells are in general free of plastic relaxation.

In this section we showed that the In content of the (In,Ga)N shells strongly depends on the growth conditions, i. e. the V/III and the In/Ga ratio as well as the rotation speed and that the principle understanding of the core-shell growth by MBE we developed in section 5.1 can be transferred to the case of (In,Ga)N shells. The analysis of the (In,Ga)N shells in this section suggests that the different rotation phases that the side facets pass through during one rotation round, from wetting phase over metal-rich and N-rich growth phase to the dissociation phase, have a significant influence on the In incorporation. For instance, the higher the V/III ratio, the earlier the N-rich growth phase sets in, which leaves less time for deposited adatoms to diffuse away before being incorporated. The latter aspect is also true for faster rotation speeds, since the time until

a respective side facet is exposed to the N beam is shorter. Moreover, a faster rotation may reduce thermal dissociation of the shell. Another interesting study, which was out of scope for this work, would be an investigation of the influence of different azimuthal angles between the different material sources on the shell growth.

## 5.3. Summary and Conclusions

In this chapter, we have investigated in detail the effect of the inherently sequential deposition in MBE on the growth of GaN and (In,Ga)N shells around GaN NWs. Our experimental results showed that it is not straightforward to obtain shells with homogeneous thickness along the whole NW length.

By modeling the shell growth of GaN shells on GaN NWs *with* and *without* substrate rotation in section 5.1, we found that the hourglass shape observed for most growth conditions is the result of strong Ga adatom diffusion processes on the NW. These diffusion processes are decisively influenced by the fact that on the top facet and substrate growth is always possible, while on the sidewalls, growth only takes place when the respective side is exposed directly to the N beam. The resulting gradients in chemical potential drive Ga adatom diffusion fluxes between these three regions, which are modulated by the subsequent exposure of the sidewall to the different molecular beams during substrate rotation. Modeling shell growth for various conditions, we found that homogeneous shells can be achieved for small azimuthal angles between Ga and N, where both materials impinge from the same direction. However, the positioning of material sources next to each other is not always practical or feasible, especially considering the growth of complex core-shell structures where ternary or quaternary alloys and doping are involved. As a solution to this impediment, we showed that also for very high rotation speeds rather homogeneous shells can be obtained. However, the necessary rotation speeds are rather fast and might not be realizable in every MBE system.

Beyond the pragmatic benefit of providing guidance for the design of growth protocols resulting in homogeneous shells, our model has also enabled a comprehensive understanding of the adatom concentration on the NW at all times during the growth. We found that the growth on the side facets can be categorized in four different phases: the wetting phase, the metal-rich growth phase, the N-rich growth phase, and the dissociation phase. The absolute and relative length of these phases during one rotation period may not only affect the thickness homogeneity of the shell along the NW as discussed above, but also its local surface roughness. The fact that for larger azimuthal angles, Ga and N are deposited at different times during the rotation leads to an extensive Ga diffusion during the wetting and the metal-rich growth phase, similar to an MEE growth process.[79,206] This may explain the smooth side facets generally observed for NWs also for very low substrate temperatures and nominally N-rich growth conditions. The striking difference to growth processes on planar samples is that in our case, diffusion takes

place between different regions, i. e. the sidewall vs. the top facet and substrate, out of which on one N impinges not continuously, resulting in complex gradients in chemical potential that are modulated in time by substrate rotation.

Our analysis in section 5.1 has shown that even for a binary material like GaN, shell growth by MBE is very complex. This finding raises the question how the shell growth of ternary or even more complex nitride alloys may be influenced by the chamber geometry. Indeed, the investigation of radially symmetric (In,Ga)N shells presented in section 5.2 suggests that the principle understanding of the core-shell growth by MBE we developed in section 5.1 can also be transferred to the case of (In,Ga)N shells. Hence, the model of the different rotation phases that the side facets pass through during one rotation round - from the wetting phase over the metal-rich and N-rich growth phase to the dissociation phase - can also be applied to the shell growth of the ternary alloy (In,Ga)N. Moreover, in this section we showed that the In content of the (In,Ga)N shells strongly depends on the growth conditions, i. e. the V/III and the In/Ga ratio as well as the rotation speed, which determines the duration of the different rotation phases. For instance, for a high In incorporation a high V/III ratio and a fast rotation are beneficial, since in this scenario, the N-rich growth phase is reached more quickly. A comparatively longer N-rich phase leaves less time for deposited adatoms to diffuse away before being incorporated and the faster rotation may reduce thermal dissociation of the shell.

In general, we were able to demonstrate that (In,Ga)N shells emitting in the green spectral range are feasible by MBE and that also active regions emitting in the deep red might be within reach. However, in order to use such core-shell structures as a basis for NW LEDs, there are still some open challenges that have to be tackled. For instance, the length variation of the template NWs, or the large top segments may affect a homogeneous processing of the final LED device. As a solution, in the following chapter 6, we will introduce a novel approach for the fabrication of ensembles of highly ordered NWs with well defined dimensions as well as a new growth process which allows the controlled deposition of shells on different sides of the NW and may reduce the formation of enlarged top segments.

# 6. Sequential directional deposition of III-nitride shells on lateral side facets of GaN NWs

In face of the increasing demand for multifunctional and more compact devices in areas like communication, lighting, energy harvesting, and medicine,[7,207,208] conventional semiconductor-based technologies reach their operation limits. Hence, new technological approaches are needed for the integration of more complex functionalities, while scaling down the device size. However, regarding conventional planar heterostructures, the design diversity, i e. the possibilities to combine different active regions with different functionalities on one chip, is strongly restricted to material compounds with similar lattice parameters.[209] A promising solution to this impediment came with the enormous progress in the field of 3D nano- and microstructures. In this thesis, we showed that with NWs one can grow high crystal quality material on rather dissimilar substrates, even on metals like TiN. Moreover, growing (In, Ga)N shells on the NW side facets as a basis for LEDs, we made use of the fact that the area of the active region of the device can be drastically increased beyond the footprint of the nanowire on the substrate.[14] Despite such advantages of NWs, in the previous chapter we learned that already the growth of NWs with only one functional active region can be very challenging. For instance, we discussed the difficulty to manufacture an (In, Ga)N shell emitting in a certain spectral range, while maintaining a NW morphology which is suitable for device processing. Usually, the realization of a device with multiple active regions with different individually controllable functions requires (i) complex processing steps where different elements with different functionalities are realized on one common substrate or (ii) the elements with different functionalities are fabricated separately and, subsequently, are integrated on a common platform.[5,170,210,211]

In this chapter, we present an innovative approach exploiting the directed nature of the material beams in an MBE system, which enables a sequential directional deposition of GaN and (In,Ga)N on only one side of GaN template NWs (section 6.1). On the one hand, this approach allows to reduce metal adatom diffusion on the NW and thus, for instance, may reduce the diffusion-enhanced formation of large top segments as observed for the radial symmetric shells in chapter 5.2. On the other hand and more importantly, this growth process in general allows to combine different active regions with different properties/functionalities on different lateral sides of one and the same nano-

or microstructure and hence enables the fabrication of new typs of multifunctional nanodevices. In section 6.2, we investigate the growth of one-sided shells in more detail, in particular for (In,Ga)N, by varying a number of growth parameters like substrate temperature and In/Ga ratio, but also by studying the effect of sub-monolayer deposition and the deposition sequence of the different metal species as well as the impact of an *in situ* annealing on the shell. For these investigations, GaN NWs on TiN, as they were presented in chapter 3, are used as template NWs. To asses the feasibility of the growth of multiple one-sided shells on one and the same template structure, in section 6.3, we develop a growth approach to realize the deposition of two one-sided (In,Ga)N shells with different In content on opposite sides of the same template NWs on TiN. In order to demonstrate that the growth of one-sided (In,Ga)N shells is also feasible for ordered structures which are in general more suitable for device processing, in section 6.4, we transfer the developed growth method for one-sided shells to ordered GaN NW arrays fabricated by SAS. Finally, in section 6.5, we propose a novel device design which combines multiple active regions with different functionalities and suggest its application for the realization of a multicolor RGB-LED based on single nano- or microstructures.

Parts of this chapter have been published in D. van Treeck *et al.*, EP3531459, European Patent Office (2019).[212]

## 6.1. The sequential directional deposition process

In this and the following sections, we examine the growth of one-sided III-N shells, in particular (In,Ga)N shells on GaN NWs. There have been a few reports where certain material or a heterostructure were intentionally deposited on only one side surface of a given nanostructure.[88,91,213,214] Since, so far, there are no reports on the one-sided growth of III-N materials on 3D structures by MBE, we first introduce the sequential directional deposition (SDD) process we developed.

Figure 6.1 (a) sketches the SDD of a one-sided GaN shell on a GaN core NW. As a first step (i), a certain amount of Ga (usually < 1 ML) is deposited on one specific side of the NW by opening the shutter of the Ga source. In the subsequent step (ii), after closing the Ga shutter, the very same side on which Ga was deposited is rotated towards the N source. All shutters are closed during the rotation. In the last step (iii), the shutter of the N source is opened and GaN is grown. After closing the N shutter, the NW is rotated back to position (i) and the deposition cycle starts again.

Figure 6.1 (b) shows a bird's eye SE micrograph of sample 6.X, where a one-sided GaN shell was grown on GaN template NWs using the SDD approach depicted in Figure 6.1 (a). The GaN template NWs on TiN were grown at similar conditions as the ones presented in the previous chapter 5, hence, they have a mean diameter of about 35 nm and a mean length of around 770 nm. The GaN shell was grown at a substrate tempera-

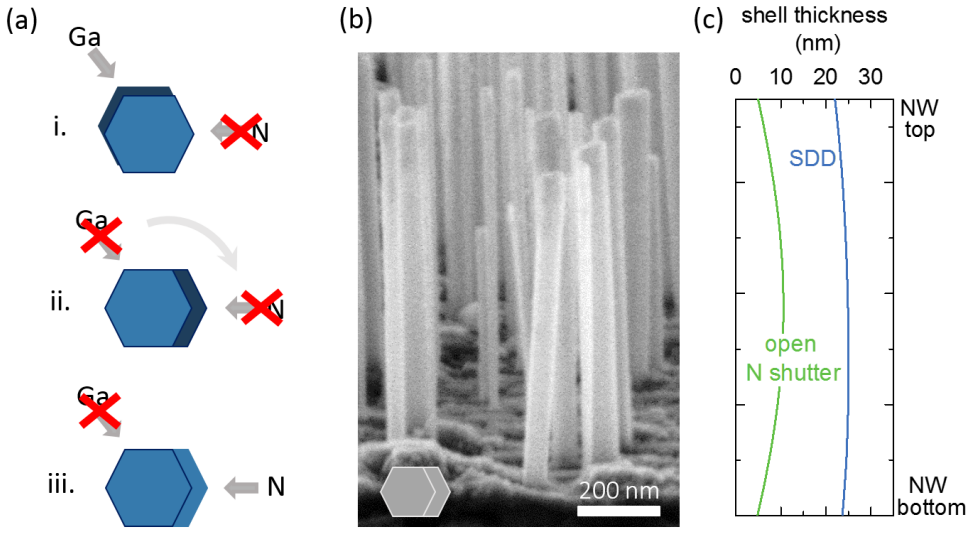


**Figure 6.1**: (a) Sketch of the SDD of a one-sided GaN shell on a GaN core NW. Steps (i)–(iii) are described in detail in the main text. (b) Bird's eye SE micrograph of sample 6.X, where one-sided GaN shells were grown on GaN template NWs using the SDD approach depicted in sketch (a). (c) Modeled shell thickness of a one-sided GaN shell on a GaN template NW using the SDD approach (blue profile) and for constantly open N shutter (green profile) at otherwise similar modeling parameters. The modeling is based on the model for the shell growth of GaN presented in section 5.1.3 of the previous chapter using the growth conditions of sample 6.X (see main text) and the modeling parameters of sample 5.B2 of chapter 5.1. SE micrographs acquired by A.–K. Bluhm.

ture of about 490 °C with a Ga flux of 2.4 nm/min (1.5 ML/s) and a N flux of 12.4 nm/min (direct fluxes). In each cycle the respective side of the NW was exposed to the Ga beam for 4 s which corresponds to deposition of about 0.6 ML and 0.8 ML of Ga on the side facets and the top facet/substrate, respectively. Subsequently, the wetted NW side was rotated towards the N beam and exposed to N for 25 s. The duration of the rotation phases where both shutters are closed was 4 s. In total 130 cycles have been carried out. This way a 20–25 nm thick shell was grown on the right side of the NWs as depicted by the top view sketch in the bottom left of Figure 6.1 (b). The shell thickness has been estimated analyzing the NW diameter along the growth direction of the shell from the SE micrographs. In contrast to the radially symmetric GaN shells presented in chapter 5, the one-sided shells are very homogeneous along the whole NW length as the micrograph of Figure 6.1 (b) reveals.

In order to better understand the SDD, in Figure 6.1 (c) we modeled the shell thickness of a one-sided GaN shell on a GaN template NW based on the model for the shell growth of GaN presented in section 5.1.3 of the previous chapter. Instead of modeling the shell growth for *continuous rotation* or *no rotation*, here, the different deposition and rotation sequences of the SDD mode as described for Figure 6.1 (a) were simulated (blue profile). As input parameters we used the growth conditions of sample 6.X (as described above)

and the modeling parameters of sample 5.B2 shown in Table 5.2 of chapter 5. Moreover, besides the modeling of the shell thickness obtained by the SDD approach, Figure 6.1 (c) also shows the shell profile which results from a constantly open N shutter (green profile) at otherwise similar modeling parameters. The modeled shell profile for the SDD approach (blue) shows a rather uniform shell thickness along the NW, similar to the experimentally observed morphology, with a slight belly-shape in the NW center.

The homogeneous shell thickness can be explained by the fact that during step (i) and (ii), when the N shutter is still closed, the differences in Ga adatom concentration between the side facets and the top facet/substrate are equalized. Or in other words, the Ga adatom concentration in each region reaches an equilibrium state where the surface is wetted rather homogeneously. Note that due to the higher adatom concentration on the top facet/substrate in comparison to the side facet, there may be a small diffusion fluxes onto the side facet to reach the equilibrium state. Only when the N shutter is opened for step (iii), Ga adatoms diffuse from the NW side towards the NW top and the substrate due to the higher incorporation rates in these regions (mainly caused by the MBE geometry, see chapter 5.1). Due to these diffusion effects, the belly shape is much more pronounced once the N shutter is kept open throughout all three deposition and rotation steps as shown by the green shell profile. Moreover, the increased Ga diffusion away from the side facet results in a much smaller mean thickness of the shell, namely less than 10 nm. In summary, regarding the shell growth of GaN, the SDD mode not only allows the deposition of individual shells on selected lateral sides of a nano- or microstructure, but also enables the growth of a homogeneous GaN shells along the whole NW length.

With regard to ternary alloys, Figure 6.2 sketches the SDD of a one-sided (In,Ga)N shell. The illustrated source arrangement corresponds to the one of our MBE system. As a first step (i), similar to the SDD of GaN presented above, Ga is deposited on the respective side of the NW. In a second step (ii), after rotating the NW side towards the In source, In is deposited. Only then, as a last step (iii), the side is rotated towards the N source, the N shutter is opened and (In,Ga)N growth takes place. Also here all shutters are closed during the rotation phases. In the next section 6.2, we investigate the growth of one-sided (In,Ga)N shells in detail and discuss the influence of different growth conditions.

## 6.2. One-sided III-Nitride shells

With the samples 6.A – 6.D, Figure 6.3 shows the morphology of GaN NWs with a one-sided (In,Ga)N shell and the respective CL line scans of single NWs as a function of the growth temperature and the nominal In/Ga ratio. The GaN template NWs were grown at similar conditions as the ones presented in chapter 5 and are with a mean diameter of about 35 nm and a mean length of around 770 nm comparable. The (In,Ga)N shells were grown according to the SDD procedure presented in Figure 6.2, where the total amount of deposited metal was kept constant at 0.3 ML (0.4 ML) on the side facet (top facet) per

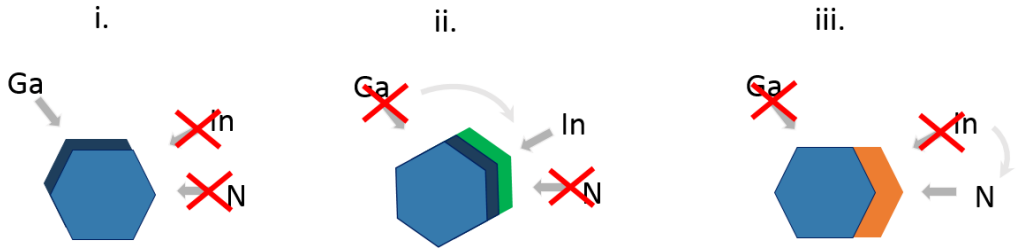


**Figure 6.2**: Sketch of the SDD process of a one-sided (In,Ga)N shell. (i) Ga deposition on the side of the NW. (ii) Rotation towards the In source and In deposition. (iii) Rotation towards the In source and N shutter is opened for (In,Ga)N growth. Note that all shutters are closed during the rotation phases.

deposition cycle. Only to achieve an In/Ga ratio of 5 as for sample 6.D, the total metal deposition had to be increased to 0.45 ML (0.6 ML) for the side facet (top facet) to maintain a reasonable calibration of Ga flux and shutter response times. All samples were exposed to a N flux of 16.2 nm/min for about 25 s seconds. By adjusting the number of SDD cycles for each sample, we aimed for the same shell thickness of around 10–15 nm. The bird's eye SE micrographs shown for the individual growth conditions give a representative impression of the NW morphology. The table shown in the inset depicts the amount of In and Ga that has been deposited during one deposition cycle as well as the total number of cycles carried out for the respective sample. Regarding the CL measurements, besides the broad emission band of the (In,Ga)N shell at higher wavelengths, most line scans also depict luminescence at around 357 nm (3.47 eV), which can be attributed to emission from donor-bound and free excitons in the GaN core NWs. Only sample 6.D does not show a GaN emission band.

In general, the growth map reveals that with decreasing growth temperature from 540 °C to 440 °C and increasing In/Ga ratio from 1 to 5, the NWs are more and more bent and the CL emission of the (In,Ga)N shell shifts from around 380 nm (3.26 eV) for sample 6.B1 to about 480 nm (2.58 eV) for sample 6.D. Only for the highest growth temperature and an In/Ga ratio of 1, as shown for sample 6.A, no (In,Ga)N shell emission can be detected. It should be noted that, similar to the radially symmetric shells presented in chapter 5, also one-sided (In,Ga)N shells show luminescence even without a passivation by an outer GaN shell.

The bending of the NWs visible in the SE micrographs results from the fact that (In,Ga)N has a larger lattice constant than GaN. Hence, once an (In,Ga)N shell is grown on the right side of the GaN NWs, as it is the case for the different samples shown in Figure 6.3, the NWs bend towards the left side (opposite side). The bending of the NWs thus is a clear indication for the existence of a one-sided (In,Ga)N shell. With increasing In content, the difference in lattice constant between the (In,Ga)N shell and the GaN core increases and leads to a more pronounced bending of the core-shell NWs. In sample 6.A, grown at the highest growth temperature and lowest In/Ga ratio, the NWs are straight which

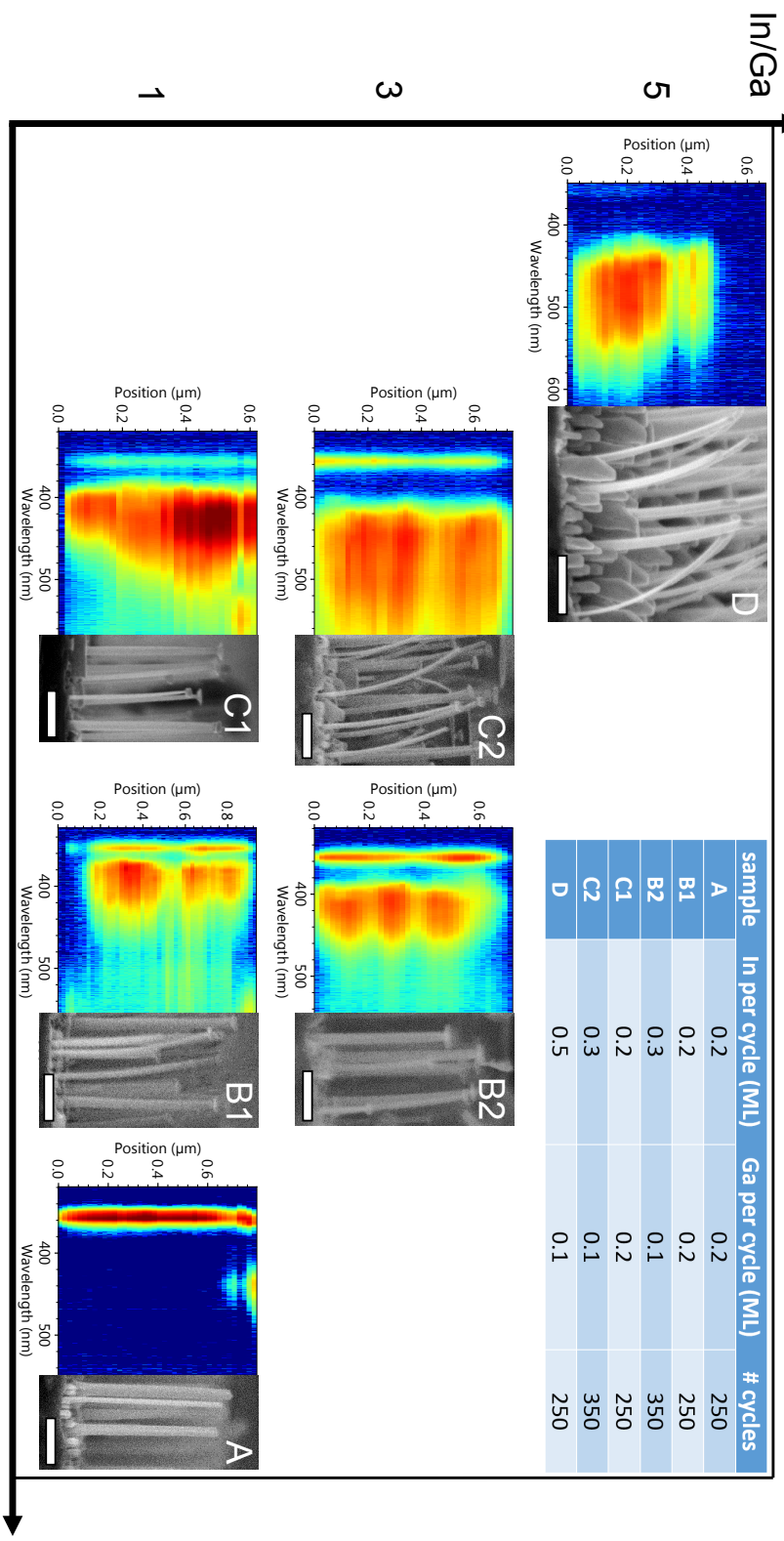


| sample | In per cycle (ML) | Ga per cycle (ML) | # cycles |
|---|---|---|---|
| A | 0.2 | 0.2 | 250 |
| B1 | 0.2 | 0.2 | 250 |
| B2 | 0.3 | 0.1 | 350 |
| C1 | 0.2 | 0.2 | 250 |
| C2 | 0.3 | 0.1 | 350 |
| D | 0.5 | 0.1 | 250 |

**Figure 6.3**: SE micrographs of GaN NWs with a one-sided (In,Ga)N shell and the respective CL line scans (measured at 10 K) of single NWs as a function of the growth temperature and the nominal In/Ga ratio. The inset (table) depicts the amount of deposited In and Ga per deposition cycle as well as the total number of cycles carried out for the respective sample. SE micrographs acquired by A.–K. Bluhm and CL measurements performed by Jonas Lähnemann.

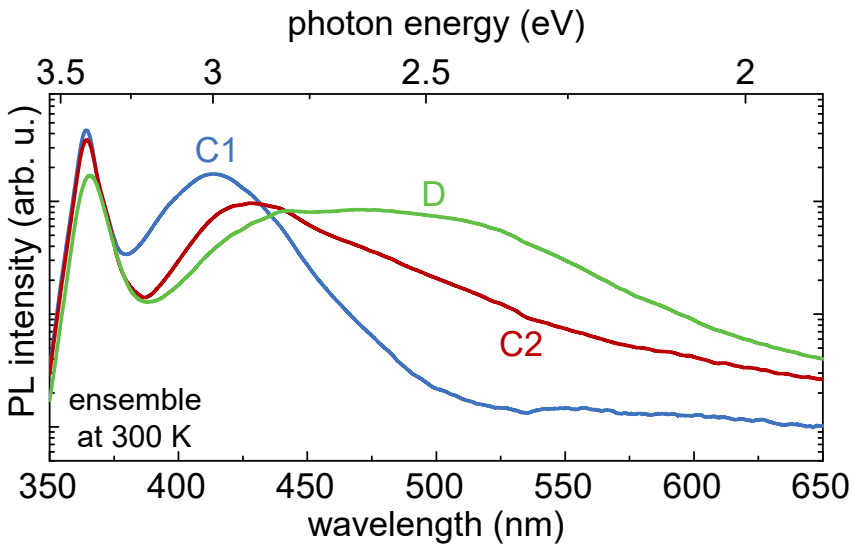


**Figure 6.4**: Ensemble PL of the samples 6.C1, 6.C2, and 6.D acquired at room temperature.

indicates no or only little In incorporation in the (In,Ga)N shell. The absence of a distinct emission band besides the GaN core luminescence in the CL line scan of sample 6.A supports this conclusion. The blue-shift of the shell luminescence band in the CL line scans with increasing growth temperature can be attributed to a decrease in In incorporation resulting from an increased desorption of In and a higher dissociation rate of InN inhibiting high InN mole fractions.[171,173,174,190] Only for sample 6.A the growth temperature was too high to form a stable (In,Ga)N shell. It should be noted that the bending of a NW results in an inhomogeneous strain distribution in the core-shell structure which may influence the bandstructure and hence the emission wavelength of the (In,Ga)N shell. Also other common effects like piezoelectricity or Fermi-level pinning at surface states may alter the electronic band structure.

Comparing the CL line scans of representative NWs from samples 6.B1 and 6.B2 as well as 6.C1 and 6.C2, the increasing In/Ga ratio seems to result in a higher incorporation of In corresponding to a red-shift of the shell luminescence. This red-shift is also visible analyzing the ensemble PL of the samples 6.C1 and 6.C2 shown in Figure 6.4. Moreover, an increase in the In/Ga ratio results in a broadening of the PL spectrum of sample 6.C2 towards higher wavelengths. The PL spectrum of sample 6.D grown at the lowest growth temperature of 440 °C and the highest In/Ga ratio of 5 shows a very broad emission band with rather similar emission intensities between 440 nm (2.82 eV) and 510 nm (2.43 eV) .

Using emission energies of planar (In,Ga)N layers as a reference,[35,196] the red-shift of the shell emission band from about 410 nm (3.02 eV) to 425 nm (2.92 eV) as for the PL of samples 6.C1 and 6.C2 roughly corresponds to a change in In content from 10% to 13%, respectively. Since the different strain state of the planar (In,Ga)N layers on the

one hand, and the one-sided (In,Ga)N shells on the other hand is not considered for this comparison, the assumed In contents are only a rough estimation. Nevertheless, the In contents are far away from the nominal In/Ga ratio during the growth. This can be explained by the fact that even for sample 6.D grown at the lowest growth temperature of 440 °C there was still a distinct In desorption visible in the QMS during the metal deposition phase. This desorption process as well as diffusion of In from the side walls towards the top facet of the NW and the substrate may explain the discrepancy between nominal In/Ga ration during the growth and the actual In content in the shell.

It should be noted that a red-shift of the shell emission with increasing In/Ga ratio has not been observed for radially symmetric (In,Ga)N shells in chapter 5. The higher In incorporation with increasing In/Ga ratio for one-sided shells may be explained by a reduced In diffusion away from the side facet during the SDD process due to the sequential and directional N exposure. A broadening of the PL spectrum going to higher In/Ga ratios, however, was also visible for the radially symmetric shells. In the case of one-sided (In,Ga)N shells this effect, on the one hand, may be attributed to stronger variations of the emission wavelength from NW to NW observed for different CL line scans, on the other hand, the one-sided (In,Ga)N shells in average also show a broader shell emission for higher In/Ga ratios. Moreover, also different strain states in the one-sided (In,Ga)N shell due to the bending of the NW may alter the bandstructure and lead to a broadening of the PL emission.[91]

Regarding the growth on the NW top facet, in the case of one-sided (In,Ga)N shells, the volume of the top segments is much smaller than the one of the massive segments found for radially symmetric shells in chapter 5. This especially applies for low growth temperatures and a high In/Ga ratio as it is visible for sample 6.D. The smaller top segment volume can be attributed to the smaller amount of materials that is deposited in the case of the one-sided shells, but also to a reduced diffusion of adatoms towards the NW top for the SDD approach as explained in section 6.1. To illustrate the latter aspect, we first evaluated the actual top segment volume obtained for the growth of the one-sided shells of 6.D from SE micrographs and scaled it by a factor 3 to estimate the top segment volume for the hypothetical case of a radially symmetric shell grown by the SDD approach at the same conditions. Subsequently, this roughly estimated volume resulting from a hypothetical radially symmetric shell growth by SDD could be compared to the volume of the top segments of sample 5.F grown by the approach presented in chapter 5 for the same shell thickness. The comparison revealed that the top segment volume of a radially symmetric shell grown by SDD would be lower by a factor of 3 – 5. Since the CL analysis of the different samples focused on the emission properties of the shells, for most samples the spectral region where the top segments might emit has not been covered. Only for samples 6.B1 and 6.C1, the onset of the top segment emission at around 560 nm (2.21 eV) is visible.

The volume of parasitic growth on the NW substrate visible for the different samples shown in Figure 6.3 seems to be rather similar for all conditions, except for sample 6.D.

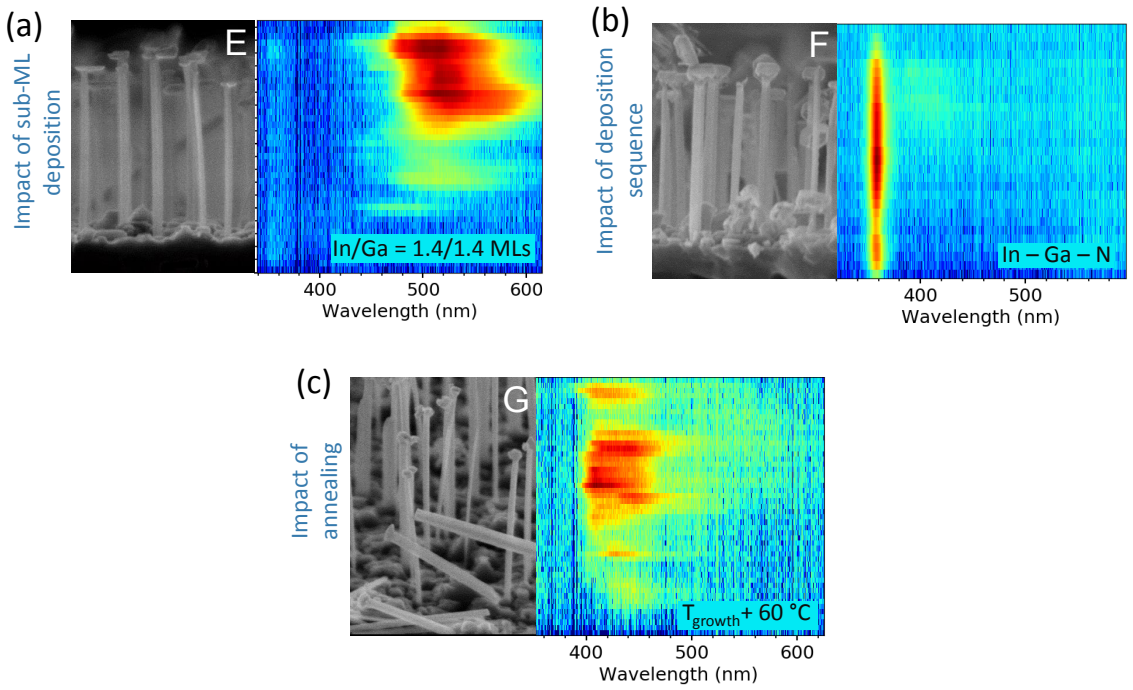


**Figure 6.5**: SE micrograph and CL line scan (measured at 10 K) of a representative NW for (a) sample 6.E, where a total amount of 2.8 MLs (In/Ga = 1.4/1.4 MLs) of metal per cycle has been deposited, (b) sample 6.F, where the deposition sequence of the different material has been changed from Ga first (Ga-In-N) to In first (In-Ga-N), and (c) sample 6.G, which was annealed at about 60 °C higher temperature for 23 min after the growth of the shell. Apart from the listed changes, all samples have been grown at otherwise similar growth conditions as for sample 6.C1. SE micrographs acquired by A.–K. Bluhm and CL measurements performed by Jonas Lähnemann.

Here, the higher amount of deposited metal in comparison to the other samples might have lead to larger parasitic NWs (note that the magnification of the SE micrograph of sample D is slightly higher than for the other images, which might intensify this impression).

The growth map in Figure 6.3 shows that the emission wavelength of one-sided (In,Ga)N shells can be shifted from the UV to the blue-green range in a rather controlled way by lowering the growth temperature and increasing the In/Ga ratio. In the following paragraphs, we investigate how the amount of deposited metal, the deposition sequence, and the annealing times after growth or between different growth steps influence the final In content of the shells.

For sample 6.E, shown in Figure 6.5 (a), a total amount of 2.8 MLs (In/Ga = 1.4/1.4 MLs) of metal per cycle has been deposited during the growth of the one-sided shells at otherwise similar growth conditions as for sample 6.C1. The NWs in the micrograph depict a clear shell on their right-hand side, however, the majority of the NWs does not show any

bending. Moreover, in contrast to sample 6.C1, the CL line scan of sample 6.E does not show an emission band around 430 nm. There is only a pronounced emission of the top segments visible at around 520 nm. The absence of the emission band at 430 nm might be attributed to a significantly reduced In incorporation caused by a strong In segregation effect at the growth front once the amount of deposited Ga exceeds one ML. Such segregation effects have been investigated theoretically for planar Ga- and N-polar GaN and (In,Ga)N surfaces and were attributed to strain release due to the sizable misfit between In and Ga atoms and the energetically more favorable bonding configuration of Ga-N bonds compared to In-N bonds.[174,215] Obviously, such segregation effects are less pronounced for a sub-ML deposition of Ga where the surface is not fully covered by Ga adatoms which thus allows a more stable local incorporation of In adatoms in the lattice. Interestingly, we also only achieved high In contents for the radially symmetric shells presented in chapter 5.2 once the Ga flux and the rotation speed was adjusted in a way that a sub-ML depositions of Ga on the side facets was achieved. Hence, sub-ML deposition of the metals seems to be important for the growth of high In-content shells by MBE.

Figure 6.5 (b) shows the micrograph and the CL line scan of a representative NW for sample 6.F. The growth conditions were the same as for sample 6.C1, however, the rotation sequence for the deposition of the different materials has been changed from Ga first (Ga-In-N) to In first (In-Ga-N). Also for this sample there is no emission at 430 nm visible in the CL line scan despite the formation of a one-sided shell. Hence, this suggests that the change of the rotation sequence prevented In incorporation in the shell. A remarkable detail regarding the growth process is that in the case of the In-Ga-N sequence, the QMS showed a dramatically increased In desorption from the sample once the Ga shutter was opened.

A possible scenario to explain the absence of an (In,Ga)N-related emission and the increased desorption of In during the deposition of Ga might be the following. For a better illustration, the clean *m*-plane surface on the NW side walls can be imagined as a hilly landscape which represents the surface potential for a certain adsorbate. Now, once a sub-ML amount of In is deposited first on the *m*-plane surface with closed In and Ga shutters (In-Ga-N sequence), the In adatoms can diffuse rather "freely", i. e. hop from dip to dip on the potential landscape, and/or eventually get trapped in a deeper minimum. With Ga being deposited in the next sequence step, the adsorped In atoms are likely to be superseded from the energetically favorable sites on the surface by Ga adatoms due to a more favorable bonding configuration. A favorable bonding configuration for Ga was also found by Duff *et al.*[174] in a first-principles study investigating surface energetics for the Ga-polar and N-polar (In,Ga)N surfaces. Such a dynamic exchange process between In and Ga increases the probability for In to desorb from the surface as it was observed by QMS, which in the end results in a very low or no In incorporation at all. In the rotation scenario where Ga is deposited first (Ga-In-N sequence), this exchange process is reduced, since most Ga adatoms have already found a more stable configuration once

In is deposited in the second deposition step. Thus, the probability for In adatoms to form a stable bond on the surface and to be incorporated in the lattice once N is supplied is much higher in this scenario.

Sample 6.G, shown in Figure 6.5 (c), was grown under the same conditions as sample 6.C1, but was annealed at about 60 °C higher temperature for 23 min after the growth. The ramp of the temperature increase and decrease (after annealing) was 0.2 °C/s and 0.5 °C/s, respectively. The idea of this sample was to test the temperature stability of the (In,Ga)N shell. This is a crucial factor, once more complicated structures are grown where subsequent shells need higher growth temperatures. An analysis of the NW diameter from SE micrographs showed that in average, the NWs are slightly thinner and the top segments are reduced significantly. Moreover, the CL line scan of an exemplary NW shows that the shell emission is not homogeneous along the length of the NW anymore which indicates an already advanced decomposition of the shell for the present annealing conditions. In general, the experiment shows that for more complex structures including more than one one-sided shell, the growth conditions and the sequence of the different shells have to be planed and optimized carefully. Nevertheless, annealing might be a possibility to remove the large top segments, which, due to a significantly higher In content, may dissociate much faster than the shells.

In order to further analyze the structure of one-sided (In,Ga)N shells, in Figure 6.6 we analyzed sample 6.D with TEM and EDX. Figure 6.6 (a) reveals a cross-sectional TE micrograph of several long bent NWs between small parasitic NWs. As already observed in SE micrographs, the bending may vary from NW to NW as well as the shape of the top segment. Figure 6.6 (b) shows a bright-field TE micrograph of the mid segment of a representative NW. The about 10 nm thick shell is clearly visible on only one side of the NW, whereas the opposite side does not show any shell growth. A TEM-EDX scan along the NW diameter (blue arrow) is displayed in Figure 6.6 (c). The intensity profile shows a clear increase of the In signal for the position of the shell and hence proves that the shell indeed contains a significant amount of In. Unfortunately, the EDX measurements did not allow to derive a meaningful value for the In content of the shells. Figure 6.6 (d) depicts a high-resolution TE micrograph of the interface between the (In,Ga)N shell and the GaN template NW. The analysis of high resolution images along the NW showed that there is no sign of plastic relaxation or dislocations in the shells. Obviously, most of the strain resulting from the different lattice constants of GaN and (In,Ga)N is released by the bending of the NW.

## 6.3. Multiple one-sided (In,Ga)N shells

To asses the feasibility of the growth of multiple one-sided shells with different properties on one and the same template structure, in this section, we investigate the growth of two one-sided (In,Ga)N shells with a different In content on opposite sites of the same

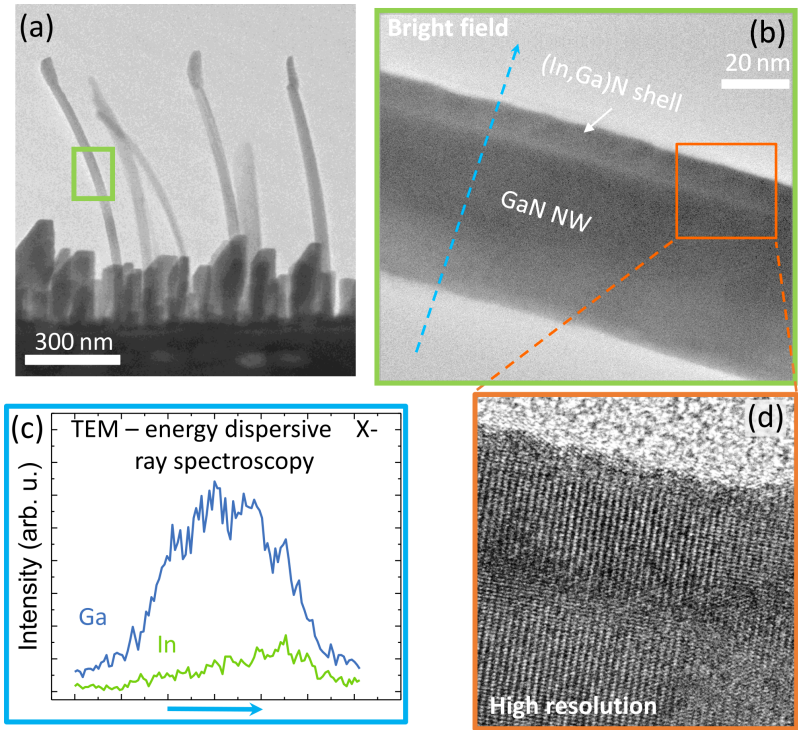


**Figure 6.6**: (a) Cross-sectional TE micrograph of sample 6.D. (b) Bright-field TE micrograph of the mid segment of a representative NW of sample 6.D which shows the about 10 nm thick (In,Ga)N shell on one side of the NW. (c) TEM-EDX scan along the NW diameter (blue arrow) of the NW presented in graph (b), which depicts the intensity profiles of the In and Ga signal. (d) Exemplary high-resolution TE micrograph of the interface between the (In,Ga)N shell and the GaN template NW. TEM and EDX measurments performed by Guanhui Gao.

template NWs on TiN. An outlook of possible applications of such a device architecture is given in section 6.5 at the end of this chapter.

For sample 6.H, we grew two different active regions on opposite sides of GaN template NWs using the conditions of sample 6.C1 and 6.D for the growth of shell one and shell two, respectively. We chose the conditions of these two samples to ideally get well separated emission peaks in the CL and PL spectra and thus prove the feasibility of the proposed device structure. The morphology of sample 6.H is shown in Figure 6.7 (a). First, the shell with the 6.C1 conditions has been deposited (on the right side of the NWs in the micrograph), i. e. the shell with the higher growth temperature (490 °C) and the lower In/Ga ratio (In/Ga=1). The only change with respect to the recipe of sample 6.C1 was that only 130 instead of 250 SDD cycles have been carried out. This resulted in a thinner shell and hence less bending of the NWs. Subsequently, the growth temperature has been lowered to 440 °C (with 0.2 °C/s) and the second shell with the conditions of sample 6.D (In/Ga=5) has been deposited (on the left side of the NWs in the micrograph). The idea of growing the second shell at much lower temperatures was to avoid the thermal dissociation of the first shell. The slight bending of the NWs towards the right-hand side

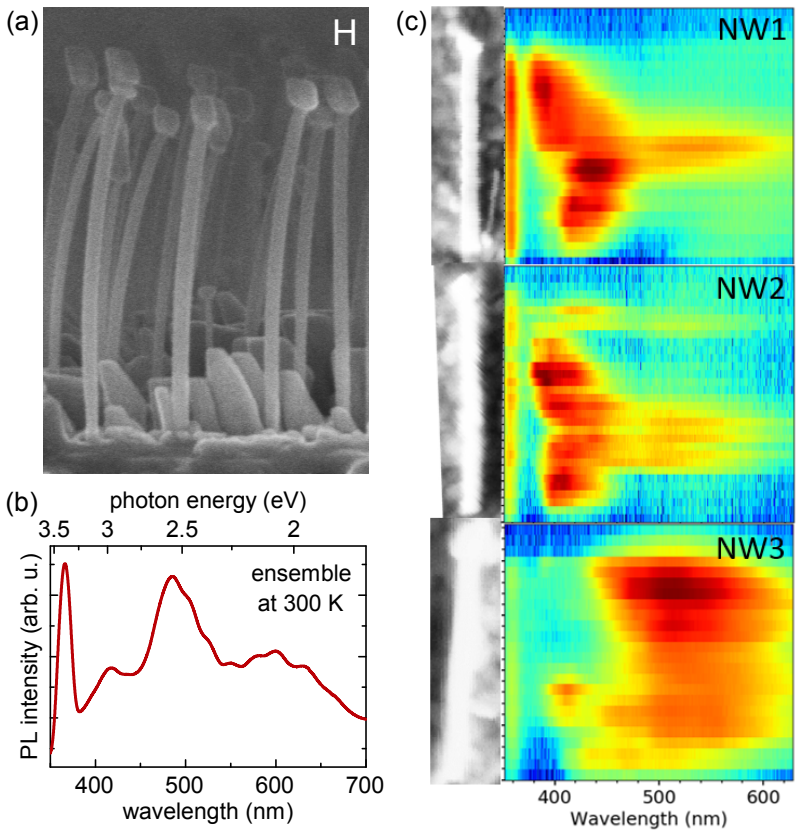


**Figure 6.7**: SE micrograph of sample 6.H where two different shells have been grown on opposite sides of the template NWs (high In content left side - low In content right side). The scale bar corresponds to 200 nm. (b) PL spectrum of the NW ensemble of sample 6.H acquired at room temperature. (c) SE micrographs and CL line scans of three exemplary NWs of sample 6.H measured at 10 K. SE micrograph acquired by A.–K. Bluhm and CL measurements performed by Jonas Lähnemann.

can be ascribed to the fact that the second shell contains a higher InN mole fraction and hence has a larger lattice constant than the GaN core and the first shell on the opposite side.

Figure 6.7 (b) depicts the PL spectrum of the NW ensemble of sample 6.H at room temperature. There are several distinct (In,Ga)N related emission bands visible for the two-sided shell structure at around (i) 418 nm (2.97 eV), (ii) 486 nm (2.55 eV), and (iii) 600 nm (2.07 eV), respectively. The latter band (iii) emitting in the red spectral range most likely originates from the the top segments of the NWs. Interestingly, the emission energies of band (i) and (ii) resemble the ones of sample 6.C1 and 6.D, respectively.

To clarify the origin of the luminescence bands (i) and (ii), it is instructive to analyze CL line scans of single NWs, as shown in Figure 6.7 (c). And indeed, all three exemplary NWs show distinct CL in the range of the emission bands (i) and (ii). However, whereas NW1 and NW2 depict clear shell luminescence along the whole NW length around band (i), they only show sparse CL around band (ii), which only occurs partially along the NW.

In contrast NW3 depicts rather homogeneous shell emission from NW top to bottom for band (ii) but shows almost no luminescence in the range of band (i).

At this point of the study, we can only speculate about the reason for the sparse luminescence of either one of the shells in the CL measurements. One possible explanation which cannot be ruled out yet, may be the NW orientation on the Au substrate during the line scans. If the NW is oriented in a way that one shell is facing the substrate, the topmost shell will be excited much more than the bottom one due to the rapidly decaying excitation profile of the electron beam. As a result, one shell emission would always dominate the spectrum. Even though the bending of the NWs might favor a certain positioning of the NWs on the substrate, it seems very unlikely that for all NWs (we investigated 23 NWs) only one of the two shells is excited. In general, the growth of a homogeneous shell may also be affected by the bending of the NW. The second shell is grown on the opposite, inner side of the bent GaN core where there is the highest compressive strain. Increased or inhomogeneous strain may prevent the growth of a homogeneous shell, especially for materials with very different lattice constants, as it is the case for GaN and (In,Ga)N. Apart from growth-related aspects, axial and radial strain gradients in the bent NW might have an effect on the diffusion of charge carriers. Investigating GaAs NWs with a one-sided (Al,In)As shell, Lewis *et al.*[91] found that due to the bending of the NWs, the photoexcited charge carriers drift towards the tensilely strained outer part of the bent NW. However, due to the marginal bending of the NWs after the growth of the first shell (less than for sample 6.C1) and the generally small diffusion length of charge carriers in (In,Ga)N at low temperatures (10 K for CL), neither strain-related effects on the growth of the second shell, nor strain-induced diffusion effects are convincing explanations for the sparse luminescence of either one of the shells in the CL line scans.

In general, due to the small dimension of the NWs under investigation, it was not possible to excite the two different shells individually to access their properties independently. Hence, in the case of structures with more than one active region, much larger template structures might allow a more detailed study of the individual shells. Moreover, growth-related problems regarding the homogeneity of the shell along the whole NW length caused by the bending of the NWs, can be avoided by core structures with a much larger diameter. In the following chapter, we present a new approach for the fabrication of larger template NWs and apply the SDD method to these new structures.

## 6.4. (In,Ga)N shells on NWs fabricated by selective area sublimation

In chapter 3, we demonstrate that the self-assembled bottom-up NWs on TiN, which were used as templates for the axial and core-shell structures presented in this and the previous chapters, are of high crystal quality and are mainly uncoaleseced. However, the self-assembly growth process does not allow the fabrication of highly ordered NW ensembles

with a certain number density, where each NW has the same length and diameter. Moreover, it is not possible to control the NW length and the NW diameter independently while avoiding coalescence. These are all aspects that are very important when it comes to the fabrication of NW-based devices.

In this section, we will use an SAS approach to fabricate GaN template NWs for core-shell heterostructures. Regarding the direct growth on the side facets, SAS has two main advantages for the preparation of template NWs over common approaches like dry etched top-down NWs or NWs grown by SAG (more information on the background of the different fabrication processes can be found in chapter 2.4). First, the SAS process can be performed right before the shell growth within the same growth run. Hence, in contrast to the dry etching process, ultra clean side facets can be expected. Secondly, by selecting a suitable cap material, unwanted top segments which grew on top of the cap can be electrically isolated from the shell area. In the best cases, the top segments can even be removed by a "lift-off process" after the growth or the cap material inhibits epitaxial growth on the top facet at all. This, for example, can not be achieved by SAG, where the top segments directly form on the NW top facet. Regarding the dimensions of the template NWs in this section, we aim for a target diameter and pitch of about 250 nm, and 1.3 µm, respectively. We chose these values because the large diameter facilitates a separate excitation of the different shells of one and the same NW by an electron beam. This allows the individual analysis of the luminescence characteristics of the various one-sided shells. Moreover, the pitch allows the growth of sufficiently long NWs (longer than 1µm) while, at the same time, making use of an enlarged active region along the NW and avoiding a mutual shadowing of the NWs during shell growth. Hence, such a NW template could serve as the basis for future core-shell devices.

To analyze the SAS process in more detail, the length of the NWs has been varied between 550 nm and 1.1 µm. The goal was to use these template NWs as a basis for the growth of multiple one-sided (In,Ga)N shells. The pitch of 1.3 µm was chosen to avoid mutual shadowing of the NWs during the shell growth up to the length of 1.7 µm (a length which enables large active regions on the side facets) and, in the end, to allow ultra high pixel densities beyond 10000 pixels-per-inch.

Due to an extended downtime of the sputter chamber in our institute, we were not able to follow the approach developed by Fernández-Garrido *et al.*, who established the use of SiN as a cap material. Hence, a new SAS process had to be developed, where we used an MBE-grown AlN layer as a mask layer for the prepatterning of the NW arrays. A sketch of the full prepatterning process is shown in Figure 6.8. At first (step A), a 15 nm thick AlN layer has been grown on a 2 inch planar GaN wafer by MBE. The growth took place under metal-rich growth conditions to preserve a smooth surface and a homogeneous thickness of the AlN film. In step B, a 100 nm thick $Si_xO_y$ layer was sputtered on top of the AlN to protect it during the dry etching steps (more details below). Subsequently, in step C the wafer was spin-coated with the positive resist AR-P 6200 (CSAR) and the

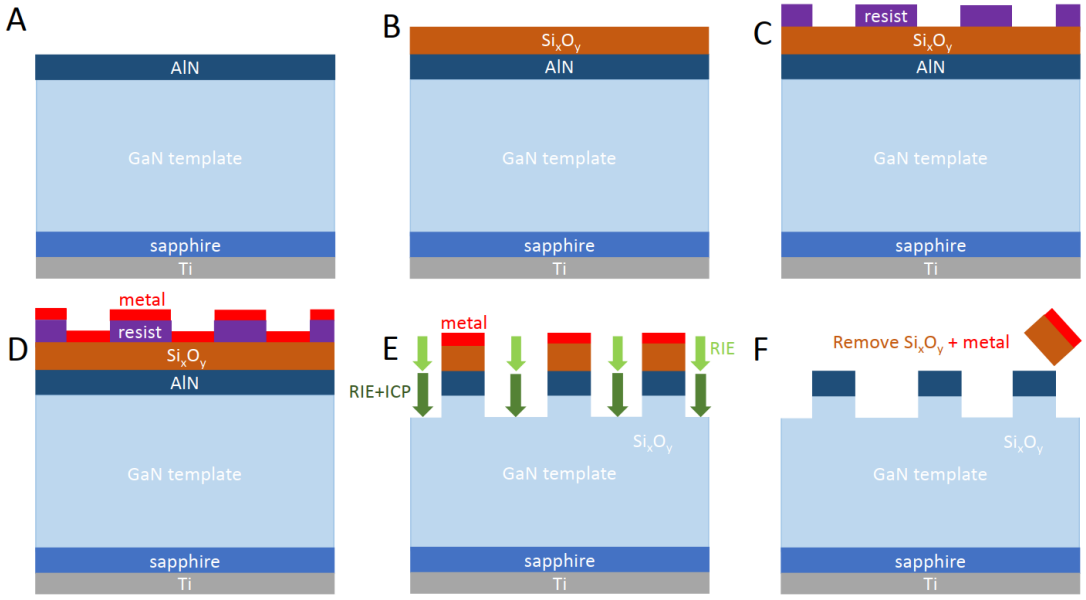


**Figure 6.8**: Sketch of the full prepatterning process for SAS. The single steps are described in detail in the main text.

pattern for the NWs was written by EBL. In step D, a 25 nm thick layer of Ni has been sputtered on top, before the redundant metal was removed by a lift-off process. In order to now structure the AlN layer (step E), the $Si_xO_y$ was etch down in between the pattern by RIE using $CHF_3$ as an an etchant. For the etching of the AlN layer, a mixture of $Cl_2$ and $BCl_3$ (1:4 flux ratio) has been used with an inductive coupled plasma. It should be noted that also a few nm of the GaN layer has been etched to ensure that all the AlN is removed from the pattern-free area. In the final step F, the $Si_xO_y$ and the metal were removed by HF (5%).

Figures 6.9 (a) and (b) depict SE micrographs of the prepatterned sample 6.K directly after step F. The AlN caps which, in the end, protect the GaN underneath from decomposition are clearly visible. It should be noted that the AlN caps were patterned with a hexagonal shape. The orientation of the sides of the hexagon were chosen to be aligned with the *m*-planes of the GaN template underneath. After the dry etching during the processing, however, the sides of the hexagon were align with the of *a*-planes. Hence, during the dry etching, a formation *a*-planes seems to be energetically favorable. Figures 6.9 (c) and (d) of sample 6.L show the morphology after sample 6.K has been thermally sublimated at 830 °C for 15 min. The NWs are about 550 nm long and have a diameter of about 240 nm. The NW sides do not consist of well defined facets, but rather show an alternating faceting on a small scale. It is likely that already the AlN caps exhibit unregular sides on the scale of a few nanometer which promote the formation of the observed sidewalls. The original (0001) GaN substrate in between the pattern forms three-dimensional islands with a six-fold symmetry during the sublimation. The facets of these islands were found to correspond to the semi-polar $\{1\bar{1}03\}$ planes.[44,45] Sample 6.M depicted in

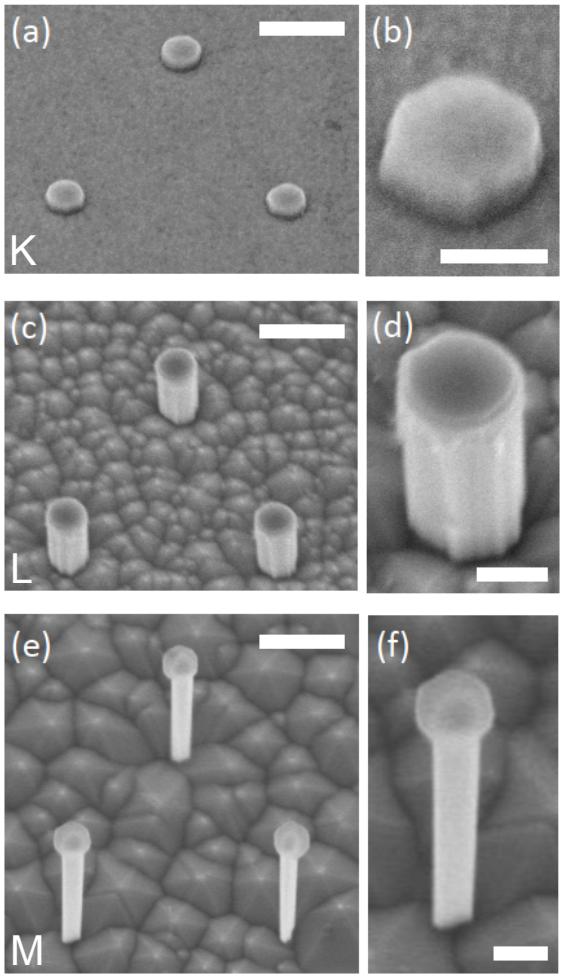


**Figure 6.9**: Bird's eye SE micrographs of (a/b) the prepatterned sample 6.K directly after step F, (c/d) sample 6.L which has been sublimated at 830 °C for 15 min, and (e/f) sample 6.M, which has been sublimated at 890 °C for 15 min. The scale bars of the micrographs (a/c/e) and (b/d/f) correspond to 500 nm and 200 nm, respectively.

Figures 6.9 (e) and (f), shows the NW morphology after sublimating sample 6.K at 890 °C for 15 min. The resulting length of the NWs is about 1.1 µm. The micrographs depict that a sublimation which targets such a NW length, leads to a thinning of the NW diameter underneath the AlN cap from originally 250 nm to about 130 nm (thickest part).

In a further study (not shown here), we found that the lateral decomposition is inherent to the sublimation process and mainly depends on the targeted NW length and hence the amount of sublimated material in between that pattern. In other words, for a certain NW length, the lateral decomposition cannot be suppressed by simply adjusting the sublimation temperature versus the duration of the sublimation. Moreover, it should be noted that there seems to be a discrepancy in the lateral decomposition rate for the decomposition of shorter and longer NWs. With about 10 nm reduction, the diameter of sample 6.L barely changed, whereas for the two times longer NWs of sample 6.M, the

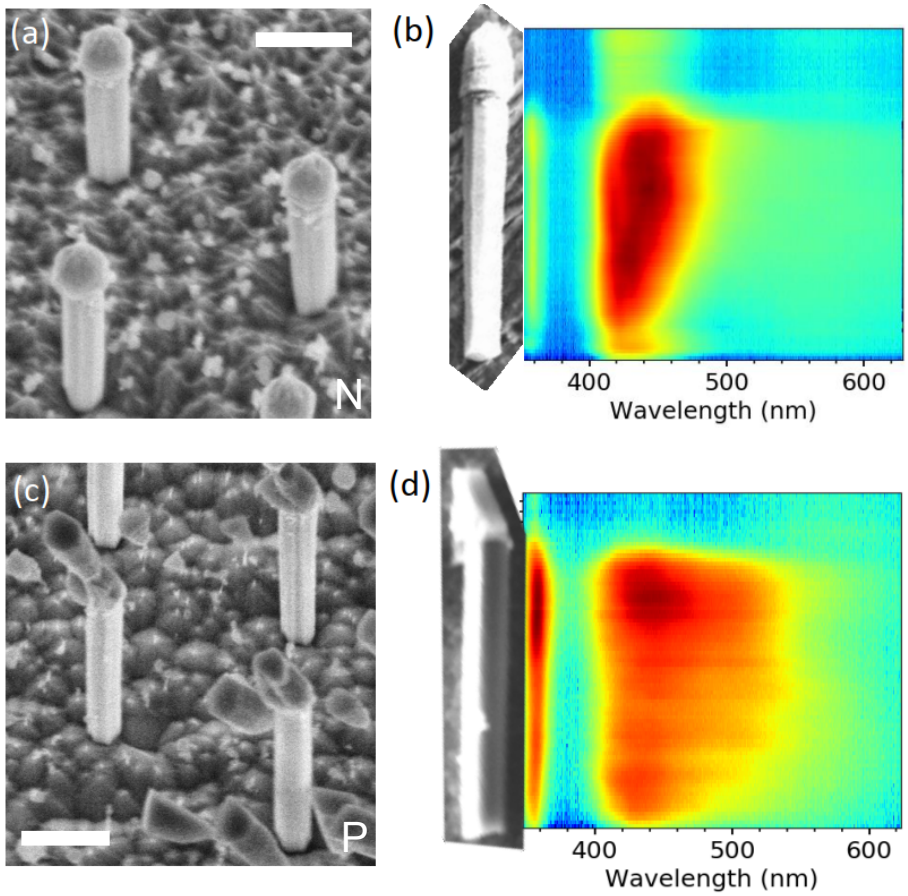


**Figure 6.10**: SE micrographs (a) and (c) as well as CL line scans (b) and (d) of a representative NW for the samples 6.N and 6.P, respectively. The Figures (b) and (d) also show an SE micrograph of the measured NW. Sample 6.N and 6.P consist of SAS template NWs (similar to sample 6.M) which were overgrown with a radially symmetric and a one-sided (In,Ga)N shell, respectively. The scale bar corresponds to 500 nm. CL measurements performed by Jonas Lähnemann.

diameter is only half the nominal one of 250 nm. At this point of the study, it is not clear why the reduction of the diameter with regard to the NW length is comparatively higher for long NWs.

Since the lateral sublimation seemed to be inherent to the present SAS approach, we did not further optimize this process, e.g., to obtain well defined facets, but used the present template to demonstrate that the SDD approach is transferable to larger and ordered NW structures.

Before applying the SDD process to the SAS template NWs, first, the feasibility of radially symmetric (In,Ga)N shells around the new SAS structures is demonstrated. The SE micrograph of Figure 6.10 (a) of sample 6.N shows the morphology of SAS template NWs (similar to sample 6.M) that were overgrown with a radially symmetric (In,Ga)N shell. The (In,Ga)N shell was grown for 30 min with an In/Ga ratio of 1 ($\Phi_{Ga}$=$\Phi_{In}$=0.1

ML/s) and a N flux of $\Phi_N$=16.2 nm/min at a growth temperature of about 520 °C. The rotation speed was 10 rpm. Apart from the growth temperature, the growth conditions are comparable to the ones of sample 5.F of chapter 5. In contrast to the facets observed for the GaN core directly after the SAS process, most of the NWs exhibit much smoother and partially well defined side facets after the shell growth. Moreover, pronounced top segments form on top of the AlN cap.

Figure 6.10 (b) shows the morphology and the respective CL line scan of a representative NW. The spectrum depicts a homogeneous and rather narrow shell emission along the whole dispersed NW at a wavelength of about 440 nm (2.82 eV). The first impression of the CL measurements reveals that the (In,Ga)N emission band of sample 6.N is much more homogeneous and narrow than the shell emission observed for one-sided or radially symmetric (In,Ga)N shells on the much smaller, self-assembled GaN NWs on TiN presented in this thesis. The blue shift of the emission band with regard to the radially symmetric shell of sample 5.F can be explained by a lower In incorporation due to the higher growth temperature. Besides the rather homogeneous emission along the whole NW, the comparatively high intensity with respect to the GaN core may be attributed to an effective charge carrier diffusion towards the (In,Ga)N shell. Furthermore, the narrow band width suggests a rather homogeneous In distribution within the whole shell. The spectral shape of the CL also suggests that the rough side facets of the core do not seem to have a negative influence on the optical properties of the shell.

Figure 6.10 (c) depicts the morphology of sample 6.P, where a one-sided (In,Ga)N shell was grown on the side facet of SAS template NWs. The SAS cores are similar to the ones shown for sample 6.M, but are with 1.5 µm about 35% longer due to a slightly higher sublimation temperature (unintentional). The (In,Ga)N shell was grown applying the SDD process with an In/Ga ratio of 3, where 0.3 ML and 0.1 ML of In and Ga, respectively, were deposited per cycle with an exposure to N ($\Phi_N$=16.2 nm/min) for 20 s. The growth temperature was about 490 °C and 365 cycles were carried out. Hence, the growth conditions are comparable to the ones of sample 6.C2. The shell was deposited on the left-hand side of the NWs with respect to the micrograph. The segments that formed on top of the AlN caps indicate the direction of the impinging fluxes.

The CL line scan shown in Figure 6.10 (d) depicts a clear and homogeneous shell emission from NW top to NW bottom peaking at around 440 nm. In general, the shell emission profile is quite similar to the one of the shells of sample 6.C2 on GaN NWs on TiN, which also exhibits a rather broad emission with a long tail towards higher wavelengths. In comparison the radially symmetric shell of sample 6.N shows a much narrower shell emission at the same wavelength. Whether this broadening effect of the shell emission is due to a more inhomogeneous In distribution for one-sided shells or whether this is a strain-related effect originating from the asymmetry of the shell is still unclear. Moreover, in contrast to sample 6.N, the GaN luminescence is much brighter for sample 6.P. This might be explained by the fact that for a one-sided shell, charge carriers generated in the GaN core are not captured as efficiently in the (In,Ga)N as in the case of a radially

symmetric shell, and hence increasingly recombine in the GaN core.

Interestingly, for both samples 6.N and 6.P there is no luminescence from the NW top segments, which was confirmed by additional CL measurements in the spectral range 600 – 700 nm (not shown here). The reason for the absence of the luminescence might be that (In,Ga)N grown on top of the AlN cap is very defective due to the large lattice mismatch between both materials. Regarding the substrate, there is hardly any parasitic growth in form of NWs, neither for samples 6.N nor for sample 6.P. The material mainly seems to grow on the semi-polar facets of the three-dimensional islands in between the template NWs. Additional PL measurements (not shown here) revealed that there is no significant luminescence originating from the substrate.

Sample 6.N and 6.P were the last samples that could be grown in the context of this thesis. Hence, no further studies on the growth of one-sided (In,Ga)N shells could be carried out to better understand the growth behavior and the optical characteristics of (In,Ga)N shells on SAS template NWs. Nevertheless, the experiments showed that there is still room to shift the emission wavelength towards higher wavelengths. Moreover, we were able to demonstrate that the SAS process can be transferred to the larger and ordered SAS structures. For many NW-based devices an ordered arrangement of the NWs is mandatory for a reliable processing and an efficient device performance, especially regarding NWs with complex structures of the active region. In the next section, in face of the possibilities the SDD growth approach offers for the controlled deposition of different materials, we propose a novel device design which allows the combination of multiple active regions with different functionalities on different lateral sides of one and the same nano- or microstructure.

## 6.5. Outlook: A novel design for a multi-functional nano-/microstructure-based device and the example of an RGB-LED

For the implementation of a multi-funtional NW-based device, active elements with different functionalities have to be combined on a common platform. In order to achieve a compact design and to avoid complex and costly processing steps, it would be of advantage if a single nano- or microstructure contained multiple active regions with different functionalities and if such a device could ideally be fabricated within a single growth run.

For conventional nano- or microstructure-based devices, the active regions are usually either grown *axially* (normal to the substrate) on top of the base structure or *radially* as a surrounding shell.[159,161,216] However, axially stacking various active regions or growing multiple consecutive radially symmetric shells with different functionalities only allows limited degrees of freedom for designing the functional nano- or microstructures. The design is, for instance, restricted to certain materials, structures or thicknesses which can be grown epitaxially on top of each other. Moreover, due to the axial or radial stacking

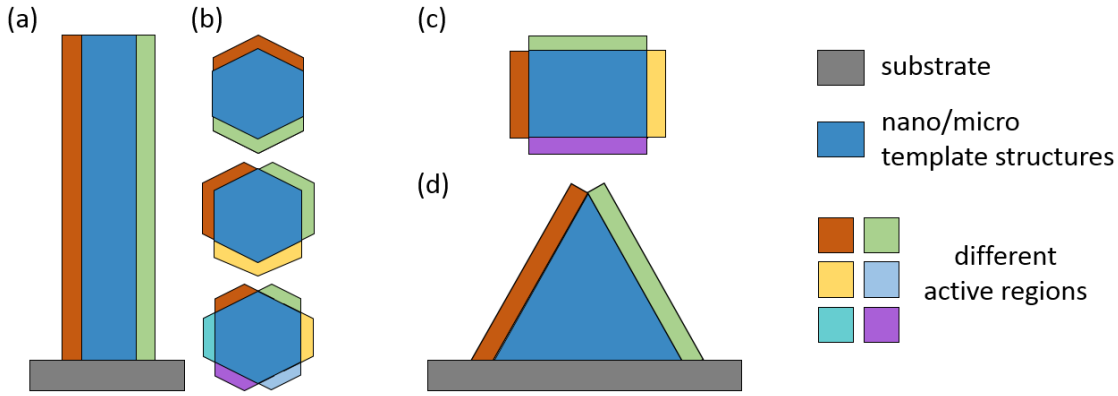


**Figure 6.11**: (a) Cross-sectional and (b) plan view sketches of different active regions on different lateral sides of a NW core structure, respectively. (c) Plan view and (d) cross-sectional sketch with a pyramid as the core structure.

of the active regions, electrically contacting and addressing the individual active regions independently is not practical.

### 6.5.1. Device design: Nano-/ Microstructure with multiple lateral active regions

The novel device architecture we propose takes one important step further. The idea is to combine different active regions with different mechanical, optical, optoelectronic, electronic, magnetic, and/or (photo-)electrochemical properties on different lateral sides of one and the same nano- or microstructure. Figure 6.11 (a) and (b) show cross section and plan view sketches of different active regions on different lateral sides of a NW core structure, respectively. The core structure may also consist of a fin or a pyramid as sketched in Figure 6.11 (c) and (d). This combination of two or more independent lateral active regions, where each active region provides a specific functionality like a tuneable conductivity or magnetization, emission/absorption at a certain wavelength, and/or substance adsorption, has several advantages over common designs. For instance, it allows to combine multiple functionalities in a very compact design where the single active regions can be addressed individually. Moreover, new device functionalities can be created by combining the properties of the various single active regions (e. g. combining different emission wavelengths to obtain a new emission color). Since the different active regions are spatially independent, they allow the use of different structures like quantum dots, quantum wells, or layers comprising materials with very different chemical composition (semiconductor, organic materials, etc.) and/or structure (crystal, amorphous, molecules, etc.). It should be noted that the final device may consist of one or multiple nano- or microstructures, where each structure comprises multiple different functionalities.

The fabrication of different active regions on different lateral sides of a base structure can be realized by using a directed growth process, where the different materials can be

deposited individually on selected sides. The advantage of such a directional deposition process, as we presented it with the SDD approach for III-N materials by MBE in section 6.1, is that different active regions can possibly be grown in the same growth run, where otherwise complex processing steps would be needed.

In the next section, we introduce a new architecture for a NW-based high-resolution multicolor display which is based on the proposed device design.

### 6.5.2. Application: Tuneable multi-colour 3D nano-/micro-LEDs for ultrahigh resolution displays

With the rising demand for wearable device technologies, e. g. virtual or augmented reality applications, there is a need for high-brightness and high-resolution multi-color compact projectors and small-size head-up displays. However, with decreasing pixel size and pitch, the brightness as well as the efficiency of conventional display technologies like LCDs and OLED-based displays drop significantly.[6,7] One promising technology are solid state-based micro-LEDs, offering high efficiencies, long lifetimes and considerably greater brightness than both, LCD and OLED displays. Hence, it is not surprising that big companies like Samsung, Google, and Apple recently made significant investments to push the development of III-N microstructure-based self-emissive multicolor displays.[9] However, there are still major drawbacks. Realizing pixels with size pitches of a few microns, where the different colors are individually controllable, either requires complex growth and processing steps to fabricate mircrostructure pixels emitting at different colors on a common substrate,[47,170,217,218] or the single mircrostructure pixels are fabricated separately and in a second step are integrated on a common chip by a complex and costly pick-and-place process, which cannot be scaled down to a few µm, not to speak about the nano scale.[5,210]

The device design we proposed in the previous section 6.5.1 is an innovative solution to overcome these drawbacks. It allows the realization of a tunable nano- or microstructure-based RGB-LED as sketched in Figure 6.12 (a) and (b). Here, the different functionalities are given by the ability to emit light at three different specific wavelengths which may be combined to tune the emission color. Hence, instead of fabricating the pixels separately, the pick-and-place process can be circumvented by directly growing the different color emitters on different sides of one and the same 3D structure, possibly within one growth run. In order to achieve emission in the blue, green, and red spectral range, the three active regions may consist, for instance, of (In, Ga)N-based quantum wells or dots with different In contents or dimensions resulting in different emission wavelengths. The different lateral active regions are embedded between n-type (p-type) core and p-type (n-type) cap layers and are contacted separately by a transparent contact layer to allow an individual control of the light emission. Similar to the active regions, also the fabrication of the individual contact layers can be achieved by using a directed deposition method, hence, avoiding complex processing steps for the contacting (for more details, see patent

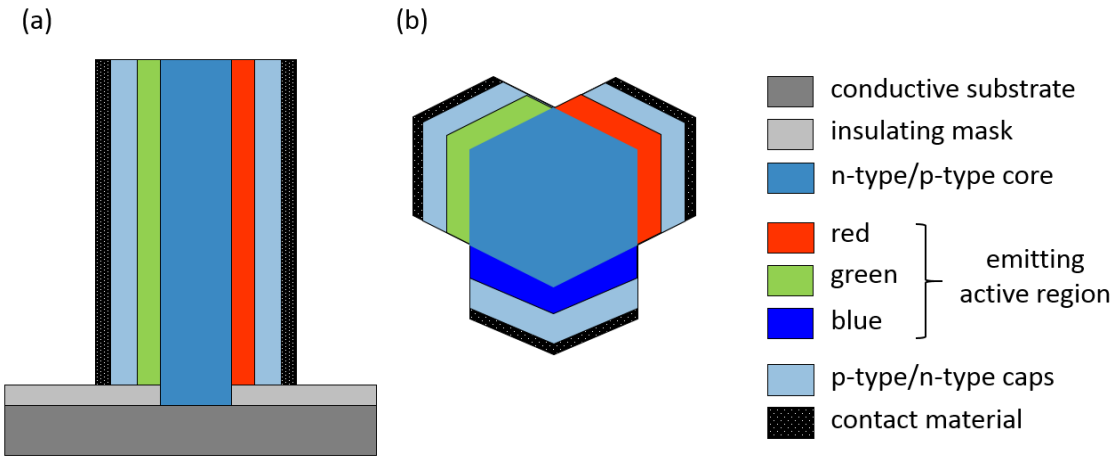


**Figure 6.12**: (a) Cross-sectional and (b) plan view sketch of a NW-based LED structure with three active regions that are located on different sides of the core NW and emit at different wavelengths.

description[212] and Figures therein).

In summary, the proposed LED design in combination with the SDD approach enables the fabrication of nanoscale RBG screen pixels for high resolution color displays, where one or several nano- or microstructures represent a pixel. This allows display resolutions which were not feasible before. Moreover, the SDD allows to fabricate vast parts of the RGB LED structure in one single growth run, a huge advantage in comparison to common approaches like pick-and-place or stacked layers.

## 6.6. Summary and Conclusions

In this chapter, we presented a sequential directional deposition method for GaN and (In,Ga)N. This growth approach allows the deposition of multiple active regions with different properties on different lateral sides of one and the same NW by depositing the different materials individually on the respective sides using MBE. In this context, we investigated one-sided (In,Ga)N shells and found that their In content can be increased by decreasing the growth temperature to very low values (down to 440 °C) and increasing the In/Ga ratio to values as high as 5. We also demonstrated that the growth of morphologically homogeneous (In,Ga)N shells on the *m*-plane facets, which emit in the green spectral range (sample 6.D and 6.H) is feasible by MBE. Furthermore, the deposition sequence of In and Ga (first Ga, then In) as well as sub-ML deposition of the metals (in particular Ga $\ll$ 1 ML/cycle) seem to be key aspects for the realization of shells with high In contents. As an explanation we suggested that with depositing a sub-ML amount of Ga first and only then adding In, it is more likely that In sticks to the surface and forms stable InN bonds.

On the way to more complex structures, we made a first growth attempt to realize a

structure with two different active regions on opposite sides of the template NWs (sample 6.H). Although we were not able to directly demonstrate two separate shells emitting homogeneously along the whole length of one and the same NW, both intended luminescence bands in the violet and green spectral range, respectively, are present in the ensemble PL and in the CL line scans of all three investigated NWs. Unfortunately, in the scope of this thesis, we were not able to carry out further systematic growth studies on two-sided shell structures to clarify why either one of the shells does not show a homogeneous luminescence along the NW. Due to the small dimension of the template NWs on TiN, it was not possible to excite the two different shells individually to access their properties independently. To overcome this impediment, we used a modified approach for the fabrication of larger template NWs by selective area sublimation. We were able to demonstrate that the SDD process can be transferred to the larger and ordered SAS structures by realizing a one-sided shell emitting in the violet spectral range (sample 6.P). Also for using the SAS structures as template NWs, we are convinced that it should be rather straight forward to increase the In content in the shells and move the shell emission towards the green or even the yellow/red spectral range by further exploring lower growth temperatures and higher In/Ga ratios. The two-sided core-shell structures based on SAS templates may give new insights on the morphology and the optical properties of different (In,Ga)N shells on one and the same core structure. The larger dimension of the SAS template NWs will allow to investigate the different shells independently and also facilitates the preparation procedure for a TEM analysis as well as the investigation of the shells by TEM-EDX. Unfortunately, due to time restrictions, we were not able to realize the latter investigations in the scope of this thesis.

As an outlook, we presented a novel device design which makes use of the sequential directional deposition approach and may allow, for example, the realization of single multi-color (sub)pixels for micro-LED displays. But the applicability of the new architecture is much wider. In general, it can be used to combine any possible functionality independently from each other on different sides of one and the same tiny structure. A vision for a future nanodevice could be that a certain substance is sensed on one active region, which changes the conductivity of the core structure. This change in conductivity in turn activates another active region which emits a signal that can be detected externally. And all this on the nano scale. Even though this example is still a vision, it illustrates the potential of the possibility to integrate multiple functionalities in a single nanodevice.

# 7. Conclusions

The research presented in this thesis addressed different open scientific questions regarding the growth of self-assembled GaN NWs and NW-based (In,Ga)N/GaN heterostructures by MBE.

In the initial part of our study, we demonstrated the growth of self-assembled, long, and thin GaN NWs on metallic TiN with a density as low as $10^9$ cm$^{-2}$. Even though, due to the influence of interfacial reactions, such morphologically well-developed NW ensembles can only be obtained for certain thicknesses of the Ti film and very specific nitridation and growth conditions, the growth of NW ensembles with such properties by self-assembly processes has been very challenging if not impossible on common substrates so far. In general, we found that the low NW density, which makes the self-assembled NW ensembles on TiN so special, can be explained by diffusion-induced repulsion of neighboring NWs. In contrast to commonly used substrates with high NW number densities like Si, on TiN the number density is limited not by shadowing that prevents the nucleation of further NWs, but by the fact that the comparatively large adatom diffusion length on TiN renders nucleation in the immediate vicinity of an already existing NW very unlikely and new nucleation centers only form at larger distances. Moreover, we learned that on TiN coalescence of NWs is largely absent for NW lengths up to about 1.5 µm. Investigating the nature of coalescence in NW ensembles on TiN, we showed that analogue to Si, also on TiN coalescence takes place mainly by bundling of NWs and that the low coalescence degree on TiN can be attributed to the low NW density. The ability to now grow self-assembled GaN NW ensembles that on the one hand consist of well-separated and uncoalesced NWs and on the other hand are grown on a metal substrate, does not only open new perspectives for the integration of III-V NWs on foreign platforms, but also offers new possibilities for the growth of more complex axial and radial heterostructures by MBE.

In our subsequent investigation, these GaN NWs on TiN were used as a basis for the fabrication of an axial six-fold (In,Ga)N/GaN QW structure. We found that in contrast to the growth on the typical irregular aggregates on other substrates, the growth on GaN NWs on TiN results in well-defined axial (In,Ga)N QWs which show a rectangular cross-section and extend along the c-plane. Contrary to our expectations, however, the well-defined morphology of the active region did not result in superior luminescence properties. In fact, even the parasitic heterostructures, like the ones which grew in between the

long GaN NWs, were found to be brighter than the QWs of the actual active region on top of the long NWs. As a likely explanation for the low luminous efficiency, we suspect nonradiative recombination channels resulting from a MBE-related high incorporation of point defects at the interfaces. In light of the fact that poor optical properties have also been observed for planar N-polar (In,Ga)N/GaN heterostructures, it is questionable whether such N-polar (In,Ga)N/GaN structures grown by MBE are generally suitable for optical applications.

Regarding the fundamental problem of the low luminous efficiency of axial QWs as well as the fact that the active region area of NW ensembles with axial structures is much smaller than for planar structures, in our further studies, we focused on the growth of nitride-based core-shell structures. Due to the small footprint on the substrate and the large active region area, the growth of core-shell heterostructures on the non-polar NW side facets seemed to be the more promising approach. To better understand the potential of MBE for the growth of core-shell structures in general, we first investigated some more fundamental growth issues. Here, we found that the aspect of the side facets of the NWs being only sequentially exposed to the different material beams has been widely ignored in literature so far, but plays an essential role to fully understand and control the shell growth on NWs by MBE. By modeling the shell growth of GaN shells on GaN NWs *with* and *without* substrate rotation, we found that with growth on the sidewalls only taking place when the respective side is exposed directly to the N beam, whereas on the top facet and substrate growth is always possible, gradients in chemical potential build between these three regions. As a result, strong Ga adatom diffusion processes take place on the NW which dominate in particular the growth on the side facets. The modeling allowed us to draw conclusions which designs of the source arrangement and which growth conditions are beneficial for the growth of homogeneous shells. For example, we found that homogeneous GaN shells can be achieved for small azimuthal angles between Ga and N or for very high rotation speeds. Moreover, our model has also enabled a comprehensive understanding of the adatom concentration on the NW at all times during the growth. We found that the growth on the side facets can be categorized in four different phases depending on the momentary rotation stage of a respective side facet:

(i) the wetting phase, where the side facet is only exposed to the metal beam(s)

(ii) the metal-rich growth phase, where the side facet is exposed to both the metal beam(s) and N beam and where the growth conditions are effectively metal-rich,

(iii) the N-rich growth phase, where the side facet is exposed to both the metal beam(s) and N beam and where the growth conditions are effectively N-rich,

(iv) and the dissociation phase, where the side facet is not exposed to any material beams and where material dissociation is the dominant process.

We showed that this fundamental understanding of the core-shell growth by MBE can also be transferred to the case of (In,Ga)N shells. In general, the absolute and relative length of these phases during one rotation period may not only affect the thickness homogeneity of the shell along the NW, but also the material composition in the case of ternary alloys like (In,Ga)N. The strength of our model is that it not only considers all relevant regions like the different NW facets and the substrate, but also the full MBE geometry by taking into account the different time-dependent orientations of the side facets with respect to the material sources. This comprehensiveness of the model provides a deep understanding of diffusion processes and the resulting adatom concentration, and could be applied to other 3D structures and material systems.

In general, MBE was often said to have high potential to achieve the still very challenging growth of high In content (In,Ga)N/GaN core-shell heterosturctures, which would be very interesting for optoelectronic applications like micro LED displays. This is an assertion that had never been proved so far. In our study on (In,Ga)N shell growth, we were able to demonstrate that (In,Ga)N shells emitting in the green spectral range are feasible by MBE and that the exploration of the growth on the *m*-plane side facet might even allow the realization of heterostructures emitting in the deep red. These results go far beyond what has been reported in literature so far, where neither green nor red emission from MBE-grown (In,Ga)N shells have been demonstrated. However, there are still open challenges regarding the application of the investigated radially symmetric core-shell structures as a basis for NW-based LEDs. The large top segments of the (In,Ga)N/GaN core-shell structures resulting from an increased material diffusion towards the NW top, for instance, may affect a homogeneous processing of the final LED device.

To tackle these challenges (among others), we developed a new growth process which allows the controlled deposition of shells on different sides of the NW that may reduce the formation of enlarged top segments. Here, we developed a sequential directional deposition method for GaN and (In,Ga)N, which in principle allows the combination of multiple active regions with different properties on different lateral sides of one and the same nano- or microstructure. To this end, the different materials, hence, In, Ga, and N are deposited individually on selected sides using MBE. One of the interesting findings in the scope of this investigation was that in order to achieve high In contents in the shells, the deposition sequence of In and Ga (first Ga, then In) as well as sub-ML deposition of the metals seem to be important requirements. With generally very small fluxes, high In/Ga ratios and extremely low growth temperatures, the growth conditions for high In content shells are rather extraordinary and close to the limit of what can be achieved by MBE. These circumstances might be one reason why, apart from the results presented in this thesis, there are no reports in literature that demonstrate MBE-grown shells emitting in the blue-green/green spectral range.

In the scope of this study, we carried out further investigations to demonstrate that (i) multiple shells on different lateral sides of one and the same NW are feasible and that (ii)

this can not only be achieved for the thin self-assembled NWs on TiN, but also for much larger and highly order template NWs:

(i) Although we were not able to directly demonstrate two separate shells emitting homogeneously along the whole length of one and the same NW, both intended luminescence bands in the violet and green spectral range, respectively, are present. Further studies on two-sided shell structures are needed to clarify why either one of the shells does not show a homogeneous luminescence along the NW.

(ii) We were able to demonstrate that the SDD process can be transferred to the larger and ordered SAS structures by realizing a one-sided shell emitting in the violet spectral range. We are convinced that it should be rather straight forward to increase the In content in the shells and move the shell emission towards the green or even the yellow/red spectral range by further exploring lower growth temperatures and higher In/Ga ratios.

In general, the investigation of one-sided (In,Ga)N/GaN core-shell heterostructures and the development of the SDD process is the first step towards the realization of single multi-color (sub)pixels for micro-LED displays. Instead of fabricating the pixels separately, with the SDD method we can circumvent the pick-and-place process by directly placing the different color emitters on different sides of one and the same 3D structure. However, the potential of the novel device design presented here goes far beyond the LED display application. In principle, it allows to combine any possible functionality independently from each other on different sides of one and the same tiny structure. Even though the practicability of possible applications has to be demonstrated first, we are convinced that with our novel design, we opened a new dimension for multifunctional nanodevices.

# A. Technical details of the shell growth model

The general representation of the one-dimensional linear parabolic diffusion equation used for the description of the adatom concentration $n$ in the different regions I – V is given by:

$$\frac{\partial n}{\partial t} = D(x,t)\frac{\partial^2 n}{\partial x^2} + p(x,t)\frac{n}{\tau} + q(x,t)\chi J_{\mathrm{Ga}} \tag{A.1}$$

where in the model presented in chapter 5.1, the diffusion coefficient $D$ is a constant for each region. The prefactors $p$ and $q$ are 1 for regions I, III, and V and vary with time depending on the rotation position for regions II and IV as describend in Eq. 5.5 and 5.6 of chapter 5.1.

In order to calculate the adatom concentration $n$ in space and time, we apply the finite difference method (FDM) with the explicit forward scheme, where each of the regions I – V is represented by a certain time-space ($k \times l$) mesh as sketched in Fig. A.1. To this end, we transform Eq. A.1 to its differential representation:

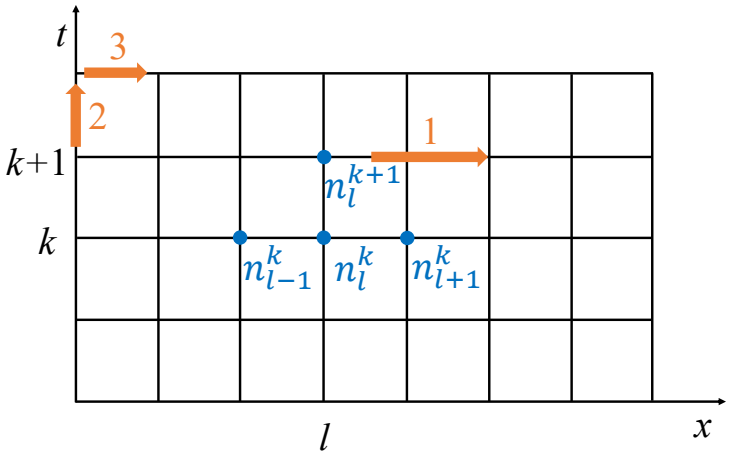


**Figure A.1**: The sketch illustrates the time-space ($k \times l$) mesh of the adatom concentration $n$. To obtain the adatom concentration $n$ in space and time applying the finite difference method (FDM) with the explicit forward scheme (1) $n_l^{k+1}$ is calculated for all $l$, (2) we move to the next $k$-value, and (3) the procedure of step (1) is repeated until $k = k_{\mathrm{max}}$. The blue dots indicate the adatom concentration at certain points in space and time according to the explicit forward scheme.

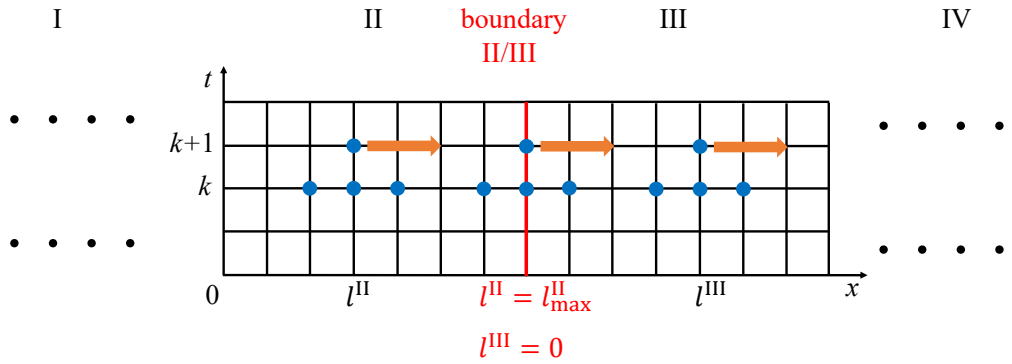


**Figure A.2**: The sketch shows the time-space ($k \times l$) mesh of the adatom concentration $n$ of region II and III with the boundary II/III between the two regions. Similar to Fig. A.1, the blue dots represent the adatom concentration at certain points in space and time according to the explicit forward scheme. The orange arrows indicate how the $n$ is calculated for a certain time step.

$$\begin{aligned} n_l^{k+1} = &\frac{D_l^k \Delta t}{(\Delta x)^2}(n_{l+1}^k - 2n_l^k + n_{l-1}^k) \\ &+ p_l^k \frac{n}{\tau}\Delta t + q_l^k \chi J_{\mathrm{Ga}} \Delta t + n_l^k \end{aligned} \tag{A.2}$$

In general, to calculate $n_l^{k+1}$ for a certain spatial point $l$ and a time $k+1$, the values of the adatom concentration at the points $l-1$, $l$, and $l+1$ at the time $k$ have to be known. In the beginning these values are obtained from the initial conditions for $k = 0$ and the two boundary conditions for $l = 0$ and $l = l_{\mathrm{max}}$. Once $n_l^{k+1}$ is calculated for all $l$, the same procedure can be repeated until $k = k_{\mathrm{max}}$. The procedure is illustrated in Fig. A.1.

Since in the model we presented in chapter 5.1, we have five different regions described by different diffusion equations, first all values of $l$ for all regions I – V are calculated for the time $k+1$ with the boundary and initial conditions given in Eq. 5.2 and 5.3 of chapter 5.1, respectively. The procedure is illustrated in Fig. A.2 and shows how the adatom concentration at the boundary between region II and III is calculated. The boundary conditions for regions II/III, namely

$$\begin{aligned} n_{\mathrm{II}}(l_{\mathrm{eff}}(t), t) &= n_{\mathrm{III}}(0, t) \\ \frac{\partial n_{\mathrm{II}}}{\partial x_{\mathrm{II}}}|_{x_{\mathrm{II}} = l_{\mathrm{eff}}(t)} &= \frac{\partial n_{\mathrm{III}}}{\partial x_{\mathrm{III}}}|_{x_{\mathrm{III}}=0}, \end{aligned} \tag{A.3}$$

can be expressed in the differential representation as follows:

$$\begin{aligned} n_{l^{\mathrm{II}}_{\mathrm{max}}}^{k+1} &= n_{l^{\mathrm{III}}=0}^{k+1}, \\ \frac{D_{\mathrm{II}}}{\Delta x_{\mathrm{II}}}(n_{l^{\mathrm{II}}_{\mathrm{max}}}^{k+1} - n_{l^{\mathrm{II}}_{\mathrm{max}}-1}^{k+1}) &= \frac{D_{\mathrm{III}}}{\Delta x_{\mathrm{III}}}(n_{l^{\mathrm{III}}=1}^{k+1} - n_{l^{\mathrm{III}}=0}^{k+1}). \end{aligned} \tag{A.4}$$

Solving the equation system Eq. A.4 delivers the unknown values for the region boundaries $n^{k+1}_{l^{\mathrm{II}}_{\mathrm{max}}}$ and $n^{k+1}_{l^{\mathrm{III}}=0}$. The values of the adatom concentration at the boundaries of regions III/IV and IV/V are calculated the same way.

It should be noted that the time step $\Delta t$ is the same for all regions and was chosen to be 9 ns. The space steps $\Delta x$ were adjusted for each region to obtain a good spatial resolution while keeping the calculation cost small. The values are $\Delta x_{\mathrm{I,II,IV,V}} = 30\,\mathrm{nm}$ and $\Delta x_{\mathrm{III}} = 10\,\mathrm{nm}$. In general, the values for $\Delta t$ and $\Delta x$ were chosen so that the prefactor $D^k_l \Delta t / \Delta x^2$ of Eq. A.1 keep small enough to maintain a continuous description.

# B. Modeling procedure and parameter analysis of the shell growth model

Due to the complexity of the model and the resulting computational costs, we did not implement an automated fitting of the shell profile as well as the top facet and the parasitic layer thickness. Since we were not interested in precise values of the modeling parameters, the fits were optimized by changing the parameters manually.

In chapter 5.1, we already describe the modeling procedure for the shell profile, where also the growth on the top facet and the substrate is taken into account. In this section, we discuss in detail the behavior and the sensitivity of the modeled shell thickness regarding a change of the different modeling parameters.

## Behavior of the shell profile regarding a change of $D$ and $\tau$

The reference shell thickness (orange curve in all figures below) is the modeled shell profile of sample 5.E presented in Figure 5.5 of chapter 5.1.2.

### $D_{\mathbf{side}}$ and $\tau_{\mathbf{side}}$

Figure SB.1 shows how the shell profile fit behaves when changing $D_{\text{side}}$ and $\tau_{\text{side}}$.

If $D_{\text{side}}$ is lowered, less Ga is able to diffuse to the NW center (diffusion length is smaller, visible in steepness of the profile) which results in less growth in the center area. The increased thickness at the top of the NW can be explained by the fact that the excess Ga adatoms from the top facet flowing onto the N exposed side facet mainly contribute to the growth near the top, because they are not able to diffuse to the NW center due to the small $D_{\text{side}}$. This effect is not present at the bottom boundary to the substrate, since this area, in contrast to the top facet, is not influenced by excess Ga adatoms diffusing from the Ga exposed side facet.

If $D_{\text{side}}$ is increased, in general, the shell is thicker because more Ga adatoms diffuse onto the side facet and towards the NW center (diffusion length is higher) where the adatoms contribute to the shell growth. In addition, a higher diffusivity of Ga along the NW side prevents a strong inhomogeneity of the diameter widening along the NW length.

A lower value of $\tau_{side}$ leads to a smaller diffusion length (visible in steepness of the profile) and a higher incorporation rate (growth rate). Hence, the shell is thicker towards the top and bottom boundaries and thinner in the center because fewer adatoms are able to diffuse there.

A higher value of $\tau_{side}$ leads to a higher diffusion length (visible in flatness of the profile) and a lower incorporation rate (growth rate). Hence, the shell is thinner towards the top and bottom boundaries and a bit thicker in the center because more adatoms are able to diffuse there.

In general, a change in $D_{side}$ leads to an asymmetric change in shell thickness along the NW. Changing $\tau_{side}$ mainly influences the general shell thickness.

It should be noted that keeping the diffusion length constant as shown in Figure B.2 and changing simultaneously $D_{side}$ and $\tau_{side}$, respectively, does not result in the same shell thickness along the NW but in shell thicknesses which increase with increasing $\tau_{side}$.

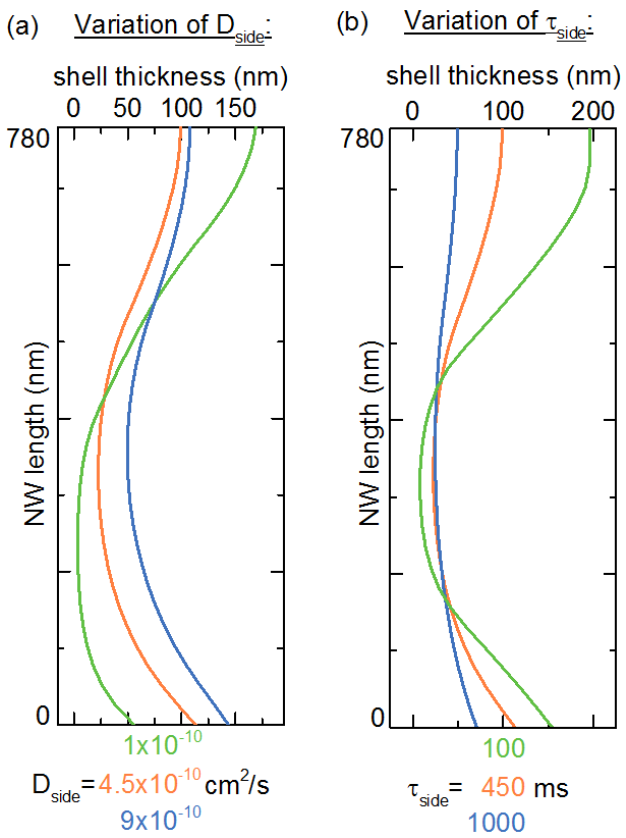


**Figure B.1**: The graphs (a) and (b) show the sensitivity of the shell thickness along the NW with increasing and decreasing $D_{side}$ and $\tau_{side}$. In both graphs, the orange curve is the modeled shell profile of sample 5.E and serves as a reference.

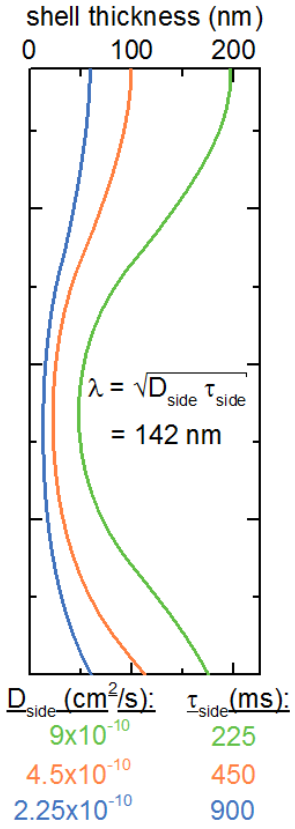


**Figure B.2**: The graph shows how the shell thickness along the NW changes for different values of $D_{side}$ and $\tau_{side}$ while keeping the diffusion length $\lambda$ constant. The orange curve is the modeled shell profile of sample 5.E and serves as a reference.

### $D_{sub}$ and $\tau_{sub}$

Figure B.3 shows how the shell profile fit behaves when changing $D_{sub}$ and $\tau_{sub}$.

A lower $D_{sub}$ leads to a higher shell thickness at the bottom boundary towards the substrate. The smaller $D_{sub}$, the smaller is the diffusion length on the substrate resulting in a steeper decrease of the adatom concentration close to the NW side facet region (see Figure 5.5 region V of chapter 5.1.2) and hence in a higher value of the adatom concentration at the boundary.

A higher $D_{sub}$ leads to a lower shell thickness at the bottom boundary towards the substrate. The higher $D_{sub}$, the higher is the diffusion length on the substrate resulting in a longer and flatter decrease of the adatom concentration close to the NW side facet region (see Figure 5.5 region V of chapter 5.1.2) and hence in a lower value of the adatom concentration at the boundary.

A lower $\tau_{sub}$ leads to a lower adatom concentration on the substrate due to the increased incorporation rate. The value of the adatom concentration at the boundary is therefore reduced and fewer adatoms are free to diffuse from the substrate onto the side facet leading to a lower shell thickness at the bottom part.

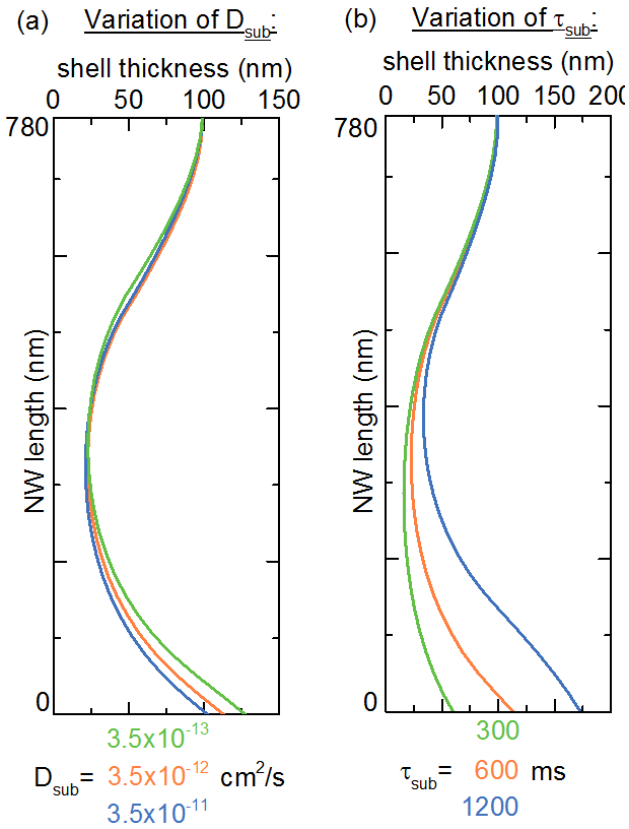


**Figure B.3**: The graphs (a) and (b) show the sensitivity of the shell thickness along the NW with increasing and decreasing $D_{sub}$ and $\tau_{sub}$. In both graphs, the orange curve is the modeled shell profile of sample 5.E and serves as a reference.

A higher $\tau_{sub}$ leads to a higher adatom concentration on the substrate due to a reduced incorporation. The value of the adatom concentration at the boundary is higher and more adatoms are free to diffuse from the substrate onto the side facet leading to an increased shell thickness at the bottom part.

In general, by changing $D_{sub}$ and $\tau_{sub}$ of the substrate the thickness and shape of the bottom part of the shell on the side facet can be modeled.

### $D_{top}$ and $\tau_{top}$

Figure B.4 shows how the shell profile fit behaves when changing $D_{top}$ and $\tau_{top}$.

The effect of the top facet diffusion coefficient $D_{top}$ on shell growth on the side facet is different and more complex than the one found for the substrate. This is mainly due to the fact that for higher values of $D_{top}$ the diffusion length reaches the dimension of the top facet leading to a stronger influence of the high Ga adatom concentrations on the Ga exposed side facet. In particular, this is the case during the early stage of the shell growth where the diameter of the top facet is with about 35 nm (diameter of template

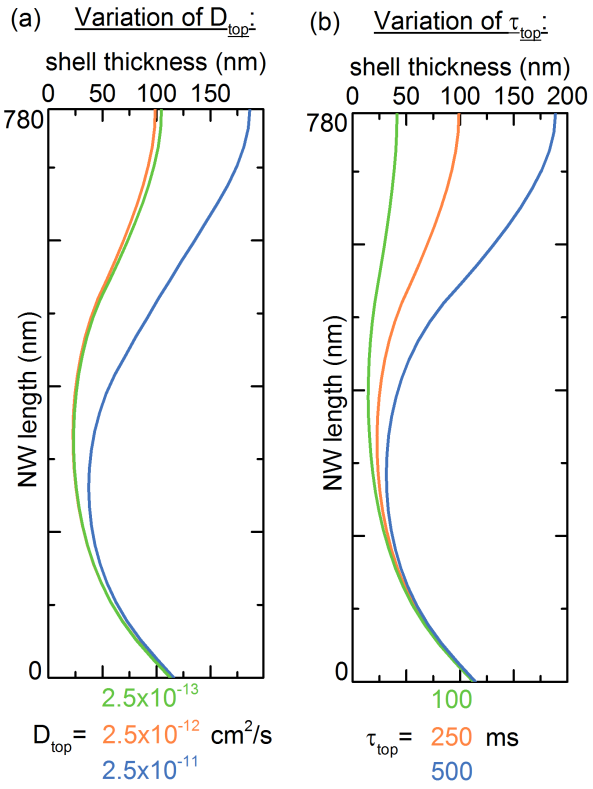


**Figure B.4**: The graphs (a) and (b) show the sensitivity of the shell thickness along the NW with increasing and decreasing $D_{\text{top}}$ and $\tau_{\text{top}}$. In both graphs, the orange curve is the modeled shell profile of sample 5.E and serves as a reference

NW) still very small. For rather low values of $D_{\text{top}}$ and hence diffusion lengths much smaller than the dimensions of the top facet, the influence of the diffusion coefficient on the final shell thickness is very small. In this regime, the shell thickness mainly depends on the equilibrium adatom concentration on the top facet which is determined by the Ga adatom lifetimes on the top facet and sets the boundary conditions to the side facet.

A smaller $\tau_{\text{top}}$ leads to a lower adatom concentration on the top facet due to the increased incorporation rate. The value of the adatom concentration at the boundary is therefore reduced and fewer adatoms are free to diffuse from the top facet onto the side facet leading to a lower shell thickness at the top part.

A higher $\tau_{\text{top}}$ leads to a higher adatom concentration on the top facet due to a reduced incorporation. The value of the adatom concentration at the boundary is higher and more adatoms are free to diffuse from the top facet onto the side facet leading to an increased shell thickness at the top part.

## Sensitivity of the shell profile regarding a change of $D$ and $\tau$

In order to get an idea about the sensitivity of the fits regarding a change of the different modeling parameters, we varied the parameters $D_{\text{top}}$, $\tau_{\text{top}}$, $D_{\text{side}}$, $\tau_{\text{side}}$, $D_{\text{sub}}$, and $\tau_{\text{sub}}$ around their optimized values found for sample 5.E. To this end, we determined the "degree of misfit" $\Xi$[219,220] resulting from the respective change of a certain parameter as follows

$$\Xi = \frac{1}{\nu} \sum_{i=1}^{\nu} \left| \log \frac{GM_{\text{side, var}}(x_{\text{i}})}{GM_{\text{side, opt}}(x_{\text{i}})} \right| \tag{B.1}$$

where $GM_{\text{side, opt}}$ is the reference fit (optimized fit of the shell profile of sample 5.E) and $GM_{\text{side, var}}$ is the shell profile fit resulting from a respective change in a fitting parameter at the NW length $x_{\text{i}}$. Furthermore, $\nu$ is the number of considered data points of the shell profile fits (here $\nu = 32$). The logarithmic function in Eq. B.1 is zero when both contributions are equal. Hence, a perfect fit would result in a $\Xi$ of zero. It also assigns an increasing weight to points which are far away from the reference values. The absolute value of the quotient is taken to prevent that an error obtained by values higher than the data cancels out the errors from values lower than the measured ones. In the end, the sum over all errors of each point gives a good measure for the deviation of two fits and hence their sensitivity regarding a change in parameter values. To make the "degree of misfit" more vivid, it can also be expressed in the form of a mean deviation $\Delta$ of the varied fit $GM_{\text{side, var}}$ with respect to the reference $GM_{\text{side, opt}}$. The deviation $\Delta$ can be derived from the following equation:

$$|\log(1 \pm \Delta)| = \Xi \tag{B.2}$$

Table I shows the respective deviations $\Delta$ from the reference fit $GM_{\text{side, opt}}$ for variations of the different modeling parameters. The parameter variations are given in percent around the respective optimized value, i. e. regarding $\tau_{\text{top}}$, for instance, changing the value 0.25 s by $\pm$10% ($\pm$0.025 s) results in a deviation $\Delta$ of the resulting shell profile of about $\pm$5% with respect to the profile obtained for the reference value.

In summary, the sensitivity of all the incorporation times $\tau_{\text{top}}$, $\tau_{\text{side}}$, and $\tau_{\text{sub}}$ as well as of the diffusion coefficient $D_{\text{side}}$ is rather good. A variation of these parameters by about $\pm$10% results in a $\Delta$ of the modeled shell profile of about $\pm$5%. The dependence of the fits on the parameters $D_{\text{top}}$ and $D_{\text{sub}}$ is comparatively less sensitive. These parameters have to be varied by at least $\pm$85% to obtain a similar $\Delta$ of the modeled shell profile of about $\pm$5%. However, it should be noted that changes of $D_{\text{top}}$ and $D_{\text{sub}}$ only result in local changes of the shell profile, namely at the top and the bottom part, respectively, whereas the deviation $\Delta$ takes into account the whole shell profile. Hence, the local deviation of the fit (at the top or bottom part) is much higher resulting in a higher local sensitivity.

| parameter | optimized value | parameter variation in % | Δ in % |
|---|---|---|---|
| $D_{top}$ | $2.5\times10^{-12}\,cm^2/s$ | ±85 | ±4 |
| $\tau_{top}$ | 0.25 s | ±10 | ±5 |
| $D_{side}$ | $4.5\times10^{-10}\,cm^2/s$ | ±10 | ±7 |
| $\tau_{side}$ | 0.45 s | ±10 | ±3 |
| $D_{sub}$ | $3.5\times10^{-12}\,cm^2/s$ | ±85 | ±5 |
| $\tau_{sub}$ | 0.6 s | ±10 | ±4.5 |

**Table B.1**: Deviations Δ from the reference fit $GM_{side,\,opt}$ (optimized fit of the shell profile of sample 5.E) for variations of the different modeling parameters.

It should be noted that by exchanging $GM_{side,\,opt}$ of Eq. B.1 by the experimental data for the shell thickness $GM_{side,\,exp}$, also the deviation Δ of the optimized fits for sample 5.B2 and 5.E regarding the experimentally observed shell profile can be obtained. For the optimized fit of sample 5.B2 (see Figure 5.7) one obtains a Δ of about 3%. In comparison, the optimized fit of sample 5.E (see Figure 5.5) has a rather high Δ of about 14%, which can be explained by the larger deviation of the fit in the upper part of the shell profile.

# Bibliography


[1] H. Morkoç, *Handbook of Nitride Semiconductors and Devices - Volume 2: Electronic and Optical Processes in Nitrides*, volume 2, Wiley-VCH (2008).

[2] H. Morkoç, *Handbook of Nitride Semiconductors and Devices - Volume 1: Materials Properties, Physics and Growth*, volume 1, Wiley-VCH (2008).

[3] C. Weisbuch, Review—On The Search for Efficient Solid State Light Emitters: Past, Present, Future, *ECS Journal of Solid State Science and Technology* **9**, 016022 (2020).

[4] H. Chen, R. Zhu, M.-C. Li, S.-L. Lee, and S.-T. Wu, Pixel-by-pixel local dimming for high-dynamic-range liquid crystal displays, *Opt. Express* **25**, 1973–1984 (2017).

[5] M. S. Wong, S. Nakamura, and S. P. DenBaars, Review—Progress in High Performance III-Nitride Micro-Light-Emitting Diodes, *ECS Journal of Solid State Science and Technology* **9**, 015012 (2019).

[6] F. Templier, GaN-based emissive microdisplays: A very promising technology for compact, ultra-high brightness display systems, *J. Soc. Inf. Disp.* **24**, 669–675 (2016).

[7] T. Wu, C.-W. Sher, Y. Lin, C.-F. Lee, S. Liang, Y. Lu, S.-W. Huang Chen, W. Guo, H.-C. Kuo, and Z. Chen, Mini-LED and Micro-LED: Promising Candidates for the Next Generation Display Technology, *Appl. Sci.* **8**, 1557 (2018).

[8] E. Barrigón, M. Heurlin, Z. Bi, B. Monemar, and L. Samuelson, Synthesis and Applications of III–V Nanowires, *Chemical Reviews* **119**, 9170–9220 (2019).

[9] S. K. Moore, Cash Comes in for Nanowire Display Startups, https://spectrum.ieee.org/nanoclast/semiconductors/optoelectronics/cash-comes-in-for-nanowire-display-startups, IEEE Spectrum (2018).

[10] S. D. Hersee, A. K. Rishinaramangalam, M. N. Fairchild, L. Zhang, and P. Varangis, Threading defect elimination in GaN nanowires, *J. Mater. Res.* **26**, 2293–2298 (2011).

[11] K. Ding, V. Avrutin, N. Izyumskaya, U. Özgür, and H. Morkoç, Micro-LEDs, a Manufacturability Perspective, *Applied Sciences* **9** (2019).

[12] V. Consonni, Self-induced growth of GaN nanowires by molecular beam epitaxy: A critical review of the formation mechanisms, *physica status solidi (RRL) – Rapid Research Letters* **7**, 699–712 (2013).

[13] A. Trampert, J. Ristić, U. Jahn, E. Calleja, and K. Ploog, TEM study of (Ga, Al) N nanocolumns and embedded GaN nanodiscs, In *IOP Conf. Ser. No. 180*, volume 180, page 167 (2003).

[14] A. Waag, X. Wang, S. Fündling, J. Ledig, M. Erenburg, R. Neumann, M. Al Suleiman, S. Merzsch, J. Wei, S. Li, H. H. Wehmann, W. Bergbauer, M. Strassburg, A. Trampert, U. Jahn, and H. Riechert, The nanorod approach: GaN NanoLEDs for solid state lighting, *Phys. status solidi* **8**, 2296–2301 (2011).

[15] R. R. LaPierre, A. C. E. Chia, S. J. Gibson, C. M. Haapamaki, J. P. Boulanger, R. Yee, P. Kuyanov, J. Zhang, N. Tajik, N. Jewell, and K. M. a. Rahman, III-V nanowire photovoltaics: Review of design for high efficiency, *Phys. Status Solidi - Rapid Res. Lett.* **7**, 815–830 (2013).

[16] R. Calarco, R. J. Meijers, R. K. Debnath, T. Stoica, E. Sutter, and H. Lüth, Nucleation and growth of GaN nanowires on Si(111) performed by molecular beam epitaxy, *Nano Lett.* **7**, 2248–51 (2007).

[17] O. Brandt, S. Fernández-Garrido, J. K. Zettler, E. Luna, U. Jahn, C. Chèze, and V. M. Kaganer, Statistical Analysis of the Shape of One-Dimensional Nanostructures: Determining the Coalescence Degree of Spontaneously Formed GaN Nanowires, *Cryst. Growth Des.* **14**, 2246–2253 (2014).

[18] M. Wölz, *Control of the emission wavelength of gallium nitride-based nanowire light-emitting diodes*, PhD thesis, Humboldt-Universität zu Berlin (2013).

[19] M. Wölz, C. Hauswald, T. Flissikowski, T. Gotschke, S. Fernández-Garrido, O. Brandt, H. T. Grahn, L. Geelhaar, and H. Riechert, Epitaxial Growth of GaN Nanowires with High Structural Perfection on a Metallic TiN Film., *Nano Lett.* **15**, 3743–3747 (2015).

[20] B. Neubert, P. Brückner, F. Habel, F. Scholz, T. Riemann, J. Christen, M. Beer, and J. Zweck, GaInN quantum wells grown on facets of selectively grown GaN stripes, *Appl. Phys. Lett.* **87**, 1–3 (2005).

[21] T. Wernicke, L. Schade, C. Netzel, J. Rass, V. Hoffmann, S. Ploch, A. Knauer, M. Weyers, U. Schwarz, and M. Kneissl, Indium incorporation and emission wavelength of polar, nonpolar and semipolar InGaN quantum wells, *Semicond. Sci. Technol.* **27**, 024014 (2012).

[22] A. Kapoor, N. Guan, M. Vallo, A. Messanvi, L. Mancini, E. Gautier, C. Bougerol, B. Gayral, F. H. Julien, F. Vurpillot, L. Rigutti, M. Tchernycheva, J. Eymery, and C. Durand, Green Electroluminescence from Radial m-Plane InGaN Quantum Wells Grown on GaN Wire Sidewalls by Metal–Organic Vapor Phase Epitaxy, *ACS Photonics* **5**, 4330–4337 (2018).

[23] J. Lähnemann, O. Brandt, U. Jahn, C. Pfüller, C. Roder, P. Dogan, F. Grosse, A. Belabbes, F. Bechstedt, A. Trampert, and L. Geelhaar, Direct experimental determination of the spontaneous polarization of GaN, *Phys. Rev. B* **86**, 081302 (2012).

[24] T. Takeuchi, S. Sota, M. Katsuragawa, M. Komori, H. Takeuchi, H. Amano, and I. Akasaki, Quantum-Confined Stark Effect due to Piezoelectric Fields in GaInN Strained Quantum Wells, *Jpn. J. Appl. Phys.* **36**, 382–385 (1997).

[25] S. Chichibu, A. Uedono, T. Onuma, B. Haskell, A. Chakraborty, T. Koyama, P. Fini, S. Keller, S. Denbaars, J. Speck, U. Mishra, S. Nakamura, S. Yamaguchi, S. Kamiyama, H. Amano, I. Akasaki, J. Han, and T. Sota, Origin of defect-insensitive emission probability in In-containing (Al,In,Ga)N alloy semiconductors, *Nature Materials* **5**, 810–816 (2006).

[26] A. Y. Cho, How molecular beam epitaxy (MBE) began and its projection into the future, *J. Cryst. Growth* **201**, 1–7 (1999).

[27] J. Ristić, E. Calleja, S. Fernández-Garrido, L. Cerutti, A. Trampert, U. Jahn, and K. H. Ploog, On the mechanisms of spontaneous growth of III-nitride nanocolumns by plasma-assisted molecular beam epitaxy, *J. Cryst. Growth* **310**, 4035–4045 (2008).

[28] B. Heying, R. Averbeck, L. F. Chen, E. Haus, H. Riechert, and J. S. Speck, Control of GaN surface morphologies using plasma-assisted molecular beam epitaxy, *J. Appl. Phys.* **88**, 1855 (2000).

[29] C. Chèze, *Investigation and comparison of GaN nanowire nucleation and growth by the catalyst-assisted and self-induced approaches.*, PhD thesis, Humboldt-Universität zu Berlin (2013).

[30] C. A. Schneider, W. S. Rasband, and K. W. Eliceiri, NIH Image to ImageJ: 25 years of image analysis, *Nat. Methods* **9**, 671–675 (2012).

[31] V. M. Kaganer, S. Fernández-Garrido, P. Dogan, K. K. Sabelfeld, and O. Brandt, Nucleation, Growth, and Bundling of GaN Nanowires in Molecular Beam Epitaxy: Disentangling the Origin of Nanowire Coalescence, *Nano Lett.* **16**, 3717–3725 (2016).

[32] C. Pfüller, *Optical properties of single semiconductor nanowires and nanowire en- sembles*, PhD thesis, Humboldt-Universität zu Berlin (2011).

[33] D. Volm, K. Oettinger, T. Streibl, D. Kovalev, M. Ben-Chorin, J. Diener, B. K. Meyer, J. Majewski, L. Eckey, A. Hoffmann, H. Amano, I. Akasaki, K. Hiramatsu, and T. Detchprohm, Exciton fine structure in undoped GaN epitaxial films, *Phys. Rev. B* **53**, 16543–16550 (1996).

[34] K. Kornitzer, T. Ebner, K. Thonke, R. Sauer, C. Kirchner, V. Schwegler, M. Kamp, M. Leszczynski, I. Grzegory, and S. Porowski, Photoluminescence and reflectance

spectroscopy of excitonic transitions in high-quality homoepitaxial GaN films, *Phys. Rev. B* **60**, 1471–1473 (1999).

[35] J. Lähnemann, *Luminescence of group-III-V nanowires containing heterostructures*, PhD thesis, Humboldt-Universität zu Berlin (2013).

[36] I. Pelant and J. Valenta, *Luminescence Spectroscopy of Semiconductors*, Oxford University Press (2012).

[37] H. Küpers, *Growth and properties of GaAs/(In,Ga)As core-shell nanowire arrays on Si*, PhD thesis, Humboldt-Universität zu Berlin, Mathematisch-Naturwissenschaftliche Fakultät (2018).

[38] C. Hauswald, *Dynamics of free and bound excitons in GaN nanowires: Origin of the non-radiative recombination channel*, PhD thesis, Humboldt-Universität zu Berlin (2014).

[39] C. H. Chiu, T. C. Lu, H. W. Huang, C. F. Lai, C. C. Kao, J. T. Chu, C. C. Yu, H. C. Kuo, S. C. Wang, C. F. Lin, and T. H. Hsueh, Fabrication of InGaN/GaN nanorod light-emitting diodes with self-assembled Ni metal islands, *Nanotechnology* **18**, 445201 (2007).

[40] Y. Wu, C. Chiu, C. Chang, P. Yu, and H. Kuo, Size-Dependent Strain Relaxation and Optical Characteristics of InGaN/GaN Nanorod LEDs, *IEEE Journal of Selected Topics in Quantum Electronics* **15**, 1226–1233 (2009).

[41] Q. Li, K. R. Westlake, M. H. Crawford, S. R. Lee, D. D. Koleske, J. J. Figiel, K. C. Cross, S. Fathololoumi, Z. Mi, and G. T. Wang, Optical performance of top-down fabricated InGaN/GaN nanorod light emitting diode arrays, *Opt. Express* **19**, 25528–25534 (2011).

[42] Q. Li, J. B. Wright, W. W. Chow, T. S. Luk, I. Brener, L. F. Lester, and G. T. Wang, Single-mode GaN nanowire lasers, *Opt. Express* **20**, 17873–17879 (2012).

[43] W. J. Tseng, M. Gonzalez, L. Dillemans, K. Cheng, S. J. Jiang, P. M. Vereecken, G. Borghs, and R. R. Lieten, Strain relaxation in GaN nanopillars, *Appl. Phys. Lett.* **101**, 253102 (2012).

[44] B. Damilano, S. Vézian, J. Brault, B. Alloing, and J. Massies, Selective Area Sublimation: A Simple Top-down Route for GaN-Based Nanowire Fabrication, *Nano Lett.* **16**, 1863–1868 (2016).

[45] S. Fernández-Garrido, T. Auzelle, J. Lähnemann, K. Wimmer, A. Tahraoui, and O. Brandt, Top-down fabrication of ordered arrays of GaN nanowires by selective area sublimation, *Nanoscale Adv.* **1**, 1893–1900 (2019).

[46] S. D. Hersee, X. Sun, and X. Wang, The Controlled Growth of GaN Nanowires, *Nano Letters* **6**, 1808–1811 (2006).

[47] H. Sekiguchi, K. Kishino, and A. Kikuchi, Emission color control from blue to red with nanocolumn diameter of InGaN/GaN nanocolumn arrays grown on same substrate, *Appl. Phys. Lett.* **96**, 231104 (2010).

[48] T. Schumann, T. Gotschke, F. Limbach, T. Stoica, and R. Calarco, Selective-area catalyst-free MBE growth of GaN nanowires using a patterned oxide layer, *Nanotechnology* **22**, 095603 (2011).

[49] M. Musolino, A. Tahraoui, S. Fernández-Garrido, O. Brandt, A. Trampert, L. Geelhaar, and H. Riechert, Compatibility of the selective area growth of GaN nanowires on AlN-buffered Si substrates with the operation of light emitting diodes, *Nanotechnology* **26**, 085605 (2015).

[50] C. Chèze, L. Geelhaar, A. Trampert, O. Brandt, and H. Riechert, Collector Phase Transitions during Vapor-Solid-Solid Nucleation of GaN Nanowires, *Nano Letters* **10**, 3426–3431 (2010).

[51] L. Geelhaar, C. Chèze, W. M. Weber, R. Averbeck, H. Riechert, T. Kehagias, P. Komninou, G. P. Dimitrakopulos, and T. Karakostas, Axial and radial growth of Ni-induced GaN nanowires, *Appl. Phys. Lett.* **91**, 093113 (2007).

[52] L. Geelhaar, C. Chèze, B. Jenichen, O. Brandt, C. Pfüller, S. Münch, R. Rothemund, S. Reitzenstein, A. Forchel, T. Kehagias, P. Komninou, G. P. Dimitrakopulos, T. Karakostas, L. Lari, P. R. Chalker, M. H. Gass, and H. Riechert, Properties of GaN Nanowires Grown by Molecular Beam Epitaxy, *IEEE J. Sel. Top. Quantum Electron.* **17**, 878–888 (2011).

[53] M. Yoshizawa, A. Kikuchi, M. Mori, N. Fujita, and K. Kishino, Growth of Self-Organized GaN Nanostructures on $Al_2O_3$(0001) by RF-Radical Source Molecular Beam Epitaxy, *Jpn. J. Appl. Phys.* **36**, L459–L462 (1997).

[54] M. A. Sanchez-Garcia, E. Calleja, E. Monroy, F. J. Sanchez, F. Calle, E. Muñoz, and R. Beresford, The effect of the III/V ratio and substrate temperature on the morphology and properties of GaN- and AlN-layers grown by molecular beam epitaxy on Si(1 1 1), *J. Cryst. Growth* **183**, 23–30 (1998).

[55] L. Cerutti, J. Ristić, S. Fernández-Garrido, E. Calleja, A. Trampert, K. H. Ploog, S. Lazić, and J. M. Calleja, Wurtzite GaN nanocolumns grown on Si(001) by molecular beam epitaxy, *Appl. Phys. Lett.* **88**, 213114 (2006).

[56] R. Songmuang, O. Landré, and B. Daudin, From nucleation to growth of catalyst-free GaN nanowires on thin AlN buffer layer, *Appl. Phys. Lett.* **91**, 251902 (2007).

[57] K. A. Bertness, A. Roshko, L. Mansfield, T. Harvey, and N. a. Sanford, Mechanism for spontaneous growth of GaN nanowires with molecular beam epitaxy, *J. Cryst. Growth* **310**, 3154–3158 (2008).

[58] T. Stoica, E. Sutter, R. J. Meijers, R. K. Debnath, R. Calarco, H. Lüth, and D. Grützmacher, Interface and wetting layer effect on the catalyst-free nucleation and growth of GaN nanowires., *Small* **4**, 751–4 (2008).

[59] F. Schuster, F. Furtmayr, R. Zamani, C. Magén, J. R. Morante, J. Arbiol, J. a. Garrido, and M. Stutzmann, Self-assembled GaN nanowires on diamond., *Nano Lett.* **12**, 2199–204 (2012).

[60] M. Sobanska, K. Klosek, J. Borysiuk, S. Kret, G. Tchutchulasvili, S. Gieraltowska, and Z. R. Zytkiewicz, Enhanced catalyst-free nucleation of GaN nanowires on amorphous Al2O3 by plasma-assisted molecular beam epitaxy, *J. Appl. Phys.* **115**, 043517 (2014).

[61] G. Calabrese, P. Corfdir, G. Gao, C. Pfüller, A. Trampert, O. Brandt, L. Geelhaar, and S. Fernández-Garrido, Molecular beam epitaxy of single crystalline GaN nanowires on a flexible Ti foil, *Appl. Phys. Lett.* **108**, 202101 (2016).

[62] B. J. May, A. T. M. G. Sarwar, and R. C. Myers, Nanowire LEDs Grown Directly on Flexible Metal Foil, *Appl. Phys. Lett.* **108**, 141103 (2016).

[63] K. Tomioka, J. Motohisa, S. Hara, and T. Fukui, Control of InAs Nanowire Growth Directions on Si, *Nano Letters* **8**, 3475–3480 (2008).

[64] A. Urban, J. Malindretos, J.-H. Klein-Wiele, P. Simon, and A. Rizzi, Ga-polar GaN nanocolumn arrays with semipolar faceted tips, *New Journal of Physics* **15**, 053045 (2013).

[65] F. Glas, Critical dimensions for the plastic relaxation of strained axial heterostructures in free-standing nanowires, *Phys. Rev. B* **74**, 121302 (2006).

[66] E. Ertekin, P. A. Greaney, D. C. Chrzan, and T. D. Sands, Equilibrium limits of coherency in strained nanowire heterostructures, *J. Appl. Phys.* **97** (2005).

[67] S. Fernández-Garrido, J. Grandal, E. Calleja, M. A. Sánchez-García, and D. López-Romero, A growth diagram for plasma-assisted molecular beam epitaxy of GaN nanocolumns on Si(111), *Journal of Applied Physics* **106**, 126102 (2009).

[68] V. Consonni, M. Hanke, M. Knelangen, L. Geelhaar, A. Trampert, and H. Riechert, Nucleation mechanisms of self-induced GaN nanowires grown on an amorphous interlayer, *Phys. Rev. B* **83**, 035310 (2011).

[69] V. G. Dubrovskii, V. Consonni, A. Trampert, L. Geelhaar, and H. Riechert, Scaling thermodynamic model for the self-induced nucleation of GaN nanowires, *Phys. Rev. B* **85**, 165317 (2012).

[70] H. Li, L. Geelhaar, H. Riechert, and C. Draxl, Computing Equilibrium Shapes of Wurtzite Crystals: The Example of GaN, *Phys. Rev. Lett.* **115**, 085503 (2015).

[71] V. Consonni, V. G. Dubrovskii, A. Trampert, L. Geelhaar, and H. Riechert, Quantitative description for the growth rate of self-induced GaN nanowires, *Phys. Rev. B* **85**, 155313 (2012).

[72] S. Fernández-Garrido, V. M. Kaganer, K. K. Sabelfeld, T. Gotschke, J. Grandal, E. Calleja, L. Geelhaar, and O. Brandt, Self-Regulated Radius of Spontaneously Formed GaN Nanowires in Molecular Beam Epitaxy, *Nano Lett.* **13**, 3274–3280 (2013).

[73] T. Zywietz, J. Neugebauer, and M. Scheffler, Adatom diffusion at GaN (0001) and (000$\bar{1}$) surfaces, *Appl. Phys. Lett.* **73**, 487–489 (1998).

[74] D. D. Koleske, A. E. Wickenden, R. L. Henry, W. J. DeSisto, and R. J. Gorman, Growth model for GaN with comparison to structural, optical, and electrical properties, *J. Appl. Phys.* **84**, 1998–2010 (1998).

[75] L. Lymperakis and J. Neugebauer, Large anisotropic adatom kinetics on nonpolar GaN surfaces: Consequences for surface morphologies and nanowire growth, *Phys. Rev. B* **79**, 1–4 (2009).

[76] M. Tchernycheva, C. Sartel, G. Cirlin, L. Travers, G. Patriarche, J.-C. Harmand, L. S. Dang, J. Renard, B. Gayral, L. Nevou, and F. Julien, Growth of GaN free-standing nanowires by plasma-assisted molecular beam epitaxy: structural and optical characterization, *Nanotechnology* **18**, 385306 (2007).

[77] R. K. Debnath, R. J. Meijers, T. Richter, T. Stoica, R. Calarco, and H. Lüth, Mechanism of molecular beam epitaxy growth of GaN nanowires on Si(111), *Appl. Phys. Lett.* **90**, 123117 (2007).

[78] V. G. Dubrovskii, V. Consonni, L. Geelhaar, A. Trampert, and H. Riechert, Scaling growth kinetics of self-induced GaN nanowires, *Appl. Phys. Lett.* **100**, 153101 (2012).

[79] C. T. Foxon, S. Novikov, J. Hall, R. Campion, D. Cherns, I. Griffiths, and S. Khongphetsak, A complementary geometric model for the growth of GaN nanocolumns prepared by plasma-assisted molecular beam epitaxy, *J. Cryst. Growth* **311**, 3423–3427 (2009).

[80] F. Glas, Vapor fluxes on the apical droplet during nanowire growth by molecular beam epitaxy, *Phys. Status Solidi* **247**, 254–258 (2010).

[81] J.-C. Harmand, F. Glas, and G. Patriarche, Growth kinetics of a single InP(1-x)As(x) nanowire, *Phys. Rev. B* **81**, 235436 (2010).

[82] E. Galopin, L. Largeau, G. Patriarche, L. Travers, F. Glas, and J.-C. Harmand, Morphology of self-catalyzed GaN nanowires and chronology of their formation by molecular beam epitaxy., *Nanotechnology* **22**, 245606 (2011).

[83] V. G. Dubrovskii, M. A. Timofeeva, M. Tchernycheva, and A. D. Bolshakov, Lateral growth and shape of semiconductor nanowires, *Semiconductors* **47**, 50–57 (2013).

[84] K. Hestroffer and B. Daudin, A geometrical model for the description of the AlN shell morphology in GaN-AlN core-shell nanowires, *J. Appl. Phys.* **114**, 244305 (2013).

[85] A. D. Bol'shakov, M. A. Timofeeva, and V. G. Dubrovskii, Simulation of growth and shape of nanowires in the absence of a catalyst, *Tech. Phys. Lett.* **40**, 389–392 (2014).

[86] J. Tersoff, Stable Self-Catalyzed Growth of III–V Nanowires, *Nano Lett.* **15**, 6609–6613 (2015).

[87] S. Albert, A. Bengoechea-Encabo, J. Ledig, T. Schimpke, M. a. Sánchez-Garcia, M. Strassburg, A. Waag, and E. Calleja, Demonstration of (In, Ga)N/GaN Core–Shell Micro Light-Emitting Diodes Grown by Molecular Beam Epitaxy on Ordered MOVPE GaN Pillars, *Cryst. Growth Des.* **15**, 3661–3665 (2015).

[88] S. Gazibegovic, D. Car, H. Zhang, S. C. Balk, J. A. Logan, M. W. A. de Moor, M. C. Cassidy, R. Schmits, D. Xu, G. Wang, P. Krogstrup, R. L. M. Op het Veld, K. Zuo, Y. Vos, J. Shen, D. Bouman, B. Shojaei, D. Pennachio, J. S. Lee, P. J. van Veldhoven, S. Koelling, M. A. Verheijen, L. P. Kouwenhoven, C. J. Palmstrøm, and E. P. A. M. Bakkers, Epitaxy of advanced nanowire quantum devices, *Nature* **548**, 434–438 (2017).

[89] H. Küpers, R. B. Lewis, A. Tahraoui, M. Matalla, O. Krüger, F. Bastiman, H. Riechert, and L. Geelhaar, Diameter evolution of selective area grown Ga-assisted GaAs nanowires, *Nano Res.* **11**, 2885–2893 (2018).

[90] F. Oehler, A. Cattoni, A. Scaccabarozzi, G. Patriarche, F. Glas, and J.-C. Harmand, Measuring and modeling the growth dynamics of self-catalyzed GaP nanowire arrays, *Nano Lett.* **18**, 701–708 (2018).

[91] R. B. Lewis, P. Corfdir, H. Küpers, T. Flissikowski, O. Brandt, and L. Geelhaar, Nanowires Bending over Backward from Strain Partitioning in Asymmetric Core–Shell Heterostructures, *Nano Lett.* **18**, 2343–2350 (2018).

[92] K. Hestroffer, C. Leclere, C. Bougerol, H. Renevier, and B. Daudin, Polarity of GaN nanowires grown by plasma-assisted molecular beam epitaxy on Si(111), *Phys. Rev. B* **84**, 245302 (2011).

[93] M. D. Brubaker, I. Levin, A. V. Davydov, D. M. Rourke, N. a. Sanford, V. M. Bright, and K. A. Bertness, Effect of AlN buffer layer properties on the morphology and polarity of GaN nanowires grown by molecular beam epitaxy, *J. Appl. Phys.* **110**, 053506 (2011).

[94] L. Largeau, E. Galopin, N. Gogneau, L. Travers, F. Glas, and J.-C. C. Harmand, N-polar GaN nanowires seeded by Al droplets on Si (111), *Cryst. Growth Des.* **12**, 2724–2729 (2012).

[95] S. Fernández-Garrido, X. Kong, T. Gotschke, R. Calarco, L. Geelhaar, A. Trampert, and O. Brandt, Spontaneous Nucleation and Growth of GaN Nanowires: The Fundamental Role of Crystal Polarity, *Nano Letters* **12**, 6119–6125 (2012).

[96] S. D. Carnevale, T. F. Kent, P. J. Phillips, A. T. M. G. Sarwar, C. Selcu, R. F. Klie, and R. C. Myers, Mixed Polarity in Polarization-Induced p–n Junction Nanowire Light-Emitting Diodes, *Nano Letters* **13**, 3029–3035 (2013).

[97] O. Romanyuk, S. Fernández-Garrido, P. Jiříček, I. Bartoš, L. Geelhaar, O. Brandt, and T. Paskova, Non-destructive assessment of the polarity of GaN nanowire ensembles using low-energy electron diffraction and x-ray photoelectron diffraction, *Appl. Phys. Lett.* **106**, 021602 (2015).

[98] A. Minj, N. Garro, A. Cros, T. Auzelle, Y. M. Niquet, B. Daudin, J. Pernot, B. Daudin, N. Garro, A. Cros, T. Auzelle, Y. M. Niquet, and B. Daudin, Direct assessment of p-n junctions in GaN single nanowires by Kelvin Probe Force Microscopy, *Nanotechnology* **27**, 3–4 (2016).

[99] A. Concordel, G. Jacopin, B. Gayral, N. Garro, A. Cros, J.-L. Rouvière, and B. Daudin, Polarity conversion of GaN nanowires grown by plasma-assisted molecular beam epitaxy, *Appl. Phys. Lett.* **114**, 172101 (2019).

[100] F. Bernardini, V. Fiorentini, and D. Vanderbilt, Spontaneous polarization and piezoelectric constants of III-V nitrides, *Phys. Rev. B* **56**, R10024–R10027 (1997).

[101] K. Xu and A. Yoshikawa, Effects of film polarities on InN growth by molecular-beam epitaxy, *Appl. Phys. Lett.* **83**, 251–253 (2003).

[102] D. N. Nath, E. Gür, S. A. Ringel, and S. Rajan, Molecular beam epitaxy of N-polar InGaN, *Appl. Phys. Lett.* **97**, 071903 (2010).

[103] A. Feduniewicz, C. Skierbiszewski, M. Siekacz, Z. Wasilewski, I. Sproule, S. Grzanka, R. Jakieła, J. Borysiuk, G. Kamler, E. Litwin-Staszewska, R. Czernecki, M. Boćkowski, and S. Porowski, Control of Mg doping of GaN in RF-plasma molecular beam epitaxy, *Journal of Crystal Growth* **278**, 443 – 448 (2005), 13th International Conference on Molecular Beam Epitaxy.

[104] S. F. Chichibu, A. Setoguchi, A. Uedono, K. Yoshimura, and M. Sumiya, Impact of growth polar direction on the optical properties of GaN grown by metalorganic vapor phase epitaxy, *Appl. Phys. Lett.* **78**, 28–30 (2001).

[105] A. J. Ptak, L. J. Holbert, L. Ting, C. H. Swartz, M. Moldovan, N. C. Giles, T. H. Myers, P. Van Lierde, C. Tian, R. A. Hockett, S. Mitha, A. E. Wickenden, D. D. Koleske, and R. L. Henry, Controlled oxygen doping of GaN using plasma assisted molecular-beam epitaxy, *Appl. Phys. Lett.* **79**, 2740–2742 (2001).

[106] V. Kumaresan, L. Largeau, A. Madouri, F. Glas, H. Zhang, F. Oehler, A. Cavanna, A. Babichev, L. Travers, N. Gogneau, M. Tchernycheva, and J.-C. Harmand, Epitaxy of GaN Nanowires on Graphene, *Nano Letters* **16**, 4895–4902 (2016).

[107] S. Fernández-Garrido, M. Ramsteiner, G. Gao, L. A. Galves, B. Sharma, P. Corfdir, G. Calabrese, Z. de Souza Schiaber, C. Pfüller, A. Trampert, J. M. J. Lopes, O. Brandt, and L. Geelhaar, Molecular Beam Epitaxy of GaN Nanowires on Epitaxial Graphene, *Nano Letters* **17**, 5213–5221 (2017).

[108] A. Prabaswara, H. Kim, J.-W. Min, R. C. Subedi, D. Anjum, B. Davaasuren, K. Moore, S. Conroy, S. Mitra, I. Roqan, T. K. Ng, H. Alshareef, and B. Ooi, Titanium Carbide MXene Nucleation Layer for Epitaxial Growth of High-Quality GaN Nanowires on Amorphous Substrates, *ACS Nano* **14**, 2202–2211 (2020).

[109] A. G. Sarwar, S. D. Carnevale, F. Yang, T. F. Kent, J. J. Jamison, D. W. McComb, and R. C. Myers, Semiconductor Nanowire Light-Emitting Diodes Grown on Metal: A Direction Toward Large-Scale Fabrication of Nanowire Devices, *Small* **11**, 5402–5408 (2015).

[110] C. Zhao, T. K. Ng, R. T. ElAfandy, A. Prabaswara, G. B. Consiglio, I. A. Ajia, I. S. Roqan, B. Janjua, C. Shen, J. Eid, A. Y. Alyamani, M. M. El-Desouki, and B. S. Ooi, Droop-Free, Reliable, and High-Power InGaN/GaN Nanowire Light-Emitting Diodes for Monolithic Metal-Optoelectronics, *Nano Lett.* **16**, 4616–4623 (2016).

[111] C. Zhao, T. K. Ng, N. Wei, A. Prabaswara, M. S. Alias, B. Janjua, C. Shen, and B. S. Ooi, Facile Formation of High-Quality InGaN/GaN Quantum-Disks-in-Nanowires on Bulk-Metal Substrates for High-Power Light-Emitters, *Nano Letters* **16**, 1056–1063 (2016).

[112] B. Janjua, T. K. Ng, C. Zhao, A. Prabaswara, G. B. Consiglio, D. Priante, C. Shen, R. T. Elafandy, D. H. Anjum, A. A. Alhamoud, A. A. Alatawi, Y. Yang, A. Y. Alyamani, M. M. El-Desouki, and B. S. Ooi, True Yellow Light-Emitting Diodes as Phosphor for Tunable Color-Rendering Index Laser-Based White Light, *ACS Photonics* **3**, 2089–2095 (2016).

[113] B. Janjua, T. K. Ng, C. Zhao, H. M. Oubei, C. Shen, A. Prabaswara, M. S. Alias, A. A. Alhamoud, A. A. Alatawi, A. M. Albadri, A. Y. Alyamani, M. M. El-Desouki, and B. S. Ooi, Ultrabroad linewidth orange-emitting nanowires LED for high CRI laser-based white lighting and gigahertz communications, *Opt. Express* **24**, 19228–19236 (2016).

[114] G. Calabrese, S. V. Pettersen, C. Pfüller, M. Ramsteiner, J. K. Grepstad, O. Brandt, L. Geelhaar, and S. Fernández-Garrido, Effect of surface roughness, chemical composition, and native oxide crystallinity on the orientation of self-assembled GaN nanowires on Ti foils, *Nanotechnology* **28**, 425602 (2017).

[115] F. Furtmayr, M. Vielemeyer, M. Stutzmann, J. Arbiol, S. Estradé, F. Peirò, J. R. Morante, and M. Eickhoff, Nucleation and growth of GaN nanorods on Si (111) surfaces by plasma-assisted molecular beam epitaxy - The influence of Si- and Mg-doping, *J. Appl. Phys.* **104**, 034309 (2008).

[116] V. Consonni, M. Knelangen, A. Trampert, L. Geelhaar, and H. Riechert, Nucleation and coalescence effects on the density of self-induced GaN nanowires grown by molecular beam epitaxy, *Appl. Phys. Lett.* **98**, 071913 (2011).

[117] S. Fernández-Garrido, V. M. Kaganer, C. Hauswald, B. Jenichen, M. Ramsteiner, V. Consonni, L. Geelhaar, and O. Brandt, Correlation between the structural and optical properties of spontaneously formed GaN nanowires: a quantitative evaluation of the impact of nanowire coalescence, *Nanotechnology* **25**, 455702 (2014).

[118] S. Zhao, H. P. Nguyen, M. G. Kibria, and Z. Mi, III-Nitride nanowire optoelectronics, *Prog. Quantum Electron.* **44**, 14–68 (2015).

[119] V. Consonni, M. Knelangen, U. Jahn, A. Trampert, L. Geelhaar, and H. Riechert, Effects of nanowire coalescence on their structural and optical properties on a local scale, *Appl. Phys. Lett.* **95**, 241910 (2009).

[120] B. Jenichen, O. Brandt, C. Pfüller, P. Dogan, M. Knelangen, and A. Trampert, Macro- and micro-strain in GaN nanowires on Si(111), *Nanotechnology* **22**, 295714 (2011).

[121] K. A. Grossklaus, A. Banerjee, S. Jahangir, P. Bhattacharya, and J. M. Millunchick, Misorientation defects in coalesced self-catalyzed GaN nanowires, *J. Cryst. Growth* **371**, 142–147 (2013).

[122] S. Fan, S. Zhao, X. Liu, and Z. Mi, Study on the coalescence of dislocation-free GaN nanowires on Si and SiOx, *J. Vac. Sci. Technol. B Microelectron. Nanom. Struct.* **32**, 02C114 (2014).

[123] V. M. Kaganer, B. Jenichen, and O. Brandt, Elastic versus Plastic Strain Relaxation in Coalesced GaN Nanowires: An X-Ray Diffraction Study, *Phys. Rev. Appl.* **6**, 064023 (2016).

[124] L. J. Brillson, Interface bonding, chemical reactions, and defect formation at metal-semiconductor interfaces, *Journal of Vacuum Science & Technology A* **25**, 943–949 (2007).

[125] D. van Treeck, G. Calabrese, J. J. W. Goertz, V. M. Kaganer, O. Brandt, S. Fernández-Garrido, and L. Geelhaar, Self-assembled formation of long, thin, and uncoalesced GaN nanowires on crystalline TiN films, *Nano Res.* **11**, 565–576 (2018).

[126] G. Calabrese, G. Gao, D. van Treeck, P. Corfdir, C. Sinito, T. Auzelle, A. Trampert, L. Geelhaar, O. Brandt, and S. Fernández-Garrido, Interfacial reactions during the molecular beam epitaxy of GaN nanowires on $Ti/Al_2O_3$, *Nanotechnology* **30**, 114001 (2019).

[127] J. K. Zettler, C. Hauswald, P. Corfdir, M. Musolino, L. Geelhaar, H. Riechert, O. Brandt, and S. Fernández-Garrido, High-Temperature Growth of GaN Nanowires by Molecular Beam Epitaxy: Toward the Material Quality of Bulk GaN, *Cryst. Growth Des.* **15**, 4104–4109 (2015).

[128] P. Corfdir, J. K. Zettler, C. Hauswald, S. Fernández-Garrido, O. Brandt, and P. Lefebvre, Sub-meV linewidth in GaN nanowire ensembles: Absence of surface excitons due to the field ionization of donors, *Phys. Rev. B* **90**, 205301 (2014).

[129] T. Auzelle, B. Haas, M. Den Hertog, J. L. Rouvière, B. Daudin, and B. Gayral, Attribution of the 3.45 eV GaN nanowires luminescence to inversion domain boundaries, *Appl. Phys. Lett.* **107** (2015).

[130] C. Pfüller, P. Corfdir, C. Hauswald, T. Flissikowski, X. Kong, J. K. Zettler, S. Fernández-Garrido, P. Doğan, H. T. Grahn, A. Trampert, L. Geelhaar, and O. Brandt, Nature of excitons bound to inversion domain boundaries: Origin of the 3.45-eV luminescence lines in spontaneously formed GaN nanowires on Si(111), *Phys. Rev. B* **94**, 155308 (2016).

[131] P. Corfdir, C. Hauswald, J. K. Zettler, T. Flissikowski, J. Lähnemann, S. Fernández-Garrido, L. Geelhaar, H. T. Grahn, and O. Brandt, Stacking faults as quantum wells in nanowires: Density of states, oscillator strength, and radiative efficiency, *Phys. Rev. B* **90**, 195309 (2014).

[132] G. Calabrese, D. van Treeck, V. M. Kaganer, O. Konovalov, P. Corfdir, C. Sinito, L. Geelhaar, O. Brandt, and S. Fernández-Garrido, Radius-dependent homogeneous strain in uncoalesced GaN nanowires, *Acta Mater.* **195**, 87–97 (2020).

[133] M. Hetzl, F. Schuster, A. Winnerl, S. Weiszer, and M. Stutzmann, GaN nanowires on diamond, *Mater. Sci. Semicond. Process.* **48**, 65–78 (2016).

[134] S. D. Carnevale, J. Yang, P. J. Phillips, M. J. Mills, and R. C. Myers, Three-dimensional GaN/AlN nanowire heterostructures by separating nucleation and growth processes, *Nano Lett.* **11**, 866–71 (2011).

[135] J. K. Zettler, P. Corfdir, L. Geelhaar, H. Riechert, O. Brandt, and S. Fernández-Garrido, Improved control over spontaneously formed GaN nanowires in molecular beam epitaxy using a two-step growth process, *Nanotechnology* **26**, 445604 (2015).

[136] X. Kong, J. Ristić, M. A. Sanchez-Garcia, E. Calleja, and A. Trampert, Polarity determination by electron energy-loss spectroscopy: application to ultra-small III-nitride semiconductor nanocolumns, *Nanotechnology* **22**, 415701 (2011).

[137] T. Auzelle, B. Haas, A. Minj, C. Bougerol, J.-L. Rouvière, A. Cros, J. Colchero, and B. Daudin, The influence of AlN buffer over the polarity and the nucleation of self-organized GaN nanowires, *J. Appl. Phys.* **117**, 245303 (2015).

[138] K. Bertness, A. Roshko, L. Mansfield, T. Harvey, and N. Sanford, Nucleation conditions for catalyst-free GaN nanowires, *J. Cryst. Growth* **300**, 94–99 (2007).

[139] C. Pfüller, M. Ramsteiner, O. Brandt, F. Grosse, A. Rathsfeld, G. Schmidt, L. Geelhaar, and H. Riechert, Raman spectroscopy as a probe for the coupling of light into ensembles of sub-wavelength-sized nanowires, *Appl. Phys. Lett.* **101**, 083104 (2012).

[140] J. A. Venables, G. D. T. Spiller, and M. Hanbücken, Nucleation and growth of thin films, *Reports Prog. Phys.* **47**, 399 (1984).

[141] C. V. Thompson, On the grain size and coalescence stress resulting from nucleation and growth processes during formation of polycrystalline thin films, *J. Mater. Res.* **14**, 3164–3168 (1999).

[142] V. Consonni, A. Trampert, L. Geelhaar, and H. Riechert, Physical origin of the incubation time of self-induced GaN nanowires, *Appl. Phys. Lett.* **99**, 033102 (2011).

[143] K. Kishino, H. Sekiguchi, and A. Kikuchi, Improved Ti-mask selective-area growth (SAG) by rf-plasma-assisted molecular beam epitaxy demonstrating extremely uniform GaN nanocolumn arrays, *J. Cryst. Growth* **311**, 2063–2068 (2009).

[144] J. M. Moison, F. Houzay, F. Barthe, L. Leprince, E. André, and O. Vatel, Self-organized growth of regular nanometer-scale InAs dots on GaAs, *Appl. Phys. Lett.* **64**, 196–198 (1994).

[145] T. Krause, M. Hanke, O. Brandt, and A. Trampert, Counterintuitive strain distribution in axial (In,Ga)N/GaN nanowires, *Appl. Phys. Lett.* **108**, 032103 (2016).

[146] R. Armitage and K. Tsubaki, Multicolour luminescence from InGaN quantum wells grown over GaN nanowire arrays by molecular-beam epitaxy, *Nanotechnology* **21**, 195202 (2010).

[147] M. Wölz, J. Lähnemann, O. Brandt, V. M. Kaganer, M. Ramsteiner, C. Pfüller, C. Hauswald, C. N. Huang, L. Geelhaar, and H. Riechert, Correlation between In content and emission wavelength of InGaN/GaN nanowire heterostructures, *Nanotechnology* **23**, 455203 (2012).

[148] Y. L. Chang, J. L. Wang, F. Li, and Z. Mi, High efficiency green, yellow, and amber emission from InGaN/GaN dot-in-a-wire heterostructures on Si(111), *Appl. Phys. Lett.* **96**, 98–101 (2010).

[149] G. Tourbot, C. Bougerol, F. Glas, L. F. Zagonel, Z. Mahfoud, S. Meuret, P. Gilet, M. Kociak, B. Gayral, and B. Daudin, Growth mechanism and properties of InGaN insertions in GaN nanowires, *Nanotechnology* **23**, 135703 (2012).

[150] T. Kehagias, G. P. Dimitrakopulos, P. Becker, J. Kioseoglou, F. Furtmayr, T. Koukoula, I. Häusler, a. Chernikov, S. Chatterjee, T. Karakostas, H.-M. Solowan, U. T. Schwarz, M. Eickhoff, and P. Komninou, Nanostructure and strain in InGaN/GaN superlattices grown in GaN nanowires, *Nanotechnology* **24**, 435702 (2013).

[151] S. Y. Woo, M. Bugnet, H. P. T. Nguyen, Z. Mi, and G. A. Botton, Atomic Ordering in InGaN Alloys within Nanowire Heterostructures, *Nano Lett.* **15**, 6413–6418 (2015).

[152] C. Chèze, F. Feix, J. Lähnemann, T. Flissikowski, M. Kryśko, P. Wolny, H. Turski, C. Skierbiszewski, and O. Brandt, Luminescent N-polar (In,Ga)N/GaN quantum wells achieved by plasma-assisted molecular beam epitaxy at temperatures exceeding 700 °C, *Appl. Phys. Lett.* **112**, 022102 (2018).

[153] J. Bartolomé, M. Hanke, D. van Treeck, and A. Trampert, Strain Driven Shape Evolution of Stacked (In,Ga)N Quantum Disks Embedded in GaN Nanowires, *Nano Lett.* (2017).

[154] J. Lähnemann, C. Hauswald, M. Wölz, U. Jahn, M. Hanke, L. Geelhaar, and O. Brandt, Localization and defects in axial (In,Ga)N/GaN nanowire heterostructures investigated by spatially resolved luminescence spectroscopy, *J. Phys. D. Appl. Phys.* **47**, 394010 (2014).

[155] F. Feix, T. Flissikowski, K. K. Sabelfeld, V. M. Kaganer, M. Wölz, L. Geelhaar, H. T. Grahn, and O. Brandt, Ga-Polar (In,Ga)N/GaN Quantum Wells Versus N-Polar (In,Ga)N Quantum Disks in GaN Nanowires: A Comparative Analysis of Carrier Recombination, Diffusion, and Radiative Efficiency, *Phys. Rev. Appl.* **8**, 014032 (2017).

[156] S. Fernández-Garrido, J. Lähnemann, C. Hauswald, M. Korytov, M. Albrecht, C. Chèze, C. Skierbiszewski, and O. Brandt, Comparison of the Luminous Efficiencies of Ga- and N-Polar $In_xGa_{1-x}N/In_yGa_{1-y}N$ Quantum Wells Grown by Plasma-Assisted Molecular Beam Epitaxy, *Phys. Rev. Appl.* **6**, 034017 (2016).

[157] J. Behrend, M. Wassermeier, W. Braun, P. Krispin, and K. H. Ploog, Formation of GaAs/AlAs(001) interfaces studied by scanning tunneling microscopy, *Phys. Rev. B* **53**, 9907–9912 (1996).

[158] E. C. Young, N. Grandjean, T. E. Mates, and J. S. Speck, Calcium impurity as a source of non-radiative recombination in (In,Ga)N layers grown by molecular beam epitaxy, *Appl. Phys. Lett.* **109** (2016).

[159] M. D. L. Mata, X. Zhou, F. Furtmayr, J. Teubert, S. Gradečak, M. Eickhoff, A. Fontcuberta i Morral, and J. Arbiol, A review of MBE grown 0D, 1D and 2D quantum structures in a nanowire, *J. Mater. Chem. C* **1**, 4300 (2013).

[160] M. Mandl, X. Wang, T. Schimpke, C. Kölper, M. Binder, J. Ledig, A. Waag, X. Kong, A. Trampert, F. Bertram, J. Christen, F. Barbagini, E. Calleja, and M. Strassburg, Group III nitride core–shell nano- and microrods for optoelectronic applications, *physica status solidi (RRL) – Rapid Research Letters* **7**, 800–814 (2013).

[161] N. P. Dasgupta, J. Sun, C. Liu, S. Brittman, S. C. Andrews, J. Lim, H. Gao, R. Yan, and P. Yang, 25th Anniversary Article: Semiconductor Nanowires - Synthesis, Characterization, and Applications, *Adv. Mater.* **26**, 2137–2184 (2014).

[162] R. Koester, D. Sager, W.-A. Quitsch, O. Pfingsten, A. Poloczek, S. Blumenthal, G. Keller, W. Prost, G. Bacher, and F.-J. Tegude, High-Speed GaN/GaInN Nanowire Array Light-Emitting Diode on Silicon(111), *Nano Lett.* **15**, 2318–23 (2015).

[163] T. Schimpke, M. Mandl, I. Stoll, B. Pohl-Klein, D. Bichler, F. Zwaschka, J. Strube-Knyrim, B. Huckenbeck, B. Max, M. Müller, P. Veit, F. Bertram, J. Christen, J. Hartmann, A. Waag, H. J. Lugauer, and M. Strassburg, Phosphor-converted white light from blue-emitting InGaN microrod LEDs, *Phys. Status Solidi Appl. Mater. Sci.* **213**, 1577–1584 (2016).

[164] K. Kishino, A. Kikuchi, H. Sekiguchi, and S. Ishizawa, InGaN/GaN nanocolumn LEDs emitting from blue to red, In *Proc. SPIE*, volume 6473, page 64730T (2007).

[165] W. Guo, M. Zhang, A. Banerjee, and P. Bhattacharya, Catalyst-free InGaN/GaN nanowire light emitting diodes grown on (001) silicon by molecular beam epitaxy., *Nano Lett.* **10**, 3355–9 (2010).

[166] A.-L. Bavencove, G. Tourbot, E. Pougeoise, J. Garcia, P. Gilet, F. Levy, B. André, G. Feuillet, B. Gayral, B. Daudin, and L. S. Dang, GaN-based nanowires: From nanometric-scale characterization to light emitting diodes, *Phys. Status Solidi* **207**, 1425–1427 (2010).

[167] H. P. T. Nguyen, K. Cui, S. Zhang, S. Fathololoumi, and Z. Mi, Full-color InGaN/GaN dot-in-a-wire light emitting diodes on silicon., *Nanotechnology* **22**, 445202 (2011).

[168] F. Limbach, C. Hauswald, J. Lähnemann, M. Wölz, O. Brandt, A. Trampert, M. Hanke, U. Jahn, R. Calarco, L. Geelhaar, and H. Riechert, Current path in light emitting diodes based on nanowire ensembles, *Nanotechnology* **23**, 465301 (2012).

[169] K. Kishino, K. Nagashima, and K. Yamano, Monolithic integration of InGaN-based nanocolumn light-emitting diodes with different emission colors, *Appl. Phys. Express* **6**, 1–4 (2013).

[170] R. Wang, H. P. T. Nguyen, A. T. Connie, J. Lee, I. Shih, and Z. Mi, Color-tunable, phosphor-free InGaN nanowire light-emitting diode arrays monolithically integrated on silicon, *Opt. Express* **22**, A1768 (2014).

[171] O. Ambacher, Growth and applications of Group III-nitrides, *J. Phys. D. Appl. Phys.* **31**, 2653–2710 (1998).

[172] C. Adelmann, R. Langer, G. Feuillet, and B. Daudin, Indium incorporation during the growth of InGaN by molecular-beam epitaxy studied by reflection high-energy electron diffraction intensity oscillations, *Appl. Phys. Lett.* **75**, 3518–3520 (1999).

[173] M. Siekacz, M. Sawicka, H. Turski, G. Cywiński, A. Khachapuridze, P. Perlin, T. Suski, M. Boćkowski, J. Smalc-Koziorowska, M. Kryśko, R. Kudrawiec, M. Syperek, J. Misiewicz, Z. Wasilewski, S. Porowski, and C. Skierbiszewski, Optically pumped 500 nm InGaN green lasers grown by plasma-assisted molecular beam epitaxy, *J. Appl. Phys.* **110**, 063110 (2011).

[174] A. I. Duff, L. Lymperakis, and J. Neugebauer, Understanding and controlling indium incorporation and surface segregation on (In,Ga)N surfaces: An ab initio approach, *Phys. Rev. B* **89**, 085307 (2014).

[175] S. Albert, A. Bengoechea-Encabo, M. Sabido-Siller, M. Müller, G. Schmidt, S. Metzner, P. Veit, F. Bertram, M. Sánchez-García, J. Christen, and E. Calleja, Growth of InGaN/GaN core–shell structures on selectively etched GaN rods by molecular beam epitaxy, *J. Cryst. Growth* **392**, 5–10 (2014).

[176] D. van Treeck, S. Fernández-Garrido, and L. Geelhaar, Influence of the source arrangement on shell growth around GaN nanowires in molecular beam epitaxy, *Phys. Rev. Mater.* **4**, 013404 (2020).

[177] G. Koblmüller, R. Averbeck, H. Riechert, and P. Pongratz, Direct observation of different equilibrium Ga adlayer coverages and their desorption kinetics on GaN (0001) and (000$\bar{1}$) surfaces, *Phys. Rev. B* **69**, 1–9 (2004).

[178] T. E. Oliphant, Python for Scientific Computing, *Comput. Sci. Eng.* **9**, 10–20 (2007).

[179] S. van der Walt, S. C. Colbert, and G. Varoquaux, The NumPy Array: A Structure for Efficient Numerical Computation, *Comput. Sci. Eng.* **13**, 22–30 (2011).

[180] R. Songmuang, T. Ben, B. Daudin, D. González, and E. Monroy, Identification of III-N nanowire growth kinetics via a marker technique, *Nanotechnology* **21**, 295605 (2010).

[181] X. Zhang, B. Haas, J.-l. Rouvière, E. Robin, and B. Daudin, Growth mechanism of InGaN nano-umbrellas, *Nanotechnology* **27**, 455603 (2016).

[182] M. Gruart, G. Jacopin, and B. Daudin, Role of Ga Surface Diffusion in the Elongation Mechanism and Optical Properties of Catalyst-Free GaN Nanowires Grown by Molecular Beam Epitaxy, *Nano Lett.* **19**, 4250–4256 (2019).

[183] V. G. Dubrovskii and Y. Hervieu, Diffusion-induced growth of nanowires: Generalized boundary conditions and self-consistent kinetic equation, *J. Cryst. Growth* **401**, 431–440 (2014).

[184] O. Brandt, Y. J. Sun, L. Däweritz, and K. H. Ploog, Ga adsorption and desorption kinetics on M -plane GaN, *Phys. Rev. B* **69**, 165326 (2004).

[185] F. Widmann, B. Daudin, G. Feuillet, N. Pelekanos, and J. L. Rouvière, Improved quality GaN grown by molecular beam epitaxy using in as a surfactant, *Appl. Phys. Lett.* **73**, 2642–2644 (1998).

[186] J. Neugebauer, T. K. Zywietz, M. Scheffler, J. E. Northrup, H. Chen, and R. M. Feenstra, Adatom Kinetics On and Below the Surface: The Existence of a New Diffusion Channel, *Phys. Rev. Lett.* **90**, 4 (2003).

[187] O. Landré, R. Songmuang, J. Renard, E. Bellet-Amalric, H. Renevier, and B. Daudin, Plasma-assisted molecular beam epitaxy growth of GaN nanowires using indium-enhanced diffusion, *Appl. Phys. Lett.* **93**, 183109 (2008).

[188] M. Wölz, V. M. Kaganer, O. Brandt, L. Geelhaar, and H. Riechert, Analyzing the growth of $In_xGa_{1-x}N$/GaN superlattices in self-induced GaN nanowires by x-rax diffraction, *Appl. Phys. Lett.* **98**, 261907 (2011).

[189] R. Averbeck and H. Riechert, Quantitative Model for the MBE-Growth of Ternary Nitrides, *Phys. Status Solidi* **176**, 301–305 (1999).

[190] J. R. Lang and J. S. Speck, $NH_3$-rich growth of InGaN and InGaN/GaN superlattices by $NH_3$-based molecular beam epitaxy, *J. Cryst. Growth* **346**, 50–55 (2012).

[191] N. Grandjean and J. Massies, Real time control of $In_xGa_{1-x}N$ molecular beam epitaxy growth, *Appl. Phys. Lett.* **72**, 1078–1080 (1998).

[192] H. Chen, R. M. Feenstra, J. E. Northrup, J. Neugebauer, and D. Greve, Indium incorporation and surface segregation during InGaN growth by molecular beam epitaxy: experiment and theory, *MRS Internet J. Nitride Semicond. Res.* **6**, e11 (2001).

[193] J. Renard, G. Tourbot, D. Sam-Giao, C. Bougerol, B. Daudin, and B. Gayral, Optical spectroscopy of cubic GaN in nanowires, *Appl. Phys. Lett.* **97**, 081910 (2010).

[194] G. Jacopin, L. Rigutti, L. Largeau, F. Fortuna, F. Furtmayr, F. H. Julien, M. Eickhoff, and M. Tchernycheva, Optical properties of wurtzite/zinc-blende heterostructures in GaN nanowires, *Journal of Applied Physics* **110**, 064313 (2011).

[195] Y. H. Kim, J. Y. Lee, S.-H. Lee, J.-E. Oh, H. S. Lee, and Y. Huh, Indium-related novel architecture of GaN nanorod grown by molecular beam epitaxy, *Chemical Physics Letters* **412**, 454 – 458 (2005).

[196] P. Schley, R. Goldhahn, A. T. Winzer, G. Gobsch, V. Cimalla, O. Ambacher, H. Lu, W. J. Schaff, M. Kurouchi, Y. Nanishi, M. Rakel, C. Cobet, and N. Esser, Dielectric function and Van Hove singularities for In-rich $In_xGa_{1-x}N$ alloys: Comparison of N- and metal-face materials, *Phys. Rev. B* **75**, 205204 (2007).

[197] A. Kikuchi, M. Tada, K. Miwa, and K. Kishino, Growth and characterization of InGaN/GaN nanocolumn LED, In K. G. Eyink and D. L. Huffaker, editors, *Quantum Dots, Part. Nanoclusters III*, volume 6129, page 612905, SPIE (2006).

[198] J. Lähnemann, O. Brandt, C. Pfüller, T. Flissikowski, U. Jahn, E. Luna, M. Hanke, M. Knelangen, A. Trampert, and H. T. Grahn, Coexistence of quantum-confined Stark effect and localized states in an (In,Ga)N/GaN nanowire heterostructure, *Phys. Rev. B* **84**, 155303 (2011).

[199] A.-L. Bavencove, G. Tourbot, J. Garcia, Y. Désières, P. Gilet, F. Levy, B. André, B. Gayral, B. Daudin, and L. S. Dang, Submicrometre resolved optical characterization of green nanowire-based light emitting diodes, *Nanotechnology* **22**, 345705 (2011).

[200] D. van Treeck, J. Ledig, G. Scholz, J. Lähnemann, M. Musolino, A. Tahraoui, O. Brandt, A. Waag, H. Riechert, and L. Geelhaar, Electroluminescence and current–voltage measurements of single-(In,Ga)N/GaN-nanowire light-emitting diodes in a nanowire ensemble, *Beilstein J. Nanotechnol.* **10**, 1177–1187 (2019).

[201] Y. Sun, O. Brandt, S. Cronenberg, S. Dhar, H. T. Grahn, K. H. Ploog, P. Waltereit, and J. S. Speck, Nonpolar $In_xGa_{1-x}N/GaN(1\bar{1}00)$ multiple quantum wells grown on $\gamma$-$LiAlO_2(100)$ by plasma-assisted molecular-beam epitaxy, *Phys. Rev. B* **67**, 41306 (2003).

[202] P.-M. Coulon, S. hosseini Vajargah, A. Bao, P. R. Edwards, E. D. Le Boulbar, I. Girgel, R. W. Martin, C. J. Humphreys, R. A. Oliver, D. W. Allsopp, and P. A. Shields, Evolution of the m-Plane Quantum Well Morphology and Composition within a GaN/InGaN Core–Shell Structure, *Cryst. Growth Des.* **17**, 474–482 (2017).

[203] D. N. Nath, E. Gür, S. A. Ringel, and S. Rajan, Growth model for plasma-assisted molecular beam epitaxy of N-polar and Ga-polar (In,Ga)N, *J. Vac. Sci. Technol. B, Nanotechnol. Microelectron. Mater. Process. Meas. Phenom.* **29**, 021206 (2011).

[204] T. Böttcher, S. Einfeldt, V. Kirchner, S. Figge, H. Heinke, D. Hommel, H. Selke, and P. L. Ryder, Incorporation of indium during molecular beam epitaxy of InGaN, *Appl. Phys. Lett.* **73**, 3232–3234 (1998).

[205] D. F. Storm, Incorporation kinetics of indium and gallium in indium gallium nitride: A phenomenological model, *J. Appl. Phys.* **89**, 2452–2457 (2001).

[206] Y. Horikoshi, Advanced epitaxial growth techniques: atomic layer epitaxy and migration-enhanced epitaxy, *J. Cryst. Growth* **201-202**, 150–158 (1999).

[207] D. Jena, Successes of Wide-Bandgap Electronics and Future Directions, *12th Int. Conf. Nitride Semicond.* (2017).

[208] H. Amano, Transformative Electronics for Realizing Sustainable, Smart, Secure and Safe Society, *Int. Work. Nitride Semicond.* (2018).

[209] J. W. Matthews and A. E. Blakeslee, Defects in epitaxial multilayers I. Misfit dislocations, *J. Cryst. Growth* **27**, 118–125 (1974).

[210] F. Templier and J. Bernard, A New Approach for Fabricating High-Performance MicroLED Displays, *SID Symp. Dig. Tech. Pap.* **50**, 240–243 (2019).

[211] H. E. Lee, J. H. Shin, J. H. Park, S. K. Hong, S. H. Park, S. H. Lee, J. H. Lee, I. S. Kang, and K. J. Lee, Micro Light-Emitting Diodes for Display and Flexible Biomedical Applications, *Adv. Funct. Mater.* **29**, 1–14 (2019).

[212] D. van Treeck, S. Fernández-Garrido, and R. B. Lewis, Semiconductor device with at least one functional element containing multiple active regions, and method of manufacturing thereof, *Eur. Pat. Off.* **EP3531459** (2019).

[213] M. Heigoldt, J. Arbiol, D. Spirkoska, J. M. Rebled, S. Conesa-Boj, G. Abstreiter, F. Peiró, J. R. Morante, and A. Fontcuberta i Morral, Long range epitaxial growth of prismatic heterostructures on the facets of catalyst-free GaAs nanowires, *J. Mater. Chem.* **19**, 840 (2009).

[214] R. W. Day, M. N. Mankin, and C. M. Lieber, Plateau-Rayleigh Crystal Growth of Nanowire Heterostructures: Strain-Modified Surface Chemistry and Morphological Control in One, Two, and Three Dimensions, *Nano Lett.* **16**, 2830–2836 (2016).

[215] O. Brandt, P. Waltereit, S. Dhar, U. Jahn, Y. Sun, A. Trampert, K. H. Ploog, M. Tagliente, and L. Tapfer, Properties of (In,Ga)N/GaN quantum wells grown by plasma-assisted molecular beam epitaxy, *J. Vac. Sci. Technol. B Microelectron. Nanom. Struct.* **20**, 1626 (2002).

[216] J. K. Hyun, S. Zhang, and L. J. Lauhon, Nanowire Heterostructures, *Annu. Rev. Mater. Res.* **43**, 451–479 (2013).

[217] S. M. Sadaf, Y.-H. Ra, H. P. T. Nguyen, M. Djavid, and Z. Mi, Alternating-Current InGaN/GaN Tunnel Junction Nanowire White-Light Emitting Diodes, *Nano Letters* **15**, 6696–6701 (2015).

[218] Y.-H. Ra, R. Wang, S. Y. Woo, M. Djavid, S. M. Sadaf, J. Lee, G. A. Botton, and Z. Mi, Full-Color Single Nanowire Pixels for Projection Displays, *Nano Letters* **16**, 4608–4615 (2016).

[219] K. Suzue, S. N. Mohammad, Z. F. Fan, W. Kim, O. Aktas, a. E. Botchkarev, and H. Morkoç, Electrical conduction in platinum–gallium nitride Schottky diodes, *J. Appl. Phys.* **80**, 4467 (1996).

[220] M. Musolino, D. van Treeck, A. Tahraoui, L. Scarparo, C. D. Santi, M. Meneghini, E. Zanoni, L. Geelhaar, and H. Riechert, A physical model for the reverse leakage current in (In,Ga)N/GaN light-emitting diodes based on nanowires (2016).

# List of Figures

# Acknowledgements

When I left the Paul-Drude-Institut für Festkörperelektronik (PDI), I was very confident that I would finish my thesis within the next few months. Taking care of my baby daughter as my only task for the next half a year for sure should leave me enough time to write the last chapters of my thesis. That's what I naively thought, two years ago! Two years that taught me a lot about setting priorities in my personal life while somehow managing to finish this thesis. I am all the more pleased and relieved that I am now writing the last sentences. This work, of course, would not have been possible without the help of numerous people who supported me in many ways during my time at PDI and over the last years. To these people I want to express my deepest gratitude.

I want to thank my doctoral supervisor and the former director of the PDI, Prof. Dr. Henning Riechert, for giving me the opportunity to work at PDI and conduct my scientific studies. He always had a listening ear for the needs of his PhD students and offered help, whenever I approached him. Especially, I appreciate his support for the patenting of our idea for a multi-functional nanowire-based device. Moreover, I am very grateful to Prof. Dr. Ted W. Masselink and Prof. Dr. Bruno Daudin for reviewing this thesis.

I want to thank Dr. Lutz Geelhaar for his scientific supervision as the head of the epitaxy department and the Nanowire group. With his fine sense for the right amount of guidance and support, he helped me to confidently follow my scientific ideas and to learn the important aspects of good scientific practice. I always appreciated very much his advice, which usually got directly to the heart of the matter. I am very grateful for all the proof readings and rehearsals for manuscripts, talks and finally this thesis which taught me a great deal about good scientific style. And not to forget, thank you Lutz for all the Glühwein at the annual "Christmas field trip" of the Nanowire group.

I want to thank Dr. Sergio Fernández-Garrido who supervised me during the first part of my thesis. He taught me everything I needed to know about MBE and it is safe to say that without his work and the countless discussions about results and ideas, many studies presented in this thesis would not have been possible. It was a true privilege to work with such a skilled, honest, and sympathetic person like you, thanks Sergio. I also want to thank Dr. Oliver Brandt whose door was always open to discuss "urgent" scientific questions. From MBE growth on novel substrates to luminescence properties of weirdly shaped insertions in NWs, he always provided me with profound answers. Thanks Oliver, for all the fruitful discussions about science, the critical reading of numerous abstracts and manuscripts, and sharing the latest news about Arch-based linux distributions.

I want to thank my colleagues Dr. Thomas Auzelle, Dr. Javier Bartolomé, Dr. Gabriele Calabrese, Dr. Guanhui Gao, Jelle Goertz, Dr. Jonas Lähnemann, Dr. Ryan Lewis, Dr. Carsten Pfüller, and Kilian Wimmer who, through discussions, advice and important measurements, in one or the other way essentially contributed to my work at PDI. Thanks guys, without your support, this thesis would not have been possible.

I thank Dr. Vladimir Kaganer for his advice regarding the simulation of NW growth processes, Dr. Achim Trampert for fruitful discussions about transmission electron microscopy results, and Dr. Abbes Tahraoui for his scientific support for the optimization of the sample processing. Moreover, I thank Sebastian Meister, Sander Rauwerdink and Walid Anders for the realization of the processing of many samples and the constructive feedback which helped to further improve the outcome.

I thank Carsten Stemmler, Hans-Peter Schönherr, Michael Höricke and Katrin Morgenroth for the maintenance and constant improvement of the MBE systems. Even facing long down times of the MBE system, with your technical support, I had the privilege to focus on my research while being confident that I would soon be able to continue my studies under the best possible conditions. I thank Claudia Herrmann for taking care of the chemical lab which was important for the preparation of my samples. Furthermore, I thank Anne-Kathrin Bluhm for providing hundreds of scanning electron micrographs for my studies during my time at PDI. Thank you all very much.

I thank Andreas Hartung who was always a great help regarding the organizational and bureaucratic aspects during my time as a PhD and a Master student at PDI. Moreover, I thank Mercedes Reischel for her support with the patenting process and subsequent efforts for the further exploitation of the patent idea.

For me PDI was a very special place. I got to know a lot of great people from all over the world with very different personal backgrounds. Thanks to all of you who made my time at PDI such a memorable one. Thanks for the fun at WG parties, pub nights and lunch times, for the about 42 kg of "kinder Schokolade" I swiped from the fridge at late hours, for pistachios, Brigadeiros, and self-made nut-balls, for the deep discussions about life, the universe and everything, for regular good-morning compliments, for not always taking me seriously, for the delicious cookies and interesting talks at the student seminars, for unforgettable times at summer schools and conferences, and for all the other great memories.

Moreover, I want to thank my family and my friends who played a very important role for me in the process of finishing this thesis. To all of you, thanks a lot for your support and all the nice distractions during stressful times. And Hanno, you were perfectly right when you said that it was a great privilege, to have such a good and old friend working next door. Thank you for your countless motivation speeches and the clear words in the right moments. I also want to thank my parents for their continuous moral support and for all the babysitting which allowed me to focus on my work. Finally, I want to thank the two most important persons in my life: Sonja, Juna and Lori. You were the ones that always had my back. I am deeply grateful for your endless understanding, for all the

hardship you have put up with, for taking all my wailing, and for reminding me of the essential things in life during this never ending writing process. This thesis is dedicated to you.

# Selbstständigkeitserklärung

Ich erkläre, dass ich die Dissertation selbständig und nur unter Verwendung der von mir gemäß § 7 Abs. 3 der Promotionsordnung der Mathematisch-Naturwissenschaftlichen Fakultät, veröffentlicht im Amtlichen Mitteilungsblatt der Humboldt-Universität zu Berlin Nr. 42/2018 am 11.07.2018 angegebenen Hilfsmittel angefertigt habe.

Berlin, den 09.05.2021

David van Treeck